DYNAMIC ACCRETION DISCS AROUND SUPERMASSIVE BLACK HOLES

Thesis submitted for the degree of Doctor of Philosophy at the University of Leicester

ANAGHA RAJ

Department of Physics and Astronomy

University of Leicester

August 2020

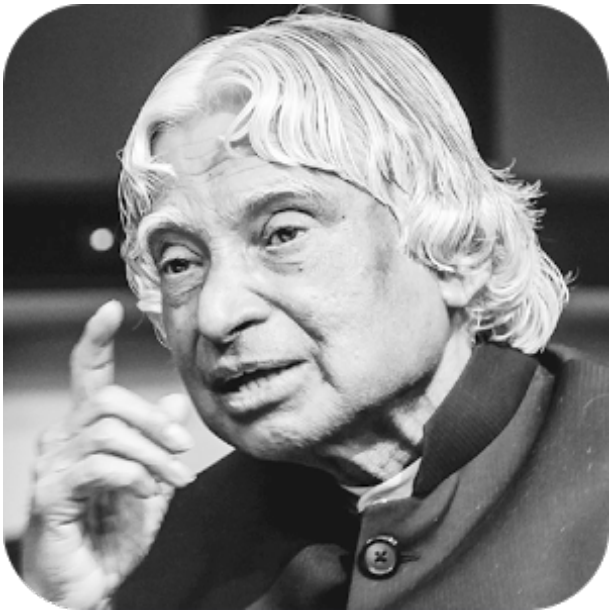

Look at the sky. We are not alone.
The whole universe is friendly to us
and conspires only to give the best
to those who dream and work.

- Dr. A P J Abdul Kalam

Abstract

Dynamic accretion discs around supermassive black holes

by Anagha Raj

Accretion discs around supermassive black holes act as the power houses of radiation to the most luminous, continuously emitting objects in the Universe; Active Galactic Nuclei (AGN). Accretion discs produce light, which we can observe by turning gravitational potential energy into heat via viscous torques. For discs around black holes, the available gravitational energy is the significant fraction of the rest mass energy of the orbiting matter. Simple, analytical models are capable of explaining the broad features of observed accreting black holes. However, recent observations have challenged existing theories by finding that AGN luminosities vary rapidly and with large amplitudes. In this thesis, we investigate the dynamics of warped discs with numerical simulations to see if such variability can be produced by these discs. Previous works have provided a criterion for warped discs to tear into discrete rings. We examine this possibility and explore how this may connect to observed disc behaviour. We demonstrate an agreement between our numerical results and the predicted criterion for disc tearing in warped discs around supermassive black holes. We also explore how our numerical analysis prove useful to illustrate the observational variability exhibited in AGN discs. In the later chapter, we show that often used initial conditions for accretion discs in simulations that employ Smoothed Particle Hydrodynamics (SPH) are not in dynamical equilibrium, and this leads to the formation of unwanted pressure waves that cannot be effectively damped at higher resolution. We propose a damping scheme, which uses an initial relaxing phase to remove these waves over a timescale comparable with the disc's dynamical timescale.

Acknowledgements

I look back with a lot of satisfaction and pride while thinking of my time spent at University of Leicester. I have met a lot of people who have inspired and helped me complete this work.

First and foremost, I would like to thank my supervisor Dr. Chris Nixon for his invaluable support, non-compromising standards of perfection at work, expert guidance, dedication and patience at every step of my research. I am deeply thankful for our numerous discussions and his useful remarks and suggestions without which I would not have been able to complete this work.

I would like to thank Prof. Jim Pringle for his insightful comments and suggestions on my work which helped me to improve different parts of my thesis. I also express my gratitude to Dr. Suzan Doğan for her enthusiasm and motivation at many stages of my work. I thank Lisa Brant, Kiri Humphreys and Patricia Russell for their help in managing my admin work and travel .

I thank my friends and colleagues, Elen Golightly, Miriam Hogg, Ryan Heath, Giulia Ballabio and Alison Young for the many delightful conversations which assisted me through my research as well as my university life in Leicester.

I owe big thanks to my mum, Tara and my sister, Meghana for their unconditional love in my life. I am grateful to Doug, my partner for his unmeasurable support and for making me realise yet again, that teaching is a great career to follow. I dedicate this thesis to the memories of my papa and grandma, whom I miss every day and who taught me the importance of working hard to reach my goals.

Contents

List of Figures

List of Tables

1

Introduction

Black holes are among the most extreme objects in the Universe. The gravitational field generated by a black hole is so strong that nothing, not even light can escape out of it. The surface bounding the region of no escape around a black hole is termed as the event horizon. Outside of the event horizon, black holes are nature's simplest objects which are defined by their mass and spin angular momentum. Black holes can also have a charge which in astrophysical concept is taken to be zero.

The possibility of the existence of black holes was first discussed at the end of the 18th century by John Michell and Pierre-Simon Laplace. The theory of relativity was first proposed by Albert Einstein in 1915. A year after, Karl Schwarzschild deduced the spherically symmetric vacuum solution of Einsteins equations describing the exterior gravitational field of a spherically symmetric body and derived the Schwarzschild solution characterising spherical, non-rotating black holes (Schwarschild radius R_s). It was not until 1963 when, Roy Kerr determined a solution corresponding to spinning black holes. This was termed as the Kerr solution, and it played an important role in understanding the energetics of a spinning black hole. This solution infers that the space outside of a spinning black hole rotates like a vortex. This tends to drag nearby matter into rotation around the black hole and this effect is termed as frame-dragging. Initially, the existence of black holes remained virtually as theoretical and mathematical ideas. While the physicists had

been struggling to research more on the theory of black holes, astronomers had looked for real examples of black holes in the Universe.

Astronomers discovered dozens of compact objects identified as black hole candidates with masses greater than the mass of a neutron star at $3M_{\odot}$ where $M_{\odot}$ is the mass of the Sun (Shapiro & Teukolsky, 1983). In terms of their masses, black holes are categorised into two classes - those with masses $\sim$ 5 - 20 $M_{\odot}$ termed as stellar mass black holes typically found in X-Ray binaries; and those with masses $\sim$ 10^6 - 10^{10} $M_{\odot}$ named as supermassive black holes residing at the centre of galaxies. For a black hole of mass M and radius R_s, the gravitational potential energy released per unit mass accreted is given as (Frank et al., 2002)

$$\Delta E_{\rm acc} = \frac{GM}{R_s} \tag{1.1}$$

where $R_s = 2GM/c^2$, so $\Delta E_{\rm acc} = 0.5c^2$. This energy yield is much higher in comparison to the nuclear fusion in stars (or burning of hydrogen to helium) with an energy release of $\Delta E_{\rm acc} = 0.007c^2$.

Quasars, first discovered in the late 50s in all sky radio surveys (the term quasars is a contraction for quasi stellar radio source) were quickly identified as accreting black holes (Matthews et al., 1964; Salpeter, 1964; Zel'dovich, 1964). Around the same time, Cygnus X-1 was discovered and identified as one of the brightest X-ray sources in the sky. In 1971, Thomas Bolton, Louise Webster and Paul Murdin found that Cygnus X-1 had a massive stellar companion. By studying the orbital motion of the companion star, the mass of the compact object in Cygnus X-1 was calculated and it exceeded the maximum value for the mass of a neutron star. As a result, Cygnus X-1 was identified as the first stellar mass black hole candidate. Thereafter, an increasing number of observations indicated the presence of stellar mass black holes in X-ray binaries (Remillard & McClintock, 2006) and supermassive black holes at the centre of many galaxies (Kormendy & Richstone,

1995).

There are several methods to estimate the mass of black holes such as, by studying the orbital motion of nearby stars or by observational techniques such as gravitational microlensing or reverberation mapping (discussed in detail in section 1.2.3). There have also been significant efforts to measure black hole spins using different methods. The two main techniques are the continuum-fitting method (Zhang et al., 1997; McClintock et al., 2014) and X-ray reflection spectroscopy or iron line method (Brenneman & Reynolds, 2006; Reynolds, 2014). With better technological progress and improvements in observational facilities over many years, there has been substantial progress in the study of astrophysical black holes. In 2015, the LIGO experiment detected gravitational waves from the coalescence of two black holes (Abbott et al., 2016) and the Event Horizon Telescope collaboration released the first image of a black hole in 2019 (Akiyama et al., 2019).

1.1 Physical properties

Each black hole is characterised by two parameters: mass M and the dimensionless spin parameter a that measures the rotation rate of the black hole and ranges between 0 (for a non spinning BH) to 1 (maximally-spinnning BH). From observational evidence, we classify astrophysical black holes into two classes: stellar-mass black holes (1 - 100 $M_{\odot}$) and the most spectacular supermassive black holes (10^5 - 10^{10} $M_{\odot}$) which power active galactic nuclei or AGN. A third class of objects named as intermediate mass black holes (100 - 10000 $M_{\odot}$) are believed to be formed by collision or merging of stellar mass black holes, but their nature still remains controversial (Bambi, 2019).

1.1.1 Stellar Mass Black Holes

Stellar mass black holes are remnants of collapsed, massive stars. Many of such candidates are expected to be found in X-ray binaries and close binary systems. The initial mass of a stellar-mass black hole depends on the properties of the progenitor star which includes: its mass, its evolution, and the supernova explosion mechanism (Belczynski et al., 2010).

It is important to distinguish the black hole candidates from the accreting neutron stars (also found in X-ray binaries). Hence, a lower bound in the maximum mass (around 2 - 3 $M_\odot$) is used to distinguish between a neutron star and black hole. A star collapses when it depletes the nuclear material and its gas pressure can no longer balance the gravitational force. At masses below 2 - 3 $M_\odot$, the quantum pressure of neutrons and electrons can prevent the star's collapse, thus forming neutron stars. On the other hand, bodies exceeding this mass limit collapse and form black holes (Rhoades & Ruffini, 1974; Kalogera & Baym, 1996; Lattimer, 2012).

Black holes in X-ray binaries (or black hole binaries) are classified into two types: low-mass X-ray binaries (LMXBs) and high-mass X-ray binaries (HMXBs). Low and high are referred in terms of the mass of the stellar companion. In LMXBs, the companion star has a mass $M < 3M_\odot$, whereas for HMXBs the companion star has $M > 10M_\odot$. The dynamical measurements of their masses are done by studying the orbital motion of the companion star. The mass function $f(M)$ is given as (Casares & Jonker, 2014)

$$f(M) = \frac{K_c^3 P_{\rm orb}}{2\pi G_N} = \frac{M \sin^3 i}{(1 + M_c/M)^2} \tag{1.2}$$

where $K_c = v_c \sin i$, v_c is the velocity of the companion star, i is the angle between the normal of the orbital plane and the observer's line of sight, $P_{\rm orb}$ is the orbital period of the system, M_c is the mass of the companion star and M is the mass detected using dynamical measurements (or mass of a black hole if $M > 3M_\odot$). Combining measurements of K_c

and $P_{\rm orb}$ with estimates of i and M_c, the masses of X-ray emitting stars in several X-ray binaries with stellar mass black hole could be measured.

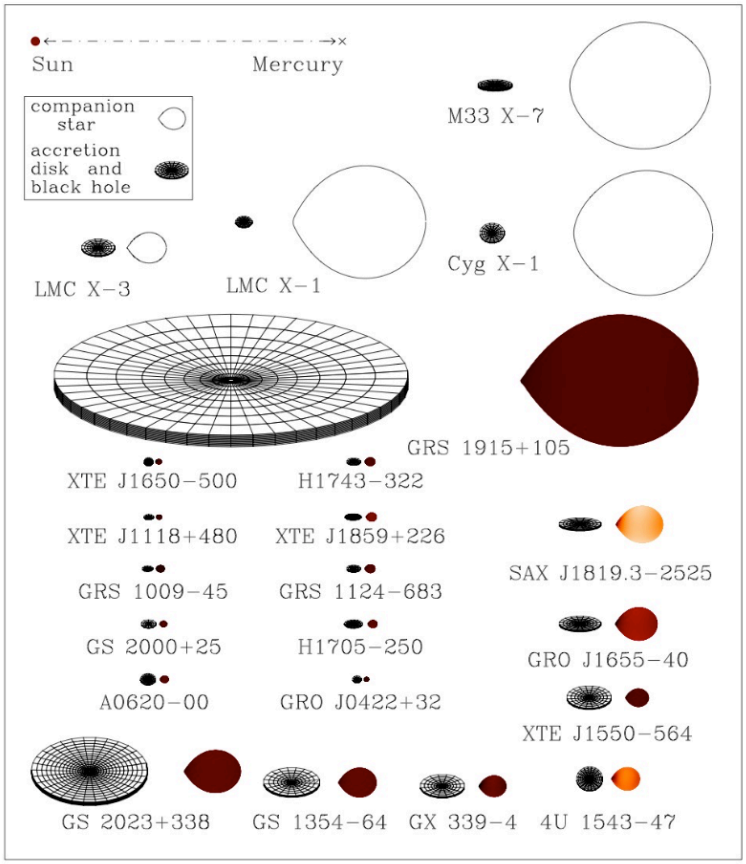

Figure 1.1: Sketch of 22 X-ray binaries with a stellar-mass black hole confirmed by dynamical measurements is shown. The black hole accretion disk is on the left, and the companion star is on the right for every system. In order to have an idea of the size of these systems, the figure also shows the Sun (whose radius is 0.7 millions km) and the distance Sun-Mercury (about 50 millions km). Figure courtesy of Jerome Orosz.

Figure 1.1 shows 22 X-ray binaries with a stellar mass black hole confirmed by dynamical measurements where Cygnus X-1, LMC X-1, LMC X-3, and M33 X-7 are HMXBs, while all other systems are LMXBs. Recently, it has become possible through gravitational wave astronomy to detect black holes, in binary systems in the process of merging. These include black hole - black hole and black hole - neutron star binaries. Figure 1.2 shows the black hole masses (pre mergers and post mergers) observed by the LIGO/Virgo collaboration.

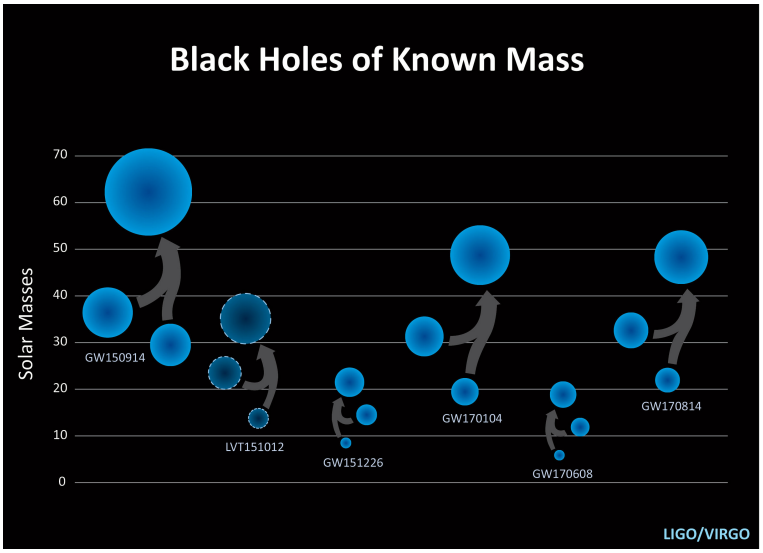

Figure 1.2: Gravitational waves events showing black holes observed by gravitational waves, with the two initial objects merging to form a larger one, as shown by the arrows (Image Credit: LIGO/NSF/Caltech/SSU Aurore Simmonet).

Furthermore, black holes with a mass range $\sim 10^2$ - 10^4 $M_\odot$ are termed as Intermediate-mass black holes (IMBHs). The existence of intermediate-mass black holes is associated with some ultra-luminous X-ray sources by the detection of quasi-periodic oscillations (QPOs) (Colbert & Mushotzky, 1999). A transient X-ray source named HLX-1 of mass ≥ 500 $M_\odot$ at the centre of the galaxy ESO 243-49 is a recognised example of an intermediate mass black hole (Farrell et al., 2009). However, there are no dynamical measurements done so far to study IMBHs since their actual nature is still not well understood. Although some studies suggest that there are intermediate-mass black holes at the centre of certain globular clusters, there is no common agreement to that theory yet (Gebhardt et al., 2002; Gebhardt et al., 2005).

1.1.2 Supermassive Black Holes

Astronomical observations indicate the presence of supermassive black holes with masses ranging $10^5 - 10^{10} M_\odot$ at the centre of a large number of galaxies. The strongest dynamical evidence for a supermassive black hole is from the centre of our own galaxy, the Milky Way. Several observations in the infrared, radio and in X-ray wavelengths showed the presence of a compact source of radiation at the Galactic Centre named as Sagittarius A^*

($Sgr\ A^*$) with mass $\sim 4 \times 10^6 M_\odot$, calculated from the proper motions of the surrounding stars (Schödel et al., 2002).

Additional evidence for a supermassive black hole comes from the maser emission due to water molecules at the centre of the galaxy NGC 4258 (Miyoshi et al., 1995). Radio interferometry measurements were used to map the radial velocities, proper motions and accelerations of the masers which were consistent with Keplerian dynamics (Bragg et al., 2000). These measurements inferred the presence of a black hole at the centre of NGC 4258 with a mass of $3.5 \times 10^7 M_\odot$.

Although, the stellar-mass black holes in the Universe are expected to be the final product of heavy stars, the exact origin of the supermassive black holes at the centre of galaxies is not fully understood. A few possibilities of their origin include, the collapse of heavy primordial clouds at initial masses much larger than stellar mass black holes or from the merger of several black holes (Volonteri, 2010). Over the last few years, it has become clear that supermassive black holes can grow to masses $\sim 10^{10}\ M_\odot$ when the Universe is only 1 Gyr old (Wu et al., 2015; McLure & Jarvis, 2002). This requires the black holes to grow with higher accretion efficiencies and higher accretion rates.

Furthermore, Willott et al. (2003) discusses near infrared observations of quasars demonstrating evidence of supermassive black holes with mass $M \geq 5 \times 10^9 M_\odot$ at a redshift of $z \simeq 6$. This finding presented a challenge to theoretical models which prompted King & Pringle (2006, 2007) to propose the idea of chaotic accretion. In this picture, accretion proceeds through a sequence of events with each accretion disc forming at a random angle to the black hole spin vector (further discussed in the following section).

1.1.3 Black hole spin

For a black hole with mass M and angular momentum J, we define the spin parameter as:

$$a = \frac{cJ}{GM^2} \tag{1.3}$$

where c is the speed of light and G is the gravitational constant. When circular orbits in a BH spacetime are considered, a key concept is the innermost stable circular orbit $R_{\rm ISCO}$ (also referred as the marginally stable orbit). In an accretion disc, the gas starts from a large radii and spirals in through a sequence of circular orbits. When the gas reaches the ISCO, there are no more stable circular orbits available. As a result, the gas accelerates radially and free falls into the BH. Therefore, circular orbits with radii $R \geq R_{\rm ISCO}$ are stable, whereas those with $R < R_{\rm ISCO}$ are unstable.

ISCO: Schwarzschild and Kerr black holes

The inner most stable orbit in an accretion disc, $R_{\rm ISCO}$ is dependent on the black hole spin a. For the general case of a spinning black hole, the spacetime is described by the Kerr metric which is simplified to the Schwarzschild metric when the spin parameter $a = 0$. In the case of a Schwarzschild black hole, the effective potential is given as (Hobson et al., 2005)

$$V_{\rm eff} = \frac{h^2}{2r^2} - \frac{GM}{r} - \frac{GMh^2}{c^2r^3} \tag{1.4}$$

where h represents the specific angular momentum.

$$\frac{dV_{\rm eff}}{dr} = -\frac{h^2}{r^3} + \frac{GM}{r^2} + \frac{3GMh^2}{c^2r^4} = 0 \tag{1.5}$$

This can be rewritten as

$$-h^2r + GMr^2 + \frac{3GMh^2}{c^2} = 0. \tag{1.6}$$

This equation is quadratic in r and the solution is given as:

$$r = \frac{h}{2GM}\left[h \pm \sqrt{h^2 - \frac{12G^2M^2}{c^2}}\right], \tag{1.7}$$

- if $h^2 - \frac{12G^2M^2}{c^2} > 0$, it can either give a minima (for stable circular orbit) or maxima (unstable orbit).
- if $h^2 - \frac{12G^2M^2}{c^2} < 0$, no circular orbits are possible.
- if $h^2 - \frac{12G^2M^2}{C^2} = 0$, the system has its critical point at $h^2 = \frac{12G^2M^2}{c^2}$.

Substituting $h^2 = \frac{12G^2M^2}{c^2}$ in equation (1.7) gives:

$$r = \frac{h^2}{2GM} = \frac{6GM}{c^2}. \tag{1.8}$$

This gives the value of the innermost stable circular orbit for a Schwarzschild black hole. The same derivation can be extended for Kerr black holes and one can examine how the ISCO values differ for spinning black holes at values of a varying between -1 and $+1$. The equation of the first derivative of the effective potential in Kerr metric is given as (Hobson et al., 2005)

$$\frac{dV_{\text{eff}}}{dr} = r^2 - \frac{6GMr}{c^2} - 3a^2\frac{G^2M^2}{c^4} + 8a\frac{GM}{c^2}\sqrt{\frac{GMr}{c^2}} = 0. \tag{1.9}$$

Therefore,

$$r^2 - \frac{6GMr}{c^2} - 3a^2\frac{G^2M^2}{c^4} + 8a\frac{GM}{c^2}\sqrt{\frac{GMr}{c^2}} = 0 \tag{1.10}$$

where a is the spin parameter and we get:

$$r_{\text{ISCO}} = \frac{6GM}{c^2} \quad \text{for} \quad a = 0 \quad \text{(Schwarzschild black hole)}, \tag{1.11}$$

$$r_{\text{ISCO}} = \frac{GM}{c^2} \quad \text{for} \quad a = +1 \quad \text{(Maximum prograde)}, \tag{1.12}$$

$$r_{\rm ISCO} = \frac{9GM}{c^2} \quad \text{for} \quad a = -1 \quad \text{(Maximum retrogade)}. \tag{1.13}$$

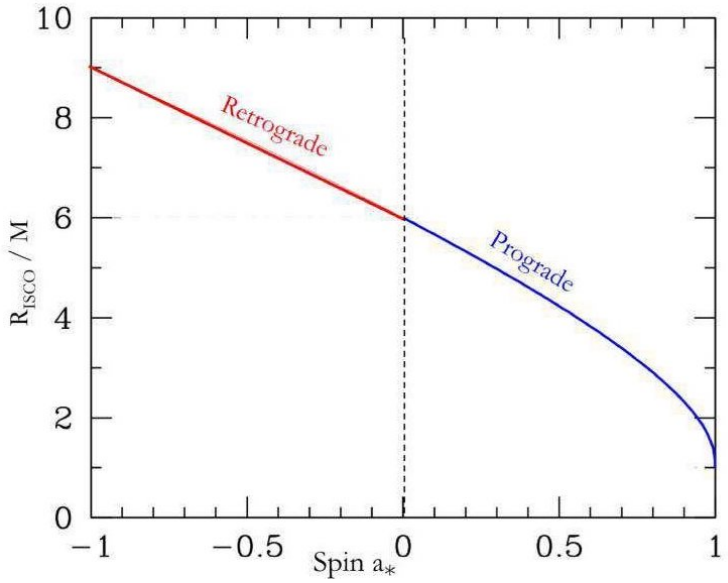

Figure 1.3: This plot shows the variation of the inner most stable orbit ($R_{\rm ISCO}$ assuming $G = M = c = 1$) varies with black hole spin a (Image taken from De Rosa et al. (2019)).

Figure 1.3 shows the variation of $R_{\rm ISCO}$ with spin a. For a maximally spinning BH ($a = +1$), $R_{\rm ISCO} = GM/c^2$ with the orbit co-rotating with the BH spin (prograde). The value of $R_{\rm ISCO} = 9GM/c^2$ with the orbit counter-rotating or in retrograde motion ($a = -1$) and for a non-spinning or Schwarzchild BH ($a = 0$), $R_{\rm ISCO} = 6GM/c^2$.

A significant quantity considered in the astronomical observations of accreting black holes is the accretion luminosity of the source measured in Eddington units. It is required that the inward gravitational force on the gas must balance or be greater than the force due to outward radiation such that the central object remains intact, i.e. $|F_{\rm rad}| \leq |F_{\rm grav}|$ where $F_{\rm rad} = \sigma_e L/4\pi r^2 c$ and $F_{\rm grav} = GMm_p/r^2$ (Peterson, 1997).

$$\sigma_e \frac{L}{4\pi r^2 c} \leq \frac{GMm_p}{r^2} \tag{1.14}$$

$$L \leq \frac{4\pi GcMm_p}{\sigma_e} \tag{1.15}$$

Therefore, the Eddington luminosity for a black hole of mass M is given as:

$$L_{\rm Edd} = \frac{4\pi G M m_p c}{\sigma_e} = 1.26 \times 10^{38} \frac{M}{M_\odot} \text{ erg s}^{-1} \tag{1.16}$$

where σ_e is the electron (Thomson) cross section and m_p is the mass of a proton (also given by equation 3.3 in Peterson (1997)). Assuming that SMBHs acquire most of their mass by accretion, Soltan (1982) showed that the accretion luminosity due to the accretion rate of mass in black holes is given as:

$$L_{\rm acc} = \epsilon \dot{M}_{\rm acc} c^2 \tag{1.17}$$

where ϵ is the accretion efficiency determined by the fractional binding energy of the innermost stable circular orbit (ISCO), c is the speed of light and $\dot{M}_{acc}$ is the rate of mass accretion.

Bardeen (1970) established the relation between $R_{\rm ISCO}$, spin a and accretion efficiency ϵ, i.e:

$$\epsilon = 1 - \left[1 - \frac{2}{3x}\right]^{1/2} \tag{1.18}$$

$$a = \frac{x^{1/2}}{3}\left[4 - (3x-2)^{1/2}\right] \tag{1.19}$$

with $R_{\rm ISCO} = x\ GM/c^2$ where x = 9,6 and 1 for spin parameters $a = -1, 0$ and $+1$ respectively. As mentioned earlier, there is observational evidence of supermasssive black holes with masses $\geq 10^9 M_\odot$ at redshift $z \approx 6$ (Willott et al., 2003). Assuming that its accretion luminosity cannot exceed the value:

$$L_{\rm acc} = \frac{4\pi G M c}{\kappa} \simeq 10^{47}\ erg\ s^{-1} \tag{1.20}$$

for $M = 10^9 M_\odot$, where $\kappa = m_p/\sigma_T = 0.4$ cm^{2}g^{-1} is the electron scattering (Thomson) opacity. King & Pringle (2006) showed that Soltan's assumption (equation 1.17) can set

a limit on the growth of SMBH. The accretion rate can be limited by the Eddington limit given by

$$\epsilon \dot{M}_{\rm acc} c^2 \leq L_{\rm Edd} = \frac{4\pi G M c}{\kappa}, \tag{1.21}$$

$$\dot{M}_{\rm acc} \leq \frac{1}{\epsilon}.\frac{4\pi G M}{\kappa c}. \tag{1.22}$$

If we assume, that the accretion of matter proceeds at a rate

$$\dot{M} = (1-\epsilon)\dot{M}_{\rm acc} \tag{1.23}$$

Substituting equation 1.22 in 1.23 gives

$$\dot{M} = \frac{1-\epsilon}{\epsilon}\frac{M}{t_{Edd}} \tag{1.24}$$

where

$$t_{\rm Edd} = \frac{\kappa c}{4\pi G} = 4.5 \times 10^8 \text{ yrs.} \tag{1.25}$$

King & Pringle (2006) shows that although the value of ϵ changes as accretion proceeds, its minimum of ϵ_{min} places a limit on the mass M to which the black hole grows from an initial seed mass of M_0 in a given time. Integrating equation 1.24 gives (King & Pringle, 2006)

$$\frac{M}{M_0} < \exp\left[\left(\frac{t}{t_{\rm Edd}}\right)\left(\frac{1}{\epsilon_{\rm min}} - 1\right)\right]. \tag{1.26}$$

At a redshift of z $\simeq$ 6, the value of $t/t_{Edd} \simeq 2$. Thus, for a maximally spinning black hole at $a = 1$, the value of $\epsilon_{\rm min} = 0.43$ and $M/M_0 \leq 20$. On the other hand, if $\epsilon_{\rm min} \simeq 0.06$ for spin parameter values $a \simeq 0.3$ - 0.4, then $M/M_0 \sim 4 \times 10^{13} M_\odot$. This shows that it is possible to grow the black holes rapidly if we can keep the spin low.

As we know, galactic nuclei are chaotic environments where random injections of energy and momentum occur. The gas falling into the nuclei, has no prior knowledge of the SMBH angular momentum and settles into a disc at a random angle of misalignment

between the disc (J_d) and the SMBH angular momentum (J_h). The chaotic infalling of gas can induce warping in discs due to the Lense Thirring effect (detailed in Section 1.5 and chapter 3) in spinning SMBHs (Bardeen & Petterson, 1975). Since accretion occurs in both retrograde and prograde discs at different epochs, the chaotic infall of gas in SMBHs is suggested as a mechanism to keep the spin low thereby allowing the growth of SMBHs from stellar mass seeds (King & Pringle, 2006, 2007; King et al., 2008).

1.2 Observational properties of AGN

The spectra of galaxies with highly luminous nuclei, termed as Active Galactic Nuclei (AGN) show broad emission lines covering a wide range of ionisation. In terms of their broad limits of luminosity, these range from the brightest quasi-stellar objects (QSOs) or quasars to the more common and less luminous Seyfert galaxies. There are two significant properties, which make AGNs very interesting to study. Firstly, their ability to generate extraordinary luminosities in tiny volumes (Edelson et al., 1996). The second are their spectral features ranging over several orders of magnitude in luminosity across the various wavebands. In this section, we review some of the observational characteristics in AGNs.

1.2.1 Spectra

As mentioned earlier, the output spectrum of AGN includes a huge range of wavelengths, covering most of the electromagnetic spectrum. The spectral energy distribution (SED) is a plot of frequency multiplied by flux (νF_ν) against frequency (ν). In the case of a typical AGN spectrum, the spectrum peaks in the infrared (named the IR bump) and the optical/UV (the UV bump). The UV bump takes the shape of the black body spectrum, which represents the thermal emission from the accretion disc. On the other hand, the IR radiation is the characteristic of the thermal emission from dust. The relative strengths of these two peaks differ for different AGN types.

Figure 1.4 shows the broadband continuum spectral energy distribution (SED) in different types of AGN. The spectrum is extended over different orders of magnitude in frequency. A lot of energy is emitted in the IR region (IR bump) as well as the optical/UV region (the Big Blue Bump). The radio-quiet spectrum is divided into three major parts: the infrared bump which is due to the reprocessing of the UV emission by dust in a range of temperatures and at a range of distances, the Big Blue Bump (BBB) which is a characteristic of the thermal emission from the accretion disc and the lastly X-ray region which is due to the high-energy continuation of the BBB along with a Comptonised power law with fluorescence and reflection from cold material (Koratkar & Blaes, 1999).

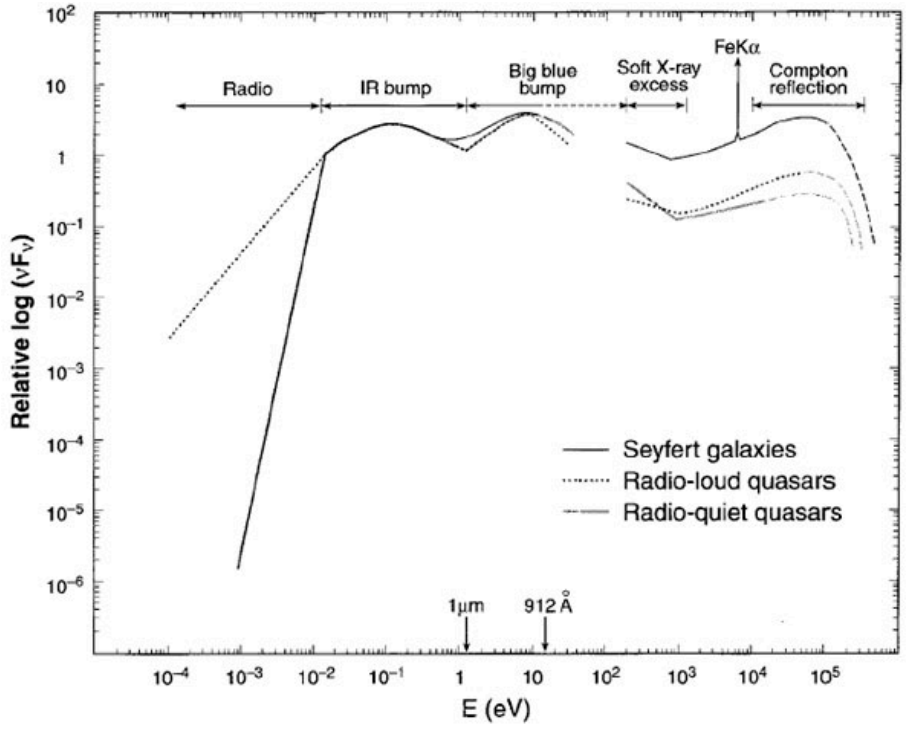

Figure 1.4: This shows the broadband continuum spectral energy distribution seen in the different types of AGNs (Peterson, 1997).

The hard X-ray band of the AGN spectrum represents a power law which can be due to Compton upscattering of optical/UV photons by hot or non thermal electrons in the central engine, possibly at a hot magnetised corona above the disk (Koratkar & Blaes, 1999). In the soft X-ray region, the spectrum of many objects show a soft X-ray excess that exceeds the extrapolation from the observed hard X-ray power-law continuum

(Turner & Pounds 1989; Masnou et al. 1992). This excess may be considered the high energy continuation of the BBB, but it doesn't have an easy explanation as it is subjected to a number of observational difficulties, making it the least well understood component of the AGNs spectral energy distribution (SED).

1.2.2 Variability

A significant trait that led to the discovery of AGN is the rapid changes in the observed luminosity. Every waveband of AGN exhibits variability, but not all AGN vary in all wavebands. Since they are multi-wavelength emitters, the changes in the flux corresponding to different wavebands can be used to deduce the sizes and locations of the various emitting regions in discs around the AGN. The time delay between the continuum fluctuations and the emission line response gives the light travel time from the black hole to the region of clouds termed as the broad line region (BLR) as shown in figure 1.5. The size of the BLR can be determined and the same principle can be used to calculate the size of the accretion discs using reverberation mapping models of AGN. One drawback of this method is its requirement of long term monitoring (Edelson et al., 2015). The technique of reverberation mapping is also used to estimate the masses of supermassive black holes (Peterson, 2014). The next section summarises the technique of reverberation mapping, and how it can be used to determine the mass estimates of black holes and to determine the size of the BLR (De Rosa et al., 2015) and accretion discs (Edelson et al., 2015).

1.2.3 Reverberation mapping

The term reverberation mapping acquired its significance when the emission variability of AGN models became an observed phenomenon (Peterson, 1993). As shown in the unified AGN model (figure 1.5), the continuum radiation originates from the inner part

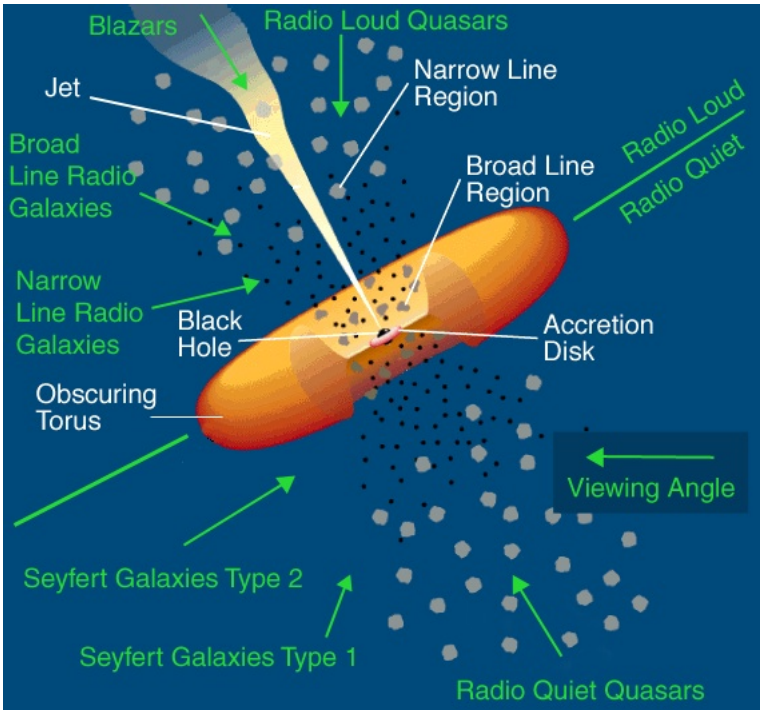

Figure 1.5: Unified AGN model showing a supermassive black hole with an obscurring dusty torus. Image taken from Urry & Padovani (1995).

of the accretion disc. There is a broad line region (BLR) with relatively cold material which absorbs the continuum radiation and re-emit at discrete wavelengths producing a series of emission lines in the AGN spectrum (Peterson & Horne, 2004). In a nutshell, the accretion disc produces a time-variable high-energy continuum flux that heats the gas and the broad emission line fluxes respond to the changes in the flux of the continuum source (Peterson & Horne, 2004). Due to the rotation of the BLR clouds around the central mass, the emission lines are broadened due to Doppler effect.

Due to the sparse availability of data, the research models could not provide adequate information on the structure of the AGN discs. This motivated the use of a technique in which the light-travel time delays between the continuum source and the line emitting clouds is utilised to examine the geometry and the velocity field of the BLR. This estimation of the distance between the broad line regions and the central source is termed as reverberation mapping (RM) (Blandford & McKee, 1982; Peterson, 1993).

As mentioned earlier, RM is also used to calculate mass estimates of a black hole (Peterson & Wandel, 1999; Peterson & Wandel, 2000; Peterson, 2014). The equation is

given as:

$$M_{\rm BH} = f\left(\frac{\Delta V^2 R}{G}\right) \tag{1.27}$$

where G is the gravitational constant, $M_{\rm BH}$ is the mass of the black hole, ΔV is the doppler width and f is a scaling factor that is different for each AGN.

The accretion discs around AGN emit radiation at varying ranges of frequencies such as optical, ultra-violet (UV) or X-rays. The principle of time delays at different wavebands can be utilised to determine the size of accretion discs (also discussed in section 1.6.1). For a time delay τ, the value of the radius R (or size) of the disc can be obtained from

$$\tau = Rc \tag{1.28}$$

where c is the speed of light.

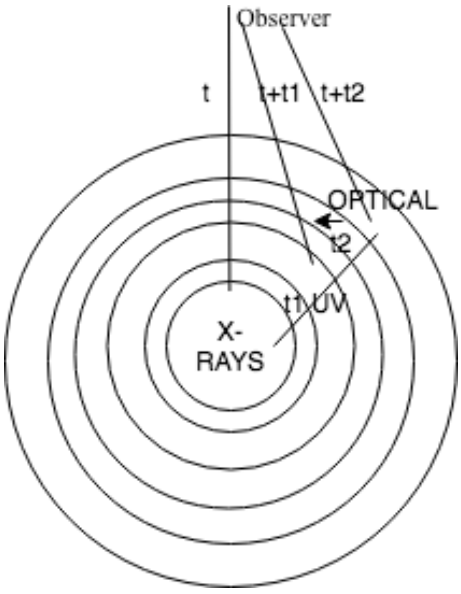

Figure 1.6: A sketch demonstrating the principle of disc reverberation mapping to observe the emitted radiation at different frequencies in an AGN accretion disc; dt_1 represents the time delay for the emission to reach the observer from the UV zone and similarly dt_2 is the time delay for the optical zone.

The sketch demonstrates the principle of disc reverberation mapping for an accretion disc (divided into several annuli) with X-rays emitted from the inner region, followed by the ultra-violet (UV) and the outer part contributed by an optical spectrum. Here, T is the time taken by the X-rays to reach the observer. Similarly, $t + dt_1$ and $t + dt_2$ are

the respective times for the emission from the UV and optical region of the disc to reach the observer with dt_1 and dt_2 being their time delays with respect to the X-rays. We can also demonstrate how the resultant luminosity at these three regions in the disc change over time, as shown in figure 1.7. Using these recorded time delays, we can calculate the sizes of the disc at each frequency or wavelength (X-rays, UV or optical) using equation (1.28).

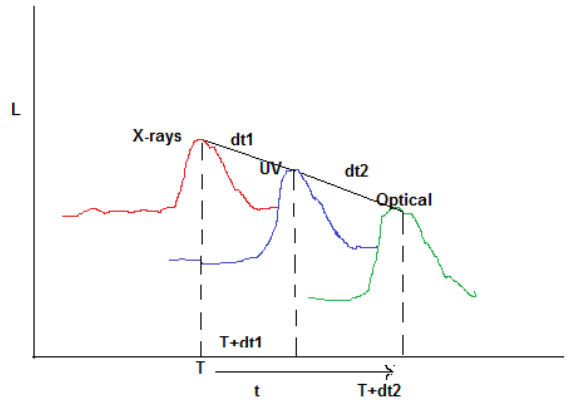

Figure 1.7: Sketch representing Luminosity-time relation, showing a distinct time difference between a variation in the spectrum observed in X-ray, UV and optical regions respectively. Here T is the time recorded from the central (x-ray) region of the disc, and the time recorded at UV and optical given resultantly as T+dt1 and T+dt2, with the corresponding time delays being dt1 and dt2 respectively

1.2.4 Types of AGN

It is very important to understand the taxonomy of AGNs and their underlying physics. Some of the differences seen among the various types of AGNs are mostly due to the way they are observed (Peterson, 1997). This section discusses the various types of AGN.

Seyfert Galaxies

Seyfert galaxies constitute the majority of AGNs with visible host galaxies. They are named after Carl Seyfert, who discovered these objects in the 1940's on photographic plates. A Seyfert galaxy when observed through a large telescope looks like a normal spiral galaxy with a high surface brightness nuclei at its centre, and are identified spectroscopically due to the presence of strong, high-ionization emission lines Peterson (1997).

Khachikian & Weedman (1974) classified the Seyfert galaxies into two distinct classes - Type 1 and Type 2 in terms of the width of their optical emission lines. Type 1 Seyfert galaxies have two sets of emission lines - narrow lines due to the low density ionised gas with widths corresponding to velocities of several hundred kilometres per second and the broad lines due to high density gas corresponding to velocities upto 10^4 km s^{-1} (as shown in fig 1.8). The difference between the type 2 Seyfert galaxies and type 1 is that, only the narrow lines are present in the spectra of type 2 Seyferts (as shown in fig 1.9). The narrow line component in Seyfert 2 spectra is thought to originate from a region of clouds at the outer edge of the active nucleus, which is illuminated by the central ionising source, termed as the Narrow Line Region (NLR). On the other hand, the Broad Line Region (BLR) observed only in Seyfert 1s lies closer to the black hole. BLR plays an important role in the understanding of AGNs. It is a useful probe of the central source because the BLR reprocesses the energy emitted by the central source at ionising ultraviolet energies, which cannot be observed directly. Hence, the emission lines of Seyfert 1s give information about this part of the continuum of the central source (Peterson, 1997).

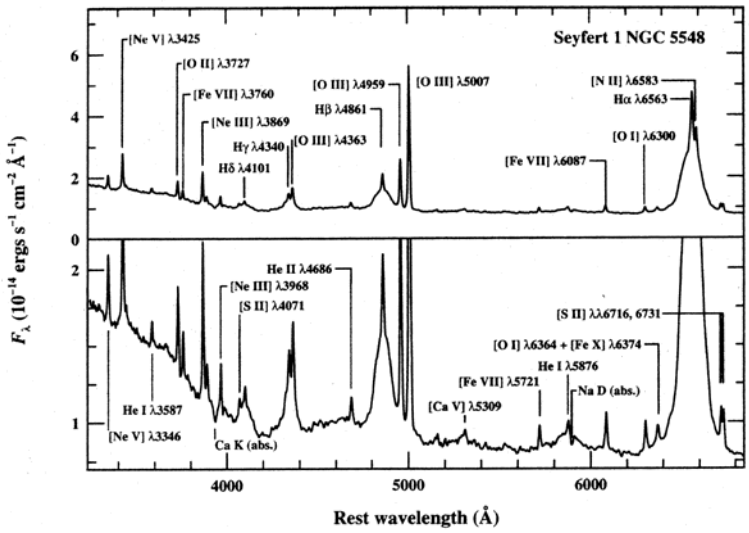

Figure 1.8: This is the optical spectrum of Type 1 Seyfert galaxy NGC 5548. The prominent broad and narrow lines are shown, representing strong absorption features of the spectrum of the host galaxy. Image taken from Peterson (1997).

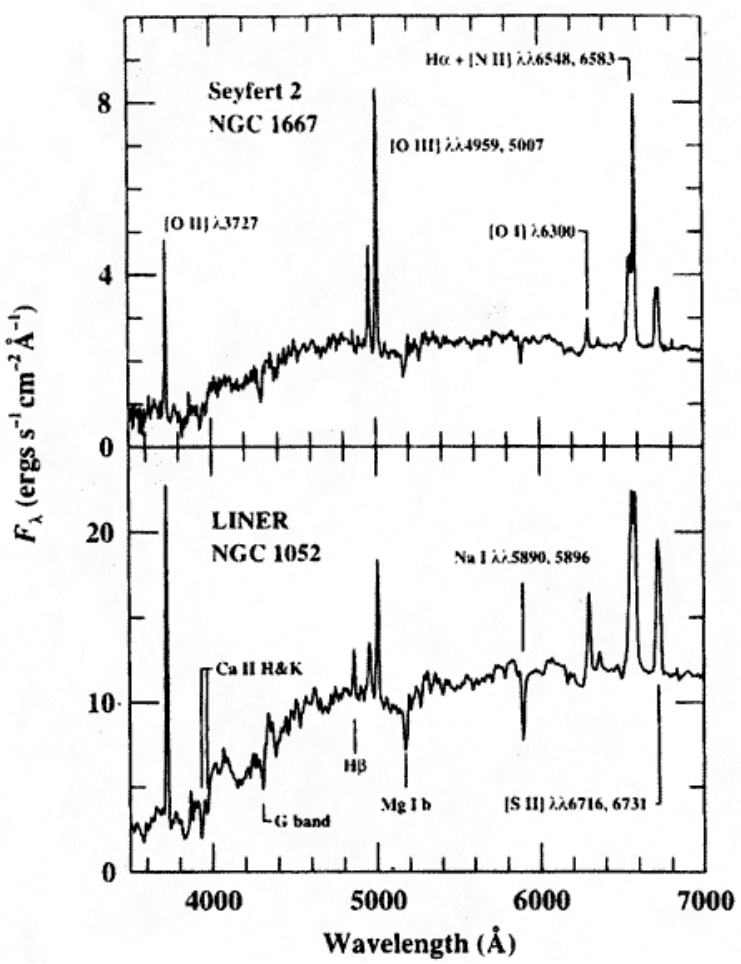

Figure 1.9: Top panel shows the optical spectrum of a Type 2 Seyfert galaxy NGC 1667 and bottom panel shows the spectrum of a LINER galaxy (which resembles the characteristics of a Seyfert 2 galaxy) except they have stronger ionization lines, eg: [OI]λ6300, [OII]λ3727, [SII]λ6548,6583 and [NII]λ6716,6731. Image taken from Peterson (1997).

Quasars

Quasars constitute the most luminous class of AGN. From the radio surveys in the 1950's and 1960's, the first quasars were discovered and described as star-like objects with radio emission. Quasars are found at higher redshifts and therefore they can probe to the early Universe and its evolution. Many of the quasar sources are surrounded by a halo namely *quasar fuzz* of low surface brightness due to the starlight from the host galaxy. Although, the quasar spectra are similar to that of the Seyferts, its stellar absorption features are very weak and the narrow emission lines are weaker relative to the broad lines in comparison to the spectra of Seyfert galaxies. A mean quasar spectrum, obtained by averaging the spectra of over 700 quasi-stellar objects (QSOs) and indicating the

prominent emission lines is shown in figure 1.10 (Francis et al., 1991).

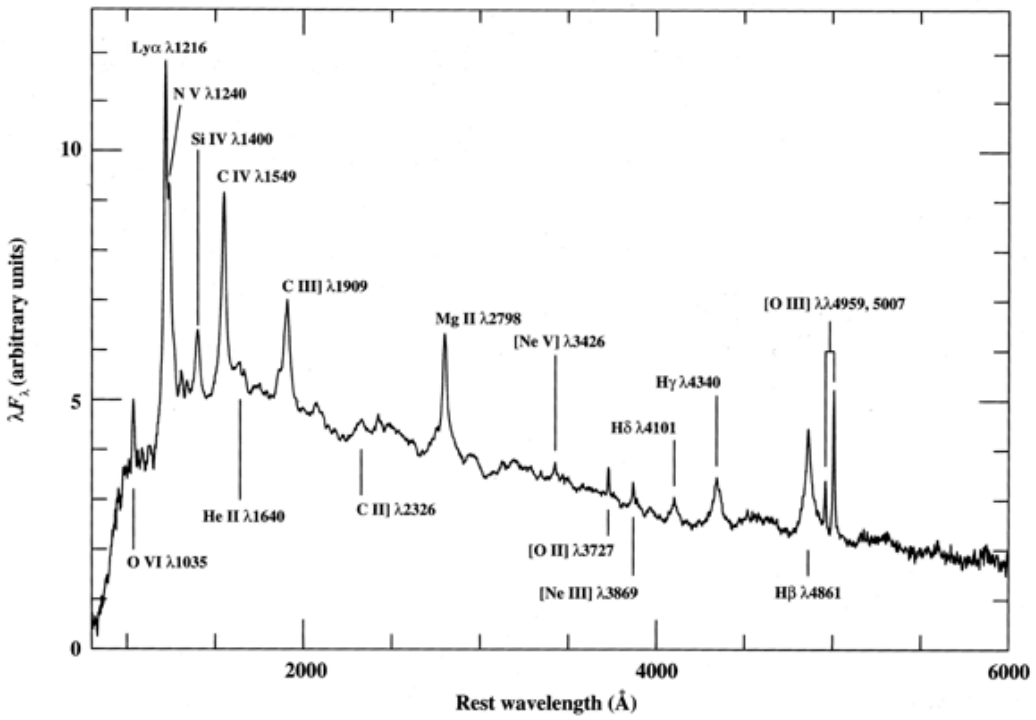

Figure 1.10: A mean QSO spectrum from averaging spectra of 700 quasar candidates from the Large Bright Quasar Survey. Image taken from Peterson (1997).

Radio Galaxies

Giant elliptical galaxies are generally identified as the optical counterparts of strong radio sources, although some bright radio sources are identified to have AGN activity. The development of unified theories of active galactic nuclei (AGN) showed that they can be categorised into two in terms of the luminosity, i.e. radio-loud and radio-quiet. Some of the differences between these two include:

- The radio-loud sources produce large scale radio jets and lobes with the kinetic power of the jets being a big fraction of the entire luminosity, whereas the radio-quiet sources have weaker jets which are energetically insignificant.

- The radio-loud AGNs are associated with elliptical galaxies, but the radio-quiets have spiral hosts.

Inspite of these differences, the thermal emissions (lines from X-ray to infrared wavelengths) of these two types when compared, look quite similar.

Blazars

Blazars constitute a subset of radio quasars with extreme properties that differentiate them from the rest. The various properties include rapid variability at all frequencies (on all timescales) and high polarisation at both optical and radio frequencies. The blazar category includes BL Lac objects and OVVs (Optically violent variables which are radio-quiet). In 1929, Cuno Hoffmeister published a catalog of 354 objects which were thought to be variable stars including an object called BL Lacertae or BL Lac, named after its constellation Lacerta (or the lizard). By the late 1960s and 1970s, astronomers began to notice that although BL Lac got brighter and fainter as predicted of variable stars, it emitted a lot of light in the radio wave regime which was unusual for stars. Also, the characteristic optical variability fitted its feature more to a quasar than a star. Eventually, in a speech given by Ed Spiegel at the Pittsburgh Meeting in 1980, the name blazars was coined by combining *BL Lac* with *quasars*.

1.3 Accretion discs in AGN

1.3.1 Disc formation

The basic idea of forming an accretion disc is very simple: consider gas flows nearer the centre of galaxies, where blobs of gas possessing angular momentum orbit around the central massive black hole instead of falling directly into it. Over time, these orbits of gas intersect which causes dissipation of orbital energy into heating and radiation. In order to conserve the angular momentum in this process, the gas settles into an orbit of lowest energy for the given angular momentum, i.e, a circle. As a result, the gas settles into a rotating configuration, forming a disc. After settling into a disc shape, accretion

proceeds through the redistribution or the outward transport of angular momentum such that matter nearer the central black hole gives up angular momentum to outer parts of the disc (Lynden-Bell & Pringle, 1974; Pringle, 1981).

Accretion discs are subjected to various instabilities such as: gravitational, thermal and magneto-rotational instabilities (MRI) which cause turbulence in discs, resulting in the outward transport of angular momentum. The effect of turbulence on the angular momentum transport in a disc is defined by the turbulent viscosity. This viscosity plays a dual role: firstly, it is responsible for the outward angular momentum transport i.e., disc instabilities produced in a turbulent disc exert strong viscous torques which redistribute angular momentum to its outer radii. Secondly, it provides a channel to convert gravitational energy due to the infall of matter into thermal energy in a disc. This dissipated energy contributes to the emitted radiation which can be observed and measured.

1.3.2 Vertical disc structure

The structure of a geometrically thin, axially symmetric accretion discs can be split into two structures corresponding to a hydrostatic vertical configuration and a radial Keplerian viscous flow. Firstly, let us consider the vertical structure of the disc as shown in figure 1.11.

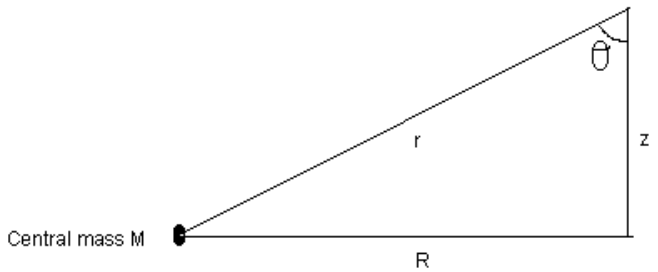

Figure 1.11: This is the vertical structure of the disc. We consider an element of gas located at a height z above the mid-plane, at a radius R from the central mass M.

The vertical component of the gravitational acceleration is given by:

$$g_z = \frac{GM}{r^2}\cos\theta = \frac{GM}{r^2}\frac{z}{r} \tag{1.29}$$

Considering z << R, the equation becomes:

$$g_z \approx \frac{GM}{R^3}z \tag{1.30}$$

We assume that the disc is isothermal in the vertical direction with sound speed c_s. Then, the pressure is given by:

$$P = \rho c_s^2 \tag{1.31}$$

The gravity force is balanced by the force produced by the pressure gradient given as

$$\frac{dP}{dz} = -\rho g_z. \tag{1.32}$$

The pressure gradient dP/dz using equation 1.31 gives

$$\frac{dP}{dz} = c_s^2\frac{d\rho}{dz}. \tag{1.33}$$

Therefore,

$$c_s^2\frac{d\rho}{dz} = -\rho g_z = -\rho\frac{GM}{R^3}z. \tag{1.34}$$

This gives

$$c_s^2\frac{d\rho}{dz} = -\Omega^2\rho z \tag{1.35}$$

where $\Omega = \sqrt{\frac{GM}{R^3}}$ is the angular velocity of the disc. Rearranging the above equation gives

$$\frac{d\rho}{\rho} = -\frac{\Omega^2}{c_s^2}z\ dz \tag{1.36}$$

Integrating equation 1.36 gives

$$\int \frac{d\rho}{\rho} = -\frac{\Omega^2}{c_s^2} \int z \; dz \tag{1.37}$$

and

$$\rho = \rho_0 e^{\frac{-\Omega^2 z^2}{2c_s^2}}. \tag{1.38}$$

This can be rewritten as

$$\rho = \rho_0 e^{\frac{-z^2}{2H^2}} \tag{1.39}$$

where H is given as

$$H^2 = \frac{c_s^2}{\Omega^2}. \tag{1.40}$$

We know, $\Omega = v/R$ where the velocity $v = \sqrt{GM/R}$ and

$$H^2 = \frac{c_s^2 R^2}{v^2}. \tag{1.41}$$

Therefore,

$$\frac{H}{R} \approx \frac{c_s}{v} \tag{1.42}$$

where H is termed as the vertical scale height of the disc. A disc with $H/R << 1$ is described as a geometrically thin disc. Thus, the thickness of the disc as a function of its radius is equal to the ratio of the sound speed to the orbital velocity. It also follows that

$$\frac{H}{c_s} \approx \frac{1}{\Omega} = t_{\rm dyn} \tag{1.43}$$

where $t_{\rm dyn}$ is the dynamical time scale of the disc.

1.3.3 Radial disc structure

The radial structure of an accretion disc is regulated by the conservation laws of mass and angular momentum. We follow Frank et al. (2002) to derive conservation of mass and

angular momentum equations. Consider an annulus in the disc at radius R and thickness ΔR. The rate of mass flow through the inner edge of the annulus is given by (also refer to equation 1.69):

$$\dot{M}_{\rm in} = 2\pi R\ v_R\ \Sigma_R \tag{1.44}$$

Similarly, the rate of mass flow through the outer edge of the annulus is:

$$\dot{M_{\rm out}} = 2\pi(R+\Delta R)\ v_{R+\Delta R}\ \Sigma_{R+\Delta R}. \tag{1.45}$$

The rate of change of the mass in the annulus is given by the difference between these quantities:

$$\frac{\partial}{\partial t}(2\pi R\Delta R\Sigma) = (2\pi R\Sigma v_R)_R - (2\pi R\Sigma v_R)_{R+\Delta R}. \tag{1.46}$$

We take the limit $\Delta R \to 0$ to get

$$R\frac{\partial \Sigma}{\partial t} + \frac{\partial}{\partial R}\Big(R\Sigma v_R\Big) = 0 \tag{1.47}$$

where $\Sigma(R)$ is the surface density and v_R is the radial velocity. This is also termed as mass continuity equation. Similarly, if we consider the angular velocity Ω and the angular momentum per unit mass to be $\Sigma R^2\Omega$, we obtain the conservation of angular momentum as

$$R\frac{\partial}{\partial t}\Big(\Sigma R^2\Omega\Big) + \frac{\partial}{\partial R}\Big(\Sigma v_R R^3\Omega\Big) = \frac{1}{2\pi}\frac{\partial G}{\partial R} \tag{1.48}$$

with

$$G = 2\pi\nu\Sigma R^3\Omega' \tag{1.49}$$

where G is the viscous torque and ν is the viscosity. Combining the two conservation equations gives the diffusion equation which shows how the surface density Σ of a viscous

disc evolves over time. From equation 1.47, we can write

$$\frac{\partial \Sigma}{\partial t} = -\frac{1}{R}\frac{\partial (R\Sigma v_R)}{\partial R}. \tag{1.50}$$

We know that viscous torque $G = 2\pi\nu\Sigma R^3\Omega'$, therefore

$$\frac{\partial G}{\partial R} = \frac{\partial (2\pi R^3 \nu \Sigma \Omega')}{\partial R} \tag{1.51}$$

$$\frac{1}{2\pi}\frac{\partial G}{\partial R} = \frac{\partial (R^3 \nu \Sigma \Omega')}{\partial R}. \tag{1.52}$$

Substituting equation 1.52 in 1.48, gives

$$\frac{\partial (\Sigma R^2 \Omega)}{\partial t} + \frac{1}{R}\frac{\partial (\Sigma v_R R^3 \Omega)}{\partial R} = \frac{1}{R}\frac{\partial (R^3 \nu \Sigma \Omega')}{\partial R}. \tag{1.53}$$

Therefore,

$$\frac{\partial (\Sigma R^2 \Omega)}{\partial t} + R^2\Omega\frac{1}{R}\frac{\partial (R\Sigma v_R)}{\partial R} + \frac{1}{R}R\Sigma v_R\frac{\partial (R^2\Omega)}{\partial R} = \frac{1}{R}\frac{\partial (R^3 \nu \Sigma \Omega')}{\partial R}. \tag{1.54}$$

The first two terms in the above equation sums to zero (from mass continuity equation), thus

$$\frac{1}{R}R\Sigma v_R\frac{\partial (R^2\Omega)}{\partial R} = \frac{1}{R}\frac{\partial (R^3 \nu \Sigma \Omega')}{\partial R}. \tag{1.55}$$

Solving for $R\Sigma v_R$ gives

$$R\Sigma v_R = \frac{\partial (R^3 \nu \Sigma \Omega')/\partial R}{\partial (R^2\Omega)/\partial R}. \tag{1.56}$$

This can be substituted in equation 1.47 to get:

$$\frac{\partial \Sigma}{\partial t} = -\frac{1}{R}\frac{\partial \left(\frac{\partial (R^3 \nu \Sigma \Omega')/\partial R}{\partial (R^2\Omega)/\partial R}\right)}{\partial R}, \tag{1.57}$$

where angular velocity

$$\Omega = \sqrt{\frac{GM}{R^3}}. \tag{1.58}$$

Substituting the values of Ω and Ω' in equation 1.57 gives:

$$\frac{\partial \Sigma}{\partial t} = \frac{3}{R}\frac{\partial}{\partial R}\left(R^{1/2}\frac{\partial}{\partial R}[\nu \Sigma R^{1/2}]\right). \tag{1.59}$$

The above equation represents the diffusion equation for a viscous accretion disc. If we compare this to equation 1.50, the radial velocity induced by the viscous torque is given as

$$v_R = -\frac{3}{\Sigma R^{1/2}}\frac{\partial}{\partial R}\left[\nu \Sigma R^{1/2}\right] \sim \frac{\nu}{R}. \tag{1.60}$$

The changes in the radial structure of an accretion disc or the viscous accretion in a disc occurs over a time scale termed as the viscous time scale, $t_{\rm visc}$.

$$t_{\rm visc} = \frac{R}{v_{\rm visc}} \approx \frac{R^2}{\nu} \approx \alpha^{-1}\frac{H}{c_s}\left(\frac{H}{R}\right)^{-2}. \tag{1.61}$$

The relation between viscous and dynamical timescales is[1]:

$$t_{\rm visc} \approx \alpha^{-1}\left(\frac{H}{R}\right)^{-2} t_{\rm dyn}. \tag{1.62}$$

This proves that the role of viscosity is very important in the evolution of a disc. During the accretion process, the matter falls into the central object producing gravitational energy. This gravitational energy is liberated as heat energy which contributes to the emitted spectrum of the disc. This energy dissipated due to viscosity calculated per unit area per unit time or the energy dissipation rate is given as (Frank et al., 2002):

$$Q(R) = \frac{1}{2}\nu \Sigma (R\Omega')^2, \tag{1.63}$$

[1]In chapter 4, we evaluate the viscous timescales (see table 4.2) at different radii of NGC 5548 to study its time-variability across different (UV to optical) wavelengths.

where the angular velocity $\Omega = \sqrt{\frac{GM}{R^3}}$. This gives

$$Q(R) = \frac{9}{8}\nu\Sigma\frac{GM}{R^3}. \tag{1.64}$$

1.3.4 Steady state disc structure

In this section, we consider how a viscous accretion disc settles to a steady state structure. This can be studied by considering $\frac{\partial}{\partial t} = 0$ in conservation equations (equations 1.47 and 1.48). Firstly, the mass continuity equation for a steady disc gives

$$\frac{\partial\Sigma}{\partial t} = 0. \tag{1.65}$$

Therefore

$$\frac{\partial}{\partial R}\Big(R\Sigma v_R\Big) = 0, \tag{1.66}$$

$$\Big(R\Sigma v_R\Big) = \text{constant}. \tag{1.67}$$

Multiplying the above equation by 2π gives

$$2\pi R\Sigma v_R = \text{constant}. \tag{1.68}$$

Here, the conservation equation is derived by assuming the transport of material within the two annuli of the disc at radii R and $R + \Delta R$ with its total mass given as $2\pi\mathrm{R}\Delta\mathrm{R}\Sigma$ (Frank et al., 2002). Using dimensional analysis, we have

$$2\pi R\Sigma v_R = L \times \frac{M}{L^2} \times \frac{L}{T} = \frac{M}{T} = \dot{M} \tag{1.69}$$

where M, L and T are dimensions for mass, length and time respectively. Therefore

$$\dot{M} = 2\pi R\Sigma(-v_R) \tag{1.70}$$

The negative sign is due to the inward flow of matter due to accretion. Hence, the rate of mass flow can be expressed in terms of the surface density. Furthermore, the first term vanishes in the angular momentum conservation (equation 1.48) for a disc in its steady state and therefore

$$\frac{\partial}{\partial R}\left(\Sigma v_R R^2 \Omega\right) = \frac{1}{2\pi}\frac{\partial}{\partial R}\left(2\pi\nu\Sigma R^3\Omega'\right) \tag{1.71}$$

Integrating this equation gives

$$\Sigma v_R R^3 \Omega = \nu\Sigma R^3\Omega' + \frac{\text{constant}}{2\pi}. \tag{1.72}$$

Multiplying the above equation by 2π gives:

$$2\pi\Sigma v_R R^3 \Omega = 2\pi\nu\Sigma R^3\Omega' + \text{constant}. \tag{1.73}$$

We know from mass continuity equation that:

$$2\pi R\Sigma v_R = -\dot{M} \tag{1.74}$$

Substituting equation 1.74 in 1.73 gives:

$$-\dot{M} R^2 \Omega = 2\pi\nu\Sigma R^3\Omega' + \text{constant}. \tag{1.75}$$

To calculate the value of the constant, we use an assumption that the viscous force is zero at the inner boundary. This is equivalent to assuming that either the surface density or the radial derivative of the angular velocity (Ω') goes to zero at the inner edge. Therefore,

$$-\dot{M} R_{\text{in}}^2 \Omega_{\text{in}} = \text{constant}. \tag{1.76}$$

Thus, we can express equation 1.75 as:

$$-\dot{M}R^2\Omega = 2\pi\nu\Sigma R^3\Omega' - \dot{M}R_{\rm in}^2\Omega_{\rm in}, \tag{1.77}$$

$$\dot{M}\bigg(R_{in}^2\Omega_{in} - R^2\Omega\bigg) = 2\pi\nu\Sigma R^3\Omega'. \tag{1.78}$$

The value for $\Omega = \sqrt{\frac{GM}{R^3}}$ and its derivative can be substituted in equation 1.78, that gives

$$3\pi\nu\Sigma\sqrt{GMR} = \dot{M}\bigg(R^2\Omega - R_{in}^2\Omega_{in}\bigg), \tag{1.79}$$

$$3\pi\nu\Sigma\sqrt{GMR} = \dot{M}\bigg(\sqrt{GMR} - \sqrt{GMR_{in}}\bigg). \tag{1.80}$$

Therefore,

$$\nu\Sigma = \frac{\dot{M}}{3\pi}\bigg(1 - \sqrt{\frac{R_{in}}{R}}\bigg). \tag{1.81}$$

This equation represents the relation between the viscosity ν and accretion rate $\dot{M}$. Using equation 1.81 in 1.64 to calculate $Q(R)$, we get:

$$Q(R) = \frac{3GM\dot{M}}{8\pi R^3}\bigg[1 - \bigg(\frac{R_{in}}{R}\bigg)^{\frac{1}{2}}\bigg]. \tag{1.82}$$

As mentioned earlier, the dissipated heat energy emitted as radiation from the disc surface constitutes the disc's spectrum. Assuming the disc behaves as a black body with effective temperature $T_{\rm eff}(R)$, and the disc's temperature is calculated by equating the dissipation rate $Q(R)$ to the energy flux of a blackbody (Frank et al., 2002).

$$\sigma T_{\rm eff}^4(R) = Q(R) \tag{1.83}$$

where σ is the Stefan-Boltzmann constant. Substituting the value of $Q(R)$ from equation 1.82, we get:

$$T(R) = \bigg[\frac{3GM\dot{M}}{8\pi R^3\sigma}\bigg(1 - \bigg(\frac{R_{in}}{R}\bigg)^{\frac{1}{2}}\bigg)\bigg]^{\frac{1}{4}} \tag{1.84}$$

Therefore, the temperature profile for steady accretion discs from equation 1.84 is

$$T(R) \propto R^{-\frac{3}{4}}. \tag{1.85}$$

1.3.5 Accretion disc viscosity

From the evaluations as previously discussed, it is understood that viscosity plays an essential role in disc evolution. Viscosity acts as a main agent for proceeding the outward transport of angular momentum (Lynden-Bell & Pringle, 1974; Pringle, 1981; Frank et al., 2002). But, a major unresolved problem is the physical origin of viscosity. Standard molecular viscosity does not give suitable timescales for the evolution of a disc since it is far too small in comparison to the expected disc lifetime ($10^6 - 10^7$ years). To demonstrate this, the standard molecular viscosity estimated as $\nu \sim \lambda c_s$ (where λ is the mean free path of the molecules) and the Reynold's number

$$Re = \frac{\text{inertial force}}{\text{viscous force}} \sim \frac{\Omega R^2}{\nu} \sim \frac{t_{\text{visc}}}{t_{\text{dyn}}} \tag{1.86}$$

is used as a parameter to measure the importance of viscosity (Frank et al., 2002). The viscous force dominates the flow if $Re << 1$ and if $Re >> 1$ the viscosity is dynamically unimportant. In the case of standard molecular viscosity, Frank et al. (2002) finds that:

$$Re_{\text{mol}} \sim 0.2 N m_1^{1/2} R_{10}^{1/2} T_4^{-5/2} \tag{1.87}$$

where R_{10} is the distance from the centre of the accreting star (in units of 10^{10}cm), T_4 is the gas temperature (in units of 10^4K) and N (in cm^{-3}) is the gas density. In an accretion disc, Frank et al. (2002) assumes the values of $m^{1/2} \sim R_{10}^{1/2} \sim T_4^{-5/2} \sim 1$ and N to exceed a value of 10^{15} cm^{-3}, such that $Re > 10^{14}$. This means that the molecular viscosity is too small to give an appropriate timescale for the disc's evolution. Hence, the molecular viscosity is weak to produce the viscous dissipation and the transport of

angular momentum as expected.

It is learnt from laboratory experiments that if the Reynolds number is gradually increased, the flow becomes turbulent when it reaches a critical value. This causes large and chaotic variations in velocity over arbitrary short time scales. Similarly, in the case of discs, it is natural to assume the disc flow to become strongly turbulent. This turbulent flow is assumed to be characterised by size λ_t and velocity v_t, thus producing large eddies. Thus, we define the turbulent viscosity as

$$v_t = \lambda_t v_t. \tag{1.88}$$

Since turbulence is a complex phenomenon, we do not know how to determine the sizes and velocities of eddies without proper knowledge of the underlying physical mechanisms causing the disc to be turbulent. So far its origin is assumed to be hydrodynamic in nature; detailed studies have shown that turbulence in discs occurs mainly due to magneto-rotational (Balbus & Hawley, 1991) and gravitational instabilities (see section 1.4.1 and 1.4.3). In order to set constraints on λ_t nd v_t, firstly we assume that the size of the edddies cannot exceed the disc thickness, i.e. $\lambda < H$. Secondly, it is unlikely that the turbulence is supersonic and it is damped to subsonic values such that, $v_t < c_s$ where c_s is the speed of sound. Based on these two basic assumptions, it is suggested that the turbulent viscosity:

$$\nu \propto c_s H. \tag{1.89}$$

Thus,

$$\nu = \alpha c_s H \tag{1.90}$$

where α is a constant expected to be less than unity. This formula is the famous α-prescription for turbulent viscosity proposed by Shakura & Sunyaev (1973).

1.4 Disc instabilities

In this section, we review the different disc instabilities which play an important role in the outward transport of angular momentum, thus allowing accretion to occur.

1.4.1 Magneto Rotational Instability(MRI)

It has been a long standing problem in astrophysics to explain the nature of viscosities in accretion discs. As mentioned before, molecular viscosity alone is weak and inefficient to explain the angular momentum transport in accretion discs. Therefore, an effect due to turbulence is needed to generate the expected degree of viscosity. In other words, an instability is needed to drive the turbulence responsible for the infall of matter and the outward transport of angular momentum in discs. However in the absence of magnetic fields, no instabilities are produced to drive such turbulence in a disc. A breakthrough in the discovery of MRI (or Magneto Rotational Instability) by Balbus & Hawley (1991) explains how instabilities are produced by weak magnetic fields in differentially rotating accretion disc systems.

Balbus & Hawley (1991) showed how accretion discs are subjected to a powerful shearing instability due to the amplification of weak magnetic fields by differential rotation, thus producing a turbulent viscosity which enables the outward angular momentum transport. This idea of MRI is extended from the study of hydromagnetic instability originally discovered by Velikhov (1959) and Chandrasekhar (1960).

Figure 1.12 illustrates the growth of MRI due to differential rotation in the disc. In the presence of magnetic fields, the field lines within the disc act like springs connecting the masses at the different annuli of the disc. Consider, two masses m_1 and m_2 connected by a spring (representing magnetic force) orbiting around a central body of mass M_c. In such a system, the velocity of circular orbits near the centre is higher than that of orbits

away from the centre. However, the angular momentum is smaller for the orbits nearer to the centre. If we assume, the mass element m_1 has a higher velocity than m_2, it means that the connecting spring pulls back on m_1 and drags m_2 forward. A retarding torque acts on m_1 which loses its angular momentum and falls to a lower orbit corresponding to a smaller angular momentum. On the other hand, m_2 experiences a positive torque gaining more angular momentum and moves to a higher orbit. As a result the spring (magnetic force connecting m_1 and m_2) stretches more, the torques become larger and form instabilities within a differentially rotating disc (Balbus, 2009).

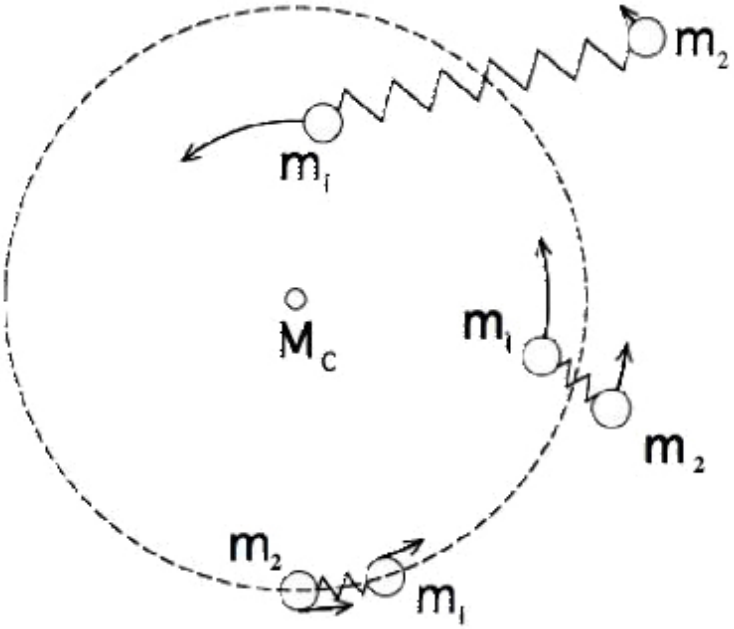

Figure 1.12: Magneto rotational instability as shown with masses in the inner and outer rings, m_1 and m_2 respectively (Image taken from Balbus (2009)).

1.4.2 Thermal instabilties

Accretion discs are known to be subjected to thermal-viscous instabilities which operate in the inner regions of the disc where radiation pressure dominates. Such systems include discs around young stars, AGNs and binary systems. Among the binaries, include a subclass of cataclysmic variables termed as dwarf novae in which a low-mass companion transfers mass onto a white dwarf. These systems undergo outbursts lasting a few days, during which their brightness increases by several magnitudes (Warner, 2003). The basic

idea is that if the inner disc is extremely opaque, it doesn't efficiently radiate heat away. This heats up the inner region, increasing its effective temperature ($T_{\rm eff}$) hot enough to ionise hydrogen and its opacity to depend strongly on temperature, thus producing an outburst (Lasota, 2001). Hence, the thermal-viscous instability triggers these outbursts when the disc opacities strongly depend on temperature (Meyer & Meyer-Hofmeister, 1981). The thermal viscous instability of the dwarf novae can be understood by the limit cycle of their outbursts in a diagram (an S-shaped curve) that plots the temperature (T) versus the disc surface density (Σ) (Bath & Pringle, 1982; Faulkner et al., 1983).

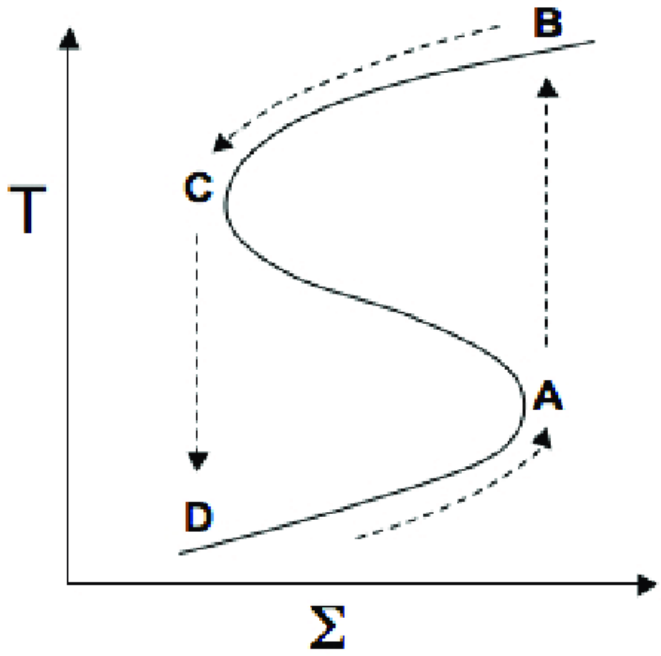

Figure 1.13: S curve showing the limit cycle of the thermal disc instabilities in an accretion disc (Image taken from Hartmann & Kenyon (1996)).

Figure 1.13 illustrates the S curve for the disc with the bend at a point where the opacity causes the thermal instability. As shown in the figure, the locus shifts to the right on the lower branch of the curve, when material is accumulated in the disc. As it reaches the point A, a small perturbation in the temperature can cause the disc to enter an unstable region where it jumps to the upper arm of the S-curve at position B. At B, the surface density and the mass accretion rate or temperature is much higher.

This elevated accretion onto the star removes the material from the disc moving down to position C of the curve. At this point, the disc becomes stable following a low accretion solution at point D. Furthermore, the timescale of these thermal instabilities ($t_{\rm th}$) is shorter than the viscous timescale ($t_{\rm visc}$) given by (Frank et al., 2002)

$$t_{\rm th} \sim \left(\frac{H}{R}\right)^2 t_{\rm visc}. \tag{1.91}$$

1.4.3 Gravitational instabilties

The gravitational field produced by the disc (or the disc's self-gravity) is an important aspect in the modelling of several systems. The influence of self gravity in discs extends over a large scale of protoplanetary discs associated with the formation of planetary systems, up to AGN discs which are relevant to the formation and the feeding of supermassive black holes.

One of the most important effects of the self gravity is the formation of gravitational instability. The physical origin of gravitational instability is related to standard Jeans instability for a homogeneous fluid, where pressure gradients cannot stabilise large scale perturbations. These instabilities are one of the agents in the redistribution of angular momentum, especially in the colder outer parts of the disc. In some cases, these instabilities are strong enough to form gravitationally bound clumps within the disc, that can lead to disc fragmentation. The stability of self gravitating discs is determined by a dimensionless parameter Q known as the Toomre parameter (Toomre, 1964). The disc becomes unstable against gravity when the value of Q is less than unity, i.e. $Q < 1$. Toomre Q parameter is given as

$$Q = \frac{c_s \Omega}{\pi G \Sigma} \tag{1.92}$$

where c_s is the sound speed, Ω is the angular velocity, G is the gravitational constant and Σ is the surface density.

1.5 Physics of warped discs

Accretion discs around astrophysical systems are often tilted and warped, where their orbital planes vary with radius. In such accretion discs around black holes, the orbital angular momentum is not always in the same direction as the angular momentum of the spin of the black hole. The various reasons for the disc to be warped or misaligned are: the Lense-thirring precession from a spinning black hole (Lense, 1918; Bardeen & Petterson, 1975), gravitational torques from a companion (Lubow & Ogilvie, 2000) and radiation from the central object (Pringle, 1996, 1997).

1.5.1 Lense Thirring Effect

The Lense-Thirring effect is due to general relativistic frame dragging which causes non-equatorial orbits to precess around a spinning black hole, i.e. the angular momentum of disc orbits precess around the angular momentum vector of the black hole. This rate of precession is dependent on the distance from the black hole where $\Omega_p \propto R^{-3}$. The differential precession produces a warp that propagates through the disc. As the inner parts precess fastest, they are subjected to more dissipation on shorter timescales and thus align quicker with the black hole spin. Therefore, the aligned inner part of the disc remains connected to the misaligned outer part by a smooth warp. This is termed as the Bardeen-Peterson effect (Bardeen & Petterson, 1975).

Planar or unwarped discs are evolved by an azimuthal shear which produces a turbulent viscosity that transports the angular momentum radially. However, its not the same in the case of warped discs. Early derivations of the evolution of warped discs produced equations that did not conserve angular momentum (e.g. Bardeen & Petterson, 1975; Hatchett et al., 1981) where they assumed the viscosity to be same in all directions. This was resolved by Papaloizou & Pringle (1983) which considered a second viscosity (ν_2),

produced from the radial pressure gradients due to the misalignment of neighbouring rings. The relation between the two viscosities is:

$$\nu_2 = \frac{\nu_1}{2\alpha^2} \tag{1.93}$$

where α is the dimensionless viscosity parameter (Shakura & Sunyaev, 1973). There are two types of warp propagation in discs. For the case of weak damping (referred to as wavelike with $\alpha < H/R$), the warp propagates as a wave (Papaloizou & Lin, 1995), while for the case of strong damping (referred to as diffusive with $\alpha > H/R$), the disc warp evolves following a diffusion equation (Pringle, 1992; Ogilvie, 1999).

The warp radius can be derived for a disc warped due to the Lense-Thirring effect of a spinning black hole (Natarajan & Pringle, 1998). The component of angular momentum parallel to the spin of the disc at a radius R in the disc is transferred in a diffusive manner over a timescale t_R given by

$$t_R \sim \frac{R^2}{\nu_1} \tag{1.94}$$

where $\nu_1 = \alpha c_s H$, α is the dimensionless viscosity parameter, c_s is the sound speed and H is the scale height of the disc. Also, Papaloizou & Pringle (1983) showed that the warp is transferred within the disc on a timescale

$$t_{\rm warp} \sim \frac{R^2}{\nu_2} \tag{1.95}$$

where $\frac{\nu_2}{\nu_1} = \frac{1}{2\alpha^2}$. The frequency at which misaligned rings precess due to the Lense-Thirring effect is given by:

$$\Omega_{\rm LT} = \frac{\omega_p}{R^3}. \tag{1.96}$$

Therefore, the Lense-Thirring timescale is given by

$$t_{\rm LT} = \frac{1}{\Omega_{LT}} = \frac{R^3}{\omega_p} \tag{1.97}$$

where ω_p is independent of radius. Scheuer & Feiler (1996) found that the radius at which the disc is aligned to the spin of the black hole is equal to the radius corresponding to the timescale at which the warp diffuses radially; i.e. $t_{\rm warp}$ is of the order of $t_{\rm LT}$. Thus equating the timescales, we get

$$\frac{R_{\rm warp}^3}{\omega_p} = \frac{R_{\rm warp}^2}{\nu_2} \tag{1.98}$$

$$R_{\rm warp} = \frac{\omega_p}{\nu_2} \tag{1.99}$$

where $\omega_p = \frac{2GJ}{c^2}$ and $J = acM\left(\frac{GM}{c^2}\right)$. This gives,

$$\omega_p = \frac{2a}{c} GM\left(\frac{GM}{c^2}\right). \tag{1.100}$$

As the Schwarzschild radius is $R_s = \frac{2GM}{c^2}$, the above equation becomes:

$$\omega_p = \left[\frac{a}{c} GM\right] R_s. \tag{1.101}$$

Therefore, equation 1.99 becomes

$$R_{\rm warp} = \frac{\omega_p}{\nu_2} = \frac{aGMR_s}{c\ \nu_2} \tag{1.102}$$

or

$$\frac{R_{\rm warp}}{R_s} = \frac{aGM}{c\ \nu_2}. \tag{1.103}$$

We have

$$\frac{\nu_2}{\nu_1} = \frac{1}{2\alpha^2}, \tag{1.104}$$

$$\nu_2 = \frac{\nu_1}{2\alpha^2} = \frac{\alpha H^2 \Omega}{2\alpha^2} = \frac{H^2\Omega}{2\alpha}. \tag{1.105}$$

Thus, equation 1.103 gives:

$$\frac{R_{\rm warp}}{R_s} = \frac{a}{c}\frac{GM}{\nu_2} = \frac{a}{c} GM. \frac{2\alpha}{H^2\Omega} \tag{1.106}$$

$$\frac{R_{\rm warp}}{R_s} = 2\alpha a\left(\frac{GM}{c}\right).\frac{1}{H^2\Omega} \tag{1.107}$$

Multiplying and divinding the equation by R^3,

$$\begin{aligned}\frac{R_{\rm warp}}{R_s} &= 2\alpha a\left(\frac{GM}{c}\right).\frac{1}{H^2\Omega}.\frac{R^3}{R^3} \\ &= 2\alpha a\frac{GM}{cR^3}.\frac{R^3}{H^2\Omega} \\ &= 2\alpha a\frac{\Omega^2}{c}.\frac{R^3}{H^2\Omega} \\ &= 2\alpha a\left(\frac{R}{H}\right)^2\left(\frac{R\Omega}{c}\right). \end{aligned} \tag{1.108}$$

where $R_s = 2GM/c^2$ is the Schwarzschild radius, we also find

$$\frac{R\Omega}{c} = \frac{1}{\sqrt{2}}\left(\frac{R_s}{R}\right)^{1/2} \tag{1.109}$$

Substituting this in equation 1.108 (evaluating at $R_{\rm warp}$) gives

$$\frac{R_{\rm warp}}{R_s} = 2^{1/3}(\alpha a)^{2/3}\left(\frac{R}{H}\right)^{4/3}. \tag{1.110}$$

The radius $R_{\rm warp}$ corresponding to the timescale of the radial diffusion of the warp ($t_{\rm warp}$) is thus derived (also shown by equation 2.6 of Natarajan & Pringle (1998)).

1.5.2 Propagation of warps

The azimuthal shear acting in a planar accretion disc produces a turbulent viscosity which transports angular momentum, whereas in a warped disc there is a second vertical type of shear such that rate of orbital shear is not parallel to the local disc normal $\boldsymbol{l}$ and is given as (Ogilvie & Latter, 2013)

$$s = R\frac{\partial s}{\partial R} = R\frac{d\Omega}{dR}\boldsymbol{l} + R\Omega\frac{\partial \boldsymbol{l}}{\partial R} \tag{1.111}$$

where the local orbital angular velocity $s(R,t) = \Omega(R)\boldsymbol{l}(R,t)$. The evolution of a warped disc is dependent on two torques which control the angular momentum along and normal to the local orbital plane respectively (Nixon & King, 2016). The planar disc viscosity is controlled by a turbulent α viscosity that radially transports the angular momentum. The second viscosity associated with the warp is caused by radial pressure gradients due to the misalignment of neighbouring rings in a disc as shown in the figure 1.14. Therefore, the dynamics of a warped disc differ from that of a planar disc primarily due to a resonance between the orbital motion and the radial pressure gradient produced by the warped disc shape (Papaloizou & Pringle, 1983). This resonance leads to strong in-plane motions which communicate the disc warp radially and are damped by the disc turbulence.

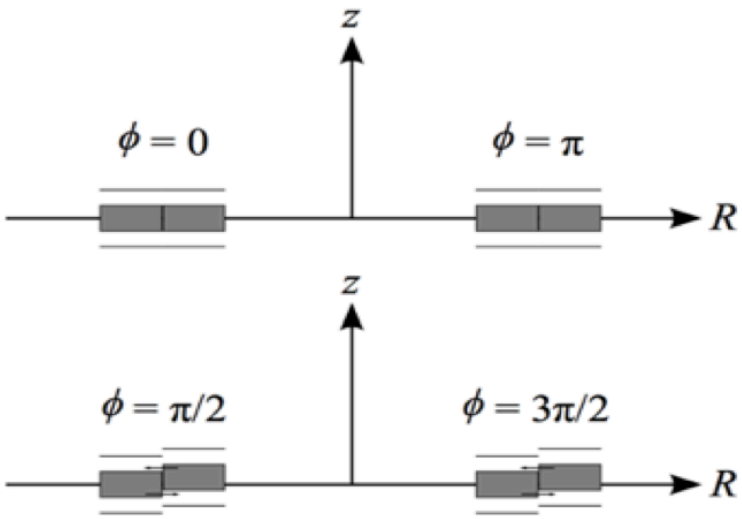

Figure 1.14: This shows how the radial pressure gradient is induced by a warp. The top and bottom panels show cross-sections of two neighbouring rings of gas, at different values of azimuthal angle, ϕ . The shaded regions represent the higher pressure regions around the local mid-plane, and the arrows show the resultant pressure gradient due to the misalignment of the rings. The azimuthal angle around a ring is measured in the direction of the flow from the descending node at $\phi = 0$. The mid-planes are in aligned contact when the tilted rings cross at the nodes. But, the ring mid-planes do not fully line up at all other azimuths, and thus form a region of overpressure above or below the mid-plane which results in an oscillating pressure gradient as a gas parcel orbits in the warp (Image taken from Nixon & King (2016)).

The coordinates to describe a warped disc are defined by cylindrical polars and Euler angles. A local annulus is described by cylindrical polars (R,ϕ,z) and is tilted in three dimensional space defined by the Euler angles $\beta(R,t)$ and $\gamma(R,t)$, termed as the local disc tilt and twist respectively. Therefore, the disc unit tilt vector is defined as:

$$\boldsymbol{l} = (\cos\gamma\sin\beta, \sin\gamma\sin\beta, \cos\beta). \tag{1.112}$$

The local angular momentum vector for the disc is

$$\boldsymbol{L} = \Sigma R^2 \Omega \boldsymbol{l} \tag{1.113}$$

where Σ is the surface density and Ω is the angular velocity of the disc.

1.5.3 Evolution equations

In this section, we discuss the evolution equations of warped accretion discs which represent how discs evolve through the angular momentum vector, $\boldsymbol{L} = \Sigma R^2 \Omega \boldsymbol{l}$. This was derived by Papaloizou & Pringle (1983) and Pringle (1992) from the conservation of mass and angular momentum equations. We consider a disc with surface density Σ, radial velocity V_R and angular velocity Ω. Consider, an annulus of gas in a disc between R and $R + \Delta R$ with mass $2\pi R \Delta R \Sigma$. The rate of change of mass is related to the flow of mass into and out of the annulus given by

$$\frac{\partial}{\partial t}(2\pi R \Delta R \Sigma) = (2\pi R V_R \Sigma)_R - (2\pi R V_R \Sigma)_{R+\Delta R}. \tag{1.114}$$

Rearranging using the limit $\Delta R \to 0$, gives the conservation of mass equation for a disc

$$\frac{\partial \Sigma}{\partial t} + \frac{1}{R}\frac{\partial}{\partial R}(R \Sigma v_R) = 0. \tag{1.115}$$

Similarly, the rate of angular momentum is related to the net flux of angular momentum and the net torques, given by

$$\begin{aligned}\frac{\partial}{\partial t}(2\pi R \Delta R \Sigma R^2 \Omega \boldsymbol{l}) = (2\pi R V_R \Sigma R^2 \Omega \boldsymbol{l})_R - (2\pi R V_R \Sigma R^2 \Omega \boldsymbol{l})_{R+\Delta R} \\ + G(R + \Delta R) - G(R)\end{aligned} \tag{1.116}$$

where the angular momentum of the annulus is $2\pi R\Delta R\Sigma R^2\Omega$ and G is the three dimensional viscous torque. By taking the limit $\Delta R \to 0$, we get:

$$\frac{\partial}{\partial t}\left(\Sigma R^2\Omega \boldsymbol{l}\right) + \frac{1}{R}\frac{\partial}{\partial R}\left(\Sigma v_R R^3\Omega \boldsymbol{l}\right) = \frac{1}{2\pi R}\frac{\partial G}{\partial R} \tag{1.117}$$

The viscous torque G has three components. The torque G_1 acts in the direction of $\boldsymbol{l}$ given by:

$$G_1 = 2\pi R\nu_1\Sigma R\Omega' R\ \boldsymbol{l} \tag{1.118}$$

where ν_1 is the azimuthal shear viscosity. The torque between two neighbouring rings with $\boldsymbol{l}$ and $\boldsymbol{l} + \Delta\boldsymbol{l}$ is

$$G_2 = 2\pi R\frac{\nu_2}{2}\Sigma R^2\Omega\ \frac{\partial \boldsymbol{l}}{\partial r} \tag{1.119}$$

where ν_2 is the vertical shear viscosity responsible for the radial communication of the misaligned component of angular momentum. The third component of the viscous torque is derived from the fluid analysis of Papaloizou & Pringle (1983) and Ogilvie (1999) given by:

$$G_3 = 2\pi R\nu_3\Sigma R^2\Omega\ \boldsymbol{l} \times \frac{\partial \boldsymbol{l}}{\partial r} \tag{1.120}$$

where ν_3 is the effective viscosity responsible for the precessional torque between misaligned rings in the disc. This torque is responsible for a ring to precess if it is inclined with respect to its neighbours. Therefore:

$$G = 2\pi R\Sigma R^2\Omega\left[\nu_1\left(\frac{\Omega'}{\Omega}\right)\boldsymbol{l} + \frac{1}{2}\nu_2\frac{\partial \boldsymbol{l}}{\partial R} + \nu_3\boldsymbol{l} \times \frac{\partial \boldsymbol{l}}{\partial r}\right]. \tag{1.121}$$

Substituting this in equation 1.117 gives:

$$\begin{aligned}\frac{\partial}{\partial t}\left(\Sigma R^2\Omega \boldsymbol{l}\right) + \frac{1}{R}\frac{\partial}{\partial R}\left(\Sigma v_R R^3\Omega \boldsymbol{l}\right) = \frac{1}{R}\frac{\partial(\nu_1\Sigma R^3\Omega'\boldsymbol{l})}{\partial R} + \frac{1}{R}\frac{\partial}{\partial R}\left(\frac{1}{2}\nu_2\Sigma R^3\Omega\frac{\partial \boldsymbol{l}}{\partial r}\right) \\ + \frac{1}{R}\frac{\partial}{\partial R}\left(\nu_3\Sigma R^3\Omega\boldsymbol{l} \times \frac{\partial \boldsymbol{l}}{\partial r}\right)\end{aligned} \tag{1.122}$$

where the radial velocity v_R is given by (Pringle, 1992),

$$v_R = \frac{\frac{\partial}{\partial r}(\nu_1 \Sigma R^3 \Omega') - \frac{1}{2}\nu_2 \Sigma R^3 \Omega |\frac{\partial \boldsymbol{l}}{\partial r}|^2}{R\Sigma \frac{\partial}{\partial R}(R^2\Omega)}. \tag{1.123}$$

When we substitute v_R in equation 1.122, the evolution equation (also refer equation 27 in Nixon & King (2016)) becomes

$$\begin{aligned}
\frac{\partial \boldsymbol{L}}{\partial t} &= \frac{1}{R}\frac{\partial}{\partial R}\left\{\frac{(\partial/\partial R)[\nu_1 \Sigma R^3(-\Omega')]}{\Sigma(\partial/\partial R)(R^2\Omega)}\boldsymbol{L}\right\} \\
&+\frac{1}{R}\frac{\partial}{\partial R}\left[\frac{1}{2}\nu_2 R|\boldsymbol{L}|\frac{\partial \boldsymbol{l}}{\partial R}\right] \\
&+\frac{1}{R}\frac{\partial}{\partial R}\left\{\left[\frac{\frac{1}{2}\nu_2 R^3\Omega|\partial/\partial R|^2}{(\partial/\partial R)(R^2\Omega)} + \nu_1\left(\frac{R\Omega'}{\Omega}\right)\right]\boldsymbol{L}\right\} \\
&+\frac{1}{R}\frac{\partial}{\partial R}\left(\nu_3 R|\boldsymbol{L}|\ \boldsymbol{l}\times\frac{\partial \boldsymbol{l}}{\partial R}\right).
\end{aligned}$$

This equation is similar to the evolution equation derived in Pringle (1992), with the addition of the last term demonstrating the precessional nature of the disc included in Papaloizou & Pringle (1983) and Ogilvie (1999).

1.5.4 Disc tearing

Accretion discs act as the feeding ground for supermassive black holes. These discs are often tilted and warped due to the Lense-Thirring effect. If the warp is too large, it causes the breaking of discs into two or more distinct planes. As mentioned earlier, the initial evolution equations of warped discs by Bardeen & Petterson (1975) couldn't conserve the angular momentum, which was later derived by Papaloizou & Pringle (1983). This evolution equation (as shown earlier in section 1.5.3) comprised of the torques due to radial and vertical components of viscosities in a linear regime. Also, Ogilvie (1999) derived the same using torque coefficients in a non linear regime. These analyses marked a great advancement in the study of warped discs.

From the conservation laws used in Ogilvie (1999), it is shown that the viscous torques in the disc doesn't effectively communicate the Lense-Thirring precession to produce a smooth warp in discs at high inclinations and spin, and at low values of the viscosity parameter α (Nixon & King, 2012). Instead, the disc is found to break between the aligned inner regions and the misaligned outer regions forming individually precessing rings. Tearing of discs in the diffusive regime is tested with simulations using the smoothed particle hydrodynamics (SPH) code PHANTOM (Nixon et al., 2012a). This study derives the criterion for the radius at which the disc tears. The breaking criterion assumes the torque resulting from Lense-Thirring effect to be greater than the local viscous torques. In other words, the disc orbits precess faster than the time required for viscosity to communicate with the precession. Therefore, if the viscosity is dominant, the whole disc precesses as a rigid body. On the contrary, if the viscosity is negligible, the orbits at different radii precess at different rates and the disc breaks into many rings.

Firstly, we examine how the breaking radius $R_{\rm break}$ is derived in Nixon et al. (2012a). The viscous force per unit area is given by

$$f_\nu = \mu R \frac{d\Omega}{dR} \tag{1.124}$$

where μ is the dynamical viscosity, $Rd\Omega/dR$ is the rate of shear, R denotes the radial coordinate and Ω is the disc angular velocity. If the area of the disc is $2\pi RH$ where H is the disc vertical thickness, the viscous force in the azimuthal direction is given as:

$$F_\nu = 2\pi RH\mu R\frac{d\Omega}{dR} = 2\pi R\nu\Sigma R\frac{d\Omega}{dR} \tag{1.125}$$

where we have $\mu = \rho\nu$ and $\Sigma = \rho H$. The viscous torque G_ν is given as:

$$G_\nu = |R \times F_\nu| = 2\pi R\nu\Sigma R^2(-\Omega') \tag{1.126}$$

where Ω is:

$$\Omega = \sqrt{\frac{GM}{R^3}}. \tag{1.127}$$

Therefore,

$$G_\nu = 3\pi\nu\Sigma(GMR)^{1/2}. \tag{1.128}$$

On the other hand, the Lense-Thirring precession induces a torque given by:

$$G_{LT} = 2\pi RH|\Omega_p \times \boldsymbol{L}| = 2\pi RH\Omega_p\Sigma R^2\Omega|\sin\theta| \tag{1.129}$$

where Ω_p is the Lense-Thirring frequency given by $\Omega_p = 2GJ_h/c^2R^3$, $\boldsymbol{L}$ is the angular momentum density given by $|\boldsymbol{L}| = \Sigma R^2\Omega$, and θ is the angle between the angular momentum of the black hole and the disc. The disc breaking criterion requires the Lense-Thirring torque to be greator than the viscous torque, thus:

$$G_{LT} \geq G_\nu. \tag{1.130}$$

If we consider the standard α-disc approximation (Shakura & Sunyaev 1973) with $J_h = aGM^2/c$, the radius at which the disc likely breaks can be derived as (also shown in equation 7 of Nixon et al. (2012a))

$$R_{\rm break} \leq \left(\frac{4}{3}|\sin\theta|\frac{a}{\alpha}\frac{R}{H}\right)^{2/3} R_g \tag{1.131}$$

where the gravitational radius, $R_g = GM/c^2$.

It can be inferred from equation 1.131 that the breaking radius is governed by the values of spin (a), viscosity (α), inclination angle (θ) and the value of H/R. Hence, at a value of large viscosity, low values of spin (at values closer to $a = 0$) or at smaller inclinations, the disc cannot break since $R_{\rm break} < R_g$. On the other had, the disc is likely to break into rings at a low viscosity value, high spin and at large inclinations since

$R_{\text{break}} > R_g$.

The criterion of R_{break} can be used to predict the results of SPH simulations and investigate tearing of discs at different values of inclinations. In addition, it also enables to study the rate of mass flow checking if disc tearing can result in a rapid accretion rate in discs and cause a dynamical infall of matter in in AGNs (in case of couter-rotating discs around SMBHs (Nixon et al., 2012a) and SMBH binaries (Nixon et al., 2012b).

Nixon et al. (2012a) considers a disc with Shakura & Sunyaev $\alpha = 0.1, H/R = 0.01$ and inner and outer radii set at 50 R_g and 250 R_g respectively. Firstly, at an initial inclination of 10°, at which the value of R_{break} is calculated as 40 R_g. But since the breaking radius lies within the inner radius, the disc is not expected to break (as shown in figure 1.15).

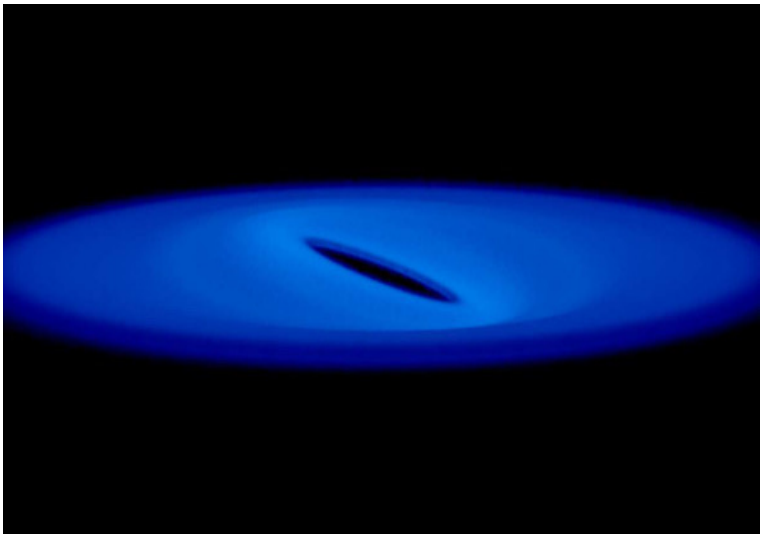

Figure 1.15: 3D simulation of the disc inclined at 10° to the hole, with no initial warp. As expected, the disc doesn't break since its R_{break} is less than the inner radius of the disc. Image taken from Nixon et al. (2012a).

Secondly, at an inclination of 60° where the calculated value of $R_{\text{break}} = 110\ R_g$, the disc is expected to break. It agrees well with the simulation which shows the tearing of disc, forming multiple inclined rings of gas (as shown in figure 1.16).

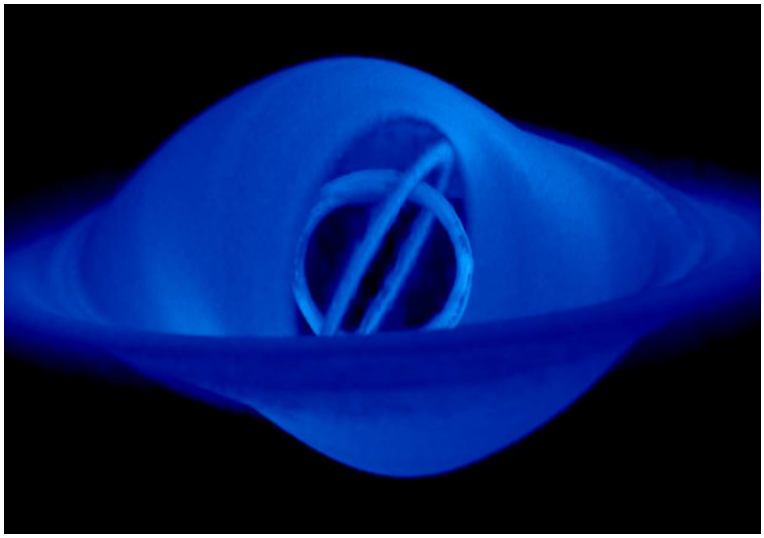

Figure 1.16: 3D simulation of the disc inclined at 60° to the hole, with no warp. The disc tearing is clearly evident at a higher inclination. Image taken from Nixon et al. (2012a).

1.6 What we don't understand?

In this section, we summarise some of ongoing challenges from the various observational and numerical investigations of accretion discs.

1.6.1 Size-variability in discs

Accretion discs around SMBHs serve as dominant sources powering active galactic nuclei. As demonstrated earlier in equation 1.84, the temperature across the disc varies as $T(r) \propto R^{-3/4}$. It is an ongoing challenge testing several theoretical models of accretion discs to measure the overall size scale or the slope of the temperature profile. The disagreement in the observed values on sizes, luminosities as well as the temperature profiles of the AGN discs in comparison to their results from theoretical models still remains unresolved.

Reverberation mapping (e.g. Edelson et al. (2015), Starkey et al. (2017)) along with gravitational microlensing (e.g. Morgan et al. (2010), Schechter et al. (2014)) are considered as two powerful techniques for probing the regions around AGNs. Reverberation mapping (RM) gives an insight into the structure of AGN accretion discs and is a standard tool to study AGN discs over the past years (Clavel et al., 1991; Peterson, 1993;

Edelson et al., 2015; Starkey et al., 2017). The basic principle of RM is the difference in the emissions at two different wavelengths such that the time delay (or lag) in their light curves represents the light-travel time within the system. This time delay is used to obtain the measurement of the systems physical size (as shown in section 1.2.3).

There are several observational papers (Edelson et al., 2015; Starkey et al., 2017) examining the reverberating disc models for Seyfert 1 galaxy, NGC 5548 (also detailed in chapter 4). Starkey et al. (2017) discusses the variability in continuum light curves of NGC 5548, and examine the temperature structure of its accretion disk. This study includes 19 overlapping continuum light curves (1158 Å to 9157 Å) combining data from Hubble Space Telescope (*HST*), *Swift*, and ground-based observations over a period of 180 days from January to July, 2014. This model yields a temperature versus radius slope ($T(R) \propto R^{-\alpha}$) of $\alpha = 0.99 \pm 0.03$. This is not in agreement to the standard thin disc model where the value of $\alpha = 0.75$ (as $T(R) \propto R^{-\alpha}$).

Furthermore, gravitational microlensing of quasars addresses the disagreement seen in disc sizes between the theory and observational models. Microlensing studies find that disc sizes appear larger (factor of 3 - 4) than predicted by thin-disk theory (Morgan et al., 2010). Also, some microlensing results show uncertainties in the temperature profiles compared to the predictions of thin-disk theory (Blackburne et al., 2011). Although, there are studies (McHardy et al., 2016) which explain the ultraviolet (UV) variability in disc models, the physical origin of the source of continuum variability remains unclear. This highlights the requirement of good theoretical explanations to study the variability in accretion discs and bridge the gap between the current theory models and observations.

1.6.2 Large amplitude, short timescale variability

Large amplitude variability at optical to X-ray wavelengths is observed in an increasing number of Seyfert galaxies and quasars. These variations imply that a change in accretion

power is too rapid to be communicated by inflow through an accretion disc if one assumes the standard thin disc model. Therefore, it will be difficult to explain the observed optical/UV emission from active galactic nuclei in case of these structures.

Furthermore, a recent crisis in the variability problem is the extreme variability (in factors of a few over a decade) in some quasars and AGNs at optical and UV wavelengths (Lawrence, 2018). Although, these changes are seen in many low luminosity objects, a recent comparison of data from the Sloan Digital Sky Survey (SDSS) and the Panoramic Survey Telescope and Rapid Response System (PanSTARRS) exhibited observations of extreme variability in AGNs and quasars at high luminosities termed as changing look AGNs (MacLeod et al., 2016). Therefore, the wide variability in their optical and far UV emissions concludes that the outer parts of the disc is undergoing a large physical change on a timescale which is not compatible to the viscous timescale.

Lawrence (2018) also suggests the idea of extreme reprocessing as a solution to explain this variability (also detailed in 4). Here, one assumes a disc with a very low viscosity, passively heated by the central source. The energy emitted from the central quasi point heats the disc, forming the viscous inner region $(3-10R_s)$ with a much shorter timescale than the outer disc $(30-100R_s)$. However, the erratic variations of the central source may impose complications in this scenario that makes it difficult to study the optical source size and the amplitude of variability of the discs at different wavelengths. Dexter & Begelman (2019) also addressed this issue of extreme variability in AGN and quasars, and suggested the idea of accretion discs supported vertically by strong magnetic fields (magnetically elevated discs) to provide an explaination. This study proposes how magnetically elevated discs can explain the large temperature fluctuations and provide an alternative scenario of extreme reprocessing in AGN discs. These studies suggest why its essential to investigate more theory models that can efficiently explain this viscosity crisis and discuss the physical origin of these changing look events.

1.6.3 Angular momentum transport

As we know, disc turbulence driving the angular momentum transport allows the mass to spiral inwards through the disc (Lynden-Bell, 1969; Pringle, 1981). Shakura & Sunyaev (1973) suggested the α-prescription by parameterising the strength of disc turbulence in terms of a dimensionless parameter α. King et al. (2007) discusses the large discrepancy between the α values required to model observations of fully ionized, time-dependent accretion discs (where $\alpha \simeq 0.1$ - 0.4) and those obtained from numerical MHD simulations without including a superimposed magnetic field (where $\alpha \leq 0.02$). Furthermore, Martin et al. (2019) extended this work to study the nature of viscosity in accretion discs. The estimated values of viscosity α from the observations is found in agreement with King et al. (2007). It is concluded that for fully ionized discs, estimates on the values of α are consistent with $\alpha \simeq 0.2$ - 0.3. In the case of partially ionized discs, the estimates of α are smaller than those found for fully ionized discs by an order or several orders of magnitude. This study also points out that the main difference between fully ionized and partially ionized discs lies not in its hydrodynamic, but in their magnetic properties i.e., a less ionized disc has a low electrical conductivity which reduces its ability to interact with magnetic fields. These studies highlight the importance of a detailed understanding on the main driving mechanism of turbulence and angular momentum transport in viscous accretion discs.

1.7 Numerical methods

Along the side of observations and analytic theory, numerical simulations constitute the backbone to study astrophysics. From an astrophysical point of view, there are two types of numerical simulations: grid-based codes (Fromang & Papaloizou, 2006; Paardekooper & Mellema, 2006) and particle based Smoothed Particle Hydrodynamics (SPH) codes

(Monaghan & Lattanzio, 1985; Monaghan, 1992). This section gives an overview to Smoothed Particle Hydrodynamics, the numerical method employed in this thesis.

1.7.1 Smoothed Particle Hydrodynamics

SPH, the acronym for Smoothed Particle Hydrodynamics was firstly introduced as a numerical approach in Gingold & Monaghan (1977) and independently in Lucy (1977) to resolve the non-axisymmetric problems involving fluid dynamics. As shown in Gingold & Monaghan (1982), SPH is a Lagrangian method allowing the conservation of linear and angular momentum and other physical invariants which cannot be easily assured from grid codes. There are many excellent papers, which review SPH (e.g. Monaghan, 1992; Cossins, 2010; Springel, 2010; Price, 2012).

There are two principal ways to develop computational simulations to facilitate the numerical simulations on fluid dynamics. Firstly, the Eulerian method that uses geometric grids either fixed or adaptive (the so-called AMR or Adaptive Mesh Refinement codes) which evaluates the fluid parameters over the grid cells. This concept was used in developing Computational Fluid Dynamics (CFD) in the late 1960s and early 70s and still remain a widely used approach. Such codes are widely used in the automotive and aerospace sectors to study industrial aerodynamics, to stress calculations and solid mechanics for civil engineering and architecture, to model chemical reactions and protein folding in biomolecular models (Cossins, 2010).

Secondly, we have Lagrangian numerical methods that evaluate fluid properties in a co-moving frame. This method uses the approach of having discrete particles that are carried with the flow - hydrodynamic properties are calculated at the particle positions and evaluated from a weighted average of the values on other local particles. This way, each particle is smoothed over a finite volume of fixed mass, thus termed as Smoothed Particle Hydrodynamics or SPH codes. Although SPH codes are extensively used in

astrophysics, it has also found applications in a range of fields, like studying dam breaks and atomised oil lubrication flows in engineering as well as designing computer games (Cossins, 2010).

Density and Fluid Quantities in SPH

The main idea employed in SPH is to define a set of mass-particles, each with a proper mass and position to evaluate the values of a set of parameters (such as velocity, density, etc.) at that particular point in space. Thus, instead of discretising space in small cells as carried out in grid-based codes, SPH discretises the mass of the fluid particles. The evolution of the quantities in time and space is determined by a set of partial differential equations obtained from a function that smoothes the discreteness due to point particles. This interpolation calculates the quantities for each particle, thus allowing the system to evolve in time using a temporal integrator. Figure 1.17 shows the common methods evaluating the density from a collection of point mass particles.

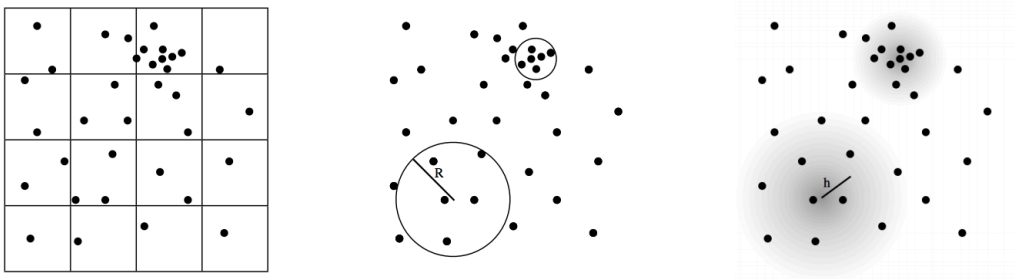

Figure 1.17: The left panel in the figure shows the particle mesh method where the density is calculated by interpolating the mass to a grid thus dividing mass by the volume. But in this method, the clustered or sparse regions in the grid aren't well resolved. The middle panel demonstrates a method which solves the clustering problem, calculating density without a mesh but by constructing a local volume around a sampling point. This scales the volume in terms of the local number density of the particles. The third panel shows the method employed in SPH, where the density is calculated from the weighted sum over the neighbouring particles. The weight decreases with distance from the sample point by a scale factor of h termed as the smoothing length. Image taken from Price (2012).

Discrete Approximations of a Continuous Field

To compute continuum quantities from point particles, let us consider a mathematical method to express a continuum function starting from a discrete set of points in space. Each point of this set gives information about position, and values of other arbitrary

quantities, e.g. density and velocity, in that position. We consider:

$$f(r) = \int f(r')\delta(r - r')dr' \tag{1.132}$$

where $f(r)$ is a function on a three-dimensional coordinate system r over a volume V, $\delta(r)$ is the Dirac delta function and r' is the dummy variable ranging over V. If we generalise the delta function to a smoothing kernel W in terms of smoothing length h, it gives:

$$\lim_{h\to 0} W(r - r', h) = \delta(r - r'). \tag{1.133}$$

Therefore,

$$f(r) = \int f(r')W(r - r', h)dr' + O(h^2). \tag{1.134}$$

The kernel function is normalised as:

$$\int W(r - r', h)dr' = 1. \tag{1.135}$$

If we discretise for a series of particles of mass m_b, equation 1.132 becomes:

$$f(r) = \int \frac{f(r')}{\rho(r')} W(r - r', h)\rho(r')dr' + O(h^2) \approx \sum_{b=1}^{N} \frac{m_b}{\rho_b} f(r_b)W(r - r_b, h) \tag{1.136}$$

where m_b and ρ_b are the mass and density of the b^{th} particle, range over a total of N particles. Hence from equation 1.136, we estimate the density as:

$$\rho(r) = \sum_{b=1}^{N} m_b W(r - r', h(r)). \tag{1.137}$$

The accuracy of this estimate of density relies on the good choice of the smoothing kernel.

The Smoothing Kernel

A good kernel has to satisfy some properties which include (Price, 2012)

- it should be positively defined.
- it should monotonically decrease with distance.
- it should have a continuous and well defined first derivative.
- it should be symmetric with respect to $r - r'$, i.e. $W(r - r', h) = W(\mid r - r' \mid, h)$.
- it should be bell-shaped, so that the density is not highly affected by a small change in the position of the near particle. One of the first choices for the smoothing kernel which satisfies these conditions is the Gaussian function.

$$W(r - r', h) = \frac{1}{(h^3\pi^{3/2})} exp\Big[- \frac{(r - r')^2}{h^2} \Big] \tag{1.138}$$

However, a Gaussian kernel has the disadvantage of being greater than zero for all $r = \mid r - r' \mid$. The computational cost of this kernel values as $O(N^2)$ where N is the number of particles in the simulation. Assuming that the long range forces are negligible, it is sensible to restrict the kernel with a compact support, i.e. the kernel needs to satisfy the condition that $W(\mid r - r' \mid, h) = 0$ where $\mid r - r' \mid /h > k$ for a constant value of k. This makes the computational cost to be measured as $O(NN_{\text{neigh}})$, where N_{neigh} is the average number of particles within a sphere of radius $r = kh$. Therefore, a common choice in SPH for the kernel are the B-spline functions (Monaghan & Lattanzio, 1985) defined as:

$$W(r, h) = \frac{1}{\pi h^3} \begin{cases} 1 - \frac{3}{2}x^2 + \frac{3}{4}x^3 & 0 \leq x \leq 1 \\ \frac{1}{4}(2 - x)^3 & 1 \leq x < 2 \\ 0 & x \geq 2. \end{cases} \tag{1.139}$$

where $x = r/h$. This is the most commonly used kernel (termed as the cubic spline) in which the kernel is truncated at $2h$ and is spherically symmetric and differentiable at all r. The gradient of the kernel from the above equation is well defined at all values of x

given by:

$$\nabla W(r,h) = \frac{\partial}{\partial r} W(r,h) = \frac{1}{\pi h^4} \begin{cases} \frac{9}{4}x^2 - 3x & 0 \leq x \leq 1 \\ -\frac{3}{4}(2-x)^2 & 1 \leq x < 2 \\ 0 & x \geq 2. \end{cases} \tag{1.140}$$

In general, the form of the kernel only makes little overall difference in the computational speed of the code. This is because, most codes tabulate the kernel and the derivatives rather than computing them directly. Therefore, the kernel may take a simple or complex form of a non-analytic functions (Cossins, 2010).

The Smoothing length

The smoothing length $h(r)$ is adopted in SPH to better resolve spatial distances where needed. In order to resolve the dense regions with respect to sparse regions, the smoothing length follows the number density (Springel & Hernquist, 2002) as:

$$h(r) \propto n(r)^{-1/d} \tag{1.141}$$

with

$$n(r) = \sum_{b=1}^{N} W(r - r_b, h(r)) \tag{1.142}$$

where $n(r)$ is the number of particles per unit volume and d is the number of spatial dimensions. Since $n(r) \propto \rho(r)$, the relation between the density and the smoothing length for particle a is (Price, 2012):

$$h_a = \eta \left(\frac{m_a}{\rho_a} \right)^{1/d}. \tag{1.143}$$

where the constant η is a free parameter. As the density is approximately a constant over the kernel radius, the number of neighbours can be calculated as a function of η in three

dimensions as

$$N_{\text{neigh}} = \frac{4}{3}\pi(\zeta\eta)^3 \tag{1.144}$$

where ζ is the compact support radius in units of h (i.e. $\zeta = 2$ for the cubic spline). At $\eta = 1.2$, the number of neighbours ≈ 58 which is commonly adopted in SPH simulations.

SPH Equations

This section discusses how to obtain the SPH equations of motion through variational principles and thermodynamics. We discuss how these equations are derived from an appropriate Lagrangian.

The Discrete Lagrangian

The Lagrangian is equated as:

$$L = T - V \tag{1.145}$$

where T is the kinetic and V is the potential or thermal energy of the system. For a system of point masses with velocity $v = dr/dt$ and an internal energy per unit mass u, we get (Price, 2012)

$$L = \sum_b m_b \left[\frac{1}{2}v_b^2 - u_b(\rho_b, s_b)\right] \tag{1.146}$$

where the internal energy u is a function of density ρ and entropy s respectively. This discrete version of the Lagrangian is used to obtain the Euler-Lagrange equations, which further derive the equations of motion.

Euler - Lagrange equations

The equations of motion can be derived from the principle of least action, given by

$$S = \int L dt \tag{1.147}$$

such that $\delta S = \int \delta L \ dt = 0$ where δ is a small change with respect to the change in the particle co ordinates δr. If we assume the Lagrangian as a differentiable function of particle positions r and velocities v, we get (Price, 2012)

$$\delta S = \int \left(\frac{\partial L}{\partial v} . \delta v + \frac{\partial L}{\partial r} . \delta r \right) dt = 0. \tag{1.148}$$

Using integration by parts, this becomes

$$\frac{\partial L}{\partial v} . \delta r - \int \delta r . \frac{d}{dt} \left(\frac{\partial L}{\partial v} \right) dt + \int \left(\frac{\partial L}{\partial r} . \delta r \right) dt = 0 \tag{1.149}$$

which can be rewritten as :

$$\delta S = \int \left\{ \left[- \frac{d}{dt} \left(\frac{\partial L}{\partial v} \right) + \frac{\partial L}{\partial r} \right] . \delta r \right\} dt + \left[\frac{\partial L}{\partial v} . \delta r \right]_{t_0}^{t} = 0. \tag{1.150}$$

Hence,for particle a:

$$- \frac{d}{dt} \left(\frac{\partial L}{\partial v_a} \right) + \frac{\partial L}{\partial r_a} = 0, \tag{1.151}$$

$$\frac{d}{dt} \left(\frac{\partial L}{\partial v_a} \right) = \frac{\partial L}{\partial r_a}. \tag{1.152}$$

Firstly, let us consider the LHS of the equation. Since $\frac{\partial L}{\partial v_a} = m_a v_a$, we get

$$\frac{d}{dt} \left(\frac{\partial L}{\partial v_a} \right) = \frac{d(m_a v_a)}{dt}. \tag{1.153}$$

Since

$$L = \sum_b m_b \left[\frac{1}{2} v_b^2 - u_b(\rho_b, s_b) \right], \tag{1.154}$$

$$\frac{\partial L}{\partial r_a} = - \sum_b m_b \left. \frac{\partial u_b}{\partial \rho_b} \right|_S \frac{\partial \rho_b}{\partial r_a} \tag{1.155}$$

where $\rho_b = \sum_{b=1}^{N} m_b W(r - r_b, h(r))$ (from equation 1.142). In order to calculate $\frac{\partial u_b}{\partial \rho_b}$, we consider the first law of thermodynamics given by

$$dU = TdS - PdV \tag{1.156}$$

where $dQ = TdS$ is the heat added to the system and $dW = PdV$ is the work done by expansion or compression. Since $dV = -\frac{m}{\rho^2}d\rho$, the internal energy for unit mass gives:

$$dU = TdS + \frac{P}{\rho^2}d\rho \tag{1.157}$$

Hence, at a constant entropy:

$$\frac{\partial u_b}{\partial \rho_b} = \frac{P}{\rho^2}. \tag{1.158}$$

In order to derive $\frac{\partial \rho_b}{\partial r_a}$, we assume the mass in the kernel volume to be a constant, i.e.

$$\rho h^3 = \text{constant} \tag{1.159}$$

where ρ is $\rho(r_a) = \sum_b m_b W(\mid r_a - r_b \mid, h_a)$ and h is $h(r_a) = \eta\left(\frac{m_a}{\rho_a}\right)^{1/d}$.

From equation 1.159, $\rho = \text{constant}/\text{h}^3$ therefore,

$$\frac{3\rho}{h} = \frac{3 \text{ constant}}{h^4}. \tag{1.160}$$

Also,

$$\frac{\partial \rho}{\partial h} = \frac{-3 \text{ constant}}{h^4}. \tag{1.161}$$

In other words,

$$\frac{\partial \rho}{\partial h} = \frac{-3\rho}{h}. \tag{1.162}$$

Hence, we have

$$\frac{\partial L}{\partial r_a} = -\sum_b m_b \frac{P_b}{\rho_b^2}\frac{\partial \rho_b}{\partial r_a} \tag{1.163}$$

where

$$\frac{\partial \rho_b}{\partial r_a} = \nabla_a \rho_b + \frac{\partial \rho_b}{\partial h_b}.\frac{\partial h_b}{\partial r_a} \tag{1.164}$$

where $\nabla_a \rho_b$ is the differentiation of ρ_b with respect to r_a keeping smoothing length a constant.

$$\frac{\partial \rho_b}{\partial h_b}.\frac{\partial h_b}{\partial r_a} - \frac{\partial \rho_b}{\partial r_a} = -\nabla_a \rho_b \tag{1.165}$$

$$\frac{\partial \rho_b}{\partial h_b}.\frac{\partial h_b}{\partial r_a}\left[1 - \frac{\partial \rho_b}{\partial r_a}.\frac{\partial h_b}{\partial \rho_b}.\frac{\partial r_a}{\partial h_b}\right] = -\nabla_a \rho_b \tag{1.166}$$

$$\frac{\partial \rho_b}{\partial h_b}.\frac{\partial h_b}{\partial r_a}\left[1 - \frac{\partial \rho_b}{\partial h_b}.\frac{\partial h_b}{\partial \rho_b}\right] = -\nabla_a \rho_b \tag{1.167}$$

Using 1.162, the above equation can be rewritten as:

$$\frac{\partial \rho_b}{\partial h_b}.\frac{\partial h_b}{\partial r_a}\left[1 + \frac{3\rho_b}{h_b}\left(\frac{\partial h_b}{\partial \rho_b}\right)\right] = -\nabla_a \rho_b. \tag{1.168}$$

Therefore,

$$\frac{\partial \rho_b}{\partial h_b}.\frac{\partial h_b}{\partial r_a} = \frac{-\nabla_a \rho_b}{\left[1 + \frac{3\rho_b}{h_b}\left(\frac{\partial h_b}{\partial \rho_b}\right)\right]}. \tag{1.169}$$

Substituting equation 1.169 in equation 1.164 gives:

$$\frac{\partial \rho_b}{\partial r_a} = \nabla_a \rho_b \left(1 - \frac{1}{1 + \frac{3\rho_b}{h_b}\left(\frac{\partial h_b}{\partial \rho_b}\right)}\right) \tag{1.170}$$

$$\frac{\partial \rho_b}{\partial r_a} = \nabla_a \rho_b \ \frac{\frac{3\rho_b}{h_b}\left(\frac{\partial h_b}{\partial \rho_b}\right)}{1 + \frac{3\rho_b}{h_b}\left(\frac{\partial h_b}{\partial \rho_b}\right)} \tag{1.171}$$

Dividing the equation by $\frac{3\rho}{h_b}.\frac{\partial h_b}{\partial \rho_b}$,

$$\frac{\partial \rho_b}{\partial r_a} = \nabla_a \rho_b \ \frac{1}{1 + \frac{h_b}{3\rho_b}\left(\frac{\partial \rho_b}{\partial h_b}\right)}. \tag{1.172}$$

Therefore

$$\frac{\partial \rho_b}{\partial r_a} = \nabla_a \rho_b \left[1 + \frac{h_b}{3\rho_b} . \frac{\partial \rho_b}{\partial h_b}\right]^{-1}. \tag{1.173}$$

If we assume, $\Omega = 1 + \frac{h_b}{3\rho_b} . \frac{\partial \rho_b}{\partial h_b}$, equation 1.173 can be written as:

$$\frac{\partial \rho_b}{\partial r_a} = \nabla_a \rho_b . \frac{1}{\Omega_b} \tag{1.174}$$

Using another index c, $\nabla_a \rho_b$ can be written as:

$$\frac{\partial \rho_b}{\partial r_a} = \frac{1}{\Omega_b} \sum_c m_c \frac{\partial W_{bc}(h_b)}{\partial r_a} (\delta_{ba} - \delta_{ca}). \tag{1.175}$$

Substituting equation 1.175 in 1.155 gives:

$$\frac{\partial L}{\partial r_a} = -\sum_b m_b \frac{P_b}{\rho_b^2} \frac{1}{\Omega_b} \sum_c m_c \frac{\partial W_{bc}(h_b)}{\partial r_a} (\delta_{ba} - \delta_{ca}) \tag{1.176}$$

and

$$\frac{dv_a}{dt} = -\sum_b m_b \left[\frac{1}{\Omega_a} \frac{P_a}{\rho_a^2} \nabla_a W_{ab}(h_a) + \frac{1}{\Omega_b} \frac{P_b}{\rho_b^2} \nabla_a W_{ab}(h_b)\right]. \tag{1.177}$$

Thus for a constant smoothing length, this equation can be simplified to a standard form,

$$\frac{dv_a}{dt} = -\sum_b m_b \left(\frac{P_a}{\rho_a^2} + \frac{P_b}{\rho_b^2}\right) \nabla_a W_{ab}. \tag{1.178}$$

1.7.2 Dissipative Effects in SPH

So far, the fluid flow is assumed to be perfectly inviscid and therefore devoid of any dissipation. But, the same assumptions cannot be used when modelling transonic and supersonic flows. This problem occurs because of a shock wavefront, wherein the flow properties such as velocity, pressure, density and entropy change very rapidly (Cossins, 2010). There are two methods to solve the shocked flows - one is the Riemann solver, second is the technique of implementing an artificial dissipative term in the momentum

and energy equations that is activated only in the presence of shocks.

Artificial viscosity

In order to resolve shocked flows, the majority of SPH codes use an artificial dissipative term or artificial viscosity that broadens the shock across a number of smoothing lengths. This will guarantee the flow gradients from not becoming infinite, and gives their accurate behaviour away from the shock. Hence, we require artificial viscosity to obey to the following rules (Cossins, 2010):

- flow equations should contain no discontinuities.
- the shock front should be smoothed over a number of smoothing lengths.
- the shock front should be of the order of a few times the smoothing length.
- the artificial viscosity should reduce to zero, at regions away from the shock front.
- the Rankine-Hugoniot conditions must be satisfied across the shock. They include

$$\rho_0 v_0 = \rho_1 v_1 \tag{1.179}$$

$$P_0 + \frac{\rho_0 v_0^2}{2} = P_1 + \frac{\rho_1 v_1^2}{2} \tag{1.180}$$

$$\frac{P_0}{\rho_0} + u_0 + \frac{v_0^2}{2} = \frac{P_1}{\rho_1} + u_1 + \frac{v_1^2}{2} \tag{1.181}$$

  where the subscripts 0 and 1 refer to the pre-shock and post-shock regions respectively.

- Although, the entropy increases when passing from a pre-shock region to a post-shock region, the total momentum and energy will be conserved.

On dimensional grounds, artificial viscosity Π is given as:

$$\Pi \propto \frac{v^2}{\rho} \tag{1.182}$$

for a local velocity scale v. Von Neumann & Richtmyer (1950) suggested a viscous term dependent on the squared velocity divergence, represented in the SPH form given as:

$$(\Pi_{ab})_{\rm NR} = \frac{\beta_{\rm SPH} h^2 \mid \nabla.v_{ab} \mid^2}{\bar{\rho_{ab}}} \tag{1.183}$$

where h is the characteristic length scale (analogous to the smoothing length in SPH), $\bar{\rho_{ab}}$ is the average density of particles a and b and $\beta_{\rm SPH}$ is a constant term of order unity. The velocity divergence is given by:

$$\mid \nabla.v_{ab} \mid = \frac{\mid v_{ab} \mid}{\mid r_{ab} \mid} \approx \frac{\mid v_{ab}.r_{ab} \mid}{\mid r_{ab}^2 + \epsilon h^2 \mid} \tag{1.184}$$

where $r_{ab} = r_a - r_b$ and if we assume

$$\mu = \frac{h v_{ab}.rab}{\mid r_{ab} \mid^2 + \epsilon h^2} \tag{1.185}$$

$(\Pi_{ab})_{\rm NR}$ becomes

$$(\Pi_{ab})_{\rm NR} = \frac{\beta_{\rm SPH} \mu^2}{\bar{\rho_{ab}}}. \tag{1.186}$$

With the inclusion of both bulk and shear viscosities, we can deduce a linear form to the aritificial viscosity given by (Cossins, 2010)

$$\Pi_{ab} = -\frac{\alpha_{\rm SPH} c_s \mu}{\bar{\rho_{ab}}} \tag{1.187}$$

where $\alpha_{\rm SPH}$ is a second constant of order unity. The negative on the RHS arises because the viscous force should be non-negative ($\Pi_{ab} > 0$) and it should be present only for convergent flows where $v_{ab}.r_{ab} < 0$. These two forms of the equation have different numerical effects. At low Mach numbers ($M \leq 5$), the linear form performs well (Monaghan & Lattanzio, 1985) whereas fails for stronger shocks. In cases, when two streams pass through each other at the shock front leading to a multi valued velocity field when two

particles with different velocities try to occupy the same position, we use a quadratic form for artificial viscosity given by:

$$\Pi_{ab} = \begin{cases} \frac{-\alpha_{\rm SPH} c_s \mu_{ab} + \beta_{\rm SPH} \mu_{ab}^2}{\rho_{ab}} & v_{ab}.r_{ab} < 0 \\ 0 & \text{otherwise.} \end{cases} \tag{1.188}$$

This represents the standard solution to the SPH viscous term using the sum of the two terms (Monaghan & Lattanzio, 1985). This general form of the viscosity can be added in the momentum equation (as derived in equation 1.178) to give:

$$\frac{dv_b}{dt} = -\sum_a m_a \left[\frac{P_b}{\rho_b^2} + \frac{P_a}{\rho_a^2} + \Pi_{ba} \right] \nabla_b W_{ba}. \tag{1.189}$$

Therefore, the main aim of introducing a dissipative term is to capture the shock and broaden across a few smoothing lengths. There are several improvements that can be implemented to control artificial viscosity as briefly discussed in the next section.

Artificial Dissipation Switches

It is very important to control and make sure only sufficient dissipation is added, i.e. to ensure the artificial viscosity is only activated at the shock front and reduces to zero away from it. But in the case of discs where shear flows play a critical role, it is noted that shear force varies with smoothing length and this component is resolution dependent (Cossins, 2010). This effect can be controlled with sensible choices of $\alpha_{\rm SPH}$ and $\beta_{\rm SPH}$ (Lodato & Rice, 2004).

Balsara Switch

Balsara (1995) introduced an attempt to reduce the induced viscosity in shear flows by adding a correction term to the standard SPH artificial known as the Balsara switch.

The standard artificial term Π_{ab} is assumed to reduce by the factor $f_{ab} = \frac{|f_a+f_b|}{2}$ where

$$f_a = \frac{\mid \nabla v_a \mid}{\mid \nabla v_a \mid + \mid \nabla \times v_a \mid + 0.0001 c_s h}. \tag{1.190}$$

The curl of the flow field (vorticity) allows this form of viscosity to work better in shear flows and obliquely shocked flows (Cossins, 2010).

Morris & Monaghan Switch

An adaptation to Balsara switch by Morris & Monaghan (1997) presented the idea of a time variant viscosity such that, Π_{ab} remains unaltered from the standard form. The value of α evolves for each particle by:

$$\frac{d\alpha}{dt} = -\frac{\alpha - \alpha_{\min}}{\tau} + S_v \tag{1.191}$$

where $\alpha_{\min}$ is a minimum value to which α decays in a time scale $\tau = kh/c_s$ (where $k \sim 0.1 - 0.2$ is a constant) and $S_v = \max(-\nabla.\mathrm{v}, 0)$ is a source term activated only if the flow is convergent. Even though the source term remains non-zero for pure shear flows, it can be balanced to a certain extent by the decay term (Cossins, 2010). An improved approach to Morris & Monaghan (1997) to detect and respond to shocks is suggested in Cullen & Dehnen (2010). This study introduces a method of using the total time derivative of the velocity divergence (i.e. $d\nabla.v/dt$) as a shock indicator to differentiate between the pre shock and post shock regions.

Moreover, it is important to know how the artificial viscosity (α_{AV}) is used to represent the Shakura-Sunyaev disc viscosity (α) in SPH code PHANTOM. Lodato & Price (2010) demonstrates the standard form of artificial viscosity in terms of a shear and bulk viscosities as:

$$\nu_{AV} = \frac{1}{10}\alpha_{AV} c_s h \tag{1.192}$$

and

$$\zeta_{AV} = \frac{1}{6}\alpha_{AV} c_s h. \tag{1.193}$$

The magnitude of the shear viscosity arising from the numerical viscosity is therefore assumed as (Lodato & Price, 2010),

$$\alpha = \frac{1}{10}\alpha_{\rm AV}\frac{\langle h\rangle}{H} \tag{1.194}$$

where $\langle h\rangle$ is the averaged smoothing length (or shell averaged smoothing length) and H is the scale height of the disc. Therefore, one can obtain a disc evolution with a single uniform value of α throughout by setting up the disc with a surface density profile such that $\langle h\rangle/H$ is a constant. In our numerical analysis, we consider the shear viscosity contribution from the linear SPH term due to the artificial viscosity derived in Meru & Bate (2012) for a Keplerian disc given by

$$\alpha = \frac{31}{525}\alpha_{\rm AV}\frac{\langle h\rangle}{H}. \tag{1.195}$$

1.8 Outline of the thesis

The core of this dissertation is divided across four chapters. Chapter 2 discusses the instability of warped discs around supermassive black holes. We use the Smoothed Particle Hydrodynamics code PHANTOM to model a warped disc (without Lense-Thirring precession) in the diffusive regime, similar to the model used in Lodato & Pringle (2007). Our analysis uses the prediction by Doğan et al. (2018) to test the criterion for discs to become unstable and tear. This criterion, derived from the stability analysis and the resulting dispersion relation infers that each disc becomes unstable at a critical warp amplitude value $|\psi|_c$, dependent on the α parameter. We connect this instability criterion to the disc tearing behaviour in warped discs using numerical simulations of discs at different

α values at different degrees of misalignment. In this analysis, the possibility of tearing is studied in each disc by examining if its warp amplitude, ($\psi = r|\partial l/\partial r|$) exceeds $|\psi|_c$, the criterion to find when and where the warped disc is likely to become unstable and tear. Our numerical results not only agree with the theoretical criterion of tearing in warped discs, but also demonstrate that these discs become unstable, and break at small α values and higher inclinations as expected from previous studies (Nixon & King, 2012; Nixon et al., 2012a).

The same analysis is extended in chapter 3 which investigates disc tearing in accretion discs around supermassive black holes warped due to Lense-Thirring (LT) precession. This chapter explains how the instability criterion predicted from Doğan et al. (2018) can be further examined in the numerical simulations of discs warped due to LT effect. In a parameter sweep, we investigate if these diffusive, warped discs become unstable and tear to form discrete rings of gas at different values of α, H/R and tilts. We check if the values of warp amplitude in each of these discs exceed its critical value predicted by Doğan et al. (2018) and become unstable to disc tearing, and form individual, precessing rings. Doğan et al. (2018) also calculates the dimensionless growth rate of the warp amplitude $\Re[s]$ in these discs, which is dependent on the value of α, i.e. the growth rates are higher at lower values of α; our research extends to check if this holds true in discs at smaller values of α and H/R. Moreover, we also examine if the maximum value, to which the warp amplitude grows in the unstable regions of the disc, closely matches with the predicted results. We draw the conclusions from finding the agreement of our numerical results with the theoretical criterion for tearing in discs (Doğan et al., 2018).

Chapter 4 highlights on the potential applications of the disc tearing behaviour in warped AGN discs, and reviews how numerical models of these discs (as studied in chapter 3) can be used to explain the deviation of the observational results from the theoretical predictions of a standard α disc model. We discuss the observational studies, such as the

observed short timescale, large amplitude variability in the UV and optical wavelengths in AGN discs (Lawrence, 2018). We analyse this further by studying the time variability of NGC 5548 from the data reported in Edelson et al. (2015). This chapter also summarises Starkey et al. (2017) that finds the disc of NGC 5548 to have a steeper fall in temperature than the expected standard α disc model. We address these examples to illustrate why its important to use theoretical and numerical models of AGN discs, and examine if disc tearing dynamics in unstable warped discs can clarify the source of variability and anomalous behaviour observed in them. In this chapter, we conclude the possibility of disc tearing in warped accretion discs, which produces variable accretion flows around supermassive black holes (Nixon et al., 2012a), to explain the source of observational variability in AGN discs.

Chapter 5 outlines the numerical methodology for setting up the initial conditions in disc simulations that employ Smoothed Particle Hydrodynamics (SPH) in PHANTOM. If the initial conditions used are not in dynamical equilibrium, we see unwanted pressure waves across the discs which can be damped using numerical viscosity. At standard resolution, these waves damp on a timescale that is comparable to the time taken for the waves to traverse the disc. However, this leads to a scenario where higher resolution simulations require a longer relaxing phase which is computationally inefficient. We show that these waves can be removed, on a timescale independent of resolution by a suitable velocity damping scheme that tapers to zero over timescale comparable with the disc's dynamical timescale. Thus, we provide an effective algorithm for injecting particles into the disc at higher resolution, and study the long-term viscous evolution of accretion discs.

2

Instability of warped discs

2.1 Introduction

Accretion discs are present around a wide range of astrophysical objects such as planets, stars and supermassive black holes (SMBHs). Accretion discs are generally warped due to different effects. Tilted discs around black holes experience a torque due to the general relativistic Lense-Thirring (LT) effect, which causes differential precession at rates dependent on the distance of each orbit from the black hole (Lense & Thirring, 1918). This differential precession forms a warp where the inner part of the disc aligns with the spin of the black hole (Bardeen & Petterson, 1975). This prediction is termed as the Bardeen-Peterson effect.

For a warped disc, the local plane of the disc changes with radius (Nixon & King, 2016). As a result, there will be a displacement of the high pressure mid-plane region from one ring of the disc to its neighbour which oscillates at an azimuthal angle ϕ. There is no displacement when the rings cross at the descending node (with azimuthal angle $\phi = 0$) and at the ascending node (with $\phi = \pi$). On the other hand, the displacement is maximal at $\phi = \pi/2$ and $3\pi/2$ (shown in figure 1.14). Therefore, a fluid element in the disc experiences an epicyclic motion due to the oscillating radial pressure gradient induced by the warp. This epicyclic motion causes the propagation of warps in discs.

Warps in discs are propagated in two distinct modes: wavelike if $\alpha < H/R$ or diffusive if $\alpha > H/R$.

A linearised fluid analysis to derive the evolution equation of a warped disc was firstly done by Papaloizou & Pringle (1983). The analysis of the warped disc equations in the non-linear regime was further studied by Ogilvie (1999, 2000) and Ogilvie & Latter (2013) using non linear torque coefficients Q_1, Q_2 and Q_3 which were found to be dependent on the warp amplitude $|\psi|$. The effect of these viscous torques on the disc structure can determine how the warps grow and become large enough to break the disc. Doğan et al. (2018) derived an instability criterion for Keplerian warped discs, in the diffusive regime to become unstable and break. This general criterion to determine instabilities in discs is represented by a dispersion relation which governs the effect of viscous torque on the disc structure through the warp amplitude $|\psi|$. The key results of Doğan et al. (2018) include: (1) a critical warp amplitude at each α value for a disc to become unstable and (2) the growth of instabilities in warped discs at different values of α.

The aim of this chapter is to test this analysis by Doğan et al. (2018) using numerical simulations. Prior to the complex numerical study of discs warped due to the LT effect, a warped disc model the same as was used in Lodato & Pringle (2007) to study the propagation of warps, can be utilised to test the disc-breaking criterion from Doğan et al. (2018). This chapter discusses how this instability criterion can be applied in numerical simulations of warped discs without LT precession, for a range of α values, at different degrees of misalignment.

2.2 Motivation

Numerous studies have been done to investigate the evolution of warped discs (Papaloizou & Pringle, 1983; Pringle, 1992; Ogilvie, 1999, 2000; Ogilvie & Latter, 2013). The behaviour of warped discs was tested numerically in the case of thick discs where the warp prop-

agation is wave-like (Lubow & Ogilvie, 2000) as well as in thin discs with the diffusive warp propagation (Lodato & Pringle, 2007; Nixon & King, 2012). Nixon & King (2012) showed the evolution of tilted discs warped by the LT effect and examined if the warp amplitude was large enough to break the disc for $0.2 \leq \alpha \leq 0.5$ (note that this paper included the non-linear fluid constraints as explained in Ogilvie (1999)). The criterion for warped discs to tear in the diffusive regime was examined using SPH simulations to study tilted discs around a central black hole (Nixon et al., 2012a). This study calculated the breaking radius for a disc by comparing the LT precession torque to the torque from the azimuthal shear viscosity. This was extended to study disc tearing in circumbinary discs (Nixon et al., 2013) and circumprimary discs (Doğan et al., 2015) around misaligned binary systems. Doğan et al. (2015) highlighted the inclusion of effective viscosity from the vertical shear in the criterion for disc breaking at small values of inclinations and α. These studies emphasise the need for an instability criterion that can be applied globally, to study disc tearing in many systems. Doğan et al. (2018) derived a general criterion for isothermal warped discs in the diffusive regime to tear, i.e. each α parameter corresponds to a critical value of warp amplitude above which the disc becomes unstable and tears. This criterion needs to be tested numerically in discs around supermassive black holes which underlines the motivation of this work. Firstly, we intend to test this using 3D hydrodynamical simulations of warped discs at different α, H/R and tilts. The warp amplitude $|\psi| = r|\partial \boldsymbol{l}/\partial r|$ is calculated from the simulations and is compared to the corresponding critical warp amplitude as derived in Doğan et al. (2018).

2.2.1 Stability analysis of warped discs

Here, we discuss how the evolution equation of warped discs is used to calculate the general instability criterion for discs to break (also detailed in section 3.2.1). The evolution

equation of a warped disc is given by (Pringle, 1992)

$$\begin{aligned}\frac{\partial \boldsymbol{L}}{\partial t} &= \frac{1}{R}\frac{\partial}{\partial R}\left\{\frac{(\partial/\partial R)[\nu_1 \Sigma R^3(-\Omega')]}{\Sigma(\partial/\partial R)(R^2\Omega)}\boldsymbol{L}\right\} \\ &+\frac{1}{R}\frac{\partial}{\partial R}\left[\frac{1}{2}\nu_2 R|\boldsymbol{L}|\frac{\partial \boldsymbol{l}}{\partial R}\right] \\ &+\frac{1}{R}\frac{\partial}{\partial R}\left\{\left[\frac{\frac{1}{2}\nu_2 R^3\Omega|\partial \boldsymbol{l}/\partial R|^2}{(\partial/\partial R)(R^2\Omega)}+\nu_1\left(\frac{R\Omega'}{\Omega}\right)\right]\boldsymbol{L}\right\} \\ &+\frac{1}{R}\frac{\partial}{\partial R}\left(\nu_3 R|\boldsymbol{L}|\ \boldsymbol{l}\times\frac{\partial \boldsymbol{l}}{\partial R}\right) \end{aligned} \tag{2.1}$$

where ν_1, ν_2 and ν_3 are effective viscosities, Ω is the local azimuthal angular velocity and Σ is the surface density. The local angular momentum of the disc $\boldsymbol{L} = \Sigma R^2\Omega\boldsymbol{l}$ and $\boldsymbol{l}$ is the unit angular momentum vector defined as:

$$\boldsymbol{l} = (\cos\gamma\sin\beta, \sin\gamma\sin\beta, \cos\beta) \tag{2.2}$$

where $\beta(R,t)$ is the local angle of the disc tilt with respect to the z-axis and $\gamma(R,t)$ being the disc twist measured from the x-axis. The first three terms in the evolution equation are derived from the conservation of mass and angular momentum as explained in Pringle (1992). The fourth term denotes the precessional torque used in the analysis of Ogilvie (1999) which causes the rings to precess when tilted with respect to their neighbours. Ogilvie (1999) uses torque coefficients (Q_1, Q_2 and Q_3) and defines them in terms of effective viscosities (ν_1, ν_2 and ν_3) as:

$$\nu_1 = \frac{Q_1\mathcal{I}\Omega^2}{\Sigma R\frac{d\Omega}{dR}} \tag{2.3}$$

$$\nu_2 = \frac{2Q_2\mathcal{I}\Omega}{\Sigma} \tag{2.4}$$

$$\nu_3 = \frac{Q_3\mathcal{I}\Omega}{\Sigma} \tag{2.5}$$

where $\mathcal{I}$ is the azimuthally averaged second vertical moment of the density which is dependent on warp amplitude $|\psi| = r|\partial \boldsymbol{l}/\partial r|$ as $\mathcal{I} = f(|\psi|)\Sigma c_s^2/\Omega^2$ (Ogilvie, 1999). The evolution equation was re-examined in Ogilvie & Latter (2013) which considered $\mathcal{I} = \Sigma c_s^2/\Omega^2$, and the $|\psi|$ dependence was established with a change of definition in the Q_i coefficients. Ogilvie & Latter (2013) presented the evolution equation as:

$$\begin{aligned}\frac{\partial}{\partial t}(\Sigma R^2\Omega\boldsymbol{l}) + \frac{1}{R}\frac{\partial}{\partial R}(\Sigma V_R R^3\Omega\boldsymbol{l}) &= \frac{1}{R}\frac{\partial}{\partial R}(Q_1\Sigma c_s^2 R^2\boldsymbol{l}) \\ &+\frac{1}{R}\frac{\partial}{\partial R}\left(Q_2\Sigma c_s^2 R^3\frac{\partial \boldsymbol{l}}{\partial R}\right) \\ &+\frac{1}{R}\frac{\partial}{\partial R}\left(Q_3\Sigma c_s^2 R^3\ \boldsymbol{l}\times\frac{\partial \boldsymbol{l}}{\partial R}\right) \end{aligned} \tag{2.6}$$

The effective viscosities are related to the Q_i coefficients as:

$$\nu_1 = \frac{-Q_1 c_s^2}{q\Omega} \tag{2.7}$$

where $q = -\frac{d\ln\Omega}{d\ln r}$.

$$\nu_2 = \frac{2Q_2 c_s^2}{\Omega} \tag{2.8}$$

$$\nu_3 = \frac{Q_3 c_s^2}{\Omega} \tag{2.9}$$

Consider the specific angular momentum $h = R^2\Omega$, $h' = dh/dr$ and by including the equation for radial velocity, the evolution equation becomes

$$\begin{aligned}\frac{\partial}{\partial t}(\Sigma R^2\Omega\boldsymbol{l}) &= \frac{1}{R}\frac{\partial}{\partial R}\Bigg[Q_1\Sigma c_s^2 R^2\boldsymbol{l} + Q_2\Sigma c_s^2 R^3\frac{\partial \boldsymbol{l}}{\partial R} \\ &+Q_3\Sigma c_s^2 R^3\ \boldsymbol{l}\times\frac{\partial \boldsymbol{l}}{\partial R} - \left(\frac{\partial}{\partial R}[Q_1\Sigma c_s^2 R^2] - Q_2\Sigma c_s^2 R|\psi|^2\right)\frac{h}{h'}\boldsymbol{l}\Bigg]. \end{aligned} \tag{2.10}$$

Doğan et al. (2018) performs the stability analysis of the evolution equation by subjecting it to linear perturbations similar to the analysis done in Ogilvie (2000). The internal torque components $g_i(r, \Sigma, \alpha, \alpha_b, q, |\psi|)$ in terms of the dimensionless basis vec-

tors $(\boldsymbol{l}, r\partial\boldsymbol{l}/\partial r, r\boldsymbol{l}\times\partial\boldsymbol{l}/\partial r)$ is defined as (Ogilvie, 2000):

$$g_i = Q_i(\alpha, \alpha_b, q, |\psi|)\Sigma c_s^2 r^2 \tag{2.11}$$

where the bulk viscosity $\alpha_b = 0$, $q = 3/2$ (Keplerian discs) and $Q_i = Q_i(\alpha, |\psi|)$. Hence, the evolution equation can be written as (or refer equation 71 in Ogilvie (2000)):

$$h\frac{\partial}{\partial t}(\Sigma\boldsymbol{l}) = \frac{1}{r}\frac{\partial}{\partial r}\left[g_1\boldsymbol{l} + g_2 r\frac{\partial\boldsymbol{l}}{\partial r} + g_3 r\boldsymbol{l}\times\frac{\partial\boldsymbol{l}}{\partial r} - \left(\frac{\partial g_1}{\partial r} - \frac{g_2|\psi|^2}{r}\right)\frac{h}{h'}\boldsymbol{l}\right]. \tag{2.12}$$

The stability of the above equation can be examined by subjecting it to linear perturbations $(\delta\Sigma, \delta\boldsymbol{l})$. Hence, the perturbed form of the equation is given as[1]:

$$h\frac{\partial}{\partial t}(\delta\Sigma\boldsymbol{l} + \Sigma\delta\boldsymbol{l}) = \frac{1}{r}\frac{\partial}{\partial r}\Bigg[\delta g_1\boldsymbol{l} + g_1\delta\boldsymbol{l} + \delta g_2 r\frac{\partial\boldsymbol{l}}{\partial r} + g_2 r\frac{\partial\delta\boldsymbol{l}}{\partial r} + \delta g_3 r\boldsymbol{l}\times\frac{\partial\boldsymbol{l}}{\partial r} + g_3 r\delta\boldsymbol{l}\times\frac{\partial\boldsymbol{l}}{\partial r} + g_3 r\boldsymbol{l}\times\frac{\partial\delta\boldsymbol{l}}{\partial r} - \left(\frac{\partial\delta g_1}{\partial r} - \frac{\delta(g_2|\psi|^2)}{r}\right)\frac{h}{h'}\boldsymbol{l} - \left(\frac{\partial g_1}{\partial r} - \frac{g_2|\psi|^2}{r}\right)\frac{h}{h'}\delta\boldsymbol{l}\Bigg] \tag{2.13}$$

where the perturbed quantities,

$$\delta g_i = \frac{\partial g_i}{\partial\Sigma}\delta\Sigma + \frac{\partial g_i}{\partial|\psi|}\delta|\psi|, \tag{2.14}$$

$$\delta|\psi| = \frac{r^2}{|\psi|}\frac{\partial\boldsymbol{l}}{\partial r}.\frac{\partial\delta\boldsymbol{l}}{\partial r} \tag{2.15}$$

and $\boldsymbol{l}.\delta\boldsymbol{l} = 0$. The solution of the perturbations $(\delta\Sigma, \delta l)$ is of the form[2]

$$\exp\left(-i\int\omega dt + i\int k dr\right) \tag{2.16}$$

where ω is the wave frequency and k is the wavenumber. The perturbed form of angular momentum equation is defined in terms of orthonormal components $(\boldsymbol{l}, \boldsymbol{m}, \boldsymbol{n})$ in the order

[1]The equation 2.12 is perturbed with $\Sigma\to\Sigma+\delta\Sigma$, $\boldsymbol{l}\to\boldsymbol{l}+\delta\boldsymbol{l}$ and $g_i\to g_i+\delta g_i$. We cancel the higher order terms and keep only the first order terms, and subtract the resultant equation with equation 2.12 to obtain the perturbed form as shown by equation 2.13.

[2]The perturbations are assumed to vary more rapidly with radius and time than the unperturbed solution, also shown by equation 75 in Ogilvie (2000).

of k (also shown in equations 22-24 in Doğan et al. (2018)) given as:

$$-i\omega hr\delta\Sigma = k^2\frac{h}{h'}\delta g_1 \tag{2.17}$$

$$-i\omega hr\Sigma\delta m = ik|\psi|\delta g_2 - k^2 g_2 r\delta m + k^2 g_3 r\delta n - ik|\psi|\frac{h}{rh'}\delta g_1 \tag{2.18}$$

$$-i\omega hr\Sigma\delta n = ik|\psi|\delta g_3 - k^2 g_2 r\delta n - k^2 g_3 r\delta m \tag{2.19}$$

These linear equations can yield a coefficient determinant (shown in equation 25 in Doğan et al. (2018)) which follows the dispersion relation given by

$$\begin{aligned} s^3 - s^2\Big[aQ_1 - 2Q_2 + |\psi|\Big(aQ_1' - Q_2'\Big)\Big] - s\Big[2aQ_1Q_2 - Q_2^2 - Q_3^2 \\ +|\psi|\Big(aQ_1Q_2' - Q_2Q_2' - Q_3Q_3'\Big)\Big] - a\Big[Q_1\Big(Q_2^2 + Q_3^2\Big) \\ +|\psi|\Big(Q_1Q_2Q_2' - Q_1'Q_2^2 + Q_1Q_3Q_3' - Q_1'Q_3^2\Big)\Big] = 0 \end{aligned} \tag{2.20}$$

where the prime on Q coefficients represents differentiation with respect to $|\psi|$, $a = h/rh' = \mathrm{dln}\, r/\mathrm{dln}\, h = 1/(2-q) = 2$ (for a Keplerian disc with $q = 3/2$). The dimensionless growth rate s is calculated as:

$$s = \frac{-i\omega}{\Omega}\left(\frac{\Omega}{c_s k}\right)^2 \tag{2.21}$$

assuming that instabilities grow over time, if $\Re[s] > 0$. The roots or solutions of the dispersion relation explains the effect of each viscous torque coefficient Q_i on the warp amplitude of the disc $|\psi|$. The solution of the dispersion relation involving Q_1, Q_2 and Q_3 gives the instability criterion for a warped disc to become unstable, given as $s_1(Q_1, Q_2, Q_3)$ [3]. The full criterion of instability is validated when $\Re[s_1(Q_1, Q_2, Q_3)] > 0$.

A key result from Doğan et al. (2018) demonstrates how the growth rate $\Re[s_1(Q_1, Q_2, Q_3)]$ as a function of $|\psi|$ behaves at different values of α as shown in figure 2.1. Therefore,

[3]The full criterion $s_1(Q_1, Q_2, Q_3)$ is given as: $s_1(Q_1, Q_2, Q_3) = \frac{1}{6}[2C_1 + 2^{2/3}(C_2 + C_3)^{1/3} + 2^{4/3}(C_2 + C_3^{1/2})^{-1/3}C_4]$ where C_1, C_2, C_3 and C_4 are expressed in terms of Q_1, Q_2 and Q_3 given by equations 33-37 in Doğan et al. (2018).

the growth rate of instabilities $\Re[s]$ is found to be inversely proportional to α, i.e. the growth rate of instabilities is higher for low values of α. The critical warp amplitudes for instability is studied for discs at different values α, thus showing the stable and unstable regions in the $(\alpha, |\psi|)$ parameter space as shown in figure 2.2. The analysis of Doğan et al. (2018) demonstrates that at each α parameter of the disc, there is a critical value for the warp amplitude (say, $|\psi|_c$) below which the disc remains stable and above which the disc becomes unstable and tears. Therefore, it is important to test this criteria in isothermal, Keplerian warped discs at various α parameters (in the diffusive case with $\alpha > H/R$) and check if it becomes unstable at its critical warp amplitude value. This illustrates the motivation of this chapter to use SPH simulations and test this theory.

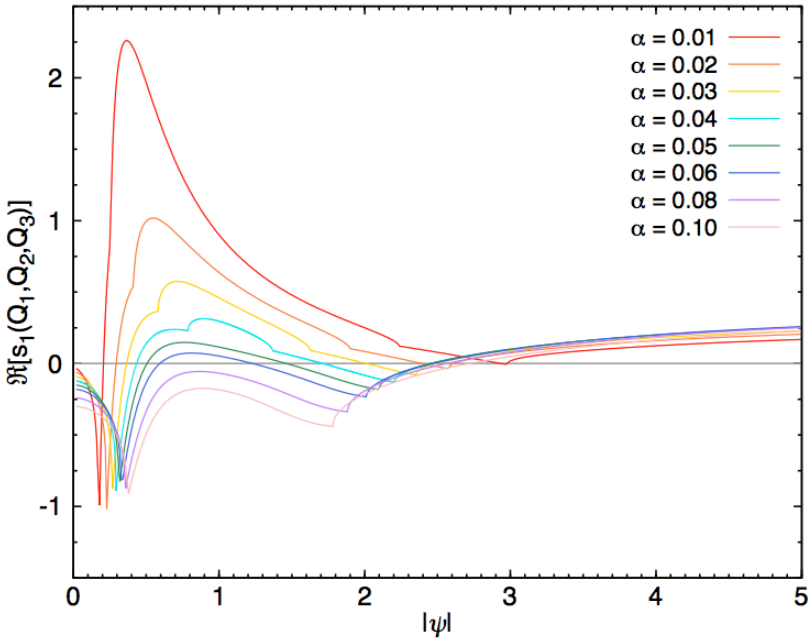

Figure 2.1: The dimensionless growth rate $\Re[s]$ is plotted as a function of warp amplitude ψ at different α values. In this analysis, the growth rate for a disc with $\alpha = 0.1$ is considered. The growth rate at $\alpha = 0.1$ increases after a critical value of $|\psi|_c = 3$ and attains a steady growth rate value of $\Re[s] = 0.2$ at values of $|\psi| > |\psi|_c$ as shown. Image taken from Doğan et al. (2018).

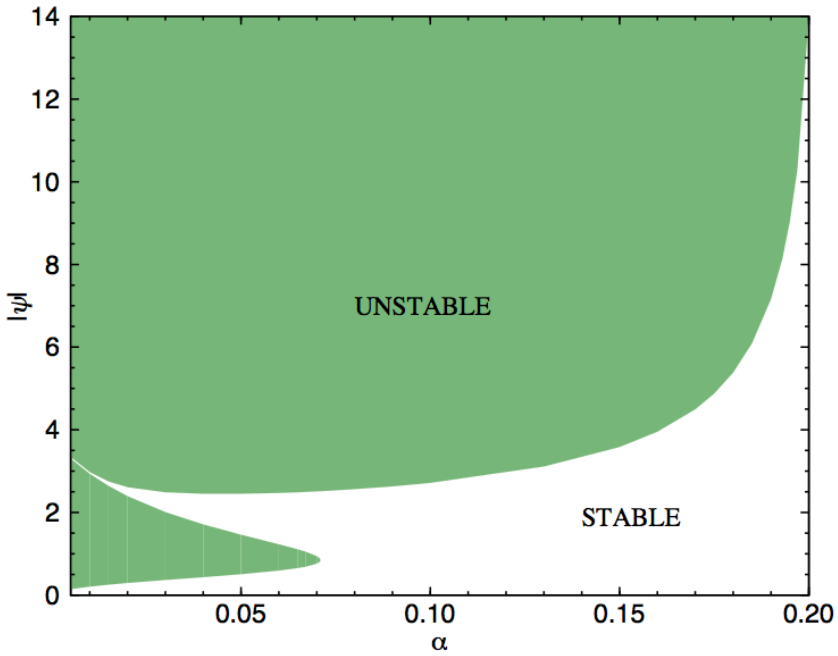

Figure 2.2: Plot showing the stable (white) and unstable (green) regions in the $(\alpha, |\psi|)$ parameter space. This demonstrates that, there is a minimum or critical value of warp amplitude for a disc at any α value ($0.01 \leq \alpha \leq 0.2$) at which it becomes unstable (Image taken from Doğan et al. (2018)).

The solutions presented by Doğan et al. (2018) represent necessary, but not sufficient, criteria for instability, with the sufficiency supplied by the condition that the background state evolve more slowly than the growth of unstable modes. Taking this into account, our aims for the simulations presented in this paper are to show in agreement with the analytical predictions of the warped disc instability, that

1. discs with $|\psi| > |\psi|_{\rm c}$ for extended periods of time lead to instability,

2. discs with $|\psi| < |\psi|_{\rm c}$ are stable, and

3. the growth rate of the warp amplitude in the unstable regions follow the general trends of the predicted growth rates, i.e. the growth rates are generally higher for smaller viscosity and depend on the warp amplitude.

2.3 Numerical Results

The aim of this project is to explore the instability criterion as explained in Doğan et al. (2018) and test it using SPH simulations. We use the smoothed particle hydrodynamics (SPH) code PHANTOM to test how a warped disc behaves at different warp amplitudes. In order to determine the instability of warped discs, we follow Lodato & Pringle (2007) to model a warped accretion disc and use the criterion of disc tearing as explained in Doğan et al. (2018).

2.3.1 Simulations

To perform 3D SPH simulations of warped discs with no LT precession, we choose a disc with Keplerian orbits around a central mass $M = 1$, the gravitational constant $G = 1$ and speed of light $c = 1$ that gives a gravitational radius $R_g = 1$ measured in code units. The accretion radius as well as the inner radius of the disc is set at $R_{\rm in} = 4R_g$ and the outer radius at $R_{\rm out} = 30R_g$. The surface density of the disc behaves as $\Sigma = \Sigma_0(R/R_{\rm in})^{-p}$ with a locally isothermal sound speed profile given as $c_s = c_{s0}(R/R_{\rm in})^{-q}$. At $p = 3/2$ and $q = 3/4$, the disc is uniformly resolved with a constant shell-averaged smoothing length per disc scale-height, i.e. $\langle h\rangle/H$ remains a constant (Lodato & Pringle, 2007). The simulations use a disc viscosity parameter $\alpha = 0.1$ and scale height $H/R = 0.03$. The disc is composed of 10 million particles with $\langle h\rangle/H \approx 0.3$ which implies that the effective viscosity arising from the numerical viscosity is $\alpha_{AV} = 0.017$; cf. Meru & Bate (2012) [4]. The warped disc in the simulations is modelled the same way as used in Lodato

[4]Meru & Bate (2012) finds that the magnitude of the shear viscosity arising from the numerical viscosity, includes a linear term controlled by $\alpha_{\rm SPH}$ and a quadratic term controlled by $\beta_{\rm SPH}$, which gives $\alpha^{\rm AV} = \frac{31}{525}\alpha_{\rm SPH}\frac{\langle h\rangle}{H} + \frac{9}{70\pi}\beta_{\rm SPH}\left(\frac{\langle h\rangle}{H}\right)^2$ (further discussed in section 3.4).

& Pringle (2007) where the components of the disc tilt vector, $\boldsymbol{l}$ are given as:

$$l_x = \begin{cases} 0 & \text{for} \quad R < R_1 \\ \dfrac{A}{2}\left[1 + \sin\left(\pi \dfrac{R - R_0}{R_2 - R_1}\right)\right] & \text{for} \quad R_1 < R < R_2 \\ A & \text{for} \quad R > R_2. \end{cases}$$

In addition, the values of $l_y = 0$ (no twist), and $l_z = \sqrt{(1 - l_x)^2}$. To set up the simulations, we consider $R_0 = R_{\rm warp} = \frac{R_{\rm in}+R_{\rm out}}{2}$ measured as $17R_g$ in code units. The extend of the warp is determined by $R_{\rm warp} \pm \Delta R$, where we use a value of $\Delta R = 3R_g$ in our disc setups which gives $R_1 = 14R_g$ and $R_2 = 20R_g$ respectively. The value of A corresponds to the inclination at the outer disc.

Firstly, we examine how the disc behaves with the outer disc inclined at 10°. The total run time of the simulation is set at $t = 8800 \approx 20$ orbits at $R_{\rm warp}$. Figure 2.3 shows the 3D column density of the disc at $t = 220$ and 5500 which are 0.5 and 12.5 orbits at $R_{\rm warp}$ respectively. As shown in the figure, the disc shows no evidence of a break. But this can be further verified from studying the behaviour of the surface density (where the value of $\Sigma = 0$ in the unstable region) and tilt of the disc.

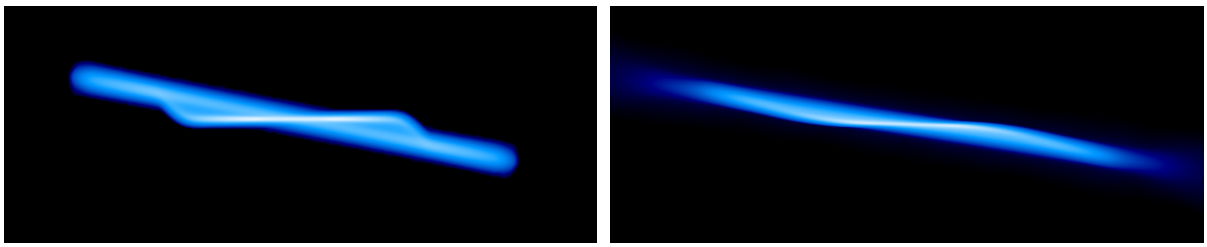

Figure 2.3: 3D column density plots of the disc inclined at 10°, $\alpha = 0.1$ and $H/R = 0.03$ at 0.5 and 12.5 orbits at $R_{\rm warp}$. There is no evidence of a disc tear at the later time as shown.

The change in the surface density as well as the tilt of the disc at times $t = 0.5$ (black line) and 12.5 orbits (red line) at $R_{\rm warp}$ are shown in figure 2.4a. The value of Σ doesn't reduce to zero anywhere in the disc at t = 12.5 orbits at $R_{\rm warp}$. Similarly, the tilt of the disc also shows no evidence of a break.

In order to verify the stability criterion of this disc setup, the warp amplitude of the disc is calculated and compared to a critical value $|\psi|_c = 3$ corresponding to $\alpha = 0.1$, as shown in figure 2.4b. At both times, the warp amplitude of the disc remains much smaller than $|\psi|_c$, which shows that this warped configuration of the disc with the outer disc aligned at 10° doesn't break and remains stable. This can be further extended to other disc setups with the outer part of the disc inclined at 30°, 45° and 60°.

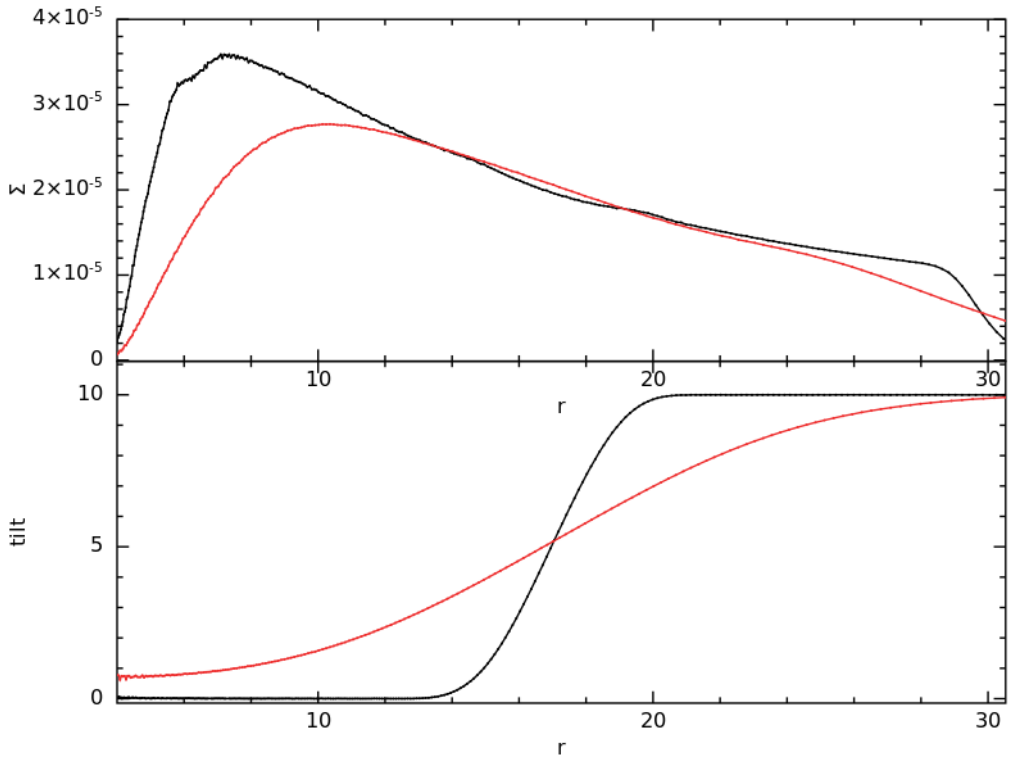

(a)

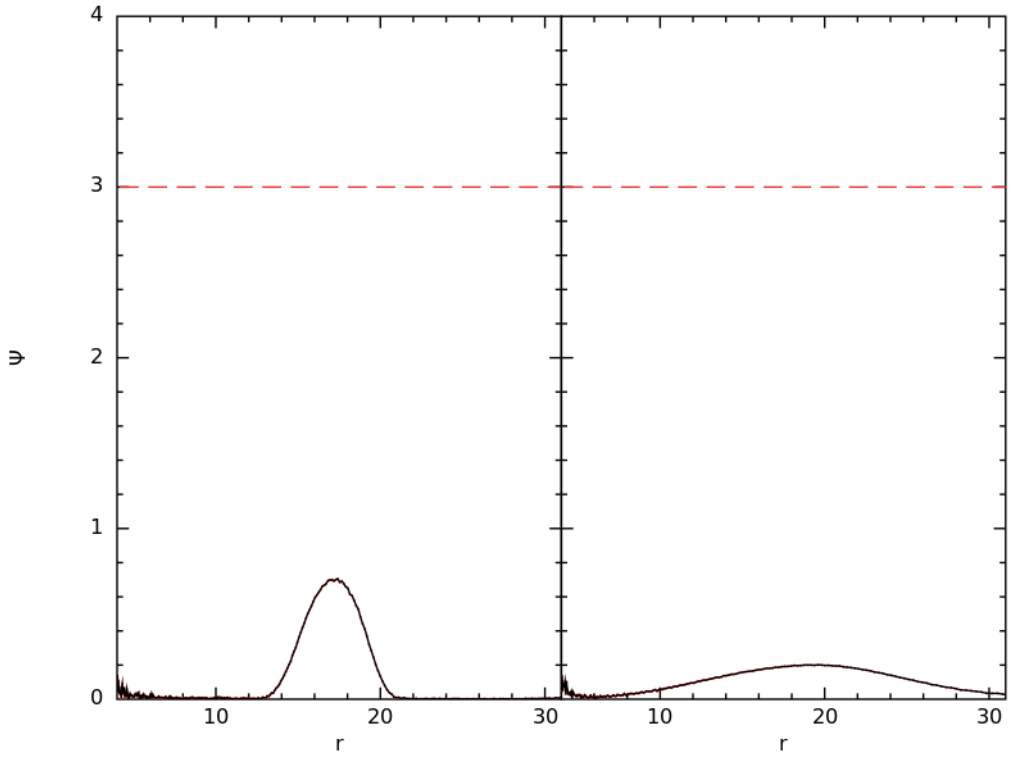

(b)

Figure 2.4: (a) The first plot shows the surface density profiles for a disc initially inclined at $10°, \alpha = 0.1$ and $H/R = 0.03$ at 0.5 (black line) and 12.5 orbits (red line) at $R_{\rm warp}$. Although the disc evolves over time, there is no evidence of a disc tear as there is no divide or split in the surface density plot. The second plot shows how the tilt changes for the same disc setup at 0.5 (black line) and 12.5 (red line) orbits at $R_{\rm warp}$. The tilt profiles from the two times show no evidence of a disc tear. (b) The plots show the warp amplitude $|\psi|$ of a disc initially inclined at $10°, \alpha = 0.1$ and $H/R = 0.03$, calculated at 0.5 and 12.5 orbits at $R_{\rm warp}$. The values are much lower than the critical value $|\psi|_c = 3$ (red dashed line), thus proving that this disc remains stable with no instabilities.

Figure 2.5 shows the 3D simulations of a warped disc inclined at $\theta = 30°$, $\alpha = 0.1$ and $H/R = 0.03$ at $t = 220$ and $t = 5500$ which are 0.5 and 12.5 orbits at $R_{\rm warp}$ respectively.

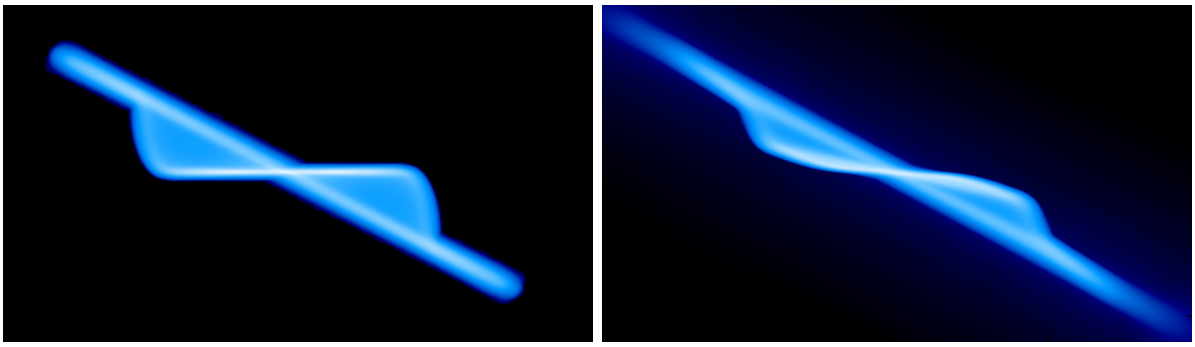

Figure 2.5: 3D simulations of a disc tilted at 30°, $\alpha = 0.1$ and $H/R = 0.03$ at 0.5 orbits and 12.5 orbits at $R_{\rm warp}$ is shown. The warped region of the disc doesn't show any breaking at a later time in the simulation.

At the initial time, we can notice an aligned inner part connected to the misaligned outer part of the disc through a warp. At the later time, the warped configuration does not tear which can be investigated using surface density profiles and corresponding changes in the tilt of the disc. The first plot of figure 2.6a shows the surface density profiles at $t = 0.5$ (black line) and $t = 12.5$ orbits (red line) at $R_{\rm warp}$. If there is a disc tear, it can be identified where the value of $\Sigma = 0$ which does not happen in this disc at a later time. Similarly, the tilt of the disc as shown in the lower panel of figure 2.6a demonstrates how the tilt of the disc behaves at $t = 0.5$ orbit (black line) and $t = 12.5$ orbits (red line) at $R_{\rm warp}$. Analogous to the surface density profiles, the tilt of disc does not show an evidence of disc break.

In order to compare this result with that predicted from Doğan et al. (2018), the warp amplitude (ψ) of the disc is calculated at $t = 0.5$ and 12.5 orbits at $R_{\rm warp}$. As shown in figure 2.6b, the values of the warp amplitude are lower than the critical value $|\psi|_c = 3$ which is denoted by the red dashed line. This once again proves that a warped disc tilted at 30° for the simulated parameters, remains stable and does not form any instabilities since the value of warp amplitude remains smaller than the critical value in the simulation.

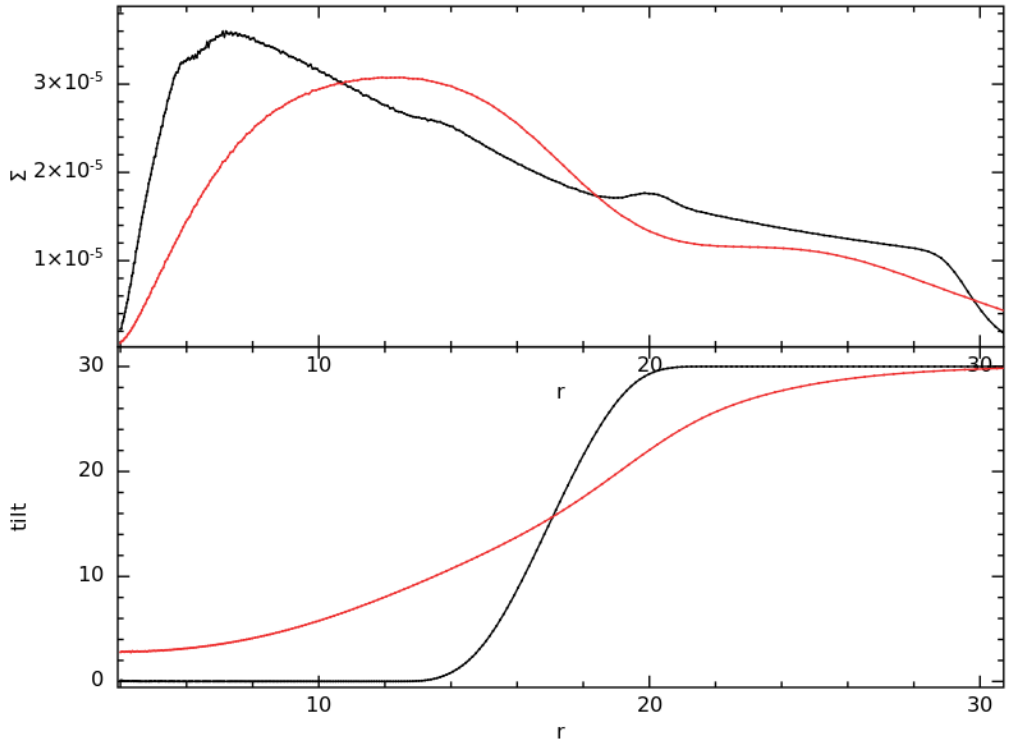

(a)

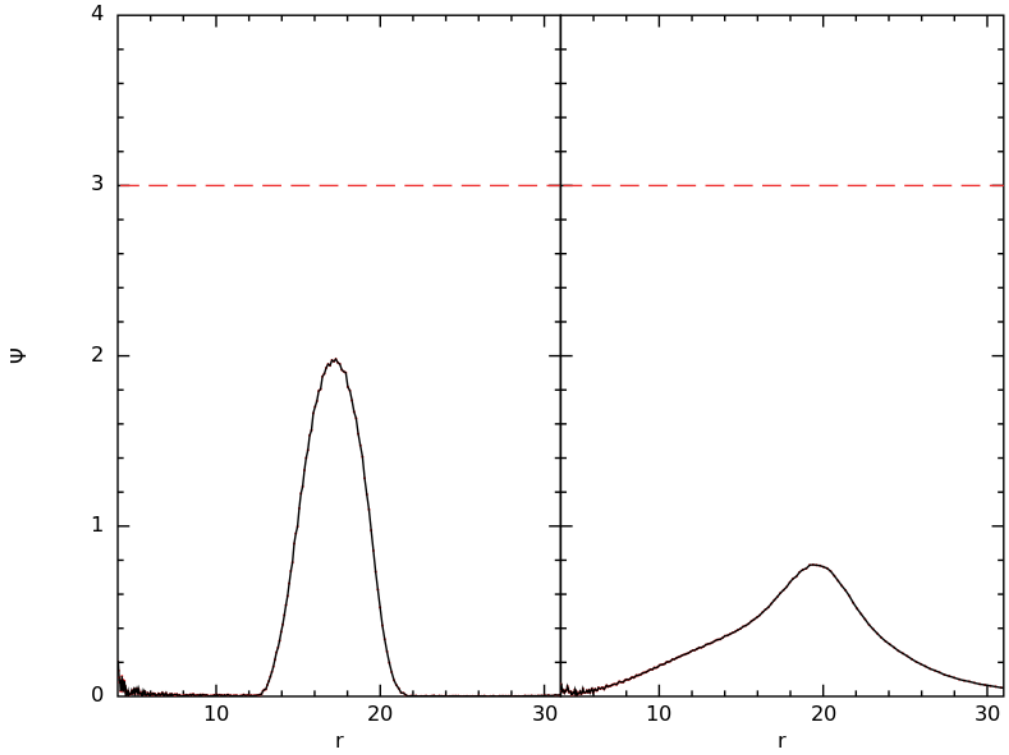

(b)

Figure 2.6: (a) The first plot shows the surface density profiles for a disc initially inclined at $30°, \alpha = 0.1$ and $H/R = 0.03$ after 0.5 (black line) and 12.5 orbits (red line) at $R_{\rm warp}$. At a later time, although the surface density is significantly affected by the warp, its value doesn't reduce to zero at any radii, thus showing that there is no disc break. The second plot shows the tilt of the disc at 0.5 (black line) and 12.5 orbits (red line) at $R_{\rm warp}$ which also indicates no evidence of a disc break. (b) The warp amplitude $|\psi|$ of the disc is calculated and plotted at times ≈ 0.5 and 12.5 orbits at $R_{\rm warp}$. The values of $|\psi|$ is compared to the critical value at $|\psi|_c = 3$ shown by the red dashed line. The values of $|\psi|$ lies well below the critical value at both times, thus proving that this disc doesn't become unstable.

This analysis is extended to highly inclined warped discs at 45° and 60° respectively. Unlike the previous cases, these discs show evidence of breaking at higher inclinations. Firstly, the 3D simulations of a disc inclined at 45°, $\alpha = 0.1$ and $H/R = 0.03$ at times t = 220 and t = 5500 which are 0.5 and 12.5 orbits at $R_{\rm warp}$ are shown in figure 2.7.

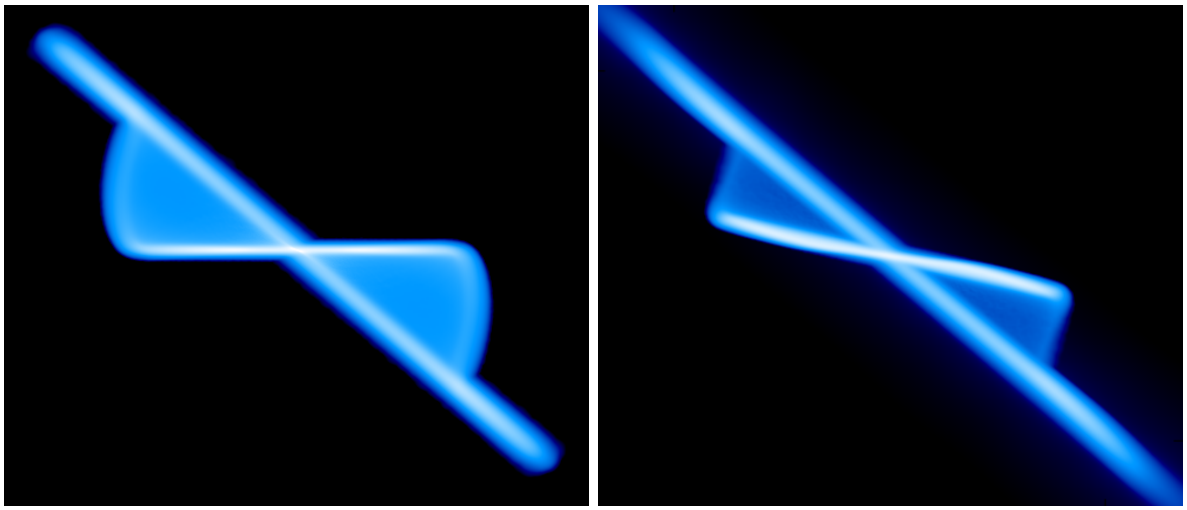

Figure 2.7: 3D simulations of a disc tilted at 45°, $\alpha = 0.1$ and $H/R = 0.03$ at 0.5 orbits and 12.5 orbits at $R_{\rm warp}$ is shown.

While it is difficult to see the break in the column density plots, it can be explained in the surface density and tilt profiles of the disc. The surface density and the tilt profiles of the disc at $t = 0.5$ orbit (black line) and $t = 12.5$ orbits (red line) at $R_{\rm warp}$ are shown in figure 2.8a. There is a clear divide in the surface density plot when the value of Σ reduces to zero at radius $r = 18$ at a later time. Similarly, in the second plot showing the tilt of the disc becomes steeper at $r = 18$, at a later time which infers the possibility of a disc tear [5].

The warp amplitude is calculated for this setup at times t = 0.5 and 12.5 orbits at $R_{\rm warp}$ and compared with the critical warp amplitude $|\psi|_c = 3$ as shown in figure 2.8b. At the earlier time, the maximum value of the warp amplitude $\psi \approx |\psi|_c$ and thus the disc might be unstable. The warp amplitude of the disc at radius $r = 18$ exceeds the critical value at a later time, hence showing that the disc becomes unstable and tears.

[5] A similar analysis is examined in Nixon & King (2012), showing the change in the disc structures of warped discs at values of α between 0.2 and 0.5.

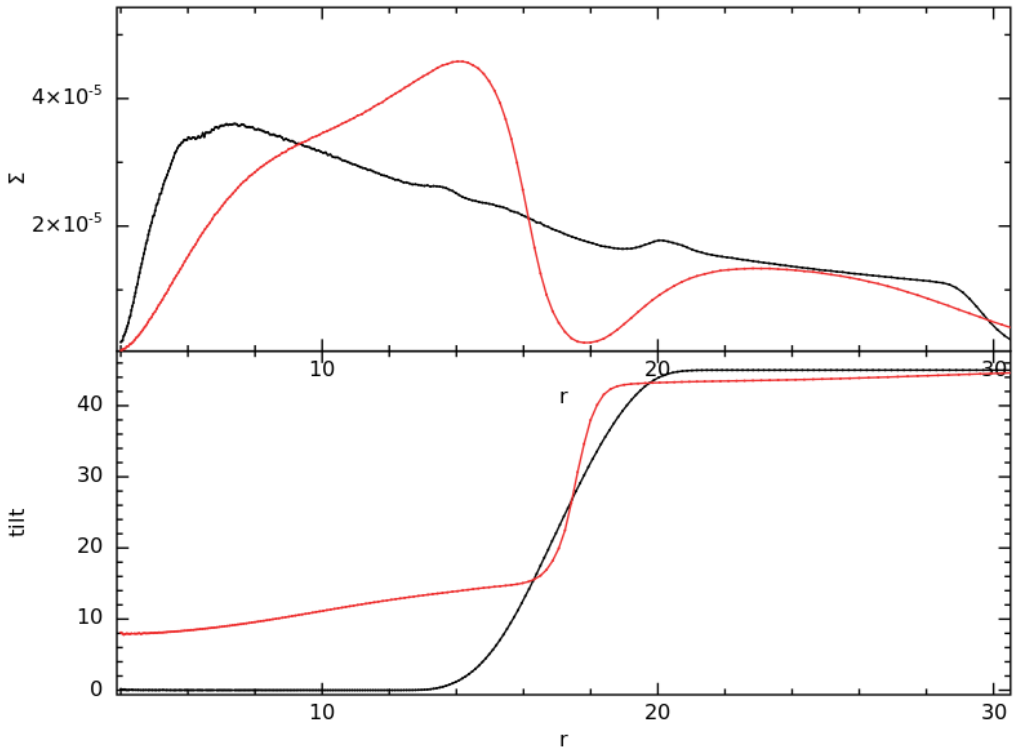

(a)

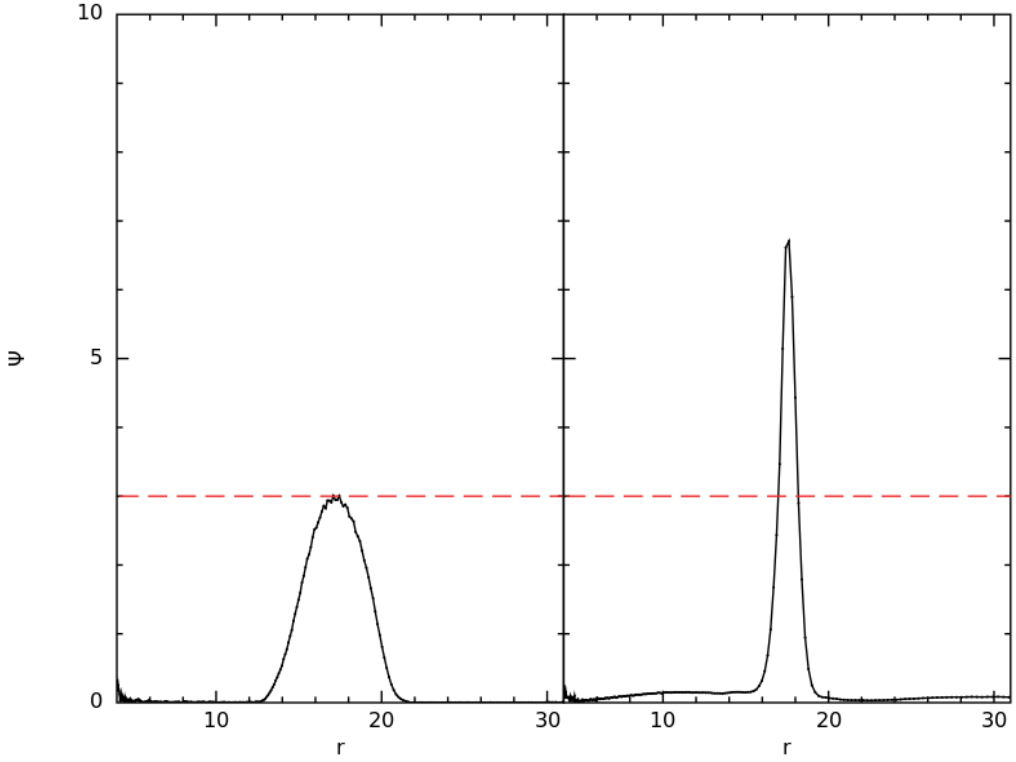

(b)

Figure 2.8: (a) The first plot shows the surface density of the disc inclined at $45°, \alpha = 0.1$ and $H/R = 0.03$ at 0.5 (black line) and 12.5 orbits (red line) at $R_{\rm warp}$. At a later time, the value of Σ reduces to zero at $r = 18$, locating the point of disc break. The second plot shows the corresponding change in the tilt of the disc at 0.5 (black line) and 12.5 orbits (red line) at $R_{\rm warp}$ and shows the possibility of a disc break at $t = 12.5$ orbits (red line) at $R_{\rm warp}$. (b) The warp amplitude $|\psi|$ of the disc is plotted at 0.5 and 12.5 orbits at $R_{\rm warp}$ for a disc inclined at $45°, \alpha = 0.1$ and $H/R = 0.03$. The red dashed line denotes the critical value $|\psi|_c = 3$. The maximum warp amplitude $\approx |\psi|_c$ at the initial time, and thus the disc might be unstable. At the later time, the value of $|\psi| > |\psi|_c$ at $r = 18$ showing that the disc becomes unstable.

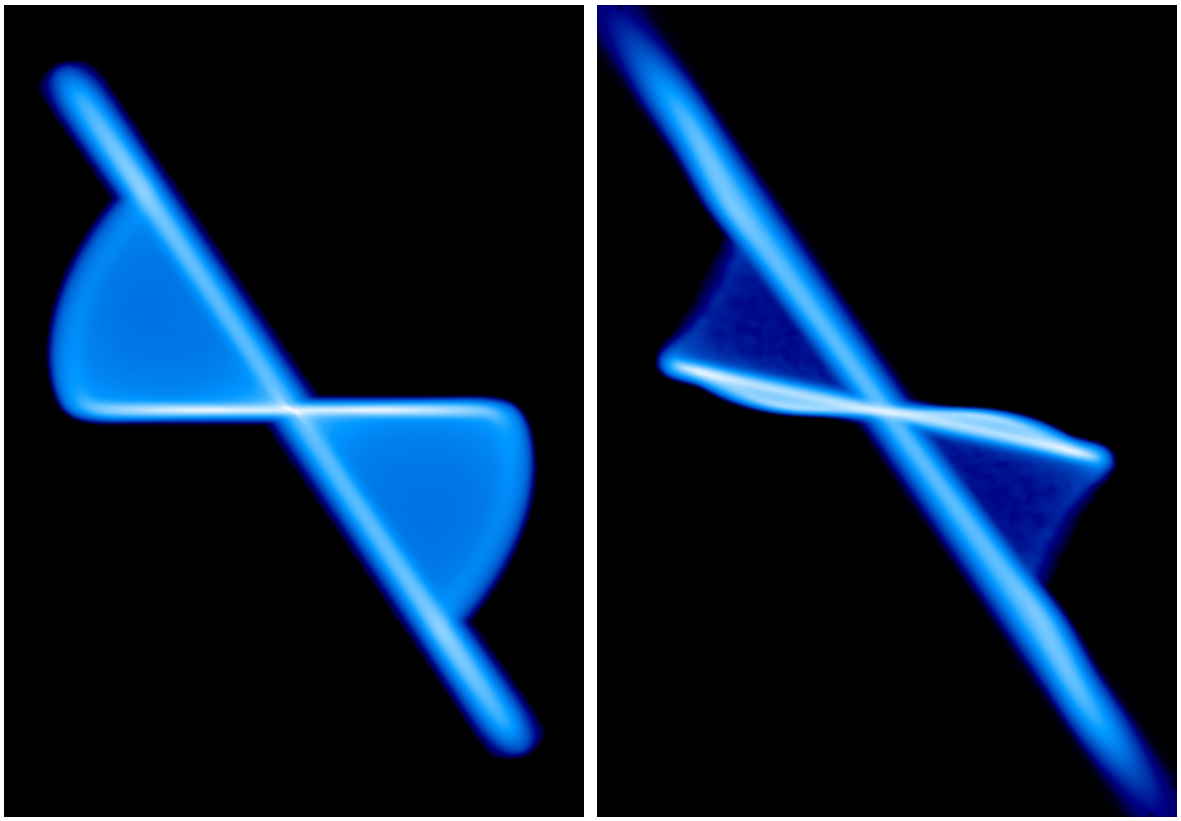

Figure 2.9: 3D simulations of a disc inclined at 60°, $\alpha = 0.1$ and $H/R = 0.03$ at 0.5 orbits and 6.25 orbits at $R_{\rm warp}$. The simulation at a later time shows the possibility of a disc break.

Figure 2.9 shows the 3D simulations of a warped disc tilted at 60° at times t = 220 and t = 2750 which are 0.5 and 6.25 orbits at $R_{\rm warp}$ respectively. At a later time, the disc shows evidence of a disc tear which can be examined from the change in the surface density and tilt of the disc at $t = 0.5$ orbit (black line) and $t = 6.25$ orbits (red line) at $R_{\rm warp}$ as shown in figure 2.10a. At radius, $r = 17$ the value of Σ reduces to zero which denotes the point of disc tear. A change in the slope of the tilt at the same radius validates on the possibility of disc tear in this setup. In this case, we expect the warp amplitude of the disc to exceed the critical value $|\psi|_c$ as examined in figure 2.10b.

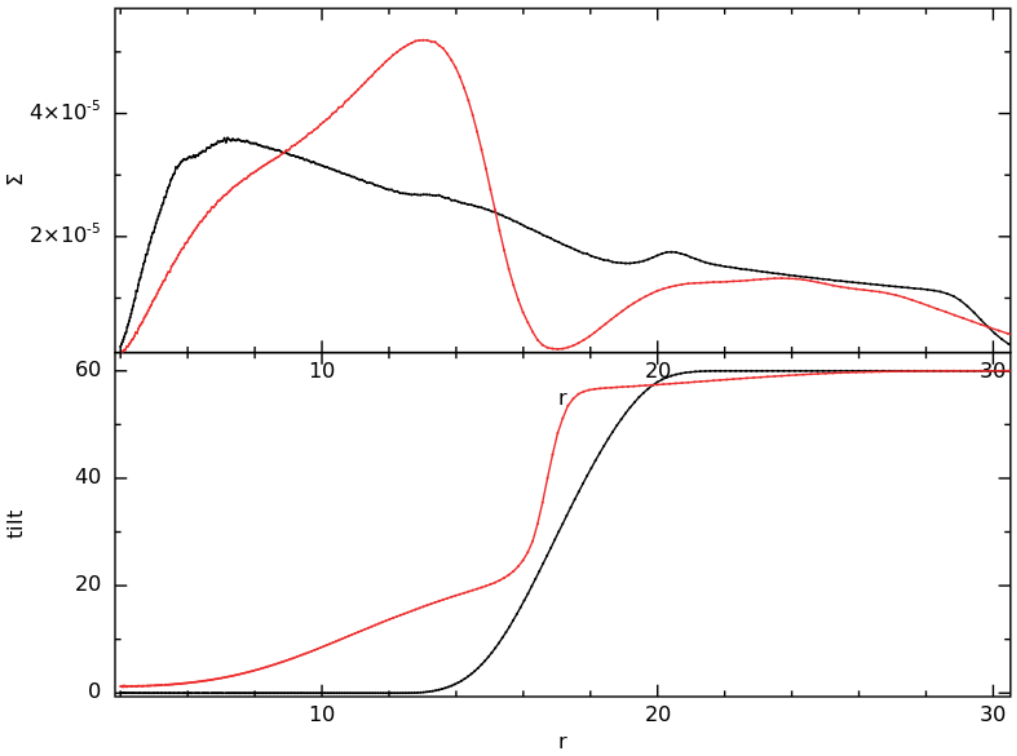

(a)

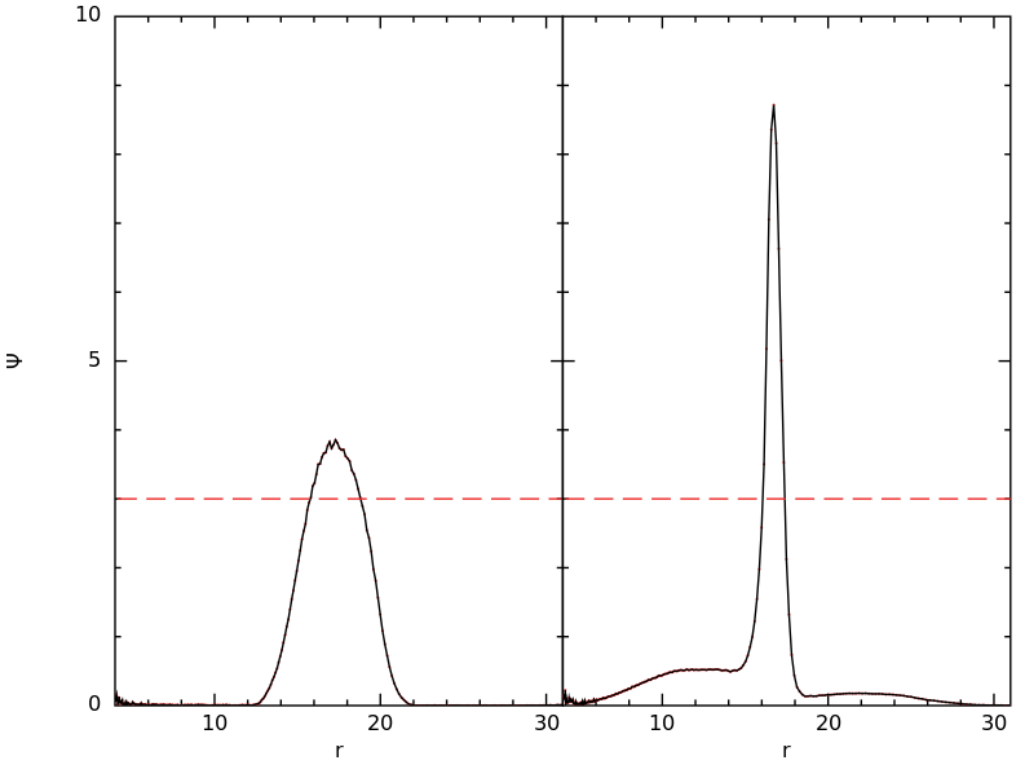

(b)

Figure 2.10: (a) The first plot shows the surface density of the disc inclined at $60°, \alpha = 0.1$ and $H/R = 0.03$ after 0.5 (black line) and 6.25 orbits (red line) at $R_{\rm warp}$. There is a clear divide in the surface density at the later time when Σ reduces to zero at $r \approx 17$. The second plot shows the change in the tilt of the disc with the warp connecting the inner part of the disc to its outer part tilted at 60° at 0.5 (black line) and 6.25 orbits (red line) at $R_{\rm warp}$. (b) The warp amplitude $|\psi|$ of the disc at $60°, \alpha = 0.1$ and $H/R = 0.03$ is calculated at $t \approx 0.5$ and 6.25 orbits at $R_{\rm warp}$. The values of $|\psi|$ is compared to the critical value $|\psi|_c = 3$ denoted by the red dashed line. The value of $|\psi| > |\psi|_c$ at $r \approx 17$ proving that the disc becomes unstable at the later time.

Depending on the inclination of the outer part of the disc, the warped region of the disc between radii $r = 14$ and $r = 20$ generates a $|\psi|$ value, either smaller or greater than the critical value $|\psi|_c$ at the initial time. In the last three cases discussed at tilts 10° and 30°, the value of ψ remains smaller than $|\psi|_c$ at an initial time. This is not true at 45° and 60° as shown in figures 2.8b and 2.10b respectively. Figure 2.10b shows the warp amplitude of the disc, inclined at 60°, at times $t = 0.5$ and 6.25 orbits at $R_{\rm warp}$. At $t = 6.25$ orbits, the value of $|\psi| > |\psi|_c$ at radius $r \approx 17$. Once again, this agrees well with the analysis of Doğan et al. (2018) showing that the value of critical warp amplitude measures the limit of stability in discs.

2.4 Warped discs at higher α values

The criterion for discs to become unstable, derived in Doğan et al. (2018) shows that each disc has a critical value of warp amplitude which increases with increasing values of α as shown in figure 2.2. Thus, at higher values of α, it requires a larger critical value $|\psi|_c$ for a disc to become unstable. This can be further tested using numerical simulations and study how warped discs at different values of α (> 0.1) behave at different inclinations.

Firstly, let us consider a disc at $\alpha = 0.16$ initially tilted at 10° with the same values previously used for $R_{\rm in}$, $R_{\rm out}$, $R_{\rm warp}$ and H/R. The total run time of the simulation is $t = 8800 \approx 20$ orbits at $R_{\rm warp}$. Figure 2.11 shows the 3D simulation of the disc at $t = 220$ and 5500, which are 0.5 and 12.5 orbits at $R_{\rm warp}$.

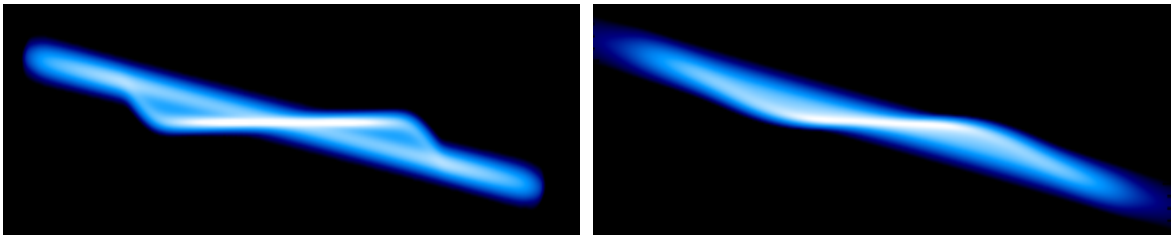

Figure 2.11: 3D column density plots of a disc inclined at 10°, $\alpha = 0.16$ and $H/R = 0.03$ at 0.5 orbits and 12.5 orbits at $R_{\rm warp}$.

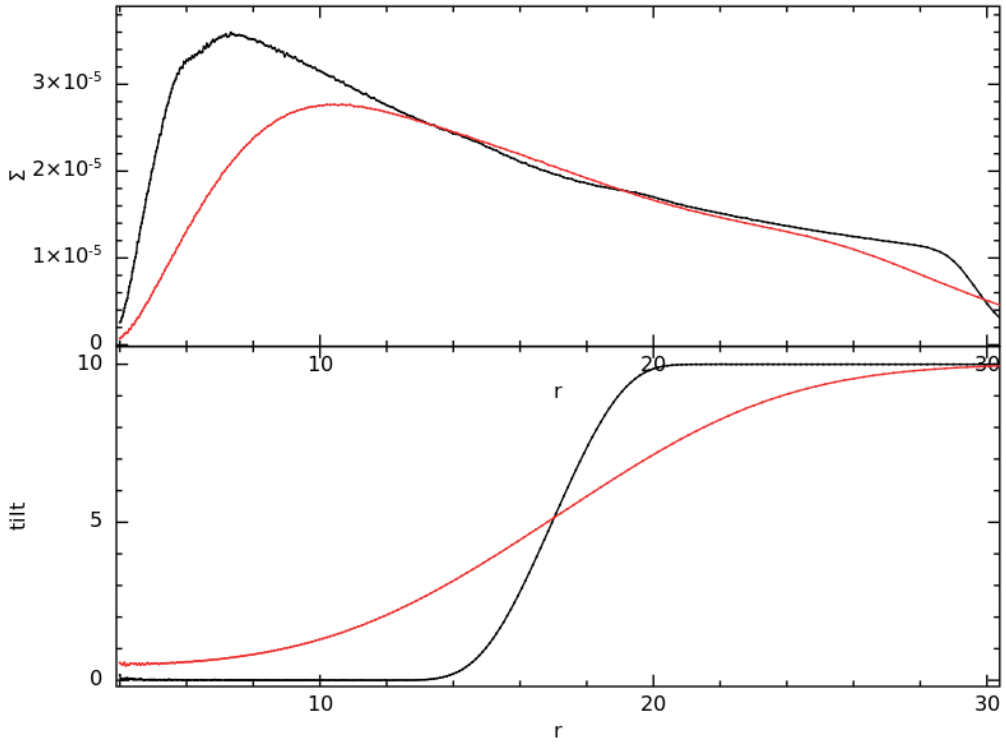

(a)

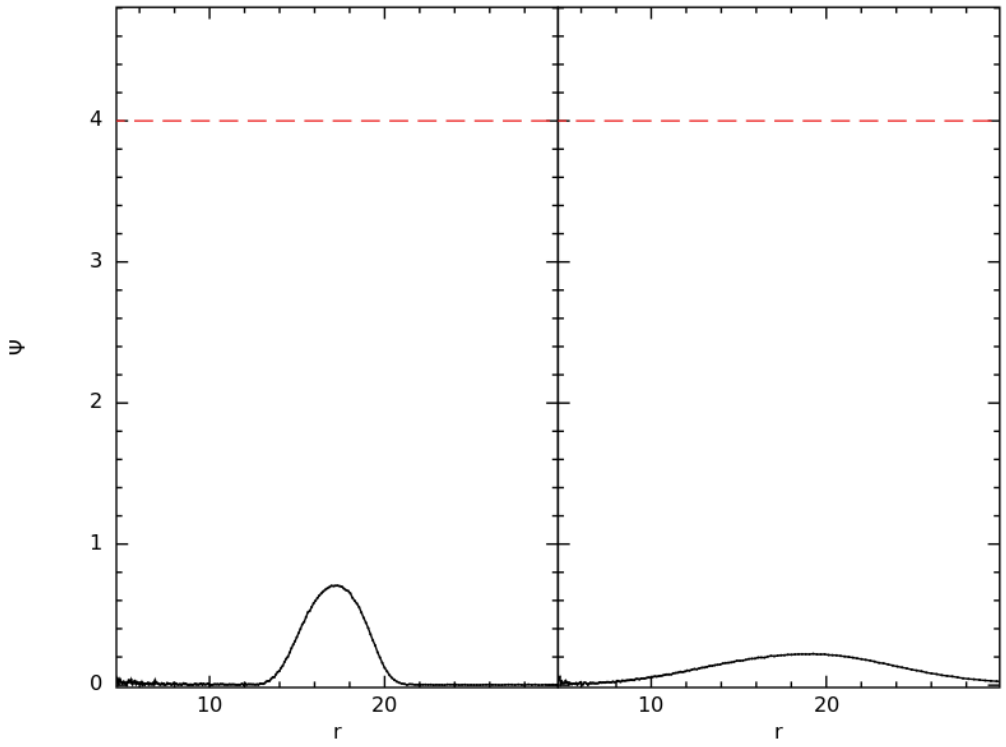

(b)

Figure 2.12: (a) The first plot shows the surface density profiles for a disc initially inclined at $10°, \alpha = 0.16$ and $H/R = 0.03$ after 0.5 (black line) and 12.5 orbits (red line) at $R_{\rm warp}$. The second plot shows the corresponding tilt changes for the same disc setup at 0.5 (black line) and 12.5 (red line) orbits at $R_{\rm warp}$. The two profiles present no evidence of a disc break as shown. (b) The warp amplitude $|\psi|$ of the disc inclined at $10°, \alpha = 0.16$ and $H/R = 0.03$ is plotted at 0.5 and 12.5 orbits at $R_{\rm warp}$ as shown. The values are compared to the critical value $|\psi|_c = 4$ denoted by the red dashed line.

The corresponding changes in the surface density and the tilt of the disc at times t = 0.5 (black line) and t = 12.5 (red line) orbits at $R_{\rm warp}$ is shown in figure 2.12a. From the 3D simulations and the parameter profiles of the disc, one can clearly verify that the disc does not become unstable and shows no disc tearing. Furthermore, the warp amplitude of the disc is calculated at times $t = 0.5$ and $t = 12.5$ orbits at $R_{\rm warp}$ and is compared to the critical warp amplitude $|\psi|_c = 4$ for $\alpha = 0.16$ as shown in figure 2.12b. At the two times, the values of the warp amplitude remain less than the critical value, proving that this agrees well with the expected criteria that the disc remains stable until $|\psi| > |\psi|_c$.

The same is checked for a disc inclined at 60°. The 3D simulations of the disc at t = 0.5 orbit and $t = 6.25$ orbits at $R_{\rm warp}$ is shown in figure 2.13. At a later time, the simulation shows a clear break in the disc. This can be further verified from the surface density and tilt of the disc at $t = 0.5$ orbit (black line) and $t = 6.25$ orbits (red line) as shown in figure 2.14a. The surface density profile of the disc shows the value of $\Sigma = 0$ at $r \approx 17$. Similarly, the tilt plot also shows a break at a later time at $r \approx 17$ in this setup.

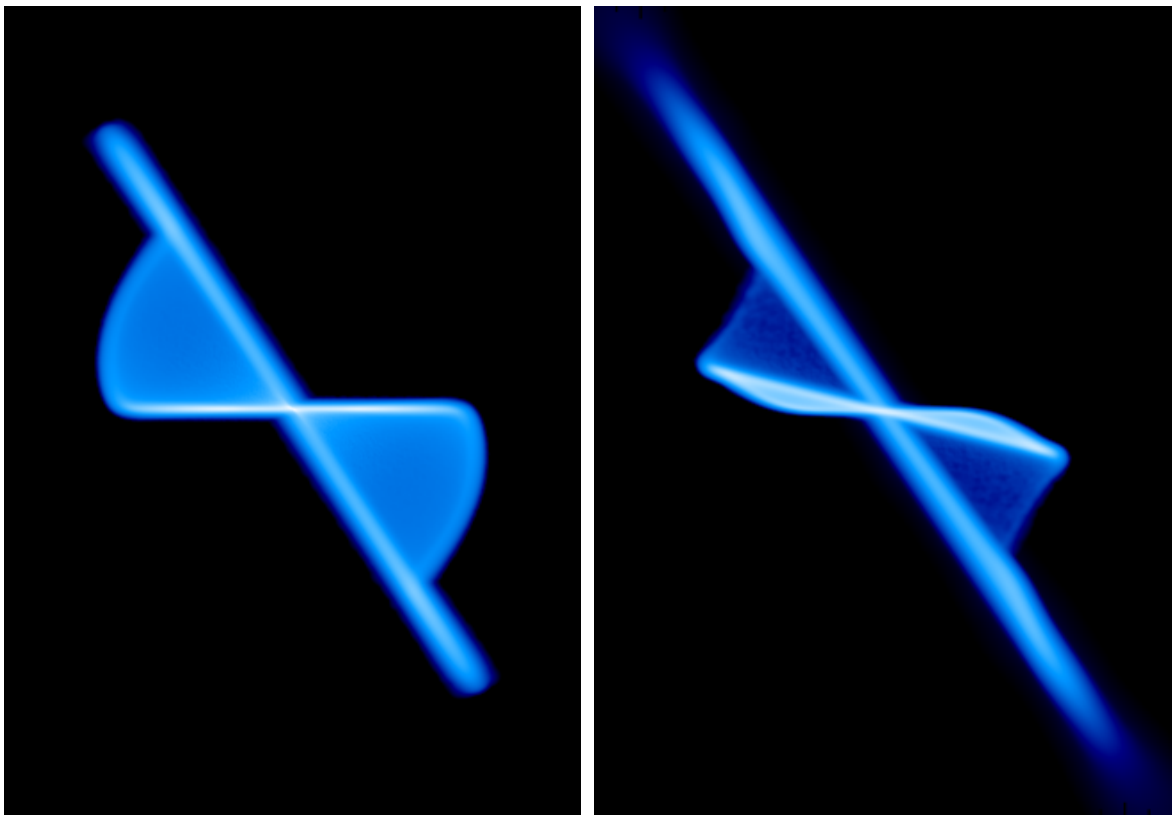

Figure 2.13: 3D simulations of a disc tilted at 60°, $\alpha = 0.16$ and $H/R = 0.03$ at 0.5 orbits and 6.25 orbits at $R_{\rm warp}$.

The warp amplitude of the disc is calculated at times $t = 0.5$ and $t = 6.25$ orbits at $R_{\rm warp}$ and is compared with the critical warp amplitude $|\psi|_c = 4$ denoted by the red dashed line as shown in figure 2.14b. Initially, the value of $|\psi| \approx |\psi|_c$, so we expect the disc to be unstable. At a later time , the value of $|\psi| > |\psi|_c$ at radius $r = 17$, where the disc tears as observed in the surface density and tilt profiles.

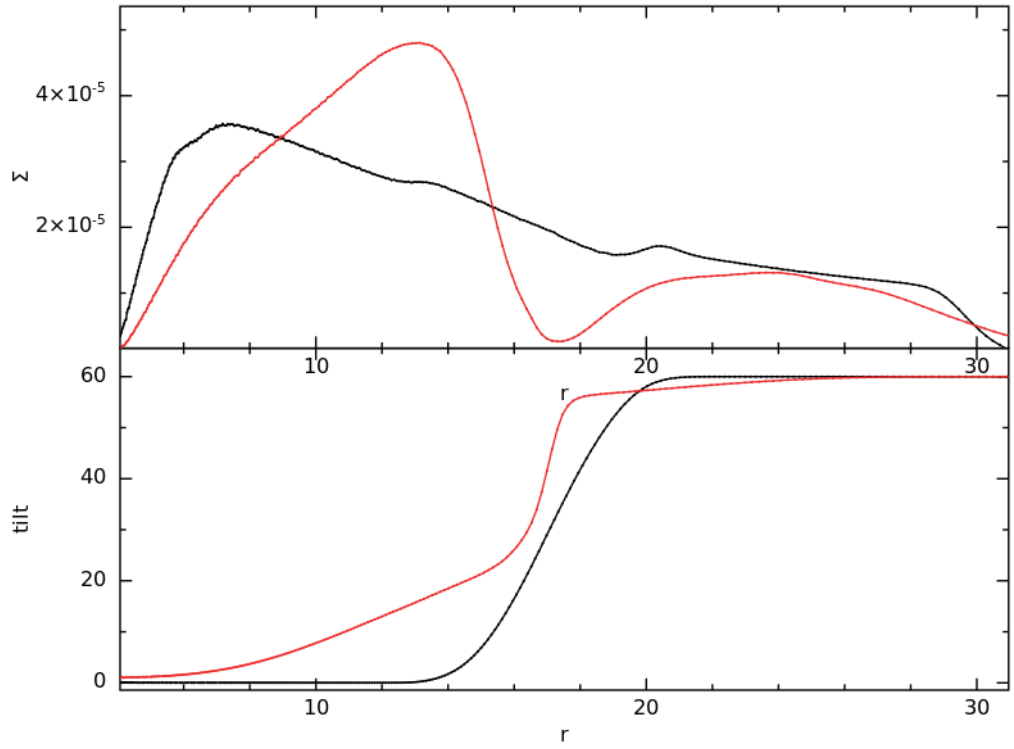

(a)

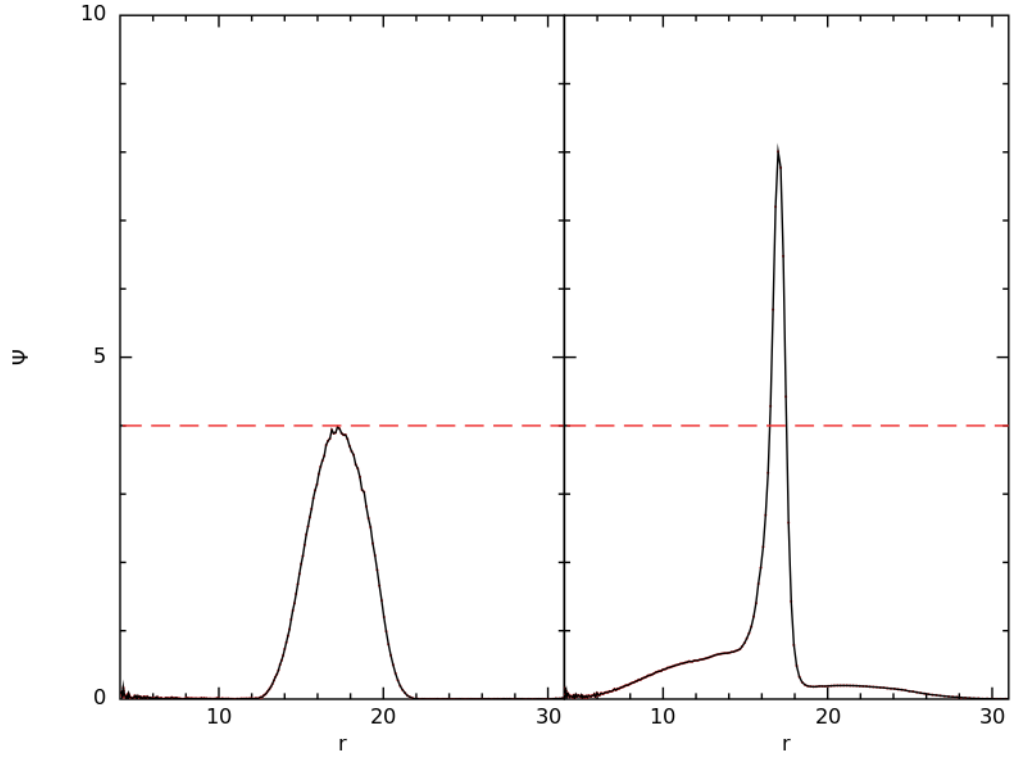

(b)

Figure 2.14: (a) The first plot shows the surface density of the disc inclined at $60°, \alpha = 0.16$ and $H/R = 0.03$ after 0.5 (black line) and 6.25 orbits (red line) at $R_{\rm warp}$. The value of Σ at $r \approx 17$ lowers to zero which denotes the point where the disc becomes unstable. The second plot shows the change in the tilt of the disc with its outer part tilted at 60° at 0.5 (black line) and 6.25 orbits (red line) at $R_{\rm warp}$. The tilt of the disc shows a break at $r \approx 17$ at a later time. (b) The warp amplitude $|\psi|$ of the disc at $60°, \alpha = 0.16$ and $H/R = 0.03$ is calculated at $t \approx 0.5$ and 6.25 orbits at $R_{\rm warp}$. The values of $|\psi|$ are compared to the critical value $|\psi|_c = 4$ denoted by the red dashed line. Initially, the maximum value of warp amplitude $\approx |\psi|_c$, so we expect the disc to be unstable. The value of warp amplitude at a later time peaks to $|\psi| = 8$ at radius $r \approx 17$, thus proving that the disc becomes unstable.

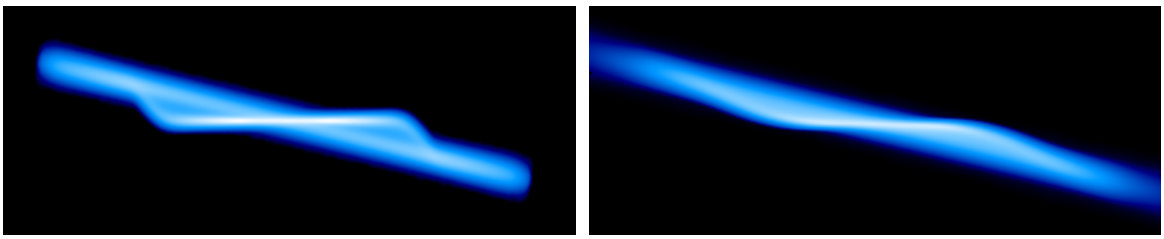

Figure 2.15: 3D simulations of a disc tilted at 10°, $\alpha = 0.18$ and $H/R = 0.03$ at 0.5 orbits and 12.5 orbits at $R_{\rm warp}$. No evidence of a disc tear is seen in this disc.

Now, we consider a disc with $\alpha = 0.18$ and inclined at 10°. Figure 2.15 shows the 3D simulation of the disc at $t = 220$ and 5500, which are 0.5 and 12.5 orbits at $R_{\rm warp}$. The 3D simulations show no disc breaking at a later time, which is further verified from the surface density and tilt plots of the disc as shown in figure 2.16a. It shows the changes in the surface density and the tilt of the disc at times $t = 0.5$ (black line) and $t = 12.5$ orbits (red line) at $R_{\rm warp}$. These figures show no evidence of disc tearing and the criterion of disc tearing can be further tested from the values of the warp amplitude at the two times.

The warp amplitude of the disc is calculated at times t = 0.5 and t = 12.5 orbits at $R_{\rm warp}$ and is compared to the critical warp amplitude $|\psi|_c = 6$ for $\alpha = 0.18$ as shown in figure 2.16b. At both times, the value of $|\psi| << |\psi|_c$ and hence the disc remains stable without forming any instabilities.

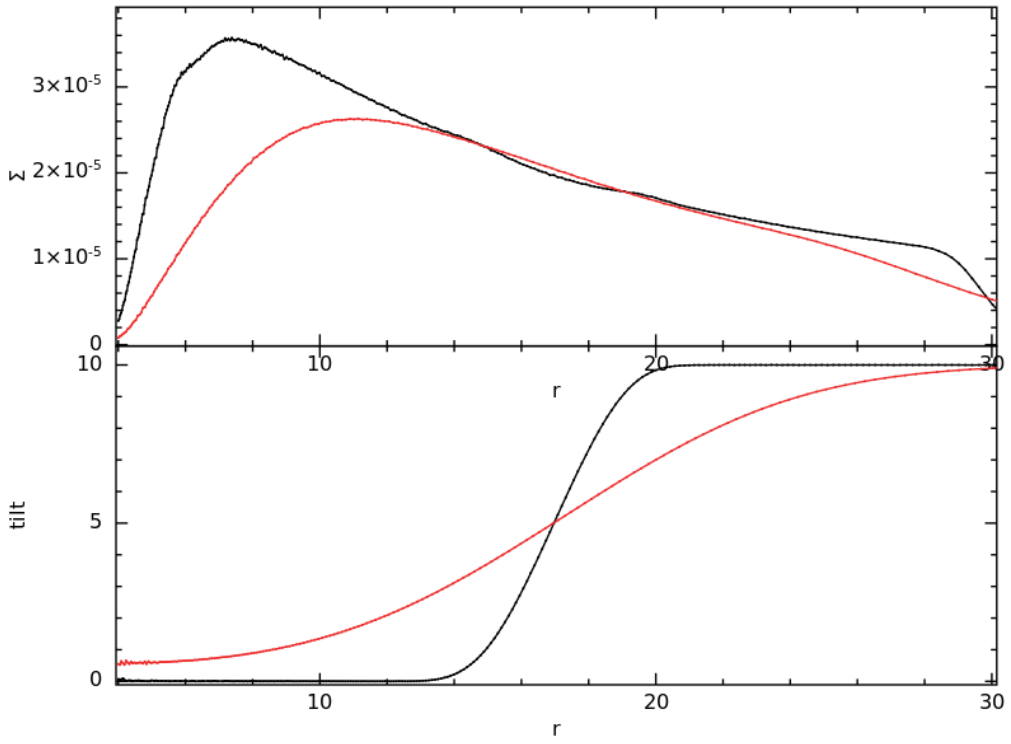

(a)

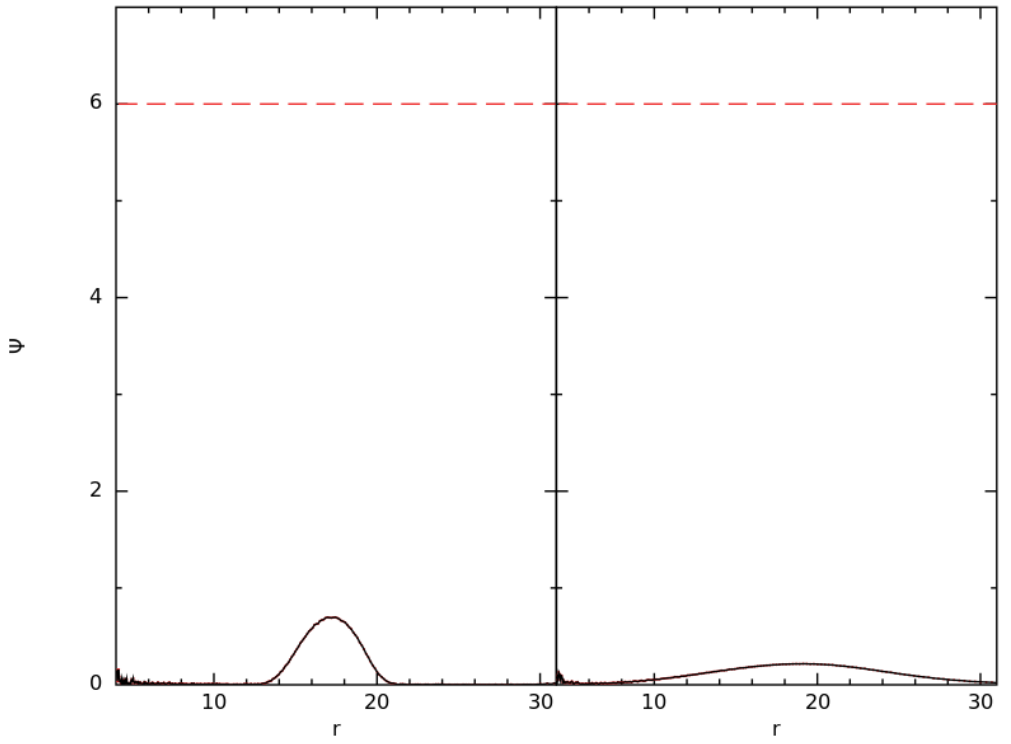

(b)

Figure 2.16: (a) The first plot shows the surface density profiles for a disc initially inclined at $10°, \alpha = 0.18$ and $H/R = 0.03$ after 0.5 (black line) and 12.5 orbits (red line) at $R_{\rm warp}$. The second plot shows the corresponding tilt changes for the same disc setup at 0.5 (black line) and 12.5 (red line) orbits at $R_{\rm warp}$. (b) The warp amplitude $|\psi|$ of the disc inclined at $10°, \alpha = 0.18$ and $H/R = 0.03$ is plotted at times 0.5 and 12.5 orbits at $R_{\rm warp}$ respectively. The values are compared to the $|\psi|_c = 6$ denoted by the red dashed line.

At the same viscosity parameter $\alpha = 0.18$, this analysis is tested for a higher inclined disc at 60°. Figure 2.17 shows the 3D simulation of the disc at $t = 0.5$ and $t = 6.25$ orbits at $R_{\rm warp}$. The surface density and the tilt of the disc at these times is examined as shown in figure 2.18a.

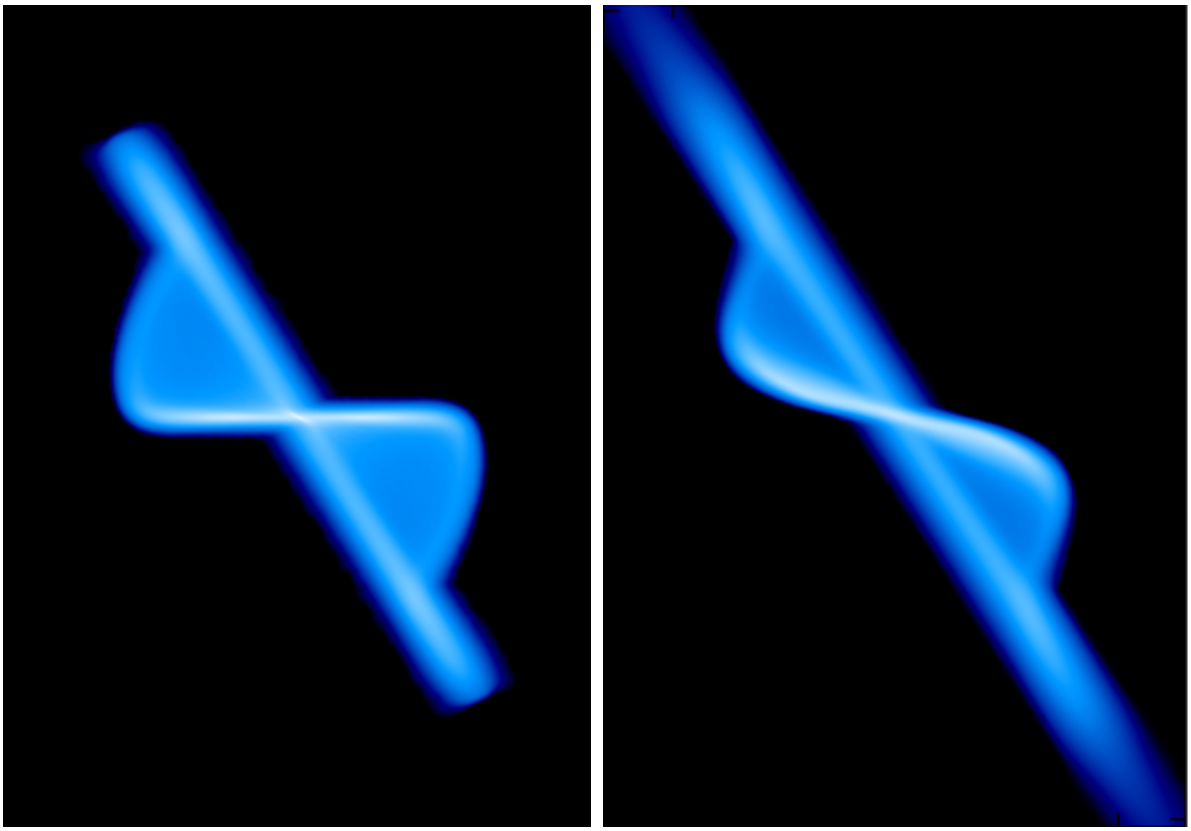

Figure 2.17: 3D column density plots of a disc tilted at 60°, $\alpha = 0.18$ and $H/R = 0.03$ at 0.5 orbits and 6.25 orbits at $R_{\rm warp}$.

Unlike the other highly inclined warped discs studies so far, this disc shows no possibility of a break as shown in the 3D simulations. This can be further studied by examining the surface density and tilt of the disc as shown in figure 2.18a. The surface density does not reduce to zero at any radii at a later time. Similarly, the tilt of the disc doesn't show any disc tear at a later time .

The theoretical criterion of disc tearing can be further examined by calculating the warp amplitude at times t = 0.5 and t = 6.25 orbits at $R_{\rm warp}$. These values of $|\psi|$ are compared to the critical warp amplitude $|\psi|_c = 6$ as shown in figure 2.18b. The value of $|\psi|$ is less than $|\psi|_c$ at both times, proving that the disc remains stable.

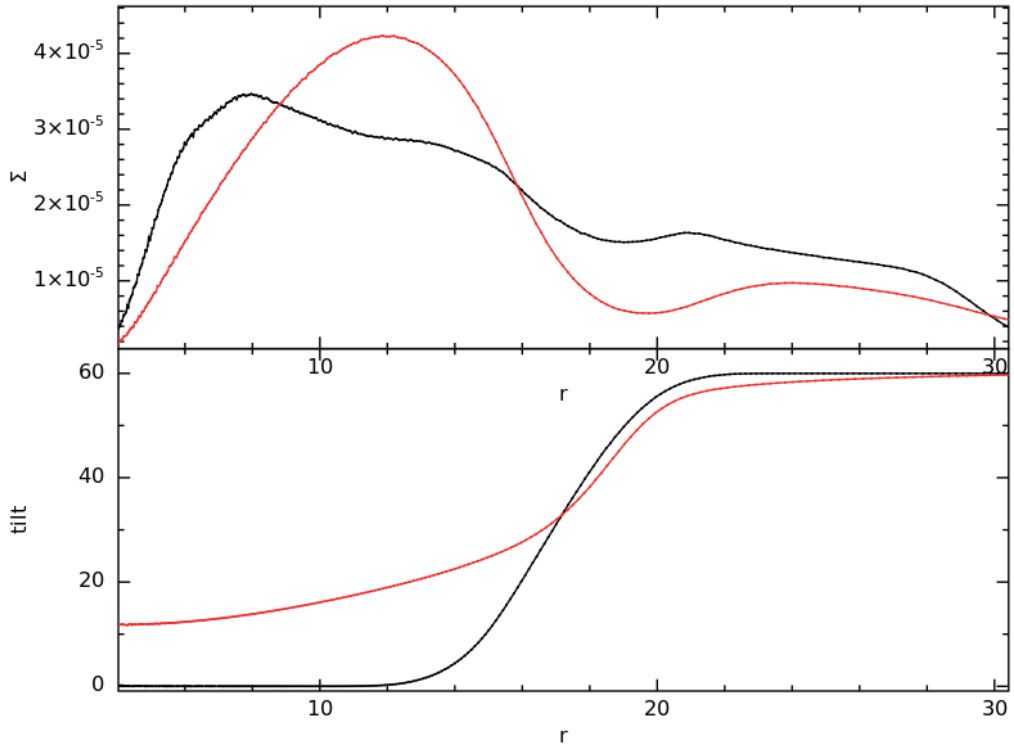

(a)

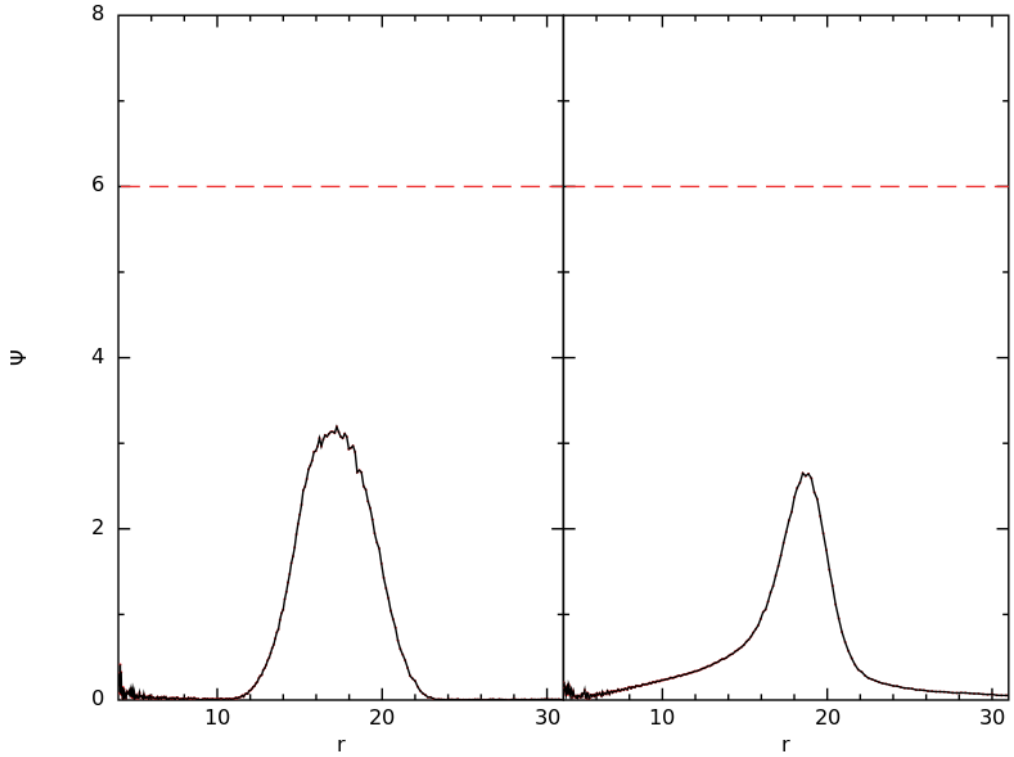

(b)

Figure 2.18: (a) The first plot shows the surface density of the disc inclined at $60°, \alpha = 0.18$ and $H/R = 0.03$ after 0.5 (black line) and 6.25 orbits (red line) at $R_{\rm warp}$. There is no divide in the surface density at any radii of the disc. The second plot shows the change in the tilt of the disc at 0.5 (black line) and 6.25 orbits (red line) at $R_{\rm warp}$ which also shows no instabilities. (b) The warp amplitude $|\psi|$ of the disc at $60°, \alpha = 0.18$ and $H/R = 0.03$ is calculated at $t \approx 0.5$ and 6.25 orbits at $R_{\rm warp}$. The values of $|\psi|$ is compared to the critical value $|\psi|_c = 6$ denoted by the red dashed line. The value of $|\psi| < |\psi|_c$ thus proving that the disc remains stable.

From figure 2.2, it is clear that the critical value of warp amplitude to become unstable increases with α. The critical value at $\alpha = 0.2$ is $|\psi|_c = 13.5$ and it increases further as α values go up. Hence, we can examine the behaviour of a warped disc at $\alpha = 0.3$ and prove that they remain stable and doesn't become unstable at any critical value of the warp amplitude. Firstly, for a disc inclined at 10°, figure 2.19 shows the 3D simulations at $t = 0.5$ orbits and $t = 12.5$ orbits at $R_{\rm warp}$. The surface density and the tilt of the disc at these times are also studied as shown in figure 2.20a. The 3D column density as well as the parameter (Σ and tilt) profiles of the disc show no evidence of instabilities. The disc remains warped without any break, thus proving that it remains stable at higher α values. This can be further proven by studying the changes in the warp amplitude as shown in figure 2.20b.

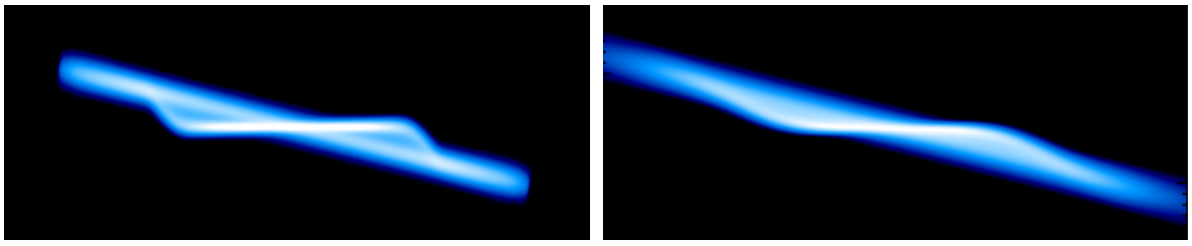

Figure 2.19: 3D simulation of a disc tilted at 10°, $\alpha = 0.3$ and $H/R = 0.03$ at 0.5 orbits and 12.5 orbits at $R_{\rm warp}$.

The warp amplitude of this disc at times $t = 0.5$ and $t = 12.5$ orbits at $R_{\rm warp}$ is calculated. The values of $|\psi|$ are much smaller than the maximum value $|\psi|_c = 13.5$ (for $\alpha = 0.2$) as shown in figure 2.20b. This proves that it is difficult for a disc at $\alpha = 0.3$ to achieve the critical value to become unstable.

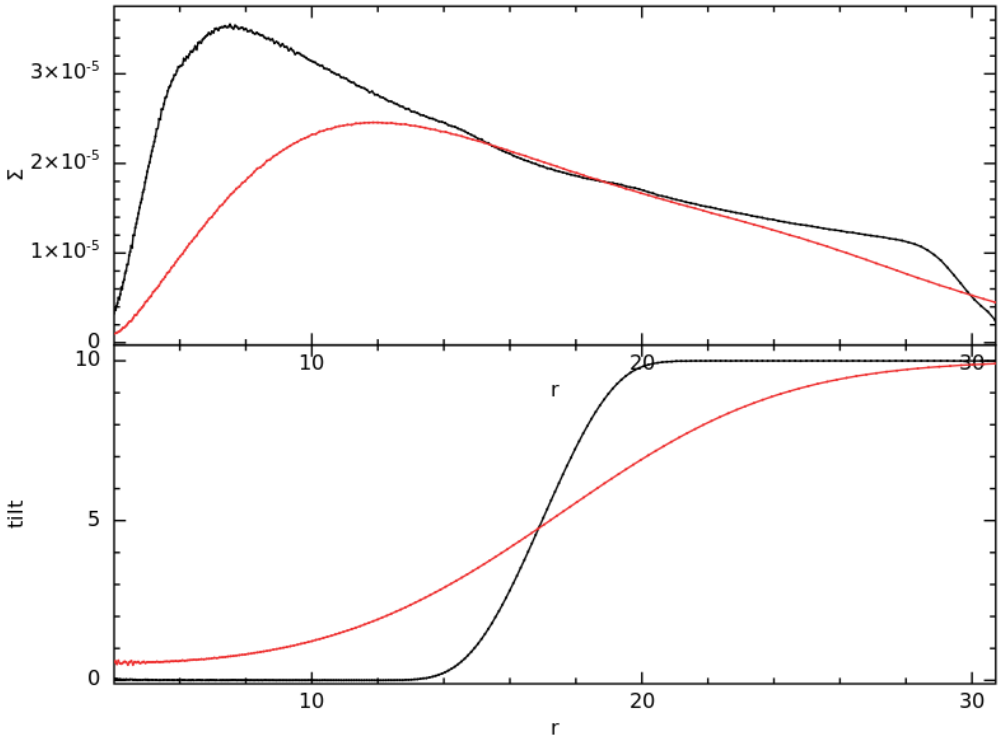

(a)

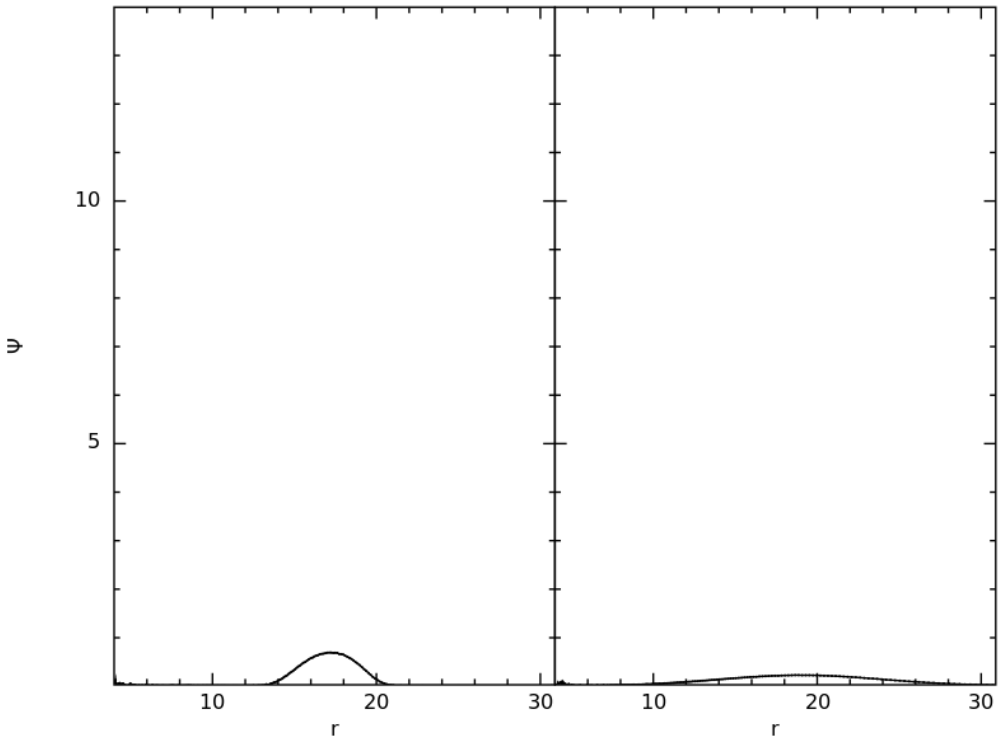

(b)

Figure 2.20: (a) The first plot shows the surface density profiles for a disc initially inclined at $10°, \alpha = 0.3$ and $H/R = 0.03$ after 0.5 (black line) and 12.5 orbits (red line) at $R_{\rm warp}$. The second plot shows the corresponding tilt changes for the same disc setup at 0.5 (black line) and 12.5 (red line) orbits at $R_{\rm warp}$. (b) The warp amplitude $|\psi|$ of the disc inclined at $10°, \alpha = 0.3$ and $H/R = 0.03$ after 0.5 and 12.5 orbits at $R_{\rm warp}$. The values of $|\psi|$ are very small at both times and therefore it is difficult for the disc to become unstable at any $|\psi|_c$ value.

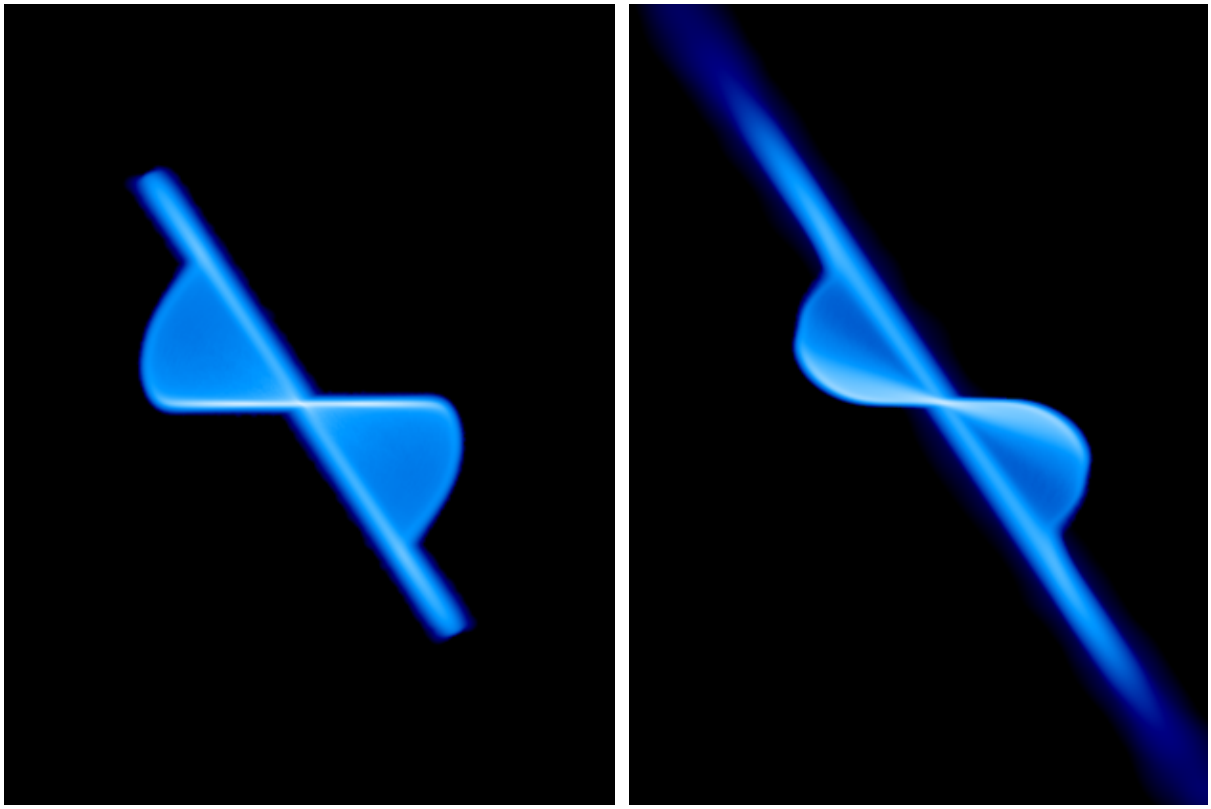

Figure 2.21: 3D column density plots for a disc tilted at 60°, $\alpha = 0.3$ and $H/R = 0.03$ at 0.5 orbits and 6.25 orbits at $R_{\rm warp}$. The disc shows no breaking at the later time.

The behaviour of a warped disc at $\alpha = 0.3$ is investigated at 60°. The disc remains stable in the 3D simulations at t = 0.5 and 6.25 orbits at $R_{\rm warp}$, and there is no disc tear at a later time as shown in figure 2.21. The surface density of the disc is calculated at t = 0.5 (black line) and t = 6.25 (red line) orbits at $R_{\rm warp}$ as given in figure 2.22a. The value of surface density $\Sigma > 0$ at all radii. The figure also shows the tilt of the disc at both times, proving that the disc remains stable without any instabilities.

We calculate the warp amplitude of the disc and test the instability criterion at $t =$ 0.5 and 6.25 orbits at $R_{\rm warp}$ respectively. As shown in figure 2.22b, the ψ values lie below any critical value at both times. This implies that the disc remains stable at $\alpha = 0.3$. Also, the growth rate of instabilities is smaller at higher α values which concludes that it is difficult for this disc to achieve the critical value to give rise to instabilities.

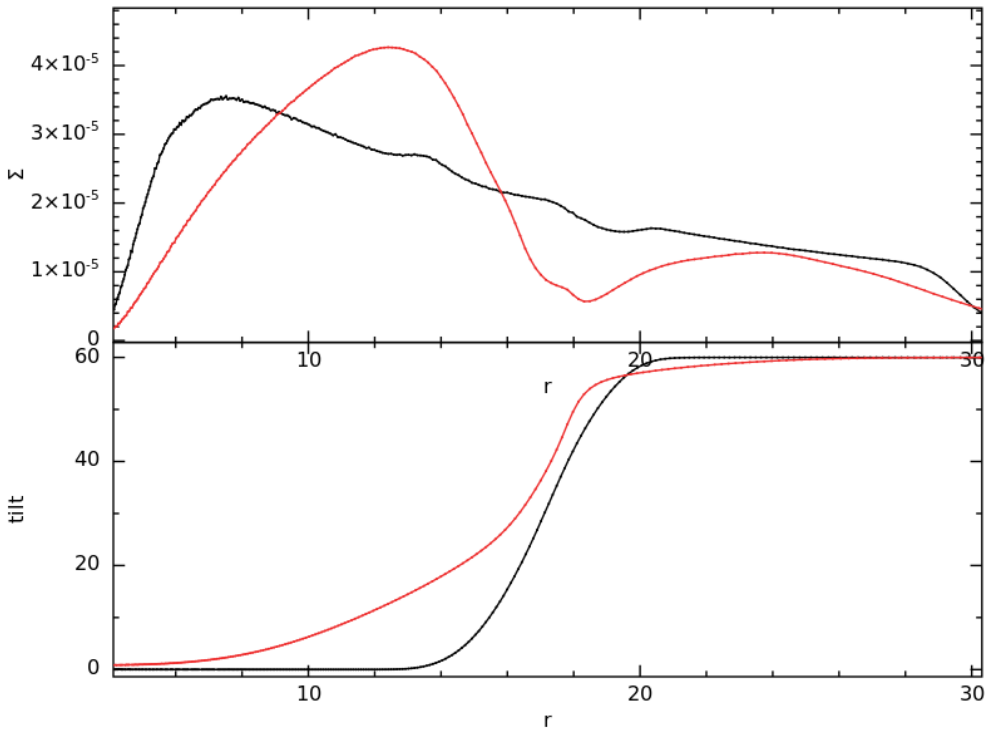

(a)

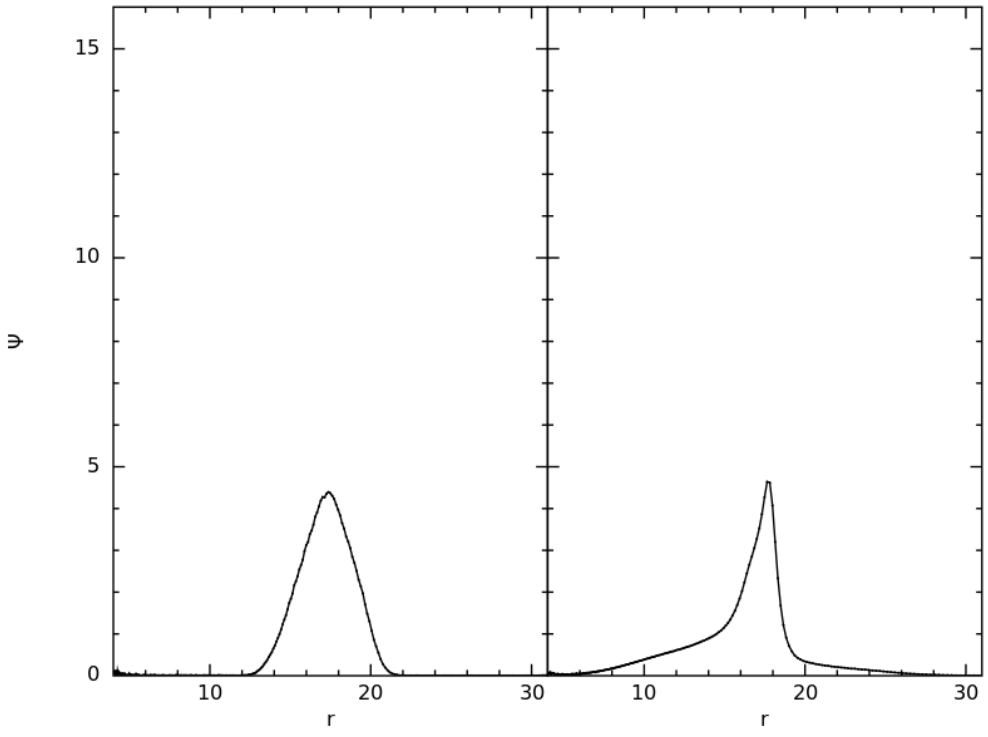

(b)

Figure 2.22: (a) The first plot shows the surface density of the disc inclined at $60°, \alpha = 0.3$ and $H/R = 0.03$ after 0.5 (black line) and 6.25 orbits (red line) at $R_{\rm warp}$. The value of Σ doesn't reduce to zero which denotes that the disc remains stable. The second plot shows the change in the tilt of the disc after 0.5 (black line) and 6.25 orbits (red line) at $R_{\rm warp}$. The tilt of the disc doesn't show a break at any radii at the later time. (b) The warp amplitude $|\psi|$ of the disc at $60°, \alpha = 0.3$ and $H/R = 0.03$ is calculated at $t \approx 0.5$ and 6.25 orbits at $R_{\rm warp}$. The values of $|\psi|$ remains small at both times proving that at $\alpha = 0.3$, it is difficult for any disc to achieve the minimum value to become unstable.

2.5 Growth of instabilities

Doğan et al. (2018) calculates the growth rate of the instabilities given by the dimensionless growth rate $\Re[s]$ where

$$s = -\frac{i\omega}{\Omega}\left(\frac{\Omega}{\mathrm{c_s k}}\right)^2. \tag{2.22}$$

Furthermore, s is written in terms of the physical growth rate $\Re[-i\omega]$ as

$$-i\omega = s\Omega\left(\frac{\mathrm{c_s k}}{\Omega}\right)^2. \tag{2.23}$$

The instabilities in discs are assumed to grow if $\Re[s] > 0$ or decay if $\Re[s] < 0$. Thus,

$$|\psi| = |\psi|_0 \exp[\Re(-\mathrm{i}\omega)\mathrm{t}]. \tag{2.24}$$

If $c_s k/\Omega \approx 1$, the equation becomes:

$$|\psi| = |\psi|_0 \exp[\Re(-\mathrm{i}\omega)\mathrm{t}] = |\psi|_0 \exp[\mathrm{s}\Omega\mathrm{t}]. \tag{2.25}$$

The dimensionless growth rate $\Re[s]$ as a function of ψ is plotted in Doğan et al. (2018) at different values of α (refer to figure 2.1). For a disc at $\alpha = 0.1$, the value of growth rate $\Re[s] = 0.2$ for ψ values between 4 and 5. So far, we explained in detail the numerical results at different disc setups where discs show instabilities at higher inclinations and lower α values. In this section, we determine the rate at which the warp amplitude grows in one such setup, i.e. we calculate the time taken for the warp to grow from $\psi = 4$ to $\psi = 5$ in the numerical simulation and compare it to the time required for the instability to grow as predicted by Doğan et al. (2018) using equation 2.25.

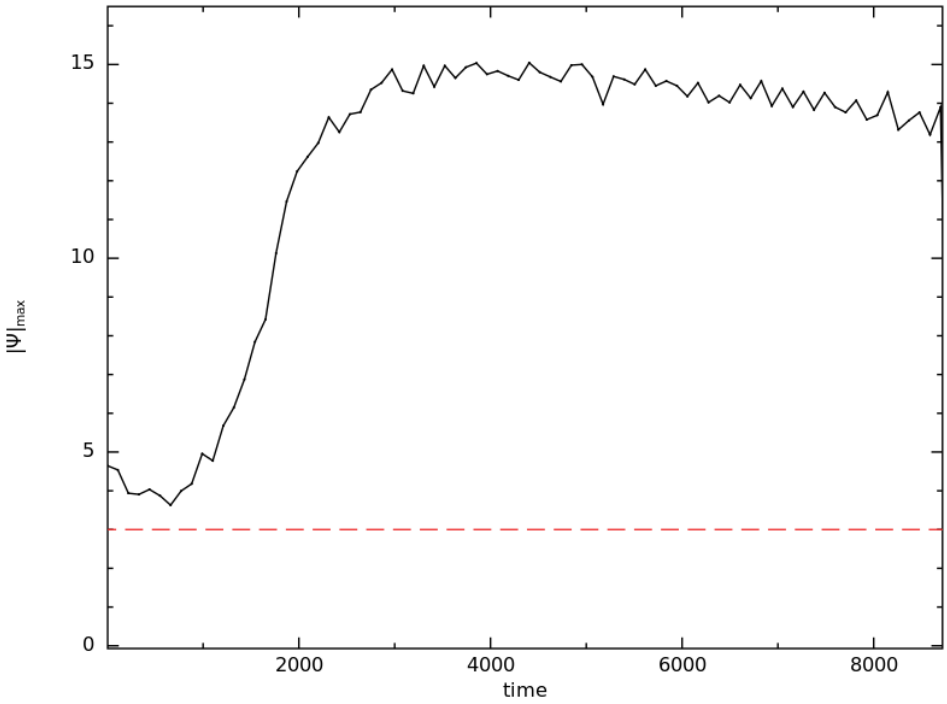

Figure 2.23: The maximum value of warp amplitude (peak value in $|\psi|$ plot) is plotted over time for a disc inclined at 60°, $\alpha = 0.1$ and $H/R = 0.03$.

The maximum warp amplitude is examined from the numerical simulations of the disc with $\alpha = 0.1$, $H/R = 0.03$ and tilted at 60° as shown in figure 2.23. Our aim is to calculate the rate at which the warp amplitude grows from values of $\psi = 4$ to $\psi = 5$ [6]. From this figure, we obtain time t_1 corresponding to a value of $\psi = 4$ and t_2 at $\psi = 5$. The values of $t_1 = 880.8$ and $t_2 = 990.9$, which gives $\Delta t = t_2 - t_1 = 110.1$. These two values of warp amplitude correspond to radii $r_1 = 16.06$ and $r_2 = 16.15$ which gives a mean value of $r \approx 16.105$.

As demonstrated by equation 2.25, the time Δt required for the warp amplitude to grow from an initial value $|\psi|_0$ is:

$$\exp[\mathrm{s}\Omega\Delta\mathrm{t}] = \frac{|\psi|}{|\psi|_0} \tag{2.26}$$

where $|\psi|_0 = 4$, $|\psi| = 5$, s $= 0.2$, $\Omega = 1/\sqrt{r^3}$ with $r = 16.105$. This gives a value of $\Delta t = 72.06$. Therefore, the time taken for the instabilities to grow in this numerical

[6] We choose these values for warp amplitude at $\psi = 4$ and 5, to study the growth rate of instabilities at values of $\psi > \psi_c$ as shown in Doğan et al. (2018) or see figure 2.1.

model is 1.5 times more in comparison to the value expected from Doğan et al. (2018).

2.6 Discussions and Conclusions

Doğan et al. (2018) derives the theoretical criterion of disc tearing in Keplerian, diffusive warped discs which is tested using SPH simulations as presented in this chapter. The critical value of warp amplitude for a disc to become unstable is inspected at different values of α. This project conducts a parameter sweep to test the instability of tilted warped discs and check if the theoretical criterion holds true in each disc setups. In this work, we consider a non precessing, warped disc model with no LT effect, similar to that used in Lodato & Pringle (2007).

Firstly, a warped disc with viscosity parameter $\alpha = 0.1$ and $H/R = 0.03$ is tested at tilts 10°, 30°, 45° and 60° respectively. The 3D simulations of a disc composed of 10 million particles with $\alpha = 0.1$ and $H/R = 0.03$ and the corresponding changes in the surface density and tilt of the disc are examined. The disc showed evidence of tearing at 45° and 60° but remained stable at lower inclinations of 10° and 30°. The instability criterion is further tested in each case, by calculating the warp amplitude of the disc and comparing it to the critical value $|\psi|_c$ corresponding to the disc's α parameter. At a value of $|\psi| > |\psi|_c$, the disc becomes unstable and tears as predicted in Doğan et al. (2018). At higher inclinations, one can identify the points of disc tear from the surface density profiles where the values of $\Sigma = 0$. The warp amplitude of these unstable discs form instabilities with values of $|\psi| > |\psi|_c$ at these exact points of disc tear. The same analysis is extended at higher $\alpha = 0.16$, 0.18 and 0.3 with higher $|\psi|_c$ values. The results show that it is difficult to form instabilities in these disc setups, thus proving that highly viscous warped discs remain stable in the simulation without any disc break. The disc only becomes unstable when inclined at 60° for $\alpha = 0.16$.

Therefore, we have demonstrated the key results of Doğan et al. (2018) using hydro-

dynamical simulations. Warped discs can be unstable and break into distinct planes. The instability is most likely to occur for small α (≤ 0.1) at higher values of $|\psi|$ ($> |\psi|_c$). The discs are found to remain stable at higher α (≈ 0.3) values and for smaller values of $|\psi|$ ($< |\psi|_c$). We have also confirmed that the rate at which the warp amplitude grows in the unstable regions is of the order of the rate at which it was predicted to grow (Ogilvie, 2000; Doğan et al., 2018).

3

A parameter study of disc-tearing

3.1 Introduction

Accretion discs are present around many astrophysical systems at scales ranging from protostars to AGN. Due to several effects, these discs can form a warped configuration. For example, discs can warp due to radiation (Pringle, 1996, 1997), due to winds (Schandl & Meyer, 1994) or due to resonant tidal effects (Lubow & Ogilvie, 2000). Accretion discs around spinning black holes can warp due to differential precession induced by the Lense-Thirring (or LT) effect (Lense & Thirring, 1918). A resultant of the LT effect, is the Bardeen Peterson effect which produces a warp that joins the aligned inner parts to the misaligned outer parts of the disc (Bardeen & Petterson, 1975).

Previous studies have considered a torque balance formula to investigate the nature of warped discs around supermassive black holes, and examine if they tear into distinct rings using numerical simulations (Nixon et al., 2012a; Nixon et al., 2013). The physics of warped discs depends heavily on how the effective viscosities and the associated torques affect the disc structure. An instability criterion is analysed in Doğan et al. (2018) which attains a general condition for warped discs to break. This criterion is derived from a dispersion relation and shows that the disc becomes unstable at a critical warp amplitude ($|\psi|_c$) dependent on the value of α. Furthermore, the growth rate of instabilities in discs

as a function of the warp amplitude is plotted at different α values. Doğan et al. (2018) also derives the maximum warp amplitude achieved by a disc with tilt β and disc thickness of H/R.

In this chapter, we test this instability criterion for discs warped due to LT effect using numerical simulations. Following the discussion in chapter 2, we summarise the key points for the stability analysis of warped discs and the general instability criterion for discs to tear (Ogilvie, 2000; Doğan et al., 2018). In a parameter sweep, the main numerical results are investigated by applying and testing this criterion at different disc variables. Finally, the conclusions are drawn by comparing these results to the expected analysis.

3.2 Motivation

There are studies which show that accretion discs become unstable and may break or tear into distinct rings when the disc viscosity is not strong enough to effectively communicate the precession radially through the disc. An evidence of disc tearing in tilted discs around a central black hole was previously established using 3D hydrodynamical simulations (Nixon et al., 2012a; Nealon et al., 2015). The criterion for disc tearing in the diffusive regime was examined by calculating the breaking radius, where the precession torque is compared to the torque from the azimuthal shear viscosity as shown in Nixon et al. (2012a). Thereafter, disc tearing in circumbinary discs around misaligned binary systems was demonstrated using SPH simulations in Nixon et al. (2013). Doğan et al. (2015) examined the same but in circumprimary discs and reckoned the inclusion of the effective viscosity from vertical shear to study the criterion of disc tear at small values of α and inclinations. Not long ago, Aly & Lodato (2020) used SPH simulations to examine the nature of evolution in circumbinary discs composed of gas and dust and the results showed the breaking of the gas component in thin discs and the forming of a smooth warp in

thick discs. This highlights the importance of having an instability criterion which can be applied globally to study disc tearing in many systems. Doğan et al. (2018) focuses on deriving a criterion for discs to become unstable by examining the behaviour of isothermal, isolated warped discs in the diffusive regime. This study emphasises the effects of viscous torques on an isolated warped disc and establishes the dependence of warp amplitude on the criterion, thus helps us to concrete the understanding of instabilities in warped discs. This demonstrates the motivation of this research work as it is vital to test the instability criterion using numerical simulations. We aim to use 3D hydrodynamical simulations to study discs around black holes warped due to LT effect. This chapter studies a parameter sweep of discs at different values of α, H/R and tilts. The criterion is examined for each disc by checking if the warp amplitude $|\psi|$ calculated from our analysis exceeds its critical value to become unstable and produce instabilities.

3.2.1 Dispersion relation & Stability analysis

In section 2.2.1, we presented the stability analysis and dispersion relation from the warped disc equations. In this section, we review the important points of the analysis, and further discuss the instability criterion for discs to break. The evolution equation is derived from the conservation of angular momentum given as

$$\begin{aligned}\frac{\partial L}{\partial t} &= \frac{1}{R}\frac{\partial}{\partial R}\left\{\frac{(\partial/\partial R)[\nu_1\Sigma R^3(-\Omega')]}{\Sigma(\partial/\partial R)(R^2\Omega)}\boldsymbol{L}\right\} \\ &+\frac{1}{R}\frac{\partial}{\partial R}\left[\frac{1}{2}\nu_2 R|\boldsymbol{L}|\frac{\partial \boldsymbol{l}}{\partial R}\right] \\ &+\frac{1}{R}\frac{\partial}{\partial R}\left\{\left[\frac{\frac{1}{2}\nu_2 R^3\Omega|\partial \boldsymbol{l}/\partial R|^2}{(\partial/\partial R)(R^2\Omega)}+\nu_1\left(\frac{R\Omega'}{\Omega}\right)\right]\boldsymbol{L}\right\} \\ &+\frac{1}{R}\frac{\partial}{\partial R}\left(\nu_3 R|\boldsymbol{L}|\ \boldsymbol{l}\times\frac{\partial \boldsymbol{l}}{\partial R}\right).\end{aligned}$$

This equation is used to derive a dispersion relation and its solution gives the criterion for warp discs to grow instabilities as demonstrated in Doğan et al. (2018) (refer equation

28 in Doğan et al. (2018) or section 2.2.1). This study performs the stability analysis of the evolution equation by subjecting it to linear perturbations (motivated by Ogilvie (2000)), thus producing solutions to the perturbation shown as:

$$\exp\left(-i\int \omega dt + i\int k dr\right) \tag{3.1}$$

where k is the wavenumber and ω is the wave frequency. This determines how fast the perturbations move and how they grow or decay in comparison to the background solution. The perturbation analysis (Ogilvie (2000); Doğan et al. (2018); see also section 2.2.1) makes use of the dimensionless growth rate given by

$$s = -\frac{i\omega}{\Omega}\left(\frac{\Omega}{c_s k}\right)^2 \tag{3.2}$$

where the perturbations grow if $\Re[s] > 0$ or decay if $\Re[s] < 0$, with the growth rate given by $\Re[-i\omega]$. A third order dispersion relation is derived from the coefficient determinant given by (or refer equation 2.20 in section 2.2.1)

$$\begin{aligned} s^3 - s^2\left[aQ_1 - 2Q_2 + |\psi|\left(aQ_1' - Q_2'\right)\right] - s\Big[2aQ_1Q_2 - Q_2^2 - Q_3^2 \\ +|\psi|\left(aQ_1Q_2' - Q_2Q_2' - Q_3Q_3'\right)\Big] - a\Big[Q_1\left(Q_2^2 + Q_3^2\right) \\ +|\psi|\left(Q_1Q_2Q_2' - Q_1'Q_2^2 + Q_1Q_3Q_3' - Q_1'Q_3^2\right)\Big] = 0. \end{aligned} \tag{3.3}$$

Doğan et al. (2018) derives the instability criterion for a warped disc to become unstable by finding the roots or solutions of this dispersion relation. It is essential to study the effect of each of the Q_i coefficients on the warp amplitude of a disc, how the coefficients behave when a disc becomes unstable and most importantly determine if a disc becomes unstable at a critical value of warp amplitude $|\psi|_c$. The dimensionless growth rate of the instability is attained as $\Re[s]$. Some of the key results from this work show how the growth

rate $\Re[s]$ behaves at different values of α (discussed earlier in figure 2.1). This shows that the growth rate of instabilities $\Re[s]$ is inversely proportional to α, i.e. the growth rate of instability are higher for low values of α. Furthermore, critical warp amplitudes for discs at different values of α are studied, which demonstrated the stable and unstable regions in the $(\alpha, |\psi|)$ parameter space (shown earlier in figure 2.2). Therefore, it is important to test this criteria in discs at various parameters and check if they become unstable and tear into discrete rings at their corresponding values of the critical warp amplitude. These tests are important because: (1) the warped disc equations do not capture the full hydrodynamical behaviour in discs (e.g. non-linear flows such as shocks, and evolution on timescales that are short compared to the local dynamical timescale) (2) the stability analysis is local to a patch of the disc, and therefore we must check whether the stable or unstable behaviour occurs in a global simulation. This forms the motivation of this research chapter to use numerical simulations and test the instability criterion of discs around supermassive black holes warped due to LT effect.

Firstly, we check how SPH simulations behave for a disc at $\alpha = 0.1$, $H/R = 0.03$, initially inclined to the black hole spin vector by 10°, 30°, 45° and 60° as discussed in the next section. In each case, the instabilities of the disc can be tested by checking the variations in its surface density, tilt and twist profiles. In order to compare our results with that predicted from Doğan et al. (2018), it is important to calculate the disc's warp amplitude from our simulations and check if it exceeds the critical warp amplitude $|\psi|_c$. As shown in section 3.4, this analysis is also examined in thinner discs at $H/R = 0.01$ where the values of artificial or numerical viscosity α_{AV} can't be ignored. As predicted by Doğan et al. (2018), the growth rate of instabilities is higher at low α values which can be investigated from numerical simulations (at $\alpha = 0.05$), further shown in section 3.5.

The growth rate of instabilities from our simulations is calculated and compared to the

theoretical analysis as explained in section 3.6. Doğan et al. (2018) derives an equation for the maximum value of warp amplitude for a disc at tilt β and scale-height H/R given as:

$$|\psi|_{\max} = \beta \frac{R}{H} \tag{3.4}$$

This is examined in our analysis as detailed in section 3.6.1. We also test the point of instability at $|\psi|_c$ in highly inclined discs, and show that each disc becomes unstable and tear to form rings exactly when the warp amplitude exceeds its critical value.

3.3 Numerical Results

Our aim is to perform 3D simulations using the smoothed particle hydrodynamics code PHANTOM and test the analysis predicted by Doğan et al. (2018). We follow Nixon et al. (2012a) to simulate discs around spinning supermassive black holes and check the criterion of disc tearing explained by Doğan et al. (2018). This section details how these simulations are set up to examine the structure of an accretion disc around a spinning black hole inclusive of the effects of Lense-Thirring precession, in the diffusive regime with $\alpha > H/R$.

3.3.1 Simulations

The parameters are chosen to produce a post Newtonian approximation for a rotating black hole. We choose units of $G = 1$, $c = 1$ and black hole mass is also unity, $M = 1$. We take the black hole spin to be $a = 0.5$ which corresponds to an inner stable circular orbit at $R_{\rm in} = 4R_g$ where $R_g = GM/c^2$ is the gravitational radius. Following Nelson & Papaloizou (2000), we use the Einstein potential given by

$$\Phi_E = \frac{-GM}{R}\left(1 + \frac{3R_g}{R}\right). \tag{3.5}$$

This potential provides a good description of the expected apsidal (Einstein) precession rate of eccentric orbits. However, this potential does not produce an innermost stable circular orbit at the correct radius (see e.g. Paczyńsky & Wiita (1980))[1]), so we impose an accretion radius at $4R_g$.

As shown by Nelson & Papaloizou (2000), the momentum equation is given as

$$\frac{d\mathbf{v}}{dt} = -\frac{1}{\rho}\nabla P + \mathbf{v} \times \mathbf{h} - \nabla\Phi + \mathbf{S}_{\rm visc} \tag{3.6}$$

where $\mathbf{v}$ is the velocity, ρ is the density, P is the pressure, Φ is the gravitational potential and $\mathbf{S}_{\rm visc}$ is the viscous force per unit mass. The term $(\mathbf{v} \times \mathbf{h})$ represents the gravito-magnetic force which is used to induce the Lense-Thirring precession, with

$$\mathbf{h} = \frac{2\mathbf{S}}{R^3} - \frac{6(\mathbf{S}.\mathbf{r})\mathbf{r}}{R^5} \tag{3.7}$$

where

$$\mathbf{S} = \frac{G\mathbf{J}}{c^2} \tag{3.8}$$

and spin angular momentum $\mathbf{J} = aGM^2\hat{\mathbf{k}}/c$ with $\hat{\mathbf{k}}$ being the unit vector in the direction of the black hole spin. We note that the value of $\mathbf{h}$ in the gravito-magnetic term reduces with radius, resulting in differential precession.

We set the inner boundary of the disc at $R_{\rm in} = 4R_g$ and the outer boundary is set at $R_{\rm out} = 30R_{\rm g}$. The disc has a surface density given by $\Sigma = \Sigma_0(R/R_{\rm in})^{-p}$ with a locally isothermal sound speed profile $c_s = c_{s_0}(R/R_{\rm in})^{-q}$ where, $p = 3/2$ and $q = 3/4$. In this way, we obtain a uniformly resolved disc with a constant shell-averaged smoothing length per disc scale-height, i.e. $\langle h \rangle / H$ remains a constant (Lodato & Pringle, 2007). The simulations use a disc viscosity with Shakura-Sunyaev $\alpha = 0.1$ and a disc angular semi-thickness of $H/R = 0.03$. The disc is composed of 10 million particles with $\langle h \rangle / H$

[1]The derivation of the last stable circular orbit at different gravitational potentials is shown in Appendix B.

≈ 0.3 which infers that the effective viscosity arising from the artificial viscosity is α_{AV} = 0.017; cf. Meru & Bate (2012). The simulations are studied at different values of the tilt (β) between the disc and the black hole spin.

Doğan et al. (2018) predicted that the criterion for a disc to become unstable is given by the critical warp amplitude $|\psi|_c$, a value dependent on the α parameter (as shown in figure 2.2). Therefore, at each value of α there is a critical value for the disc's warp amplitude ($|\psi|_c$) below which it remains stable, and above which the disc becomes unstable and tears. Here, we investigate this instability criterion by checking if the warp amplitude of each disc setup with $\alpha = 0.1$ exceeds the critical warp amplitude $|\psi|_c = 3$ or not.

Firstly, we consider a disc initially inclined at 10°. The total run time of the simulation is set at t = 54000, which is two times the precessional timescale at the outer edge of the disc. Due to Lense-Thirring (LT) precession proceeded by Bardeen Peterson effect, we observe warps in the disc.

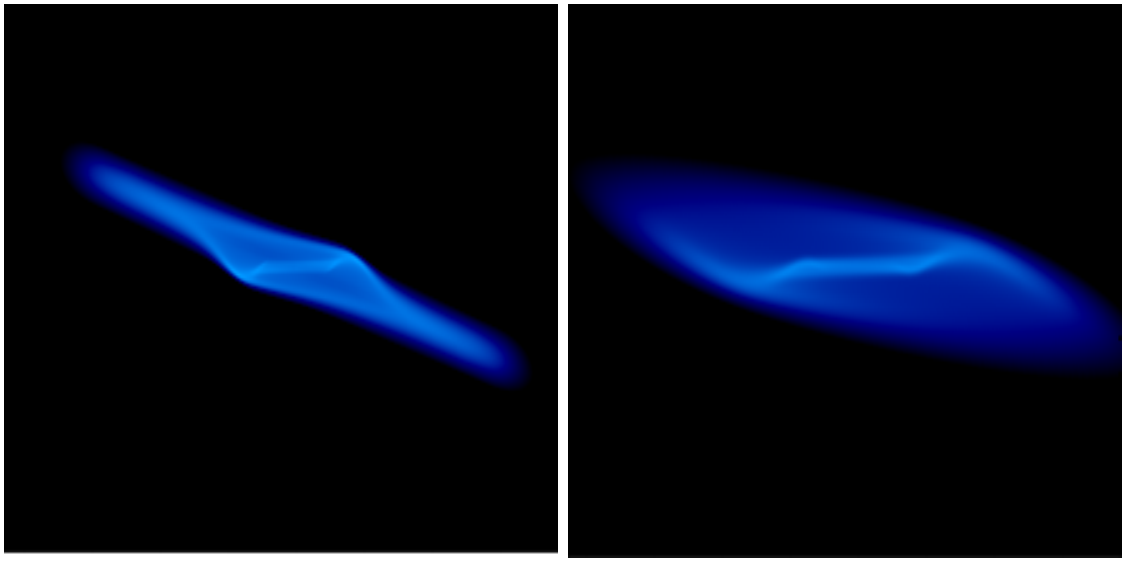

Figure 3.1: 3D simulation of the disc initially inclined at 10°, $\alpha = 0.1$ and $H/R = 0.03$ at 1.4 and 15.8 orbits at $R_{\rm out}$ respectively.

Figure 3.1 shows the 3D simulation of a disc inclined at 10°, $\alpha = 0.1$ and $H/R = 0.03$ at times t = 1485 and 16335 which are 1.4 orbits and 15.8 orbits at $R_{\rm out}$. It is shown that

the disc remains warped and does not tear at a later time. This is examined further by checking the various profiles of the disc at $t = 1.4$ (black line) and 15.8 (red line) orbits at $R_{\rm out}$ and check if there is an evidence of disc tear as shown in figure 3.2.

From the surface density profile of the disc, it is clear that the disc remains stable and does not show any instabilities. Analogous to the surface density profiles, a disc tear will be reflected by a change in the tilt of the disc. But as shown in the second panel of figure 3.2, the tilt of the disc clearly shows no disc break at a later time. There is a warp connecting the inner disc (between radii 4 and 6) to the outer part (at radii between 18 and 30) tilted at 10°. At a later time, the outer part of the disc aligns with the inner part without any break.

The behaviour of the disc's twist can also be checked as shown in the third plot of figure 3.2. The twist of the disc at $t = 1.4$ (black line) and 15.8 (red line) orbits at $R_{\rm out}$ shows no presence of an individual precessing ring, thus showing no possibility of a disc tear in this setup. To compare these results with the analysis from Doğan et al. (2018), we calculate the value of the warp amplitude ($|\psi| = r|\partial \boldsymbol{l}/\partial r|$) from the numerical data. The warp amplitude of the disc is compared to the value of the critical warp amplitude $|\psi|_c$ as shown in figure 3.3. The red dashed line shows the value of critical warp amplitude ($|\psi|_c = 3$) corresponding to $\alpha = 0.1$ (refer figure 2.2). It clearly shows that the values of warp amplitude at both times remain below the critical value and this agrees well with what predicted from Doğan et al. (2018). Therefore, this disc remains stable and does not tear to form individual rings.

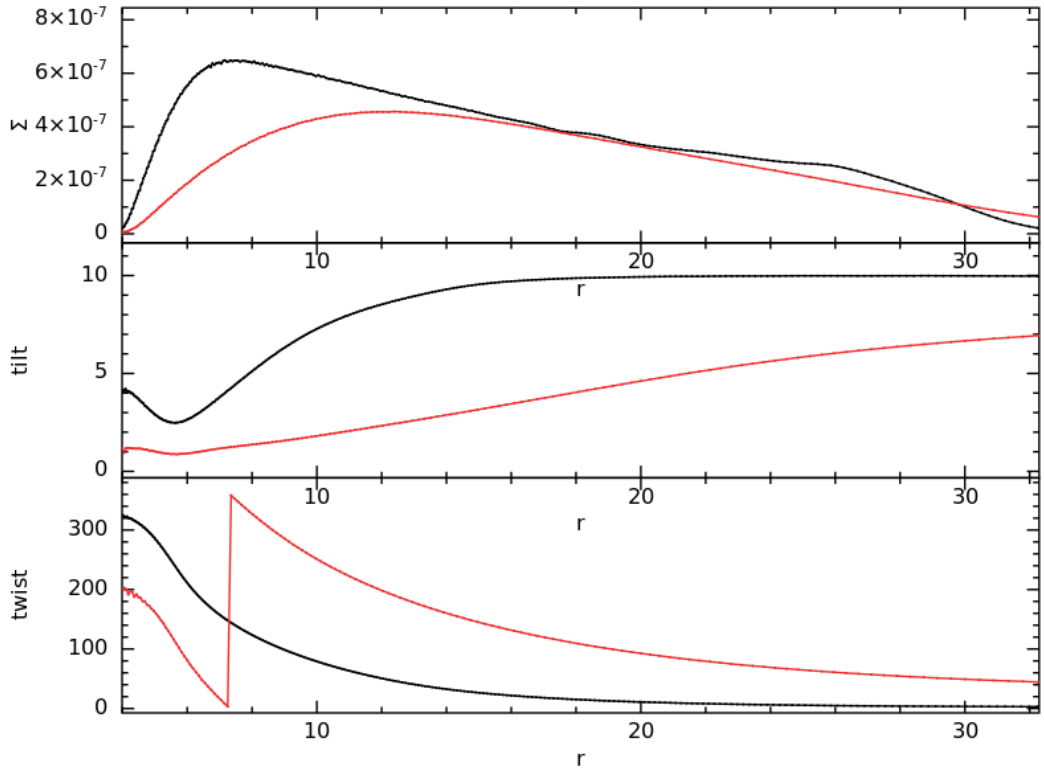

Figure 3.2: The first plot shows the surface density profiles of a disc initially inclined at $10°, \alpha = 0.1$ and $H/R = 0.03$ after 1.4 (black line) and 15.8 orbits (red line) at $R_{\rm out}$. The plots show evidence of disc evolving over time, but there is no evidence of a disc tear. If the disc tears, there will be a clear divide or split in the surface density plot which is not present in this case. The second plot shows how the tilt changes for the same disc setup at 1.4 (black line) and 15.8 (red line) orbits at $R_{\rm out}$. The third plot shows how the corresponding values of the disc's twist behave at times ≈ 1.4 (black line) and 15.8 (red line) orbits at $R_{\rm out}$.

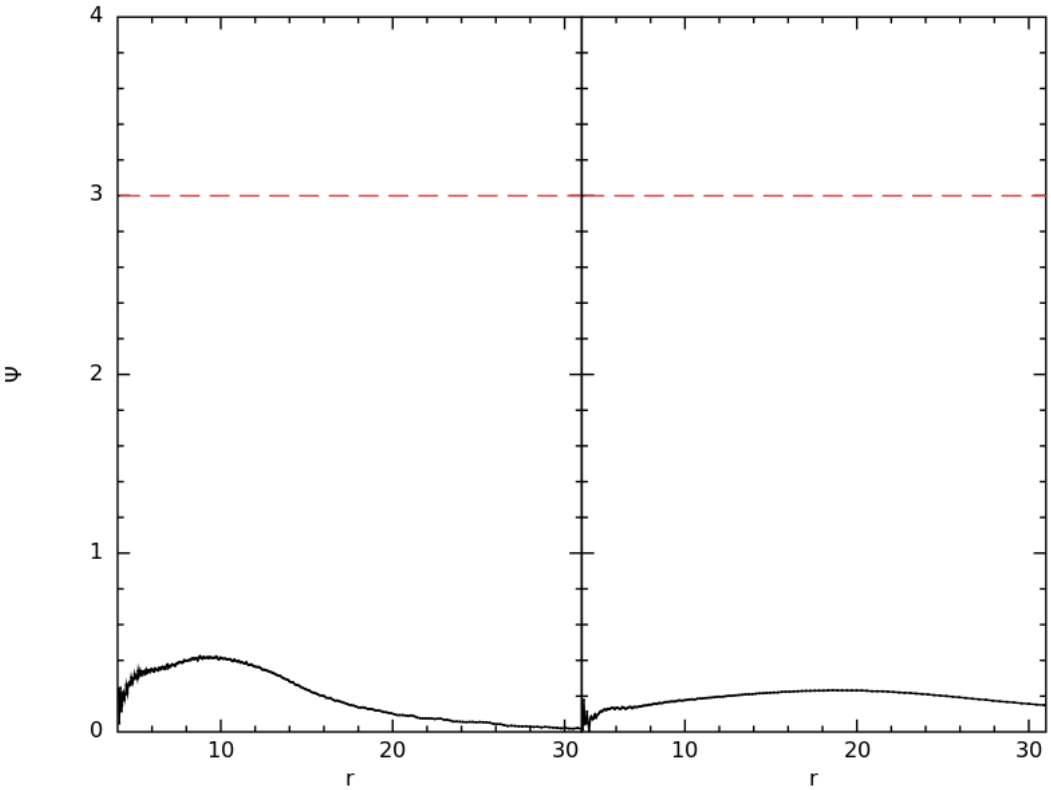

Figure 3.3: The warp amplitude $|\psi|$ of the disc inclined at $10°$, $\alpha = 0.1$ and $H/R = 0.03$ are plotted at times 1.4 and 15.8 orbits at $R_{\rm out}$ respectively. These values of $|\psi|$ are compared to the critical value $|\psi|_c = 3$ (red dashed line). The values of the warp amplitude stay much lower than the minimum value required for instability, proving that this disc remains stable.

The same analysis is studied at different inclinations of $30°, 45°$and $60°$ respectively. Figure 3.4 shows the simulations of a disc inclined at $30°$, $\alpha = 0.1$ and $H/R = 0.03$ at $t = 1485 \approx 1.4$ orbits at $R_{\rm out}$ and $t = 16335 \approx 15.8$ orbits at $R_{\rm out}$. There is no disc tearing at a later time, instead the disc settles in a warped configuration.

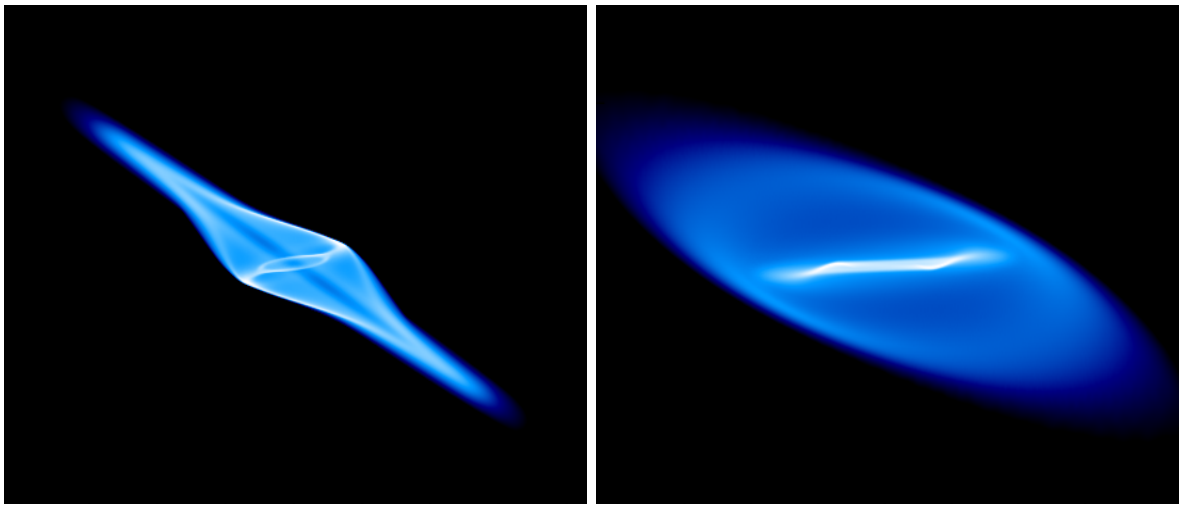

Figure 3.4: 3D simulations of a disc tilted at $30°$, $\alpha = 0.1$ and $H/R = 0.03$ at 1.4 orbits and 15.8 orbits at $R_{\rm out}$.

In addition, various profiles of the disc are also studied as shown in figure 3.5. The first plot shows the surface density profiles after 1.4 (black line) and 15.8 orbits (red line) at $R_{\rm out}$. As inferred from the 3D simulations, the inner part of the disc shows some changes in the surface density but the evidence of disc tear, where $\Sigma = 0$ is not seen. This can be further examined by studying how the tilt varies over time as shown in the second plot of figure 3.5. Once again, it strengthens a conclusion that the disc doesn't become unstable at the later time. The third plot of figure 3.5 also shows how the twist of the disc changes at the two times, demonstrating no disc tear in this setup. These results are extended to examine how the disc's warp amplitude varies over time. Figure 3.6 shows how the warp amplitude values change in the simulations after 1.4 and 15.8 orbits at $R_{\rm out}$.

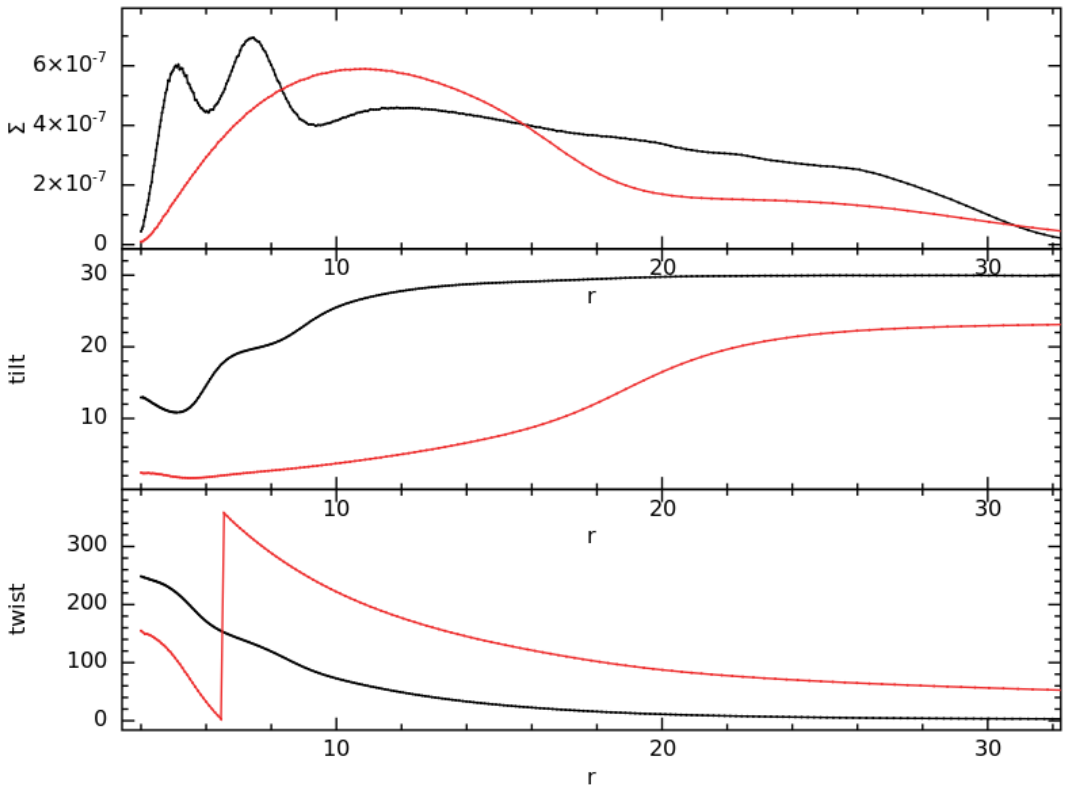

Figure 3.5: The first panel shows the surface density profiles for a disc initially inclined at $30°, \alpha = 0.1$ and $H/R = 0.03$ after 1.4 (black line) and 15.8 orbits (red line) at $R_{\rm out}$. The second plot shows how the tilt changes for the disc setup at 1.4 orbit (black line) and 15.8 orbits (red line) at $R_{\rm out}$. The third panel shows how the corresponding values of the twist of the disc behave at 1.4 (black line) and 15.8 (red line) orbits at $R_{\rm out}$.

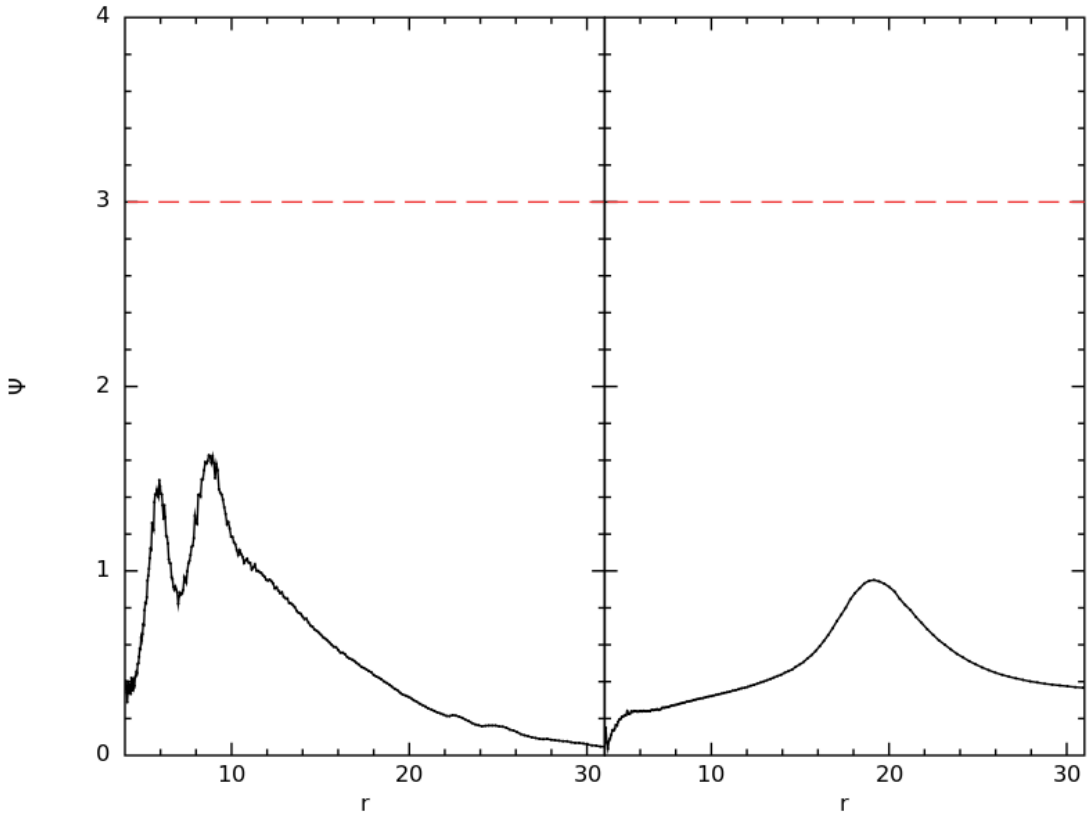

Figure 3.6: The warp amplitude $|\psi|$ of the disc is calculated for a disc inclined at $30°$, $\alpha = 0.1$ and $H/R = 0.03$. The warp amplitude values are compared to the value of critical warp amplitude $|\psi|_c = 3$ (red dashed line). The disc remains stable and doesn't show disc tearing since $|\psi| < |\psi|_c$.

The red dashed line at $|\psi| = 3$ corresponds to the critical warp amplitude of the disc at $\alpha = 0.1$. It clearly shows that the disc doesn't show any instabilities as the values of warp amplitude remain lower than the critical warp amplitude ($|\psi|_c$), hence agreeing with the analysis explained in Doğan et al. (2018).

Furthermore, we extend our analysis and check the same at higher inclinations. Unlike the behaviour of discs inclined at 10° and 30°, the disc shows evidence of breaking in this setup tilted at 45°. Figure 3.7 shows the behaviour of disc initially tilted at 45° with $\alpha = 0.1$ and $H/R = 0.03$ at times $t = 742.5$ and $t = 7425$ which are 0.7 and 7.2 orbits at $R_{\rm out}$ respectively. In the SPH simulations, one can notice the disc forming individual precessing rings at the later time. This is further examined by checking the surface density profiles for the same as shown in the first plot in figure 3.8.

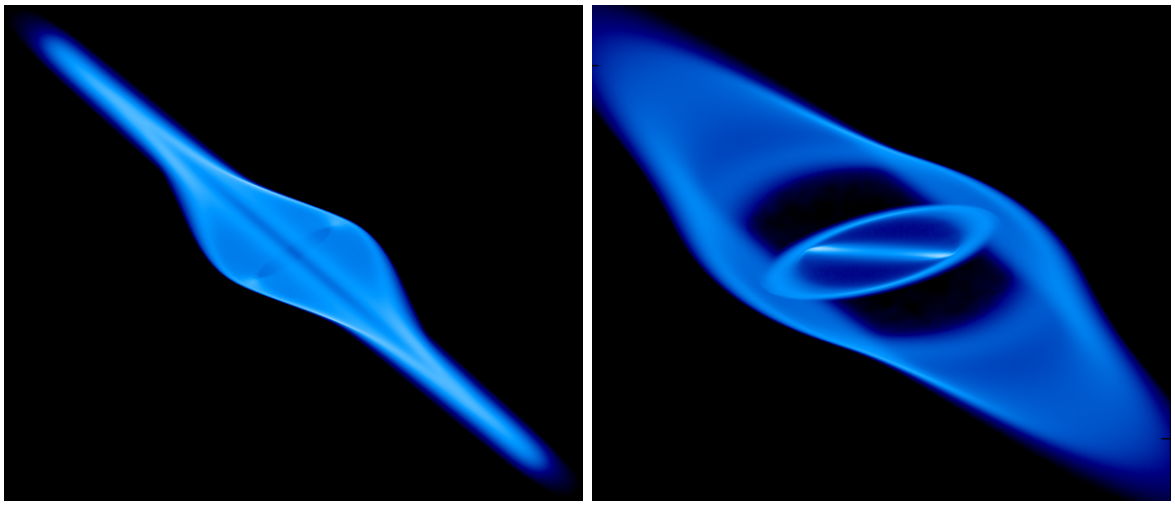

Figure 3.7: 3D column density profiles of the disc inclined at 45°, $\alpha = 0.1$ and $H/R = 0.03$. at t = 0.7 orbit and t = 7.2 orbits at $R_{\rm out}$. This clearly shows the formation of a ring in the disc at a later time.

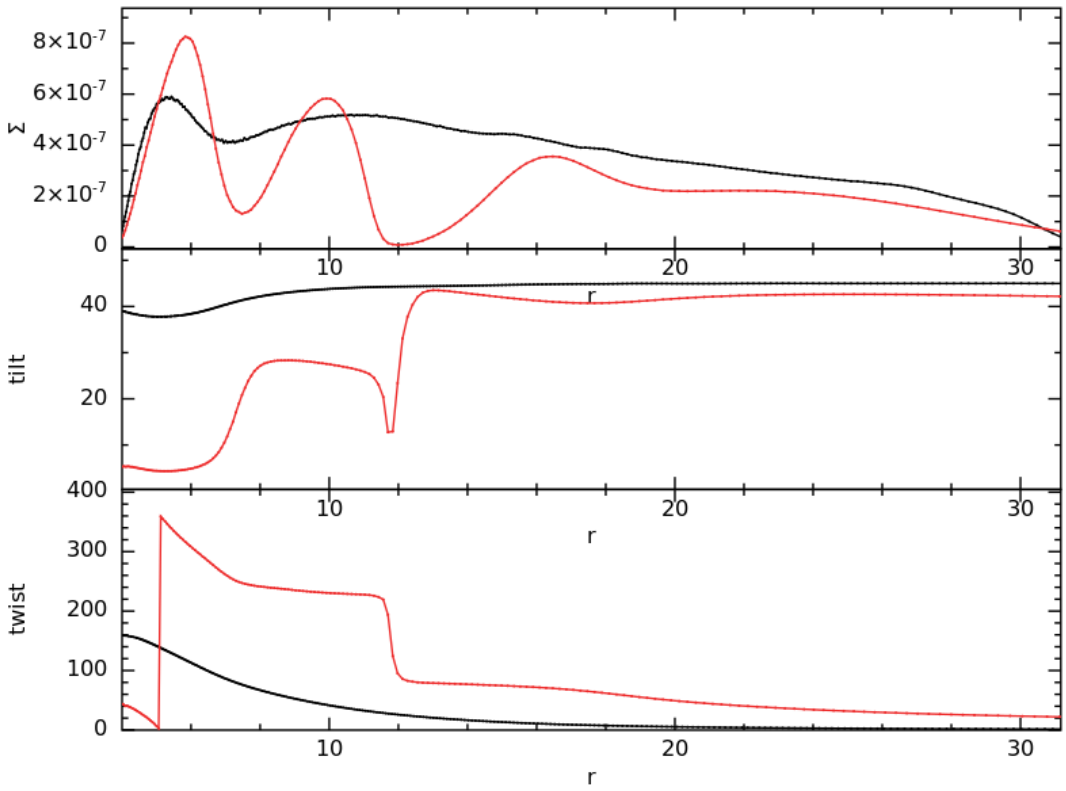

Figure 3.8: The first panel shows the surface density profiles of a disc initially inclined at 45°, $\alpha = 0.1$ and $H/R = 0.03$ after 0.7 (black line) and 7.2 orbits (red line) at $R_{\rm out}$. At $r = 12$, Σ reduces to zero forming a clear split in the surface density profile of the disc thus showing an evidence of disc tear. The second and third plots in the figure show the corresponding changes in the tilt and twist of the disc at 0.7 (black line) and 7.2 (red line) orbits at $R_{\rm out}$.

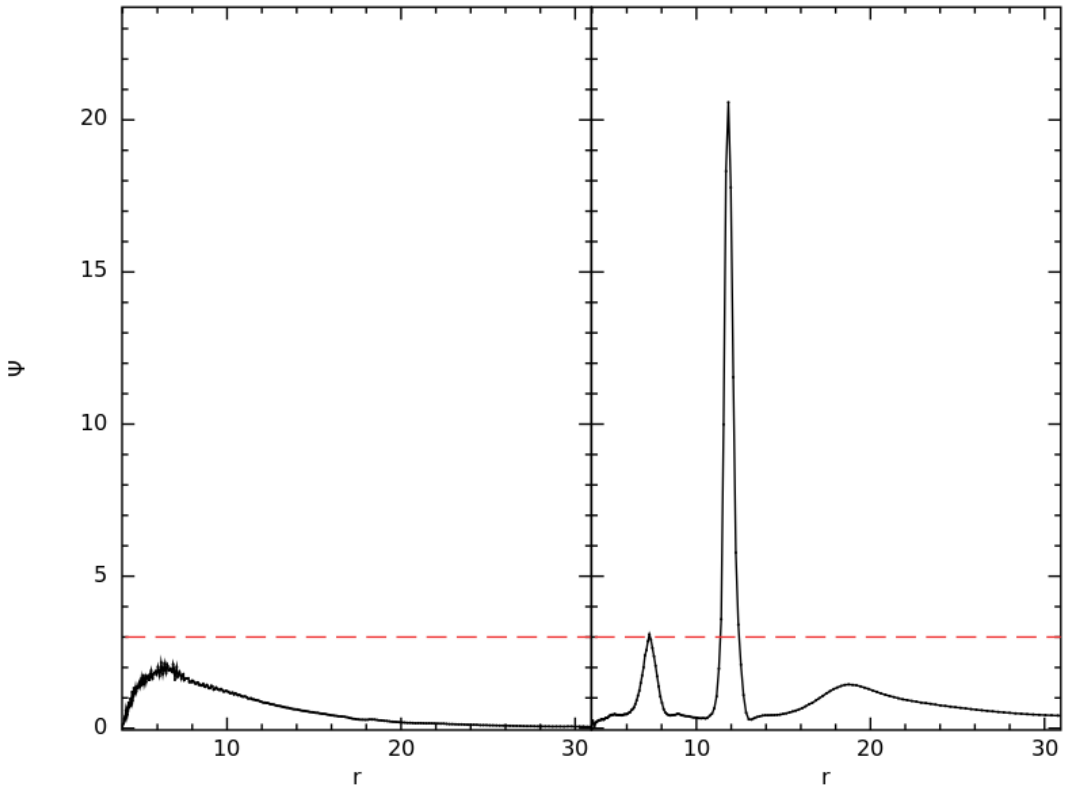

Figure 3.9: This plot explains the comparison of warp amplitude for a disc inclined at 45°, $\alpha = 0.1$ and $H/R = 0.03$ to the critical warp amplitude $|\psi|_c = 3$ (red dashed line) at 0.7 and 7.2 orbits at $R_{\rm out}$. The warp amplitude $|\psi|$ remains lower than $|\psi|_c$ at the initial time, but $|\psi|$ at $r = 12$ peaks up to 7 times the value of $|\psi|_c$ at a later time .

One can observe a drastic decrease in the value of Σ at radius $r = 8$ and Σ dropping to zero at radius $r = 12$ which denotes where the disc tears. This can be further investigated by studying the change in the tilt of the disc as shown in the second panel of figure 3.8. A possibility of disc tear is seen as the disc's tilt drops at $r = 12$. The corresponding change in the twist of the disc is also examined and the presence of an individually precessing ring is spotted at $r = 12$. Furthermore, we must check if the warp amplitude of this disc setup at $r = 12$ exceeds its critical value.

The stability analysis of this disc setup is studied by examining the change in its warp amplitude. The warp amplitude of the disc at $t = 0.7$ orbit and $t = 7.2$ orbits at R_{out} is shown in figure 3.9. It can be clearly noted that the warp amplitude at $r = 12$ is much larger than the critical warp amplitude, $|\psi|_c = 3$. This proves that the disc becomes unstable and tears into concentric rings when $|\psi| > |\psi|_c$.

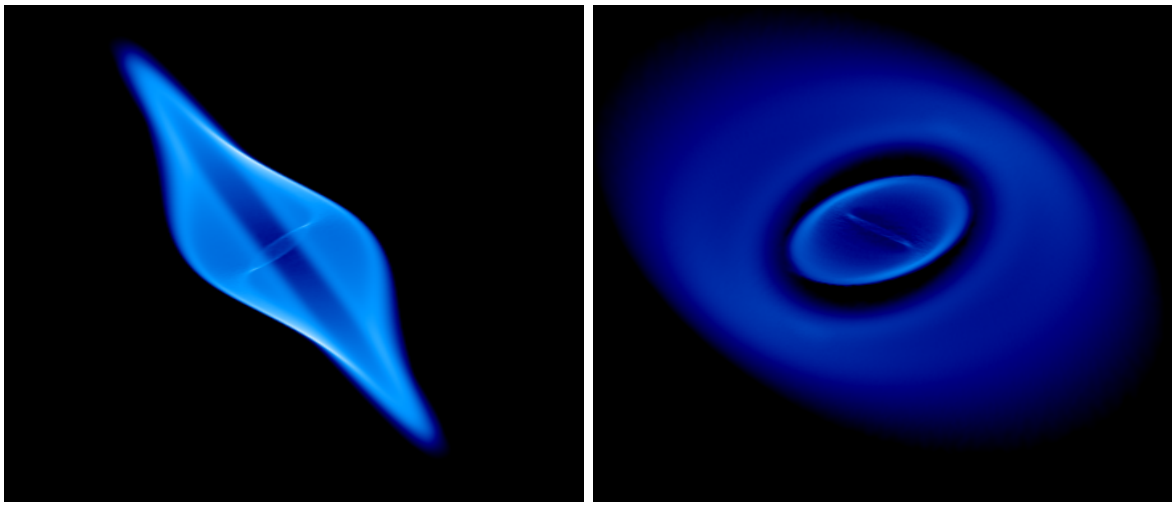

Figure 3.10: 3D simulations of a disc inclined at 60°, $\alpha = 0.1$ and $H/R = 0.03$. at times t = 2 orbits and t = 21 orbits at R_{out} is shown.

Furthermore, we check the same for a disc tilted at 60° as shown in figure 3.10. The 3D simulations for a disc tilted at 60° is examined at times $t = 2227.5 \approx 2$ orbits and $t = 22275 \approx 21.5$ orbits at R_{out}. These simulations show an evidence of tearing at the later time. In addition, we examine the surface density profiles for the same as shown in the first plot of figure 3.11. One can observe a drastic decrease in the value of Σ, dropping

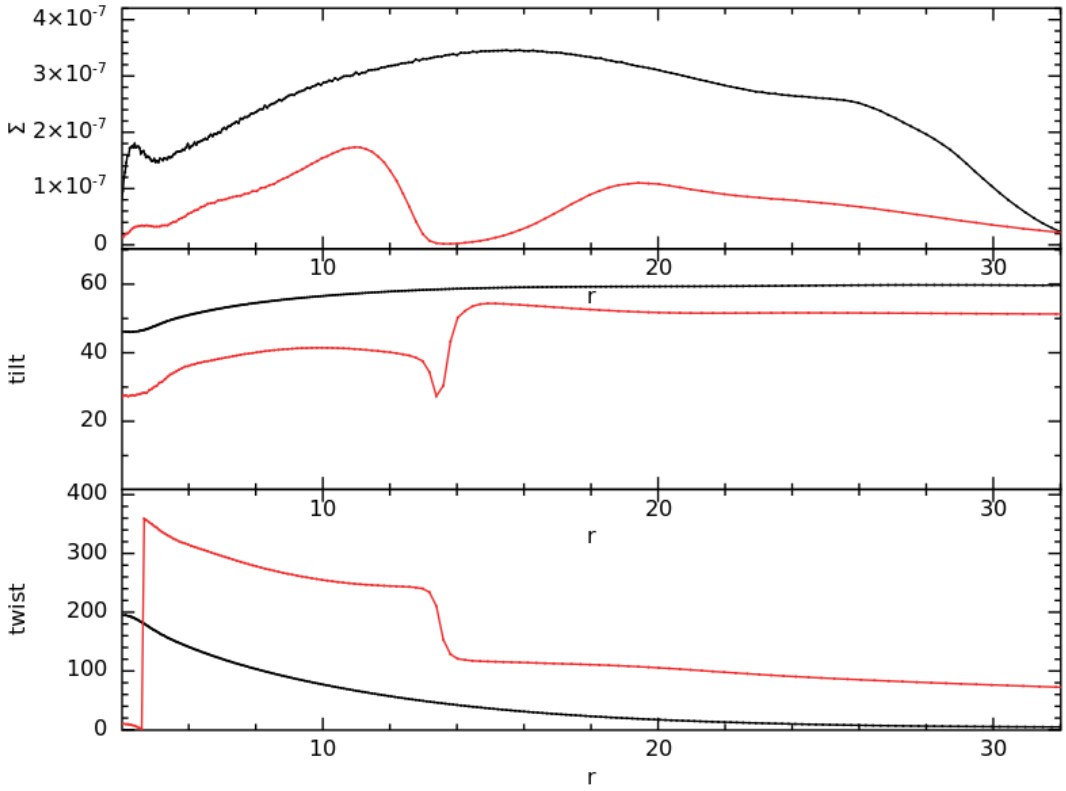

Figure 3.11: The first plot shows the surface density profiles for a disc initially inclined at $60°, \alpha = 0.1$ and $H/R = 0.03$ after 2 (black line) and 21.5 orbits (red line) at R_{out}. A clear divide in the surface density profile is seen at $r = 14$. The second and third panels show how the tilt and the twist of the disc change for the same disc setup at 2 (black line) and 21.5 (red line) orbits at R_{out}. The tilt and the twist plots show a discontinuity at $r = 14$ which locates the point of disc tear.

to zero at radius $r = 14$. Disc tearing can be further investigated by studying the change in the tilt of the disc as shown in the second plot of figure 3.11. Similarly, an analogous change in the twist is examined in the last panel of figure 3.11. These plots confirm the possibility of a tear in the disc at $r = 14$. We also check if the warp amplitude for this disc setup exceeds the critical warp amplitude at the estimated point of disc tear at $r = 14$.

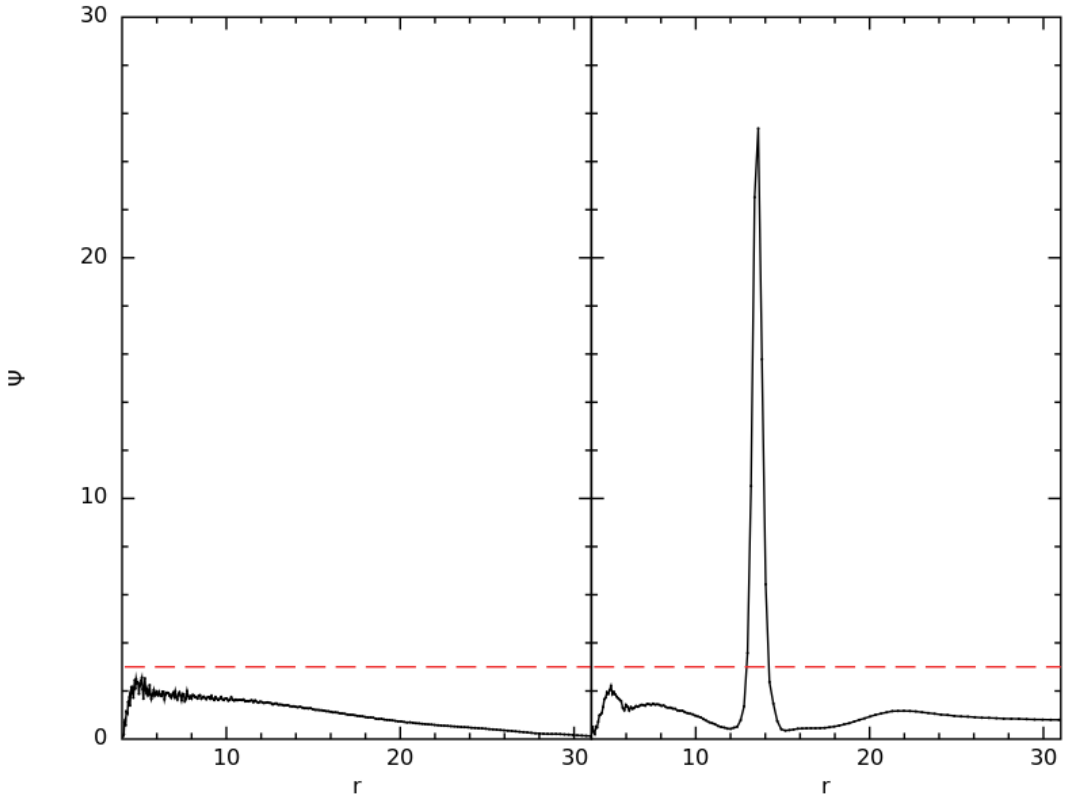

Figure 3.12: The warp amplitude is calculated for a disc inclined at 60°, with $\alpha = 0.1$ and $H/R = 0.03$. These values are compared to the critical warp amplitude $|\psi|_c = 3$ (red dashed line) at 2 orbits and 21 orbits at $R_{\rm out}$. At the initial time, we note that $|\psi| < |\psi|_c$. On the other hand, at a later time the warp amplitude $|\psi|$ exceeds to ≈ 7 times $|\psi|_c$ at $r = 14$.

From figure 3.12, it is shown at a later time that the warp amplitude of the disc, $\psi \approx 25$ at $r = 14$, much larger than the value of critical warp amplitude at $|\psi|_c = 3$. Therefore, this setup demonstrate that a highly inclined disc becomes unstable and tears to form rings when its warp amplitude $|\psi| > |\psi|_c$, thus agreeing with the predicted analysis of Doğan et al. (2018).

3.4 Effect of α_{AV} on $|\psi|_c$

The instability criterion predicted by Doğan et al. (2018) to check the possibility of disc tearing is further examined in thinner and unstable discs at smaller values of H/R and α. Even for discs composed of 10 million particles, one must consider the effect of artificial viscosity since the value of $\langle h \rangle / H$ for a disc at a smaller H/R, contributes to an increase in the value of artificial viscosity α_{AV}. Therefore in our numerical analysis, the criterion for

thinner discs to become unstable is estimated at the critical warp amplitude $|\psi|_c$, which corresponds to a value of α given by the sum of the physical and artificial viscosities.

Initially, we examine the parameter study of a thin disc with $H/R = 0.01$. Discs are studied at different inclinations and the criterion for discs to tear is examined in each case. The possibility of disc tearing in each disc setup is examined from the change in the disc's warp amplitude in comparison to its critical value. In the numerical analysis of thinner discs at $H/R = 0.01$, we use the value of $|\psi|_c$ corresponding to an α value inclusive of the artificial viscosity [2].

First, let us consider a disc comprising 10 million particles, at $\alpha = 0.1$, $H/R = 0.01$ and initially inclined at 10°. Figure 3.13 shows the SPH simulations of this disc at $t = 1485 = 1.4$ orbits and $t = 31185 = 30$ orbits at $R_{\rm out}$. At a later time, there is no evidence of a disc tear and instead the disc settles into a warped configuration. The surface density, tilt and twist profiles of the disc at 1.4 orbits (black line) and 30 orbits (red line) are shown in figure 3.14. These results agree with the 3D simulations, and show no evidence of a disc tear.

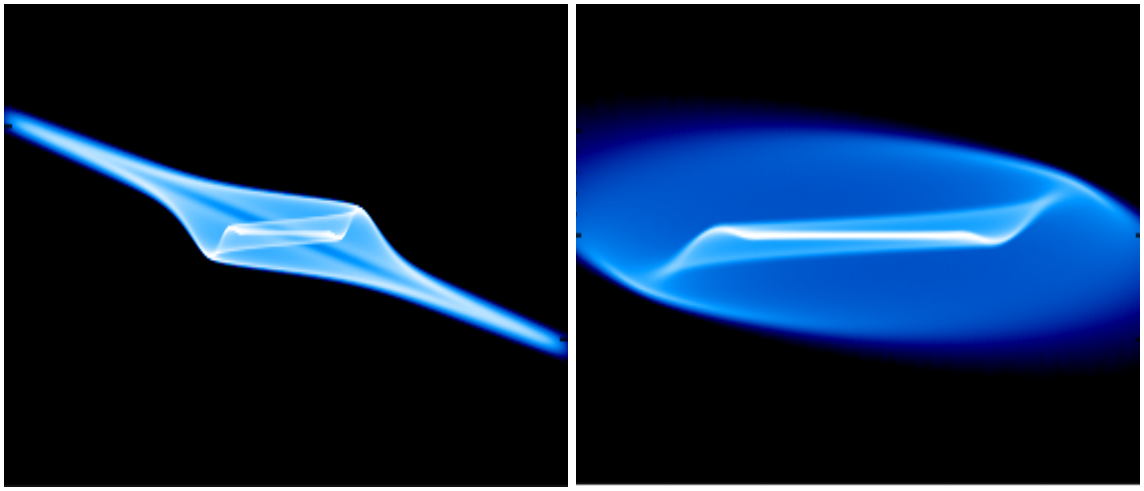

Figure 3.13: 3D simulations of a disc tilted at 10°, $\alpha = 0.1$ and $H/R = 0.01$ at times $t = 1.4$ and $t = 30$ orbits at $R_{\rm out}$ is shown.

[2]The artificial viscosity in SPH calculations is controlled by the linear term $\alpha_{\rm SPH}$ which accounts for the viscosity that dissipates kinetic energy to reduce particle oscillation as particles approach each other. This contribution of the linear term in the artificial viscosity can be compared to the Shakura-Sunyaev viscosity (Meru & Bate, 2012) as $\alpha_{\rm SS,lin} = \frac{31}{525}\alpha_{\rm SPH}\frac{\langle h\rangle}{H}$.

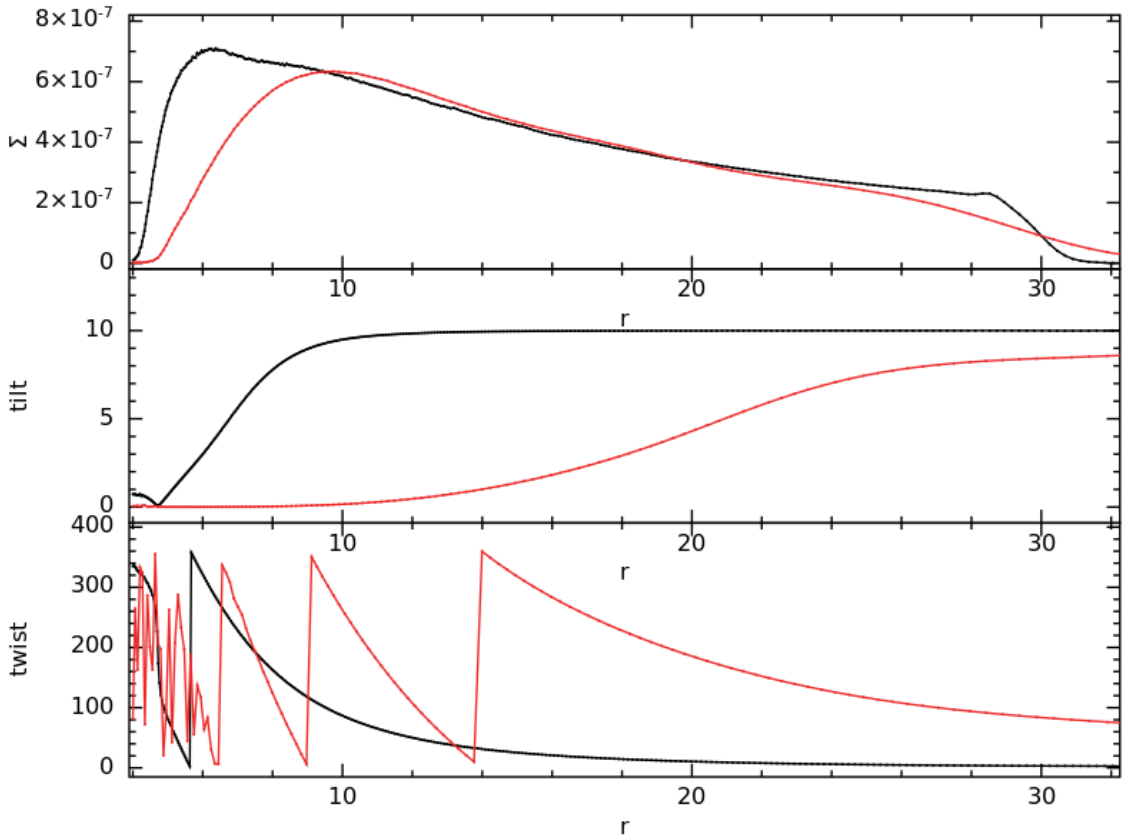

Figure 3.14: The first plot shows the surface density profiles of a disc initially inclined at $10°, \alpha = 0.1$ and $H/R = 0.01$ at 1.4 (black line) and 30 orbits (red line) at $R_{\rm out}$. It shows no split in the surface density at the two times where Σ reduces to zero. The second plot shows how the tilt changes for the same disc setup at 1.4 (black line) and 30 (red line) orbits at $R_{\rm out}$. The third plot shows the corresponding change in the twist of the disc. The plots shows how disc evolves over time, but there is no evidence of a disc tear.

In addition, we examine the artificial viscosity in this disc setup and check if it is smaller or comparable to the value of the physical viscosity $\alpha_{SS} = 0.1$. If the artificial viscosity (α_{AV}) is less than α_{SS}, we can ignore α_{AV} and assume $\alpha \approx \alpha_{SS}$. On the other hand if the value of α_{AV} is comparable to the value of α_{SS}, the total value of $\alpha = \alpha_{SS} + \alpha_{AV}$. The values of numerical viscosity for this disc lie between 0.03 and 0.05 (as shown in fig. 3.15) which gives a mean value of 0.04, lesser than $\alpha_{SS} = 0.1$. Hence, the effect of artificial viscosity is ignored for this disc and we consider the critical warp amplitude $|\psi|_c = 3$ corresponding to $\alpha = 0.1$.

The change of warp amplitude in the simulation at t = 1.4 and 30 orbits at $R_{\rm out}$ is examined as shown in figure 3.16. The results show that the values of ψ are smaller than $|\psi|_c$ at both times. This agrees well with the predicted analysis that the disc does

not tear until its warp amplitude exceeds the critical value. The same analysis can be extended to discs at higher inclinations of $30°, 45°$ and $60°$ respectively.

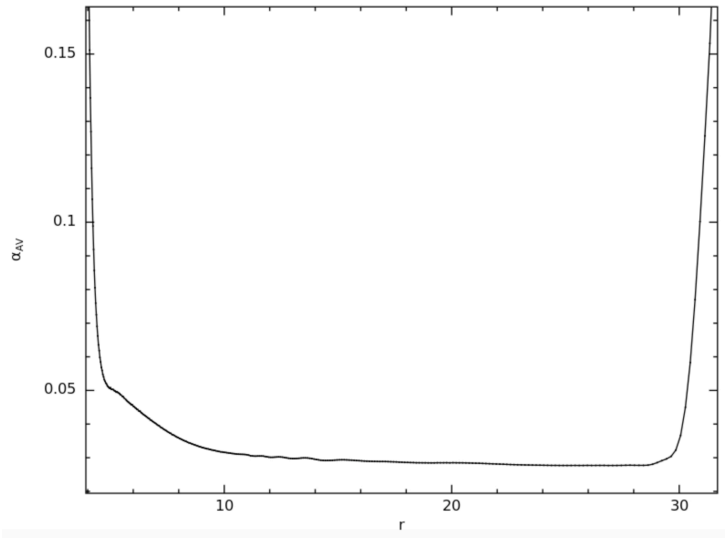

Figure 3.15: The artificial viscosity is calculated and plotted for a disc inclined at $10°$, $\alpha = 0.1$ and $H/R = 0.01$. The value of $\alpha_{AV} \sim 0.03 - 0.05$ as shown in this plot.

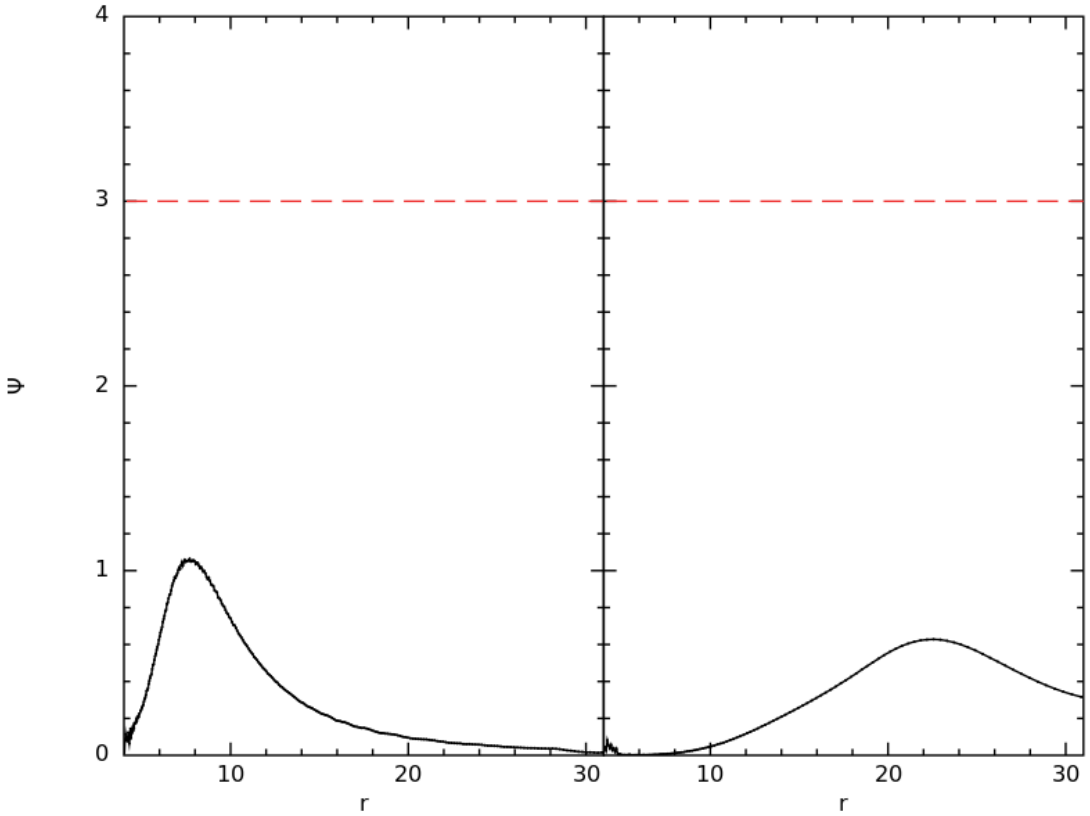

Figure 3.16: The warp amplitude of the disc is calculated after 1.4 orbits (left) and 30 orbits (right) at R_{out}. It is then compared to the critical warp amplitude $|\psi|_c = 3$ denoted by the red dashed line. The disc remains stable and does not show disc tearing since $|\psi| < |\psi|_c$ throughout.

The same disc setup at an inclination of $30°$ is examined. Figure 3.17 shows the

3D simulation of this disc at $t = 742.5$ and $t = 7425$ which are 0.7 and 7.2 orbits at $R_{\rm out}$ respectively. It clearly shows an evidence of disc tearing at the later time. This is established further by checking the surface density profiles as shown in the first plot of figure 3.18 . Tearing of the disc is observed at radii $r = 9$ and 11, where the values of Σ reduce to zero. Similarly, the tilt and the twist of the disc are studied as shown in the second and third plots in figure 3.18. Just as observed from the surface density profiles, one can also notice the changes in the tilt and twist of the disc at $r = 9$ and 11 which show an indication of disc tearing. Furthermore, these results are compared to the analysis from Doğan et al. (2018) by studying the changes in the disc's warp amplitude.

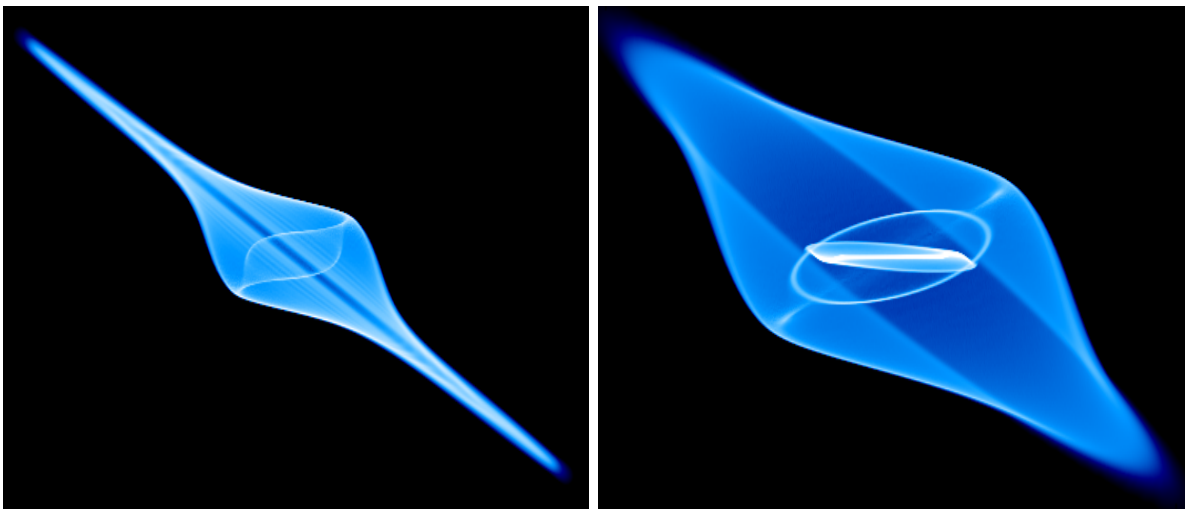

Figure 3.17: 3D column density plots for a disc inclined at 30°, $\alpha = 0.1$ and $H/R = 0.01$ at 0.7 and 7.2 orbits at R_{out} is shown.

The value of the artificial viscosity for this disc setup is calculated and as shown in figure 3.19, α_{AV} lies around 0.08 which is comparable to the value of the physical viscosity at 0.1. Hence, the total value of $\alpha = 0.18$ $(\alpha_{SS} + \alpha_{AV})$ is used to find the corresponding value of critical warp amplitude to examine the instability criterion of the disc.

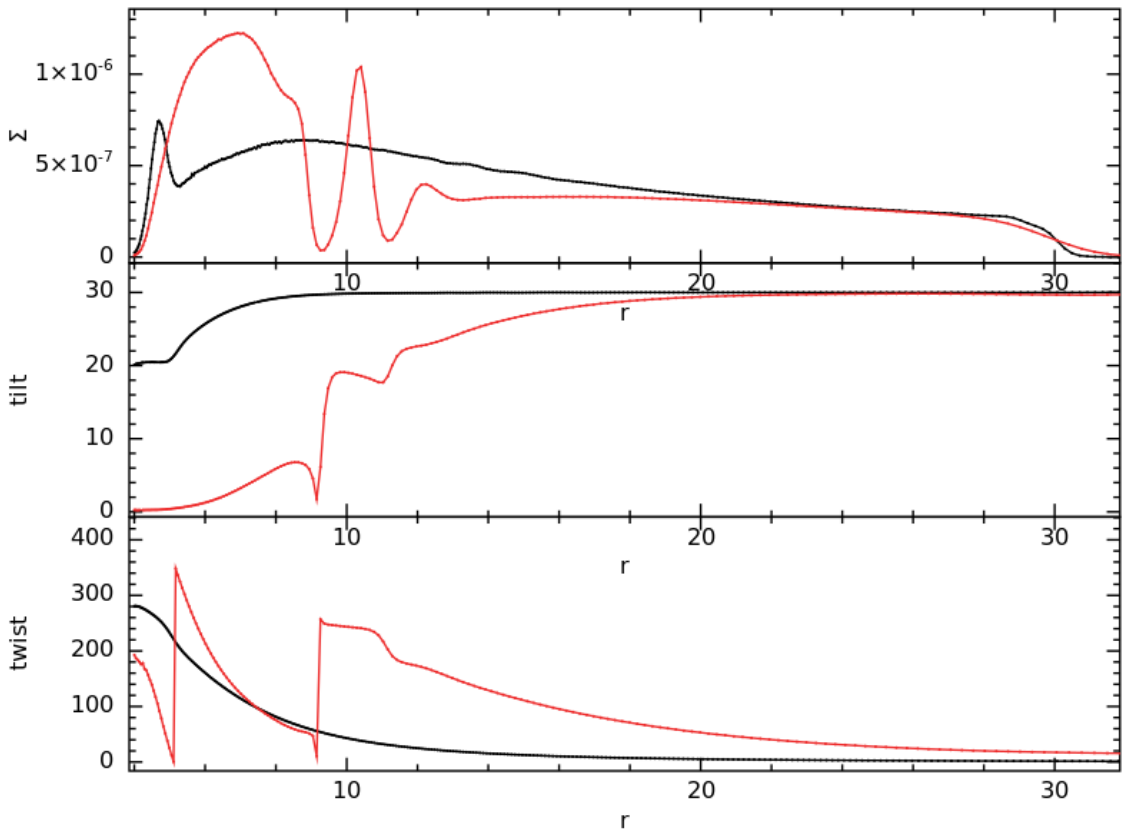

Figure 3.18: The first plot shows the surface density profiles for a disc initially inclined at $30°, \alpha = 0.1$ and $H/R = 0.01$ after 0.7 (black line) and 7.2 orbits (red line) at $R_{\rm out}$. There are two points at $r = 9$ and $r = 11$, where the surface density Σ drops to almost zero which marks where the disc breaks. The second figure shows the corresponding change in the tilt of the disc at 0.7 (black line) and 7.2 (red line) orbits at $R_{\rm out}$. The third figure shows how the twist of the disc at 0.7 (black line) and 7.2 (red line) orbits at $R_{\rm out}$. As mentioned in the surface density profiles, the tilt and the twist values also show a break at $r = 9$ and $r = 11$.

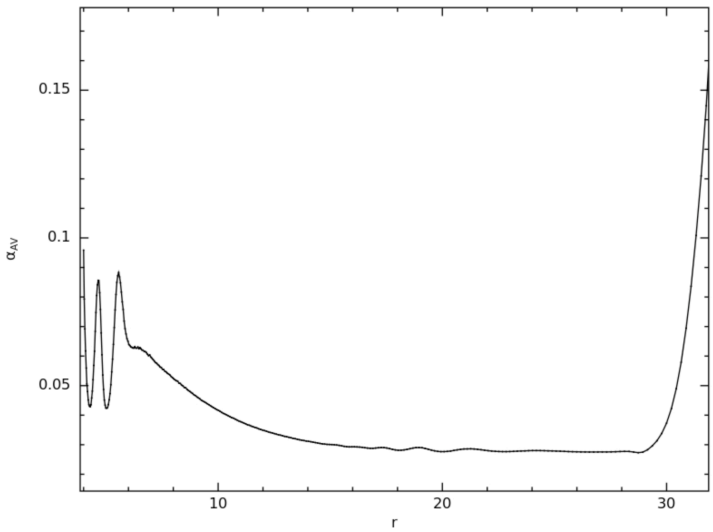

Figure 3.19: The artificial viscosity of the disc inclined at $30°, \alpha = 0.1$ and $H/R = 0.01$ is calculated and is found to lie between 0.05 and 0.1 thus giving an average value of $\alpha_{AV} = 0.08$.

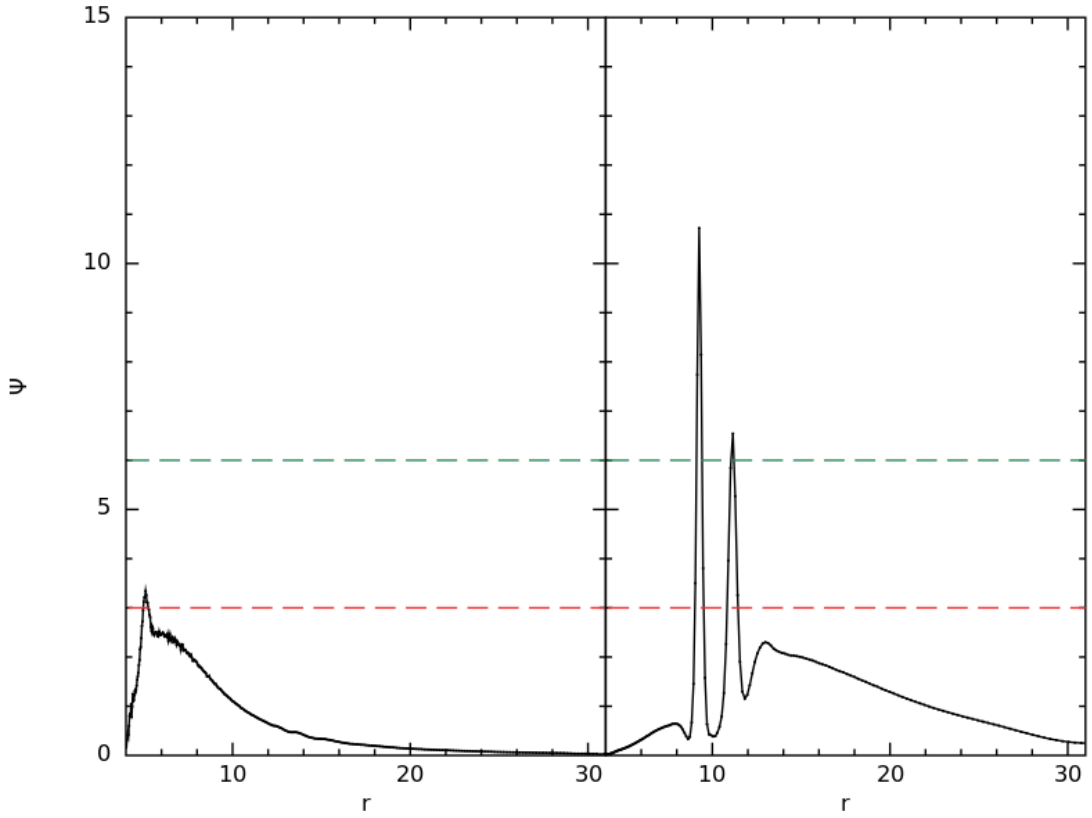

Figure 3.20: The warp amplitude $|\psi|$ of the disc is calculated and compared to the critical warp amplitude $|\psi|_c = 3$ (red dashed line) and the critical warp amplitude $|\psi|_c = 6$ corresponding to α inclusive of artificial viscosity. At a later time, the disc shows instabilities at $r = 9$ and 11 where the warp amplitude values $|\psi| > |\psi|_c$ which confirms where the individual rings are formed in the disc.

In figure 3.20, the warp amplitude of the disc is studied at t = 0.7 orbits and t = 7.2 orbits at R_{out} where we compare and check how the warp amplitude changes in comparison to the critical warp amplitude $|\psi|_c$. The figure shows a red dashed line that corresponds to $|\psi|_c = 3$ for $\alpha = 0.1$ (without the artificial viscosity) and the green dashed line at $|\psi|_c = 6$ for $\alpha = 0.18$ (with the artificial viscosity). The figure clearly shows that $|\psi|$ values at radii $r = 9$ and 11 exceed $|\psi|_c = 6$ at the later time, thus demonstrating where the disc tears.

Furthermore, we check how the disc behaves when inclined at 45°. Figure 3.21 shows the 3D simulations of a disc inclined at 45°, at times t = 742.5 = 0.7 orbit and t = 7425 = 7.2 orbits at R_{out}. The simulation at a later time clearly shows an evidence of disc tear. This can be investigated from the change of surface density, tilt and twist of the disc as shown in figure 3.22. The three profiles find the possibility of disc tearing at radii,

$r = 7$ and $r = 10$.

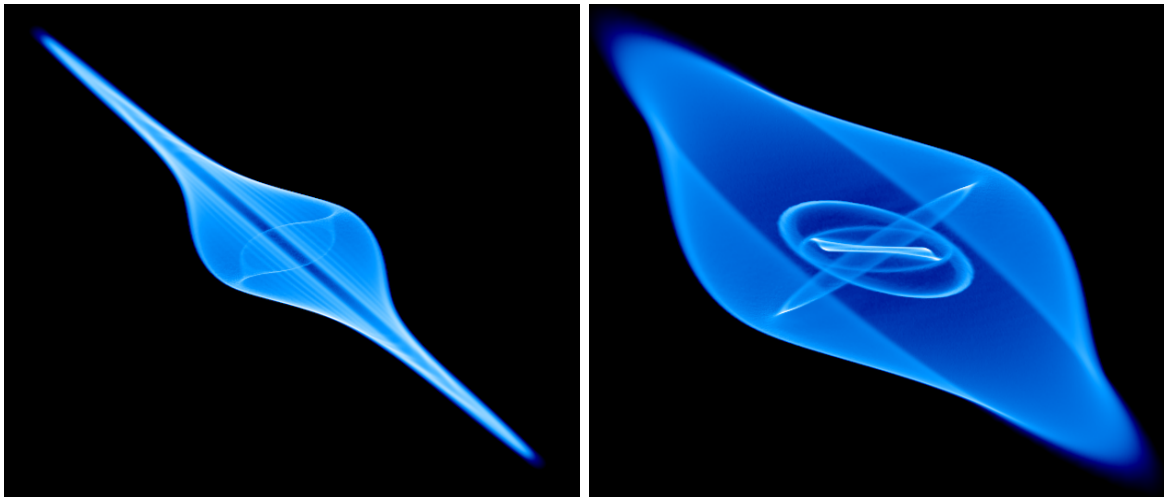

Figure 3.21: 3D simulations of a disc inclined at 45°, $\alpha = 0.1$ and $H/R = 0.01$ at 0.7 and 7.2 orbits at R_{out}.

As shown in figure 3.23, the artificial viscosity is calculated and α_{AV} lies between 0.05 and 0.13, which gives an average value of 0.09 comparable to the physical viscosity at $\alpha = 0.1$. Therefore, we consider the total value of $\alpha = 0.19$ ($\alpha_{SS} + \alpha_{AV}$) in this disc setup. The value of critical warp amplitude corresponding to $\alpha = 0.19$ is $|\psi|_c = 8$. Thus, the warp amplitude of the disc is calculated at $t = 0.7$ (black line) and 7.2 (red line) orbits at $R_{\rm out}$ as shown in figure 3.24. The figure shows the red dashed line at $|\psi|_c = 3$ for $\alpha = 0.1$ (without the artificial viscosity) and the green dashed line at $|\psi|_c = 8$ corresponds to $\alpha = 0.19$ (inclusive of α_{AV}). The $|\psi|$ values at radii r = 7 and 10 exceed $|\psi|_c$ at a later time, thus agreeing with the disc's predicted criterion to become unstable.

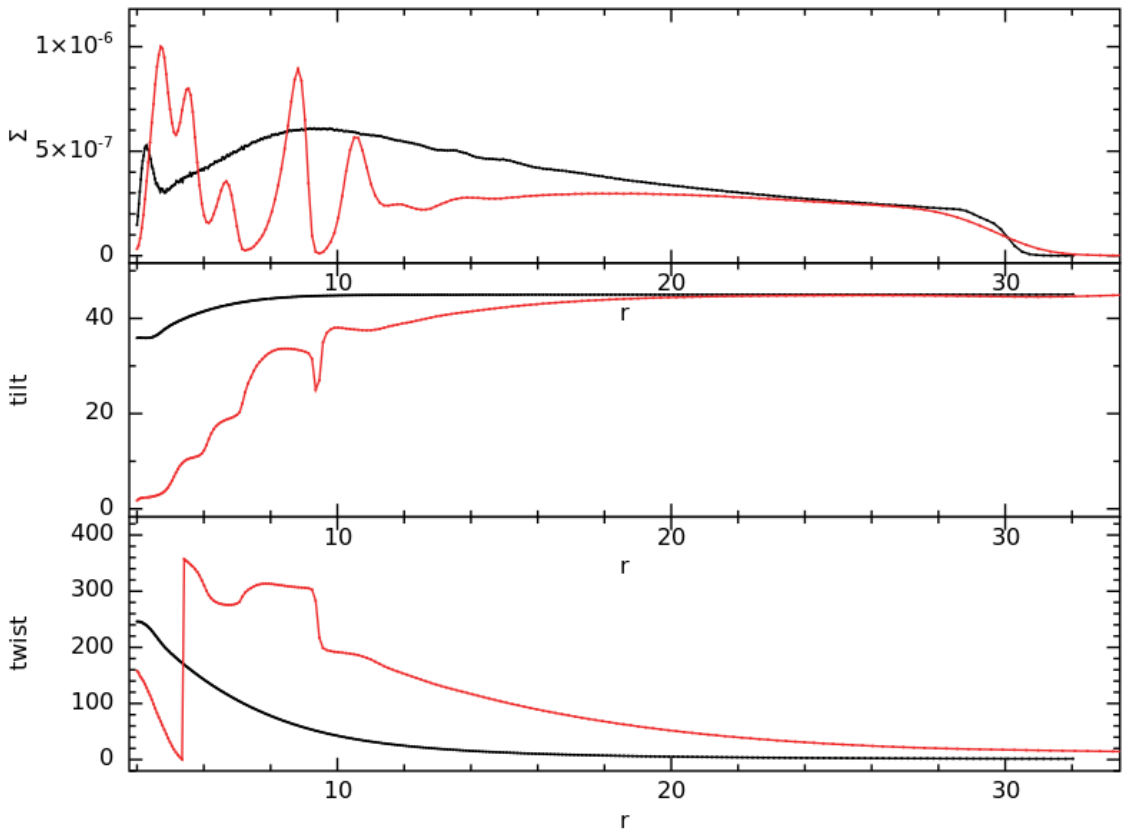

Figure 3.22: The first plot demonstrates the surface density profiles for a disc initially inclined at $45°, \alpha = 0.1$ and $H/R = 0.01$ after 0.7 (black line) and 7.2 orbits (red line) at $R_{\rm out}$. The surface density at $r = 7$ and $r = 10$ drops to zero denoting where the disc breaking occurs. The second plot shows the change in the tilt of the disc at 0.7 (black line) and 7.2 (red line) orbits at $R_{\rm out}$. The third figure shows how the twist of the disc at 0.7 (black line) and 7.2 (red line) orbits at $R_{\rm out}$. Similar to the surface density profiles, the tilt and the twist values also show a break at $r = 7$ and $r = 10$ symbolising individually precessing rings.

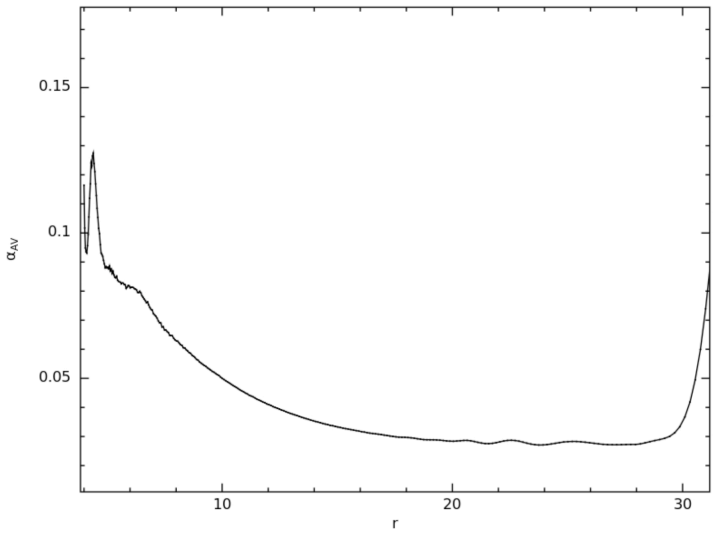

Figure 3.23: The artificial viscosity of the disc inclined at $45°, \alpha = 0.1$ and $H/R = 0.01$ is plotted as shown. The values lie between 0.05 and 0.13, which gives a mean value of 0.09.

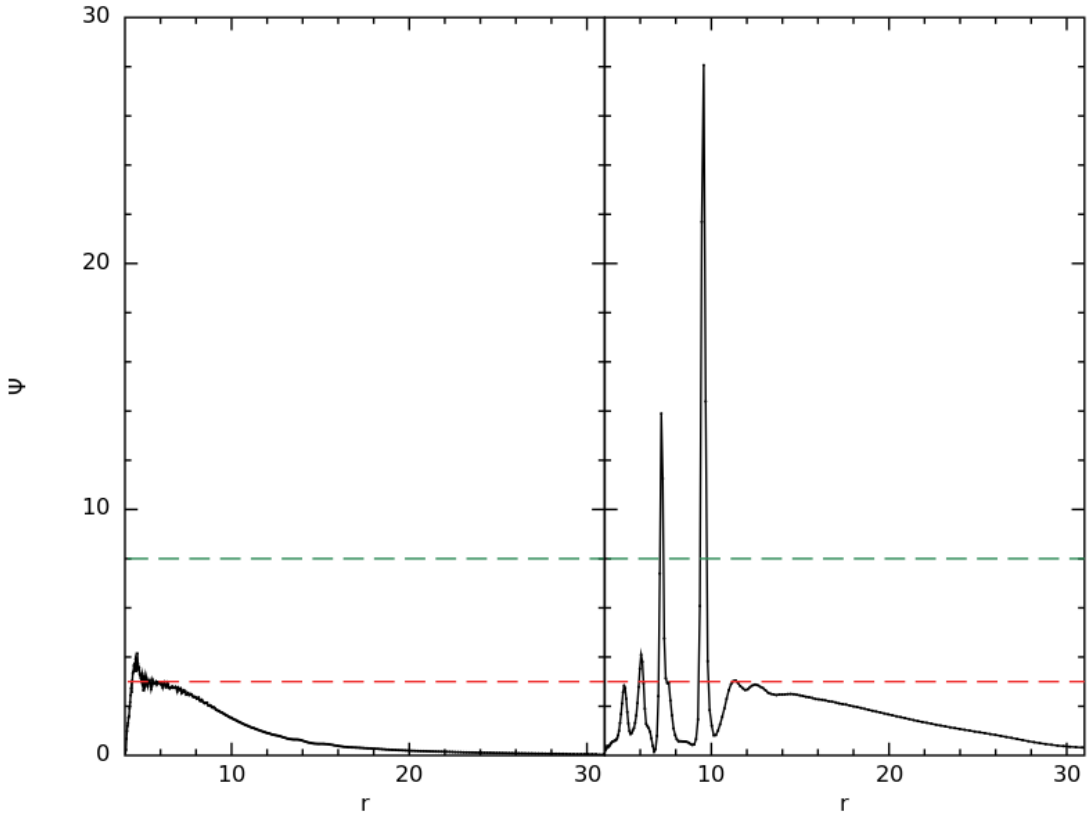

Figure 3.24: The warp amplitude $|\psi|$ of the disc is calculated and checked with the critical warp amplitude values corresponding to α values with and without adding the artificial viscosity. The red dashed line denotes the critical warp amplitude $|\psi|_c = 3$ for $\alpha = 0.1$ and the green dashed line denotes the critical warp amplitude $|\psi|_c = 8$ corresponding to α inclusive of artificial viscosity. At a later time, the disc shows instabilities at $r = 7$ and 10 where the warp amplitude values $|\psi| > |\psi|_c$ which confirms the point where individual rings are formed.

Finally, we examine how the disc behaves at an inclination of 60°. The 3D simulations of the disc is examined at $t = 742.5$ and 7425 which are 0.7 orbits and 7.2 orbits at R_{out} as shown in figure 3.25. The disc tears and forms individual rings at a later time. In addition, the possibility of disc tear is also demonstrated in the surface density profiles at the same times, as shown in the first plot of figure 3.26. The surface density profile shows disc tearing at $r = 8$ and 11. The variation of the disc tilt and twist, given by the second and third plots of figure 3.26 also agree well with the surface density profiles. The tilt and twist profiles of the disc breaks at radii $r = 8$ and 11 indicating the points of tearing in the disc. The criterion of disc tear is examined by checking the changes in the warp amplitude of the disc at the two times.

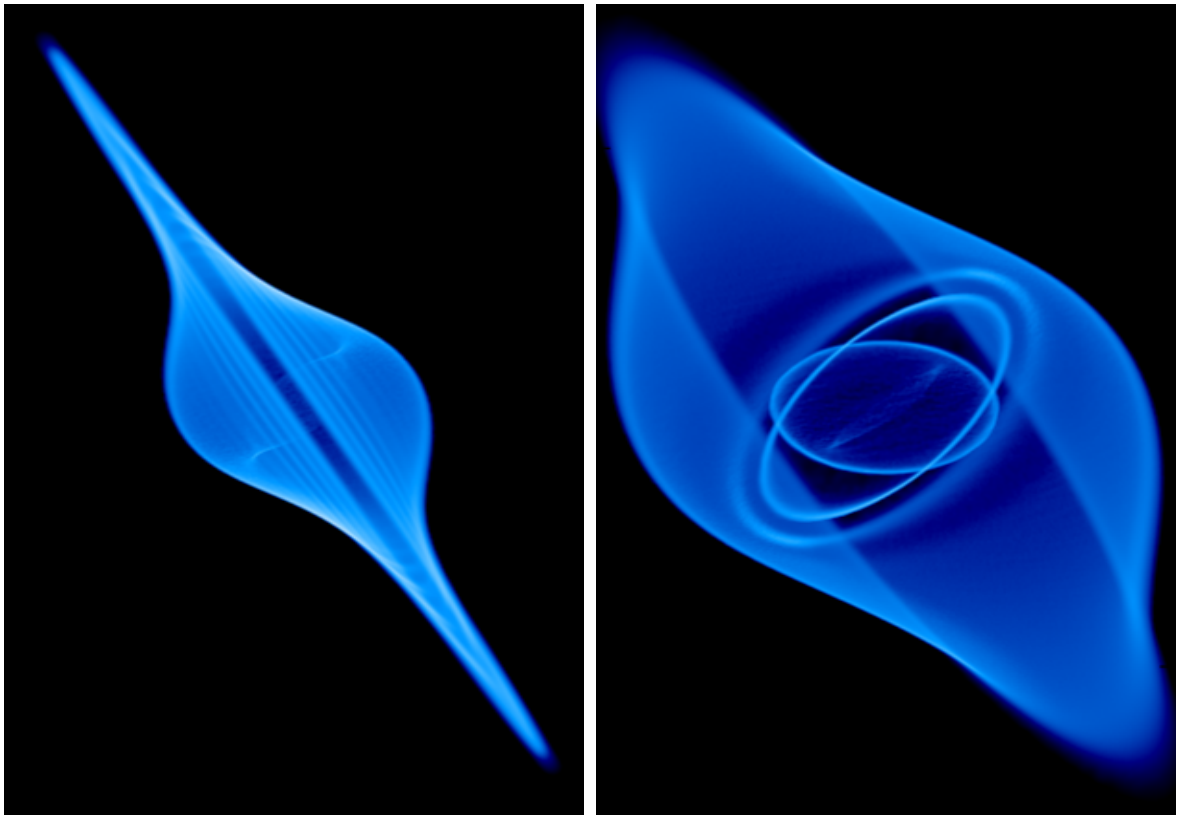

Figure 3.25: 3D simulations of a disc inclined at 60°, $\alpha = 0.1$ and $H/R = 0.01$ at 0.7 and 7.2 orbits at R_{out}.

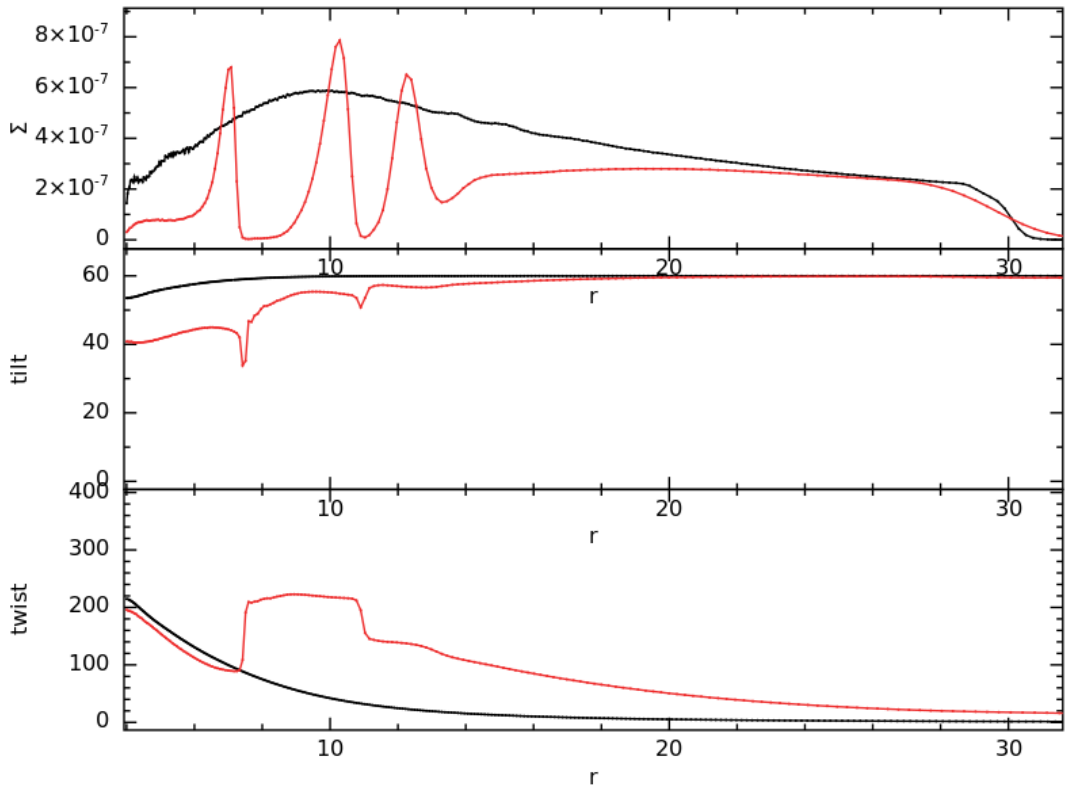

Figure 3.26: The surface density profiles for a disc initially inclined at 60°, $\alpha = 0.1$ and $H/R = 0.01$ after 0.7 (black line) and 7.2 orbits (red line) at $R_{\rm out}$ is shown in the first figure. The surface density at $r = 8$ and $r = 11$ drops to zero where the disc tears. The second figure shows the change in the tilt of the disc at 0.7 (black line) and 7.2 (red line) orbits at $R_{\rm out}$. The third figure shows how the twist of the disc at 0.7 (black line) and 7.2 (red line) orbits at $R_{\rm out}$. The tilt and the twist values of the disc also indicate a clear evidence of disc tear at $r = 8$ and $r = 11$.

The artificial viscosity calculated for this disc has a mean value of $\alpha_{AV} = 0.09$ as shown in figure 3.27. This value is comparable to the physical viscosity $\alpha = 0.1$ that gives a total value of $\alpha = 0.19$. The critical warp amplitude is $|\psi|_c = 8$ for $\alpha = 0.19$. The variation of warp amplitude is studied at times $t = 0.7$ and 7.2 orbits at $R_{\rm out}$ as shown in figure 3.28. The red dashed line at $|\psi|_c = 3$ corresponds to $\alpha = 0.1$ and the green dashed line at $|\psi|_c = 8$ matches with $\alpha = 0.19$ inclusive of α_{AV}. At radii r = 8 and 11, the values of $|\psi|$ are much higher than $|\psi|_c$. At a later time, an instability growing at radii between $r = 12$ and 14 exceeds $|\psi|_c = 3$ (red dashed line) but remains less than $|\psi|_c = 8$ (green dashed line). This indicates the forming of a ring in the disc which is not fully broken until its value of $|\psi|$ exceeds the critical value required for instability.

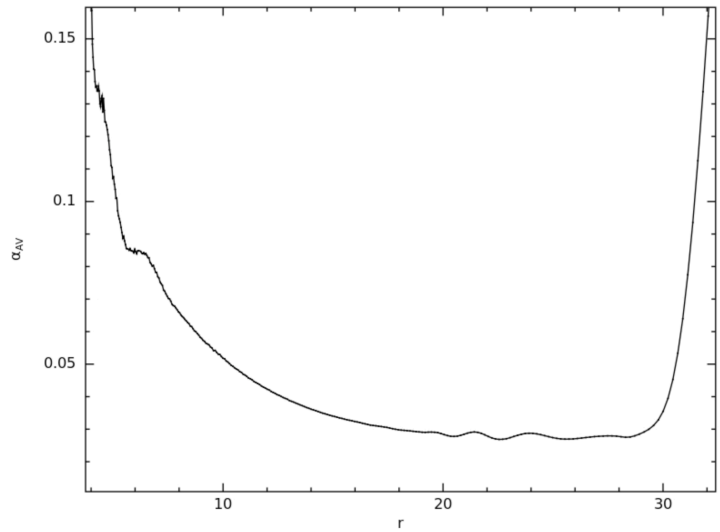

Figure 3.27: The artificial viscosity of the disc inclined at $60°, \alpha = 0.1$ and $H/R = 0.01$ is plotted and is found to lie between 0.05 and 0.13 giving a mean of 0.09.

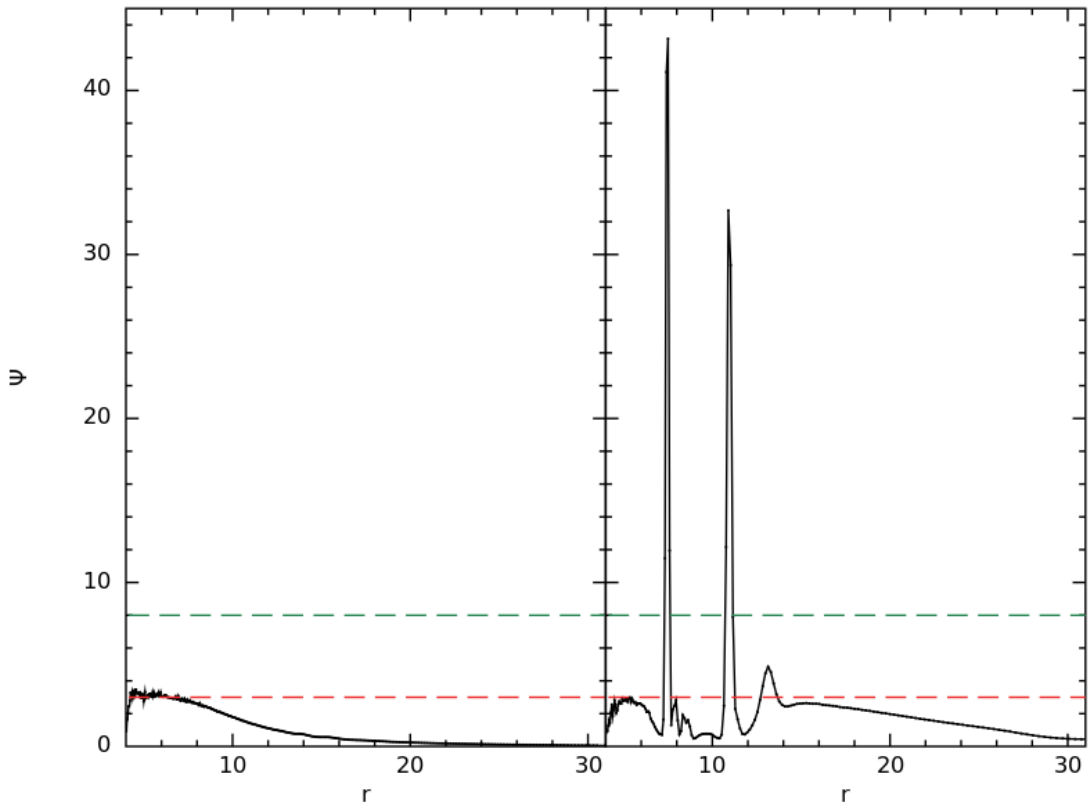

Figure 3.28: The warp amplitude $|\psi|$ of the disc is checked with the critical warp amplitude values corresponding to the value of α with and without adding the artificial viscosity. The red dashed line denotes the critical warp amplitude $|\psi|_c = 3$ for $\alpha = 0.1$ and the green dashed line denotes the critical warp amplitude $|\psi|_c = 8$ corresponding to α inclusive of artificial viscosity $\alpha_{\rm AV} = 0.19$. At a later time, the disc shows instabilities at $r = 8$ and 11 where the warp amplitude $|\psi|$ is much larger than $|\psi|_c$ which confirms the point of disc break where individual rings are formed.

3.5 Warped discs at low α values

The criterion for breaking in isolated warped discs is derived by Doğan et al. (2018) where the growth of instability is dependent on the warp amplitude. As shown in figure 2.2, the critical warp amplitudes at which the discs become unstable is smaller at lower values of α. As a result, the growth rate of instabilities is higher at low α values. In this section, we perform the numerical analysis to check the instability criterion for a disc comprising of 10 million particles at $\alpha = 0.05$, $H/R = 0.01$ when initially inclined at 10° and 60° respectively.

At an inclination of 10°, the disc behaves as shown in figure 3.29. It shows the 3D simulations of the disc at $t = 1485 = 1.4$ orbits and $t = 31185 = 30$ orbits at $R_{\rm out}$. Furthermore, the surface density profiles and the changes in the tilt and twist of the disc

at both times are shown in figure 3.30. These plots show no evidence of tearing in the disc. Hence, we expect the disc to remain stable at 10°, with $\alpha = 0.05$ and $H/R = 0.01$. This result needs to be verified by checking how the warp amplitude changes in the disc.

Firstly, the value of artificial viscosity is calculated (as shown in figure 3.31) to determine the total value of α and the corresponding value of the critical warp amplitude for the disc to become unstable. The value of $\alpha_{AV} = 0.05$ for this disc setup which gives a total α value of 0.1, and its critical warp amplitude is at $|\psi|_c = 3$. The warp amplitude of the disc is studied at $t = 1.4$ orbits and 30 orbits at $R_{\rm out}$ as shown in figure 3.32. The red dashed line corresponds to a critical warp amplitude value at $|\psi|_c = 0.5$ for $\alpha = 0.05$ (without α_{AV}) and the green dashed line denotes $|\psi|_c = 3$ for $\alpha = 0.1$ (with α_{AV}). The values of ψ remain smaller than the critical value $|\psi|_c = 3$ at both times, thus showing that the disc remains stable. As expected from Doğan et al. (2018), this confirms that it is difficult to tear discs at smaller inclinations where the disc's warp amplitude remains small, and therefore it is not likely to exceed the criterion to become unstable at $|\psi|_c$. However, it may be possible for even smaller α values, that we cannot produce in numerical simulations.

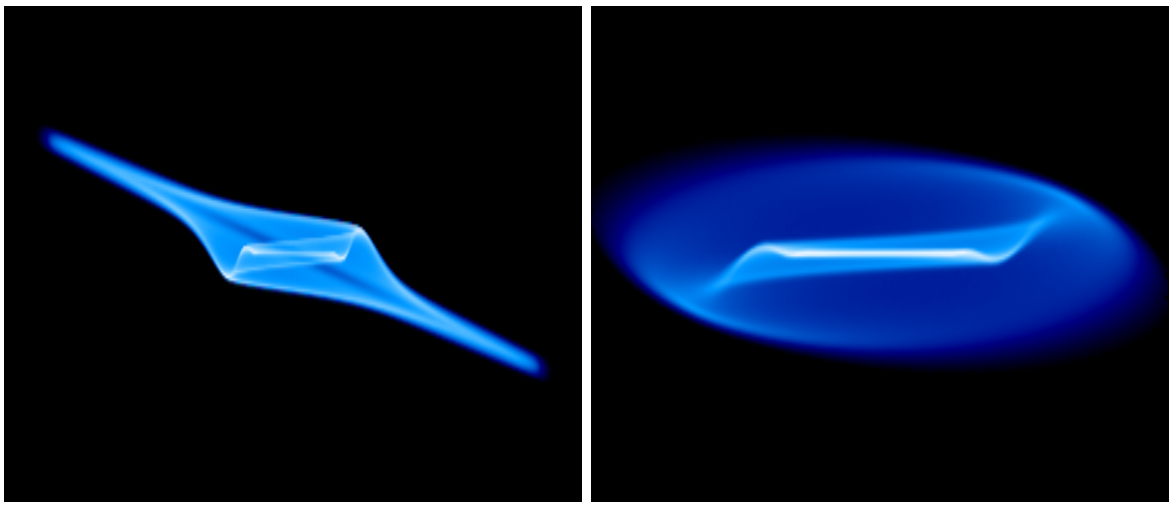

Figure 3.29: Figure shows the 3D column density of a disc initially tilted at 10°, $\alpha = 0.05$ and $H/R = 0.01$ at 1.4 and 30 orbits at R_{out}. The disc shows no evidence of a disc tearing at a later time.

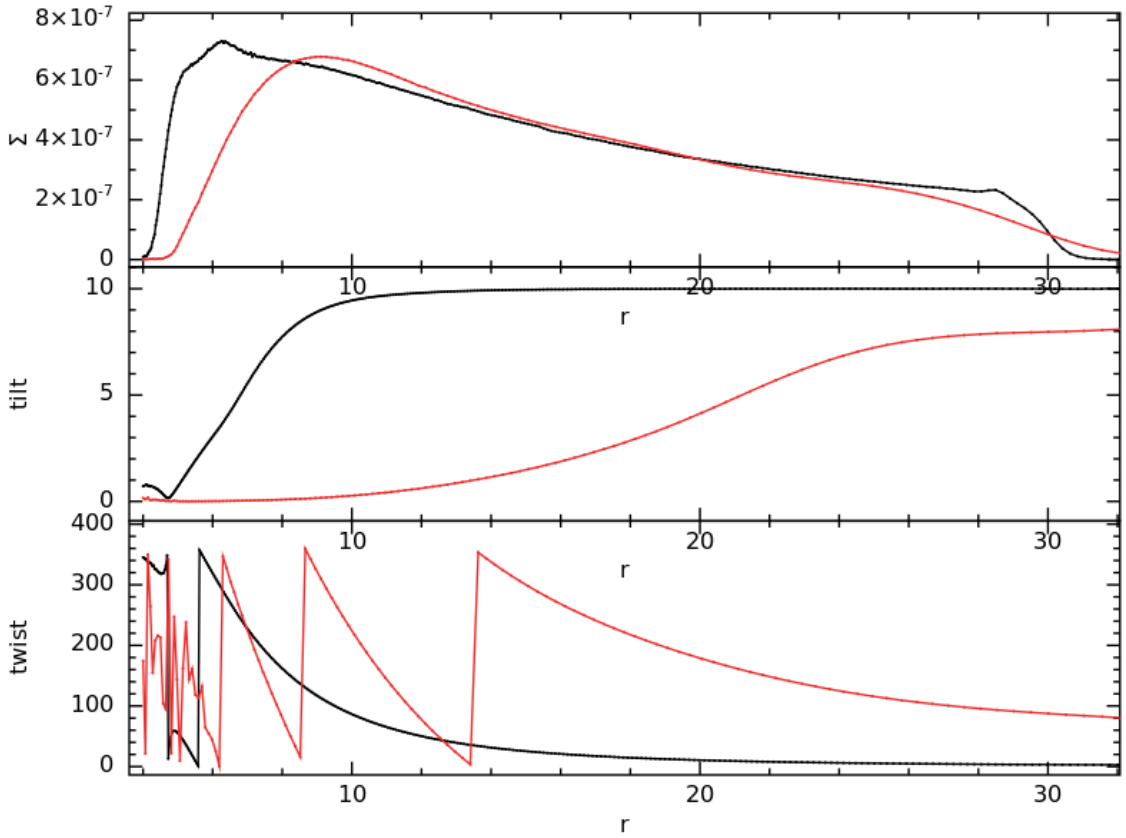

Figure 3.30: The figure shows how the different parameters behave in a disc initially inclined at $10°, \alpha = 0.05$ and $H/R = 0.01$ at 1.4 (black line) and 30 orbits (red line) at $R_{\rm out}$. The first plot represents the surface density profiles for a disc. At both times, the disc shows no divide in the surface density where Σ lowers to a value of zero. The second plot shows the corresponding change in the tilt of the disc at 1.4 (black line) and 30 (red line) orbits at $R_{\rm out}$. It clearly shows how the warp connects misaligned outer part of the disc to the aligned inner part of the disc without any disc tear. The third plot shows how the twist of the disc behaves at 1.4 (black line) and 30 orbits (red line) at $R_{\rm out}$. The twist also shows no evidence of the disc, tearing to form rings.

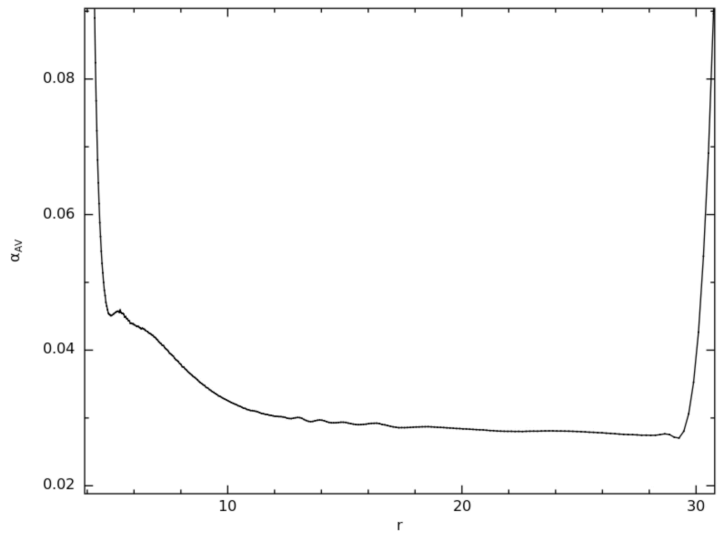

Figure 3.31: The artificial viscosity of the disc inclined at $10°, \alpha = 0.05$ and $H/R = 0.01$ is plotted and is found to be equal to 0.05. The artificial viscosity α_{AV} is of the order of the physical viscosity α_{SS} which gives a total $\alpha = 0.1$.

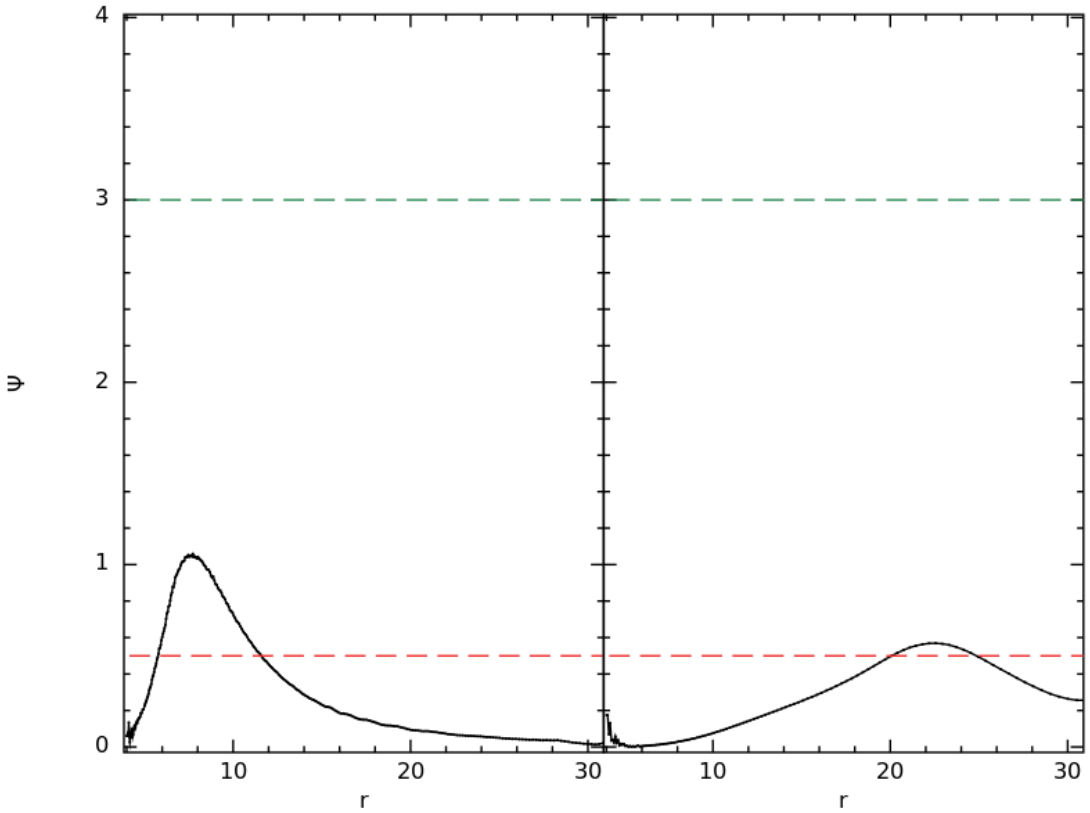

Figure 3.32: Figure shows how the warp amplitude $|\psi|$ of a disc inclined at $10°, \alpha = 0.05$ and $H/R = 0.01$ behaves at 1.4 (left) and 30 orbits (right) at $R_{\rm out}$. The warp amplitude is checked with two values of the critical warp amplitude $|\psi|_c$ represented by the dashed lines. The red dashed line denotes the critical warp amplitude $|\psi|_c = 0.5$ for $\alpha = 0.05$ and the green dashed line denotes the critical warp amplitude $|\psi|_c = 3$ corresponding to a value of $\alpha = 0.1$ inclusive of artificial viscosity $\alpha_{\rm AV} = 0.05$. The values of $|\psi|$ remain below the green dashed line, i.e. $|\psi| < |\psi|_c$ proving that the disc remains stable. This demonstrates the need to account for the value of numerical viscosity in the analysis.

This analysis is extended at a higher inclination of 60° as shown in figure 3.33. This demonstrates the 3D simulations of the disc at $t = 742.5 \approx 0.7$ orbits and $t = 7425 \approx 7.2$ orbits at $R_{\rm out}$. The disc tears to form independent, precessing rings at a later time as shown in the figure. The surface density profiles and the plots of the tilt and twist of the disc at $t = 0.7$ and 7.2 orbits at $R_{\rm out}$ are shown in figure 3.34. At a later time, we can notice a possibility of tearing in the disc where $\Sigma = 0$ at radii $r = 8, 10$ and 13. A similar change is demonstrated at radii $r = 8, 10$ and 13 in the tilt and the twist profiles of the disc as shown in the second and third plots of figure 3.34. Thus, a disc inclined at 60° for a small α parameter tears into individual precessing rings at $r = 8, 10$ and 13. Also, we expect a higher growth of instabilities in this case, which can be further examined from the change in the warp amplitude of the disc.

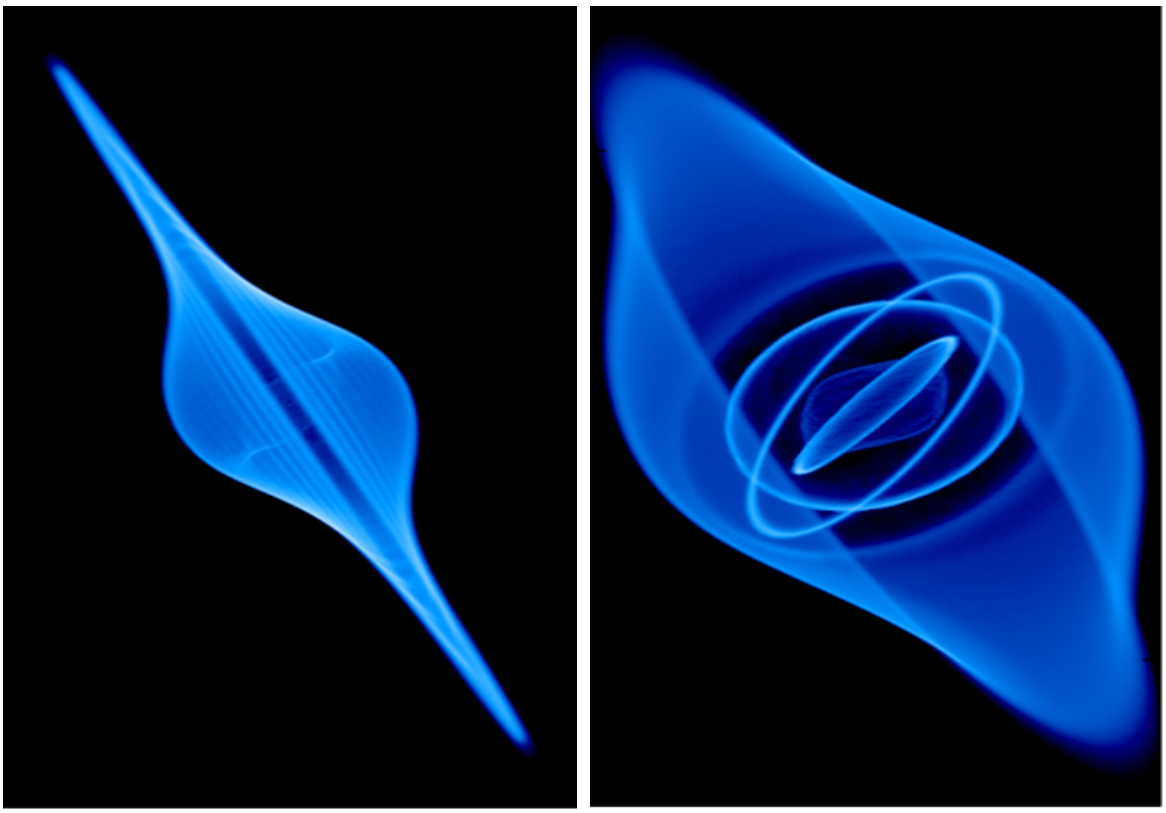

Figure 3.33: 3D simulations of a disc initially tilted at 60°, $\alpha = 0.05$ and $H/R = 0.01$ at 0.7 and 7.2 orbits at R_{out} is shown. The disc tears and forms three independently precessing rings at a later time as shown.

The artificial viscosity for this disc setup is calculated (as shown in figure 3.35) to determine the critical warp amplitude for instabilities to occur. The value of α_{AV} lies between 0.05 and 0.16 with a mean value of 0.11, that gives a total $\alpha = 0.16$ ($\alpha = \alpha_{SS} + \alpha_{AV}$). The critical warp amplitude ($|\psi|_c$) is 4 at $\alpha = 0.16$. The warp amplitude is calculated at times t = 0.7 orbits and 7.2 orbits at $R_{\rm out}$ and are compared to the critical warp amplitude as shown in figure 3.36. The red dashed line corresponds to a critical warp amplitude value at $|\psi|_c = 0.5$ for $\alpha = 0.05$ and the green dashed line is at $|\psi|_c = 4$ for $\alpha = 0.16$. In figure 3.36, one can see that the values of $|\psi|$ exceed the critical warp amplitude $|\psi|_c = 4$ causing instabilities to occur at a later time. As shown in the figure, the values of $|\psi| >> |\psi|_c$ at $r = 8$, 10 and 13 denoting the points where the disc tears to form rings. This agrees well with the predicted results from Doğan et al. (2018), and conclude that instabilities grow faster in highly inclined discs at lower values of α and H/R.

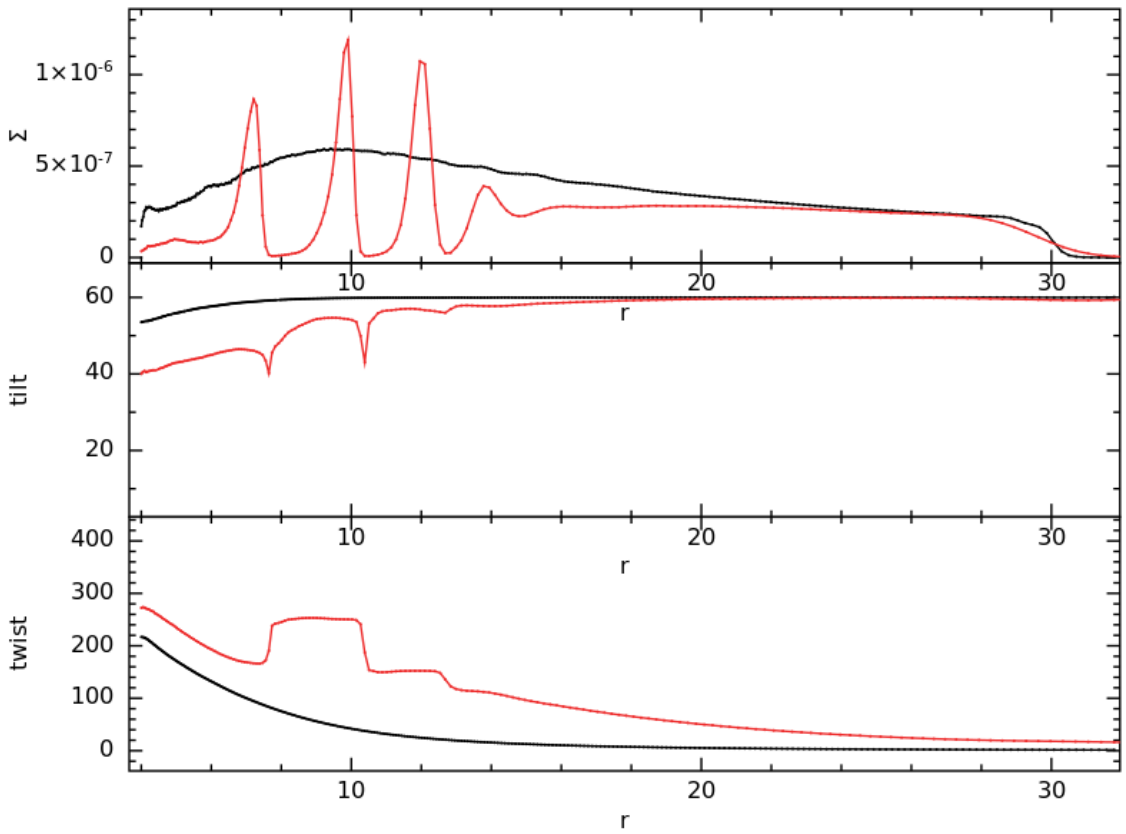

Figure 3.34: The figure shows how the various profiles behave in a disc initially inclined at $60°, \alpha = 0.05$ and $H/R = 0.01$ at 0.7 (black line) and 7.2 orbits (red line) at $R_{\rm out}$. The first plot represents the surface density profiles for a disc. The disc shows clear evidence of disc tearing where Σ reduces to zero at radii $r = 8$, 10 and 13. The second plot shows the change in the tilt of the disc at 0.7 (black line) and 7.2 (red line) orbits at $R_{\rm out}$. It agrees well with the surface density profiles showing break in the tilts at $r = 8$, 10 and 13 that denote the forming of three rings in the disc. The same analysis is done to check how the twist of the disc looks like at 0.7 (black line) and 7.2 orbits (red line) at $R_{\rm out}$, as shown in the third figure. As expected, the twist of the disc also shows a divide at $r = 8$, 10 and 13.

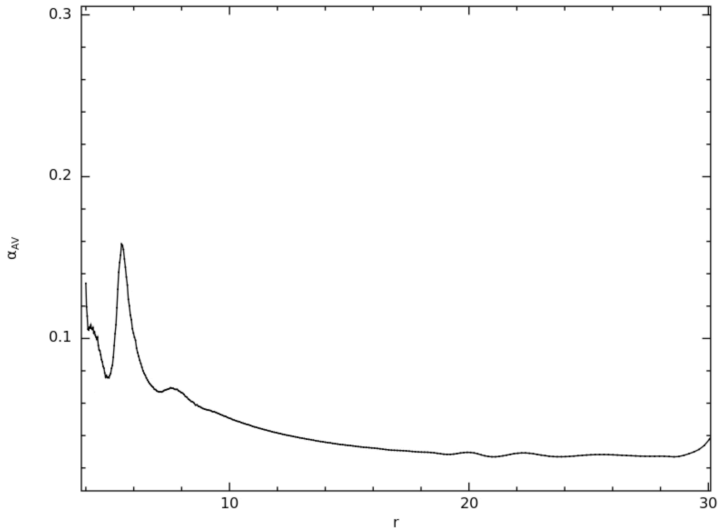

Figure 3.35: The artificial viscosity is plotted for the disc inclined at $60°, \alpha = 0.05$ and $H/R = 0.01$. The value of α_{AV} is found to lie between 0.05 and 0.16 giving a mean value of 0.11.

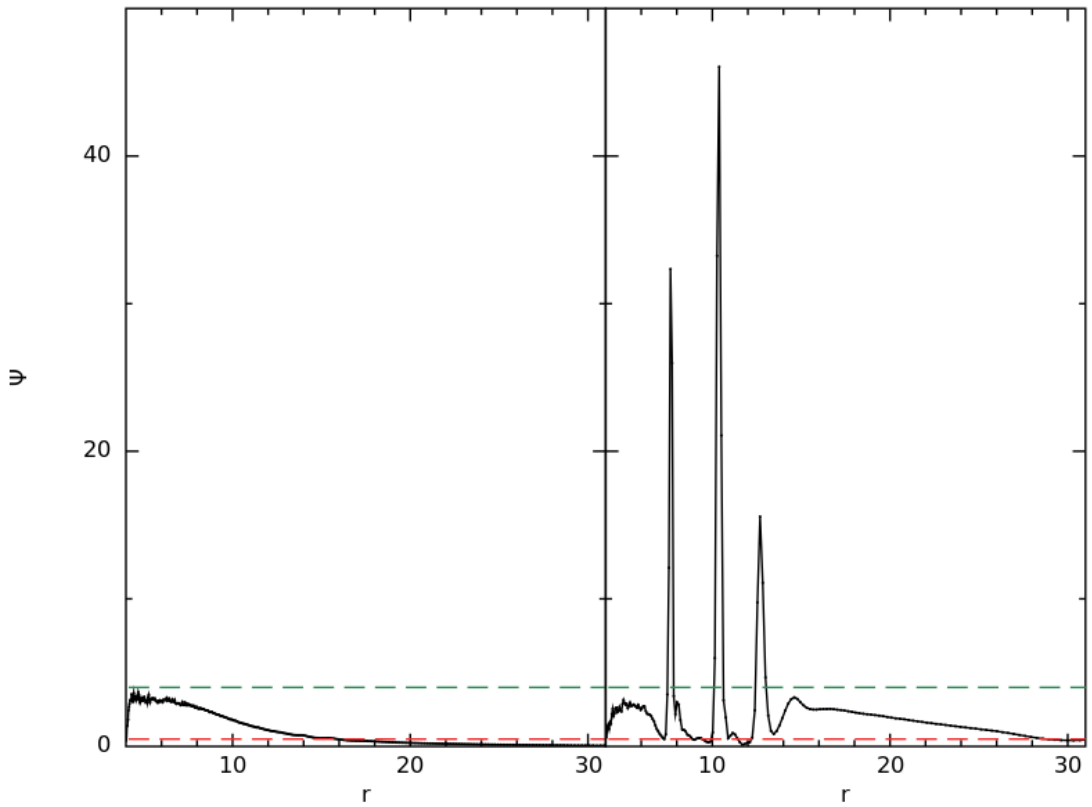

Figure 3.36: Figure shows the change in the warp amplitude $|\psi|$ of a disc inclined at $60°, \alpha = 0.05$ and $H/R = 0.01$ at 0.7 (left) and 7.2 orbits (right) at $R_{\rm out}$. The warp amplitude is checked with two values of the critical warp amplitude $|\psi|_c$ represented by two dashed lines. The red dashed line denotes the critical warp amplitude $|\psi|_c = 0.5$ for $\alpha = 0.05$ and the green dashed line denotes the critical warp amplitude $|\psi|_c = 4$ corresponding to a value of $\alpha = 0.16$ inclusive of artificial viscosity $\alpha_{\rm AV} = 0.11$. The values of $|\psi|$ doesn't exceed the green dashed line at the initial time (left), thus shows no disc tearing at 0.7 orbit at $R_{\rm out}$. But at a later time, the warp amplitude values are much greater than the critical warp amplitude $|\psi|_c = 4$ at radii r $\approx$ 8, 10 and 13.

3.6 Growth of instabilities

Doğan et al. (2018) gives the dimensionless growth rate $\Re[s]$ given by:

$$s = -\frac{i\omega}{\Omega}\left(\frac{\Omega}{\mathrm{c_s k}}\right)^2 \tag{3.9}$$

where s is related to the physical growth rate $\Re[-i\omega]$ given as:

$$-i\omega = s\Omega\left(\frac{\mathrm{c_s k}}{\Omega}\right)^2, \tag{3.10}$$

assuming that the perturbations grow ($\Re[s] > 0$) or decay ($\Re[s] < 0$) exponentially as $\exp[\Re(-\mathrm{i}\omega)\mathrm{t}]$.

Doğan et al. (2018) plots the dimensionless growth rate $\Re[s]$ as a function of $|\psi|$ for different values of α as shown in figure 2.1 in the previous chapter. From figure 2.1, it can be noted that when $\alpha = 0.1$, the value of s ≈ 0.2 for warp amplitudes $|\psi|$ between 4 and 5. In this section, we investigate the growth rate of instabilities in our numerical simulations.

It can be noted that the warp amplitude increases slowly over time in a disc due to LT precession. As soon as the warp amplitude exceeds the the critical warp amplitude $|\psi|_c$, the disc becomes unstable, and the value of ψ grows quickly to reach its peak value and thereafter decays over time. We aim to calculate the growth rate of these instabilities and compare it to the expected analysis from Doğan et al. (2018). As mentioned earlier, the instabilities are expected to grow as

$$|\psi| = |\psi|_0 \exp[\Re(-\mathrm{i}\omega)\mathrm{t}]. \tag{3.11}$$

The growth rate can thus be rewritten as $s = (-i\omega/\Omega)(Hk)^{-2}$. The strongest instability at $s \approx 1$ corresponds to dynamical timescales and length scales of the order of the scale height H, and this requires the wavenumber $k \approx 1/H$. But, this may not hold true if tested in a numerical analysis.

It can be seen from the numerical simulations that typically the discs become unstable on a radial scale $\approx H$. In this case, we expect $k \approx 1/H$ and therefore $c_s k/\Omega \approx 1$ (where scale-height $H = c_\mathrm{s}/\Omega$). Therefore from equation 3.10, we can rewrite 3.11 as:

$$|\psi| = |\psi|_0 \exp[\mathrm{s}\Omega\mathrm{t}] \tag{3.12}$$

This can be tested from the disc tearing behaviour seen in our numerical simulations, by investigating how the maximum warp amplitude of the disc changes over time. Firstly, we consider a disc inclined at 45°, $H/R = 0.03$ and $\alpha = 0.1$. We follow the start time

(t_1) of an instability when it begins to grow, and the end time (t_2) when the instability finishes its decay, noted as $t_1 = 3593.7$ and $t_2 = 23195.7$ respectively. The radial limits of this growing instability are also noted, at values of r between 10 and 14. The maximum warp amplitude of the instability, $|\psi|_{\max}$ from t_1 to t_2 is calculated and plotted over time, as shown in figure 3.37.

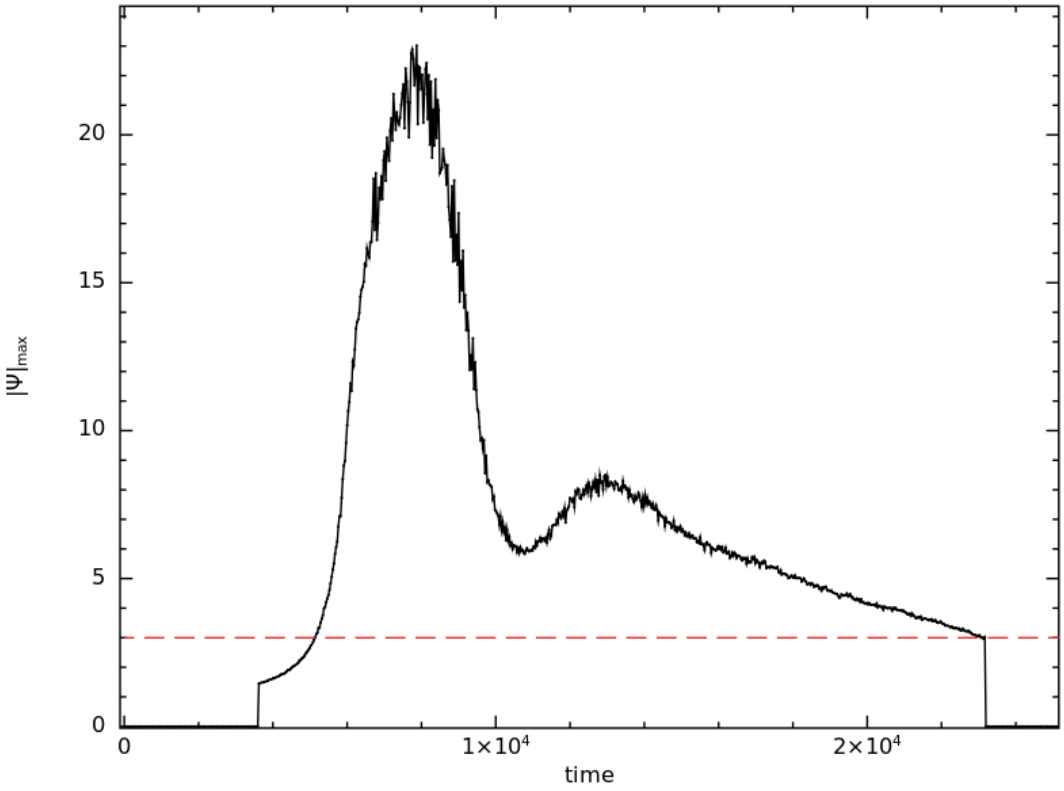

Figure 3.37: The maximum warp amplitude of an instability in a disc inclined at 45°, $\alpha = 0.1$ and $H/R = 0.03$ is plotted over time. The growth of instability is studied from start time $t_1 = 3593.7$ to $t_2 = 23195.7$ located at radii between 10 and 14.

From the data shown in the figure, the values of time at $|\psi|_1 = 4$ and $|\psi|_2 = 5$, are given as $t_1 = 5405.4$ and $t_2 = 5583.6$ respectively. Then, the time required for the instability to grow from $|\psi|_1$ to $|\psi|_2$ is given by the time difference $\Delta t = 178.2$. Furthermore, the mean of radii corresponding to $|\psi|_1$ and $|\psi|_2$ is 12.369. Therefore, equation 3.12 can be written in terms of $|\psi|_1$ and $|\psi|_2$ as:

$$|\psi|_2 = |\psi|_1 \exp[\mathrm{s}\Omega\Delta\mathrm{t}] \tag{3.13}$$

where $\psi|_1 = 4$, $|\psi|_2 = 5$, $s = 0.2$ (obtained from figure 2.1) and $\Omega = 1/\sqrt{r^3}$ with $r = 12.369$. The above equation calculates $\Delta t = 48.535$, which infers that the growth time for instabilities in our simulations is slower, in comparison to that expected from Doğan et al. (2018). In other words, the rate of growth of instabilities obtained from the numerical simulations is 1/3.67 times the value expected from the analysis in Doğan et al. (2018).

Similarly, the growth of instabilities is studied for a disc inclined at 60°, $H/R = 0.03$ and $\alpha = 0.1$. In this case, the values of t_1 and t_2 are set at 19602 and 23581.8 respectively. The warp amplitude is calculated at radii r between 12 and 18. The plot of the maximum warp amplitude over time is shown in the figure below.

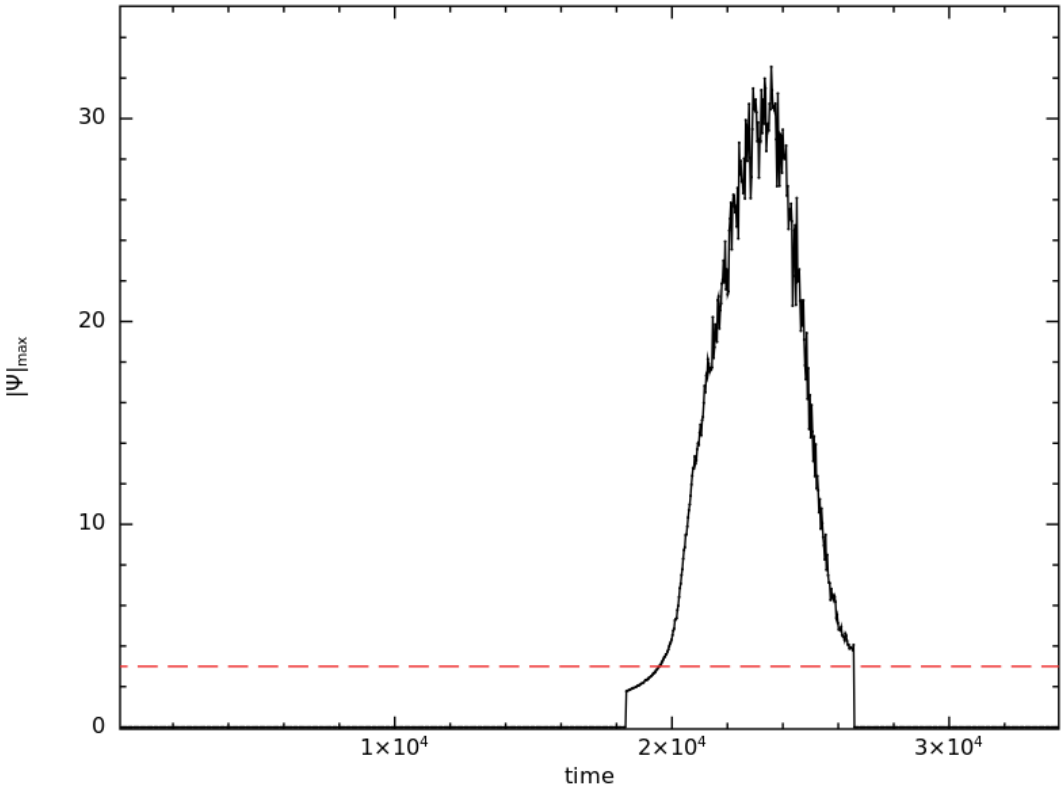

Figure 3.38: The maximum warp amplitude of an instability in a disc inclined at 60°, $\alpha = 0.1$ and $H/R = 0.03$. The instability is examined at radii r between 12 and 18 over time $t_1 = 19602$ to $t_2 = 23581.8$.

In figure 3.38, the value of $t_1 = 19928.7$ at $|\psi|_1 = 4$ and the value of $t_2 = 20077.2$ at $|\psi|_2 = 5$, giving $\Delta t = 148.5$. As done previously, the value of Δt from equation 3.13 is calculated. We consider, $|\psi|_1 = 4$ and $|\psi|_2 = 5$ and the mean of radii corresponding

to these values of warp amplitude is at $r = 14.524$, where we assume growth rate $s = 0.2$. From equation 3.13, the predicted value of $\Delta t = 61.716$ for this disc. Therefore, the rate of growth of instabilities obtained from the numerical simulations is 1/2.4 times the value predicted from Doğan et al. (2018). Once again, we show that the instabilities grow slower in numerical simulations, in contrast to what is expected theoretically.

From our numerical analysis, we studied the change in the warp amplitude of discs ($|\psi|$ vs r plots), proving that the disc becomes unstable when $|\psi| > |\psi|_c$ and produce instabilities. To learn why instabilities grow slower in numerical simulations in comparison to what is expected from Doğan et al. (2018), we examine the exponential component $\exp(-i\omega)t$ in equation 3.11 where

$$-i\omega = s\Omega\left(\frac{c_{\rm s}k}{\Omega}\right)^2. \tag{3.14}$$

Since scale-height $H = c_{\rm s}/\Omega$, we get

$$-i\omega = s\Omega(Hk)^2. \tag{3.15}$$

Thus, the exponential term $\exp(-i\omega)t$ can be written as:

$$\exp(-i\omega)t = \exp(s\Omega t(Hk)^2). \tag{3.16}$$

From the $|\psi|$ vs r plots of the two disc setups, the value of Δr is noted for the instability. Using this value of Δr, the wavenumber $k = 1/\Delta r$ and equation 3.16 becomes:

$$\exp(-i\omega)t = \exp(s\Omega t(Hk)^2) = \exp\left(s\Omega t\left(\frac{H}{\Delta r}\right)^2\right) \tag{3.17}$$

Furthermore, the value of $\Delta r/H$ in each disc setup is calculated. Firstly, for the disc inclined at 45° with $\alpha = 0.1$ and $H/R = 0.03$, the value of $\Delta r = 0.55$ ($\Delta r = r_2 - r_1$) where r_1 and r_2 are 12.1 and 12.65 respectively, and they give a mean radius of 12.375.

To calculate the value of H at $r = 12.375$, we know the sound speed

$$c_s(i) = \frac{H}{R}\sqrt{\frac{GM}{R_{\rm in}}}\left(\frac{R}{R_{\rm in}}\right)^{-q} \tag{3.18}$$

where $H/R = 0.03$, $R_{\rm in} = 4$, $q = 3/4$ and $G = M = 1$. This gives

$$c_s(i) = 0.042R^{-0.75}. \tag{3.19}$$

We know, disc thickness $H = c_s/\Omega$ and thus,

$$H(i) = \frac{c_s(i)}{\Omega(i)} = 0.042R^{0.75}. \tag{3.20}$$

Hence, at radius $r = 12.375$, the value of scale-height $H = 0.277$. This gives $\Delta r/H = 1.98$. This value of $\Delta r/H$ in equation 3.17 accounts for an increase in its value by a factor of four. This explains why the instabilities grow slower in our simulations. Therefore, once we have accounted for the length scale of the unstable region of the disc, Δr, which determines the wavenumber $k \approx 1/\Delta r$, we see that the simulations and predicted growth rate agree well.

In addition, we can also check the same for the disc setup with inclination at 60°, $\alpha = 0.1$ and $H/R = 0.03$. The value of $\Delta r = 0.65$ ($\Delta r = r_2 - r_1$) where $r_1 = 14.2$ and $r_2 = 14.85$ with a mean radius value of 14.525. The value of H at $r = 14.525$ is 0.312, which gives a value of $\Delta r/H = 2.08$. The exponential growth of instabilities is dependent on $\Delta r/H$ as shown in equation 3.17. As before, once the wavelength of the unstable region is accounted for, there is agreement between the numerical results and that predicted from Doğan et al. (2018).

3.6.1 Maximum warp amplitude

As previously described from the simulations, it is difficult to tear discs at low inclinations, and at higher values of α and H/R. This is because the maximum warp amplitude in the disc remains smaller than its critical warp amplitude for instabilities to occur. The value of the maximum warp amplitude for a disc with tilt β and H/R is calculated as (Doğan et al., 2018)

$$|\psi|_{\max} = \beta \frac{R}{H}. \tag{3.21}$$

In this section, we investigate if the above equation for the maximum warp amplitude agrees well in our numerical analysis. The values of maximum warp amplitude in discs at $\alpha = 0.1$, $H/R = 0.03$ and inclined at 45° and 60° are shown by figures 3.37 and 3.38 respectively. For a disc with tilt $\beta = 45°$, $\alpha = 0.1$ and $H/R = 0.03$, equation 3.21 becomes

$$|\psi|_{\max} = 45 \times \frac{\pi}{180} \times \frac{1}{0.03} = 26.167. \tag{3.22}$$

The peak value of $|\psi|_{\max}$ from the simulation (as shown in figure 3.37) is 23.016. This result is only 12% less than what is expected, thus in agreement with the predicted value of $|\psi|_{\max}$ from Doğan et al. (2018). Similarly, the value of maximum warp amplitude from equation 3.21 at $\beta = 60°$, $\alpha = 0.1$ and $H/R = 0.03$, gives:

$$|\psi|_{\max} = 60 \times \frac{\pi}{180} \times \frac{1}{0.03} = 34.889. \tag{3.23}$$

As shown in figure 3.38, the peak value of the disc's warp amplitude from our simulation is $|\psi|_{\max} = 32.556$. This result varies from the expected by 6%, and therefore in agreement with the value predicted by Doğan et al. (2018).

3.7 Testing the point of instability

In section 3.3, we conducted the numerical analysis of warped discs at different values of α $(0.05 - 0.1)$, H/R $(0.01 - 0.03)$ and initially inclined at different tilts. We tested the instability criterion and examined whether the discs are most likely to become unstable and tear when the disc's warp amplitude exceeds the critical warp amplitude (dependent on the value of α). In this section, we check further if the unstable warped discs tear into discrete rings exactly at the point where its warp amplitude exceeds the critical value $|\psi|_c$.

Figure 3.39 shows the 3D simulations as well as the change in the warp amplitude of a disc inclined at 45°, $\alpha = 0.1$ and $H/R = 0.03$ at successive times $t = 2.9$ and 3.1 orbits at $R_{\rm out}$ respectively. The plot of ψ at the initial time shows two peaks at $r = 6$ and 9. Lets focus on the instability in the warp amplitude profile at $r = 6$. At the initial time, the disc's warp amplitude $|\psi| \leq |\psi|_c$ which corresponds to the forming of an inner ring in the 3D simulation. But at the following time, the value of $|\psi|$ exceeds the critical value and an independent, precessing ring in the inner disc can be seen in the 3D simulations of the disc. This infers that the disc becomes unstable and tears exactly when the warp amplitude exceeds its critical value. The same is checked for a disc initially inclined at 60° for the same values of α and H/R at times $t = 14.3$ orbits and $t = 14.5$ orbits at $R_{\rm out}$ as shown in figure 3.40.

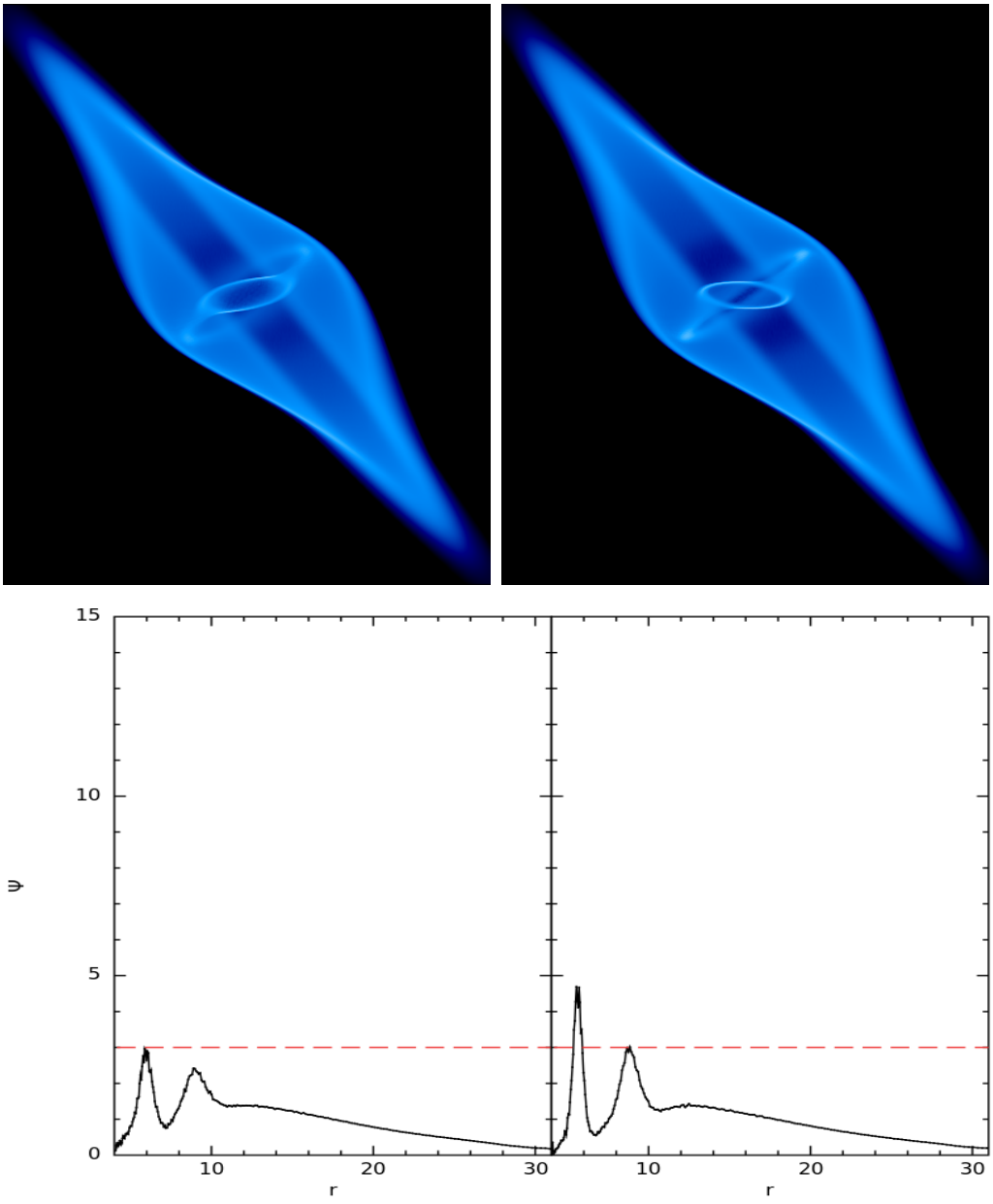

Figure 3.39: Shows the 3D column density plots and the corresponding warp amplitude profiles of a disc inclined at 45°, $\alpha = 0.1$ and $H/R = 0.03$ at times t = 2.9 and 3.1 orbits at $R_{\rm out}$. The critical value $|\psi|_c = 3$ is denoted by the red dashed line.

In figure 3.40, we observe the formation of a ring in the 3D simulation of the disc at $t = 14.3$ orbits at $R_{\rm out}$ that matches with the an increase in the warp amplitude at radii between $r = 6$ and $r = 8$. Here, the ring isn't completely broken as the warp amplitude $|\psi|$ remains lower than the critical value $|\psi|_c = 3$. On the other hand at $t = 14.5$ orbits at $R_{\rm out}$, the ring breaks completely in the simulation. Here, the warp amplitude exceeds the critical value thus strongly agreeing with the criterion presented in Doğan et al. (2018).

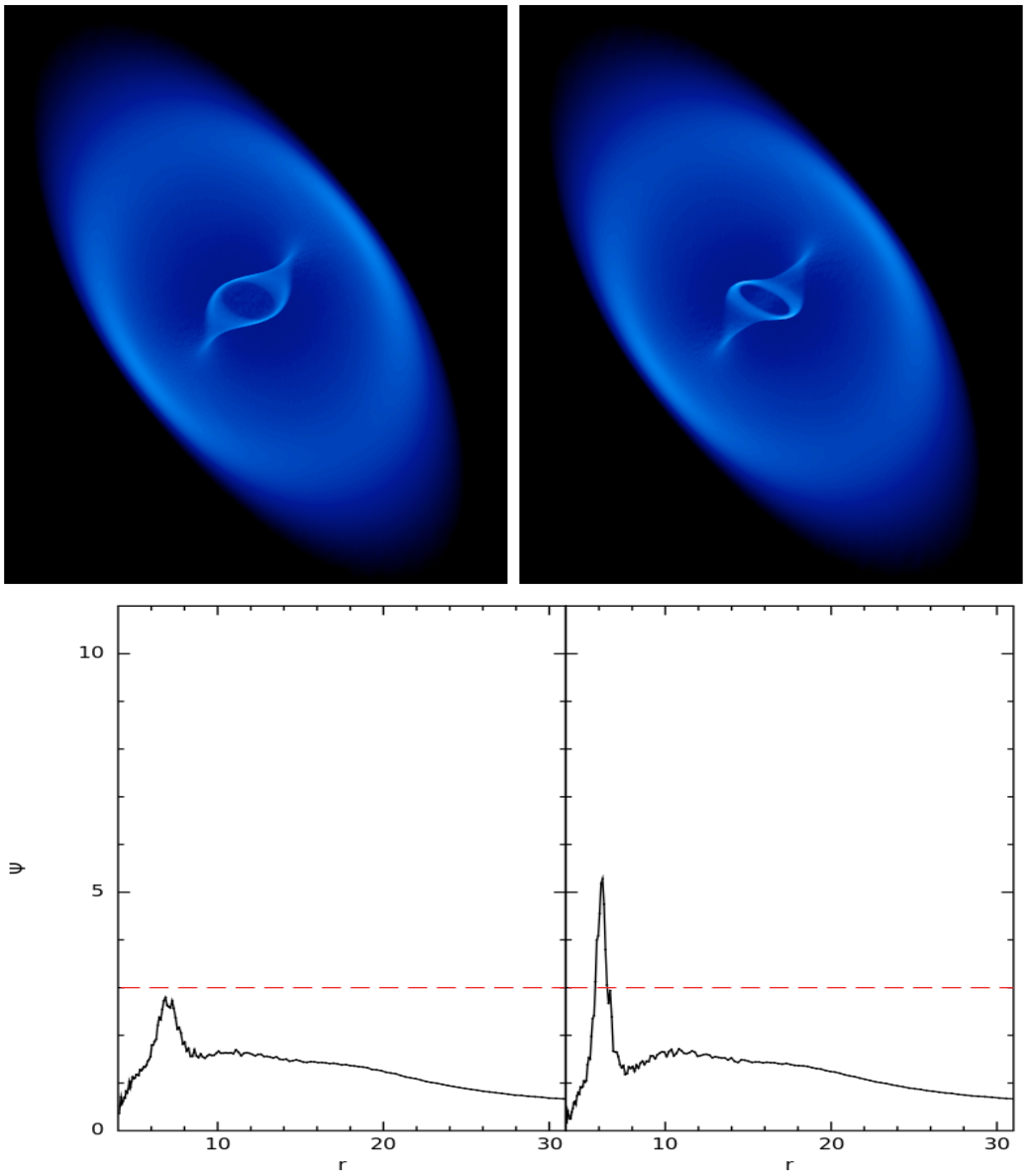

Figure 3.40: 3D simulations and the corresponding warp amplitude profiles of a disc inclined at 60°, $\alpha = 0.1$ and $H/R = 0.03$ at times t = 14.3 and 14.5 orbits at $R_{\rm out}$. The red dashed line in the $|\psi|$ vs r plots represent the critical value $|\psi|_c = 3$.

Furthermore, the numerical analysis of a disc inclined at 45°, $\alpha = 0.1$ and $H/R = 0.01$ after $t = 4$ orbits and $t = 4.2$ orbits at $R_{\rm out}$ is shown in figure 3.41. At the initial time, the warp amplitude peaks at $r = 5, 7$ and 9. If we focus on the instability at $r = 9$, it surpasses the red dashed line ($|\psi|_c = 3$ for $\alpha = 0.1$) but is below the green dashed line ($|\psi|_c = 8$ for $\alpha = 0.19$) at the initial time. The 3D simulation at this time shows that the ring is not completely broken at $r = 9$, and is still connected to the outer part of the disc. But at a later time, the warp amplitude at $r = 9$ exceeds the green dashed line which

indicates where the ring is fully broken, as observed in the corresponding 3D simulation.

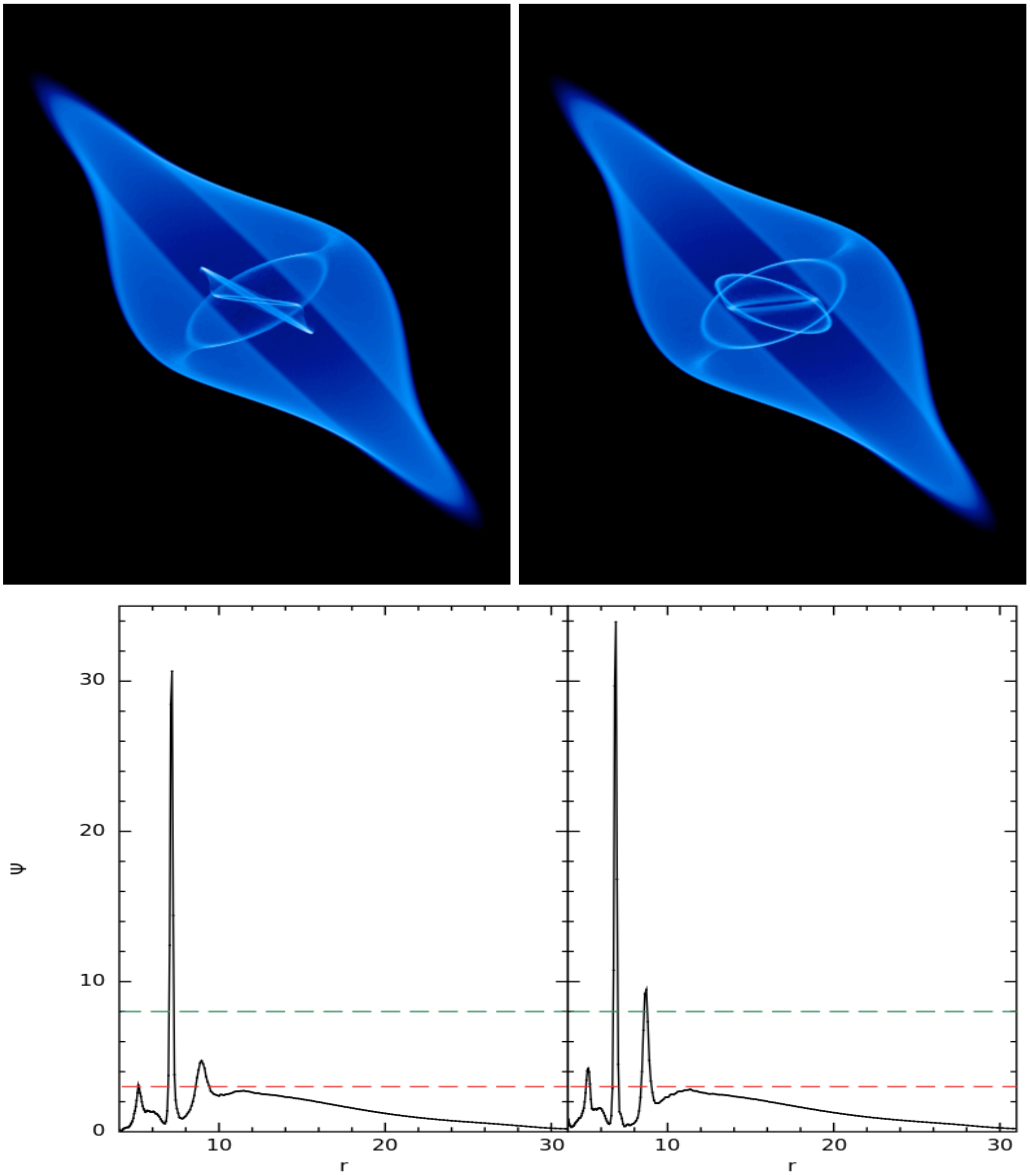

Figure 3.41: Shows the 3D simulations and the plots of warp amplitude for a disc inclined at 45°, $\alpha = 0.1$ and $H/R = 0.01$ at times t = 4 orbits and 4.2 orbits at $R_{\rm out}$. The red dashed line in the $|\psi|$ plots shows the critical value $|\psi|_c = 3$ at $\alpha = 0.1$ and the green dashed line represents $|\psi|_c = 8$ at $\alpha = 0.19$.

Figure 3.42 shows the 3D column density and the warp amplitude plots of a disc initially tilted at 60°, $\alpha = 0.1$ and $H/R = 0.01$ after $t = 4$ orbits and $t = 4.1$ orbits at $R_{\rm out}$. As shown in the warp amplitude plots, there are growing instabilities at $r \approx 5$ and $r \approx 9$. The green and red dashed lines in these plots represent the critical warp amplitude for α values, with and without the numerical viscosity $\alpha_{\rm AV}$. Although, the value of $|\psi|$ at $r \approx 9$ surpasses the red dashed line at $t = 4$ orbits at $R_{\rm out}$, it is well below the green

dashed line which shows that the ring is not fully broken in the disc as shown in the 3D simulation. But at a later time, the value of $|\psi|$ exceeds the green dashed line and the corresponding 3D simulation demonstrates that the disc is fully broken. Once again, we find that the criterion $|\psi|_c$ for disc tearing must correspond to the α value inclusive of the numerical viscosity, in discs (at smaller H/R values and higher tilts) to become unstable.

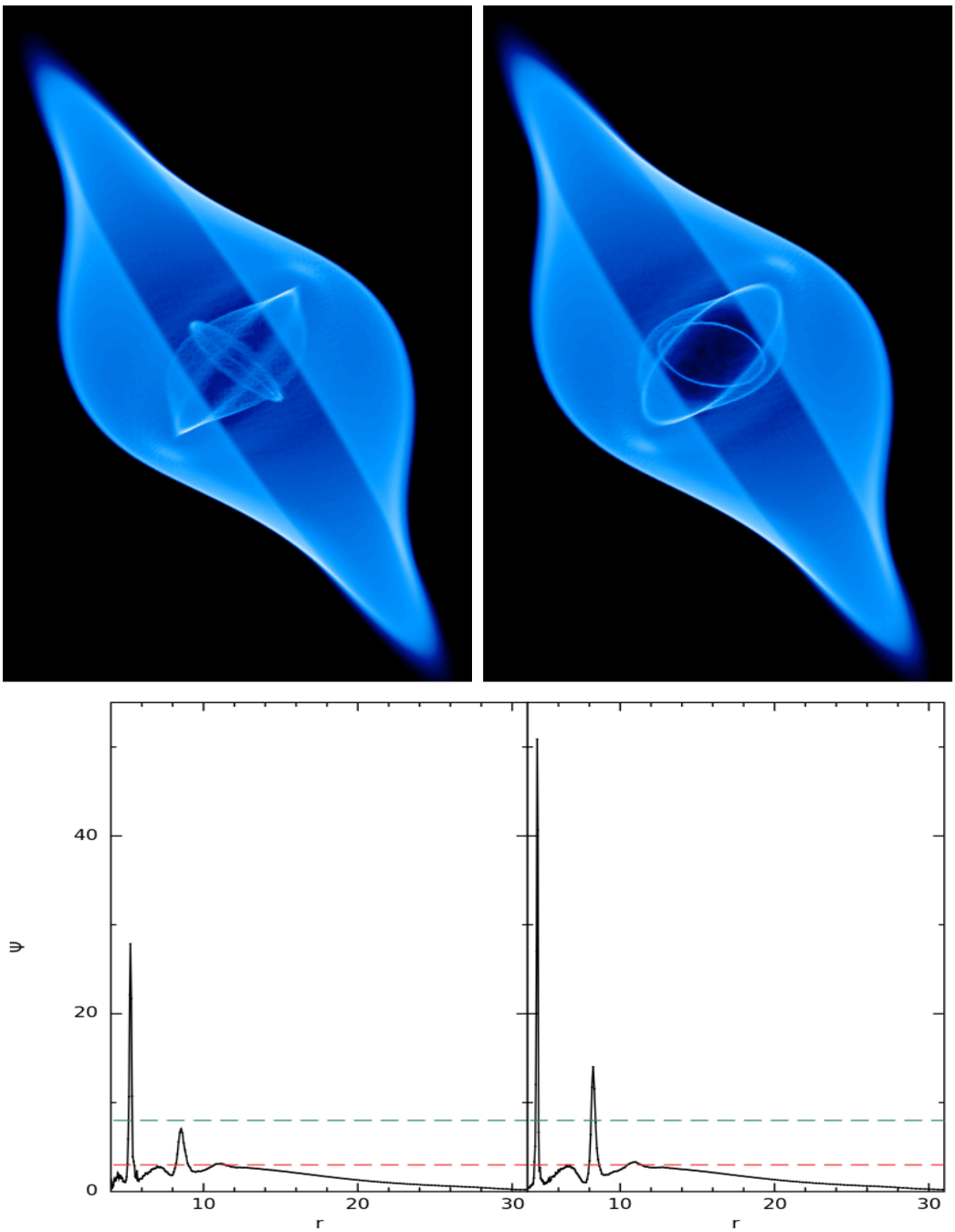

Figure 3.42: Shows the 3D simulations and the warp amplitude profiles for a disc inclined at 60°, $\alpha = 0.1$ and $H/R = 0.01$ at times t = 4 and 4.1 orbits at $R_{\rm out}$. The red dashed line in the $|\psi|$ plots denotes the critical value $|\psi|_c = 3$ at $\alpha = 0.1$ and the green dashed line represents $|\psi|_c = 8$ at $\alpha = 0.19$.

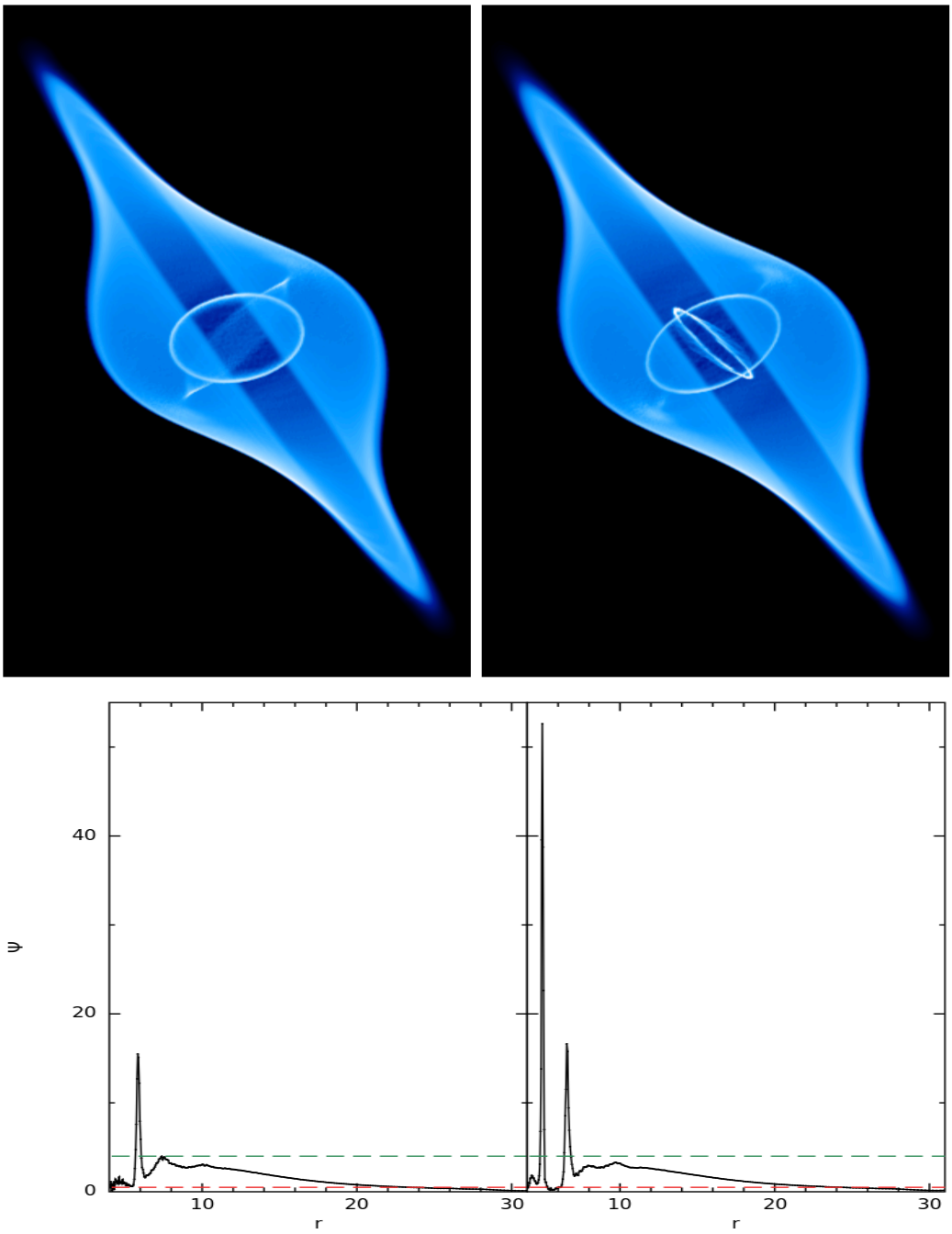

Figure 3.43: 3D column density and the corresponding warp amplitude plots for a disc inclined at 60°, $\alpha = 0.05$ and $H/R = 0.01$ at times t = 2.4 and 2.6 orbits at $R_{\rm out}$. The red dashed line in the plot shows the critical value $|\psi|_c = 0.5$ at $\alpha = 0.05$ and the green dashed line represents $|\psi|_c = 0.16$ at $\alpha = 0.16$.

Furthermore, we also examine unstable discs at values of $\alpha = 0.05$, $H/R = 0.01$ and inclined at 60°. Figure 3.43 shows the 3D column density and the warp amplitude profiles at times $t = 2.4$ orbits and $t = 2.6$ orbits at $R_{\rm out}$ respectively. There are two peaks in the warp amplitude plots at radii $r = 5$ and $r = 7$ which denote where the disc tears to form rings. If we focus on the value of ψ at $r = 7$ at the initial time, the value of

ψ is well above the red dashed line but below the green dashed line. Similarly, the 3D disc simulation shows a ring still unbroken and attached to the outer disc. But at a later time, it is well above the green dashed line at $|\psi|_c = 0.16$ which shows the possibility of disc tear at $r = 7$. Once again this result agrees well with the predicted criterion from (Doğan et al., 2018), i.e. a warped disc is most likely to become unstable and tear when $|\psi|$ exceeds $|\psi|_c$. It can also be concluded that the disc becomes easily unstable at smaller values of α due to their smaller $|\psi|_c$ values.

3.8 Discussions and Conclusions

In this work, theoretical analysis on the criterion of disc tearing is tested using SPH simulations. A parameter sweep is conducted for diffusive discs ($\alpha > H/R$) at different values of α $(0.05 - 0.1)$ and H/R $(0.01 - 0.03)$ and the criterion of disc tearing is checked in each of these disc setups.

Firstly, we examined a disc composed of 10 million particles, with $\alpha = 0.1$ and $H/R = 0.03$. We find the effect of numerical viscosity to be negligible in this disc setup. The behaviour of the disc at various inclinations (from 10° to 60°) is examined using SPH simulations. The changes in the surface density profiles as well as the tilt and twist of the disc are also studied to verify if the disc becomes unstable and tears to form discrete rings. At low inclinations of 10° and 30°, the disc doesn't show any tearing and remains warped throughout the simulation. On the other hand, we observe tearing in highly inclined discs at 45° and 60° respectively. We investigate the predicted criterion of disc tearing from Doğan et al. (2018) to show if the disc becomes unstable at a critical warp amplitude, $|\psi|_c$. Our numerical results find that the values of $|\psi| >> |\psi|_c$ at points where tearing occurs in discs tilted at 45° and 60°. We also show that it is difficult to observe disc tearing at low inclinations (10° and 30°) as their warp amplitude remains much smaller than $|\psi|_c$.

The same analysis is extended to smaller values of α and H/R where the value of artificial viscosity is expected to play a crucial role. The ratio of the shell averaged smoothing length to the scale-height ($\langle h \rangle / H$) contributes highly to the artificial viscosity at smaller H/R values. In these disc setups, we consider the value of the critical warp amplitude $|\psi|_c$ for the α parameter inclusive of the artificial viscosity α_{AV}. As explained in Doğan et al. (2018), this value of $|\psi|_c$ gives the criterion to form instabilities in a disc. Our results agree with the predicted criterion, and find that thinner discs become unstable at low α values and at higher tilts. We also find that the critical warp amplitude values are smaller and the growth rates of the instability are higher at low values of α.

Doğan et al. (2018) showed that the instabilities grow as $|\psi| = |\psi|_0 \exp[\Re(-\mathrm{i}\omega)\mathrm{t}]$, where $|\psi|_0 = 4$ and $|\psi| = 5$ are assumed to be the initial and final values of the warp amplitude where the dimensionless growth rate $\Re[s] = 0.2$. The value of Δt is calculated from the simulations and compared to the expected time required for the instabilities to grow. This is examined for a disc setup with $\alpha = 0.1$ and $H/R = 0.03$ at inclinations, 45° and 60° respectively. It is found that $\Delta r/H \approx 2$ in both disc setups, and therefore the growth rate of instabilities is found to be in agreement with that predicted from Doğan et al. (2018).

Doğan et al. (2018) gives the maximum value of warp amplitude for the instabilities to grow in a disc as $|\psi|_{\max} = \beta \frac{R}{H}$ (at disc tilt β). The values of $|\psi|_{\max}$ calculated for a disc with parameters $\alpha = 0.1$, $H/R = 0.03$ at inclinations 45° and 60°, are 26.167 and 34.889 respectively. The values of $|\psi|_{\max}$ calculated from our numerical analysis for the two disc setups are 23.016 and 32.556, which vary from the expected values by a few percent. Therefore, the theoretical prediction of $|\psi|_{\max}$ from Doğan et al. (2018) holds in agreement with our numerical analysis. Furthermore, we test the point of instability in each of the unstable and highly inclined warped discs, to demonstrate that these discs tear to form individual, precessing rings exactly at the point when its warp amplitude

exceeds the critical value, $|\psi|_c$.

We have therefore confirmed, the main properties of the warped disc instabilities in this chapter. These include

1. that warped discs with $|\psi| < |\psi|_c$ remains stable,

2. that warped disc with $|\psi| > |\psi|_c$ can become unstable and break into discrete rings, and

3. we have also confirmed that the rate at which the warp amplitude grows in the unstable regions of the disc closely matches the predicted growth rate from the stability analysis.

4

Implications of tearing in AGN discs

In our previous chapter, we used numerical simulations of diffusive warped discs around SMBHs and revealed when they become unstable and break into precessing discrete rings. We use the instability criterion proposed by Doğan et al. (2018) and show that there is a critical warp amplitude for each disc (that depends on the value of α) at which the disc becomes unstable, and we connect it to the disc tearing behaviour observed in the numerical simulations. In this chapter, we will discuss potential applications of this disc tearing behaviour to AGN discs. We note that, warped discs have been found around a variety of astrophysical systems. The most direct evidence now exists from spatially resolved observations of protoplanetary discs (e.g. Andrews (2020)), and recent observations in this area have connected the disc behaviour with the disc tearing instability (Kraus et al., 2020). Discs that are misaligned to the spin plane of a Kerr black hole precess due to the Lense-Thirring effect. This rate of precession depends on the radius of the disc orbits from the black hole, and thus over time the disc acquires a differential twist and becomes warped. A significant evidence of warps in discs around black holes comes from water masers (Miyoshi et al., 1995; Greenhill et al., 1995, 2003).

In this chapter, we review studies on the extreme variability of AGN discs such as, large deviations in the luminosities and temperature profiles in comparison to the expected standard α disc model. Firstly, we discuss Lawrence (2018) which highlights the

large amplitude variability across the various wavelengths from optical to X-ray, observed in an increasing number of AGNs and quasars. He points out (and which Antonucci (2018) argues was already well-known; cf., e.g. the discussion of Alloin et al. (1985)) that these variations are too rapid to be due to viscous inflow of matter as predicted by the standard α disc model. In the next section, we theoretically analyse what Lawrence (2018) suggests on the idea of extreme reprocessing using the AGN STORM data of NGC 5548 from Edelson et al. (2015). Thereafter, we review Starkey et al. (2017) that showed a steep fall in the temperature profile observed in NGC 5548, and we aim to explore how good numerical models of warped discs can be found useful to explain this deviation observed in AGN discs. We review how this observed disc behaviour can be connected to the possibility of disc tearing in warped discs and how it can vary the X-ray reprocessing from the inner to the outer parts of the disc.

4.1 Quasar viscosity crisis

One of the major puzzles provided by observations is the time variability across the different wavelengths in discs around supermassive black holes. An observational study of the nucleus of a type 1 Seyfert galaxy NGC 5548 by Clavel et al. (1991), has shown that the ultraviolet continuum emissions across several bands varies simultaneously over timescales of the order of weeks to months as shown in figure 4.1, This demonstrates the UV light curve of the nucleus of NGC 5548, showing the timescale variations observed at three different wavelengths.

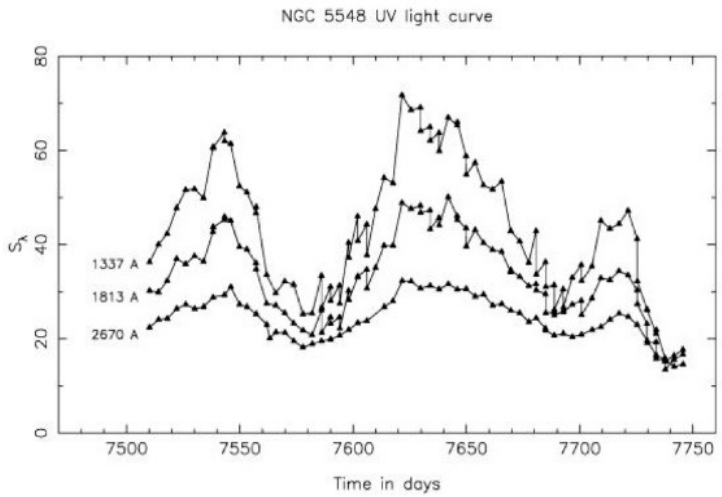

Figure 4.1: Variations at the AGN nucleus of NGC 5548 at three different wavelengths with changes in amplitude observed over a short timescale (Clavel et al., 1991). Image taken from Lawrence (2018).

This demonstrates that AGNs vary on short-timescales in the UV bands, and this variation is also observed in X-rays and optical emission. Since different wavelengths originate from different radii of the disc, these variations in time extend through the disc. The phenomenon of X-ray reprocessing can shed some light to explain the time variability in accretion discs. It states that the X-ray part of the disc heats and varies more quickly than the UV or optical regime of the disc. An important inference from observational studies on X ray reprocessing, is the consistency in the light travel delays at the different wavelengths on a scale of hours to days (Edelson et al., 2015; McHardy et al., 2016).

However, a recent crisis in the variability problem is the extreme variability (in factors of a few over a decade) in some quasars and AGNs at optical and UV wavelengths (Lawrence, 2018). Although, these changes are seen in many low luminosity objects, a recent comparison of data from the Sloan Digital Sky Survey (SDSS) and the Panoramic Survey Telescope and Rapid Response System (PanSTARRS) has shown observations of extreme variability in AGNs and quasars at high luminosities as well (MacLeod et al., 2016), and these are termed as changing look AGNs or quasars. Therefore, the wide variabilities in their optical and far UV emissions conclude that the outer parts of the disc is undergoing a large physical change on a timescale which is not compatible with

the viscous timescale.

Lawrence (2018) also suggests that the idea of extreme reprocessing can find a solution to this variability. Here, the disc is assumed to have a very low viscosity, passively heated by the central source. The energy emitted from the central source heats the disc, making the inner region $(3 - 10R_s)$ more viscous, with a much shorter timescale than the outer disc $(30 - 100R_s)$. However, the erratic variations of the central source may impose complications in this scenario, making it difficult to study the optical source size and the amplitude of variability of the discs at different wavelengths. However, we can theoretically analyse what Lawrence (2018) suggests on the idea of extreme reprocessing in NGC 5548 as discussed in the next section.

4.1.1 Timescales

In this section, we provide a discussion of the relevant timescales on which we can expect the AGN discs to show variability. The standard accretion theory by Shakura & Sunyaev (1973) predicts the basic timescale on which an accretion disc evolves or the viscous timescale on which angular momentum is transported and matter diffuses through the disc, given by (Pringle, 1981)

$$t_\nu = \frac{R^2}{\nu} = (\alpha\Omega)^{-1}\left(\frac{R}{H}\right)^2 \tag{4.1}$$

where ν is the viscosity, Ω is the local disc angular velocity and H/R is the scale height of the disc. Using the disc equations from Novikov & Thorne (1973) which accounts for the radiation pressure in the disc, Dexter & Begelman (2019) gives the equation for the viscous timescale

$$t_\nu = 500\left(\frac{\alpha}{0.02}\right)^{-1}\left(\frac{\kappa}{\kappa_{\rm T}}\right)^{-2}\left(\frac{M}{10^8 M_\odot}\right)\left(\frac{\dot{m}}{0.1}\right)^{-2}\left(\frac{R}{50R_g}\right)^{7/2} \text{ yr}, \tag{4.2}$$

where $\alpha \approx 0.1 - 0.3$ for fully ionised discs (King et al., 2007; Martin et al., 2019), κ is the opacity, κ_T is the electron scattering opacity with M being the black hole mass and $\dot{m}$ is the mass accretion rate of the disc. At first, the large amplitude variability was believed to be due to the intrinsic variation in the accretion rate within the inner regions of the disc, assuming its inner radii ranged within $R \leq 10 - 20R_g$ and equation 4.2 infers that the viscous time flow in discs may be of the order of months at very small radii. But, at large radii ($R \approx 50 - 100R_g$), the viscous timescale is way too long to explain any variability observed across the different wavelengths of discs (Cannizzaro et al., 2020).

A broad discussion of several other mechanisms to explain the variability is addressed in Cannizzaro et al. (2020). Some of the main ideas to explain this variability within discs were also assumed to be related to the fluctuations in the disc flow rate. This included thermal fluctuations within the disc or fluctuations in the local magnetic processes due to flares in corona. But, King et al. (2004) pointed out the major drawbacks of these ideas since the timescale of these fluctuations were too short and much smaller than the disc's viscous timescale, and as a result these fluctuations would not propagate to larger distances radially. This was further explored in Sniegowska et al. (2020) who argue that the source of the variability lies in instabilities operating in the accretion disc.

If we expect the disc to show variability due to the effect of disc warping, the other basic timescale is the time taken for disc orbits that are misaligned to the black hole spin to precess around the black hole spin vector, i.e. the nodal (or Lense Thirring) precession timescale given as

$$t_{\rm LT} = \frac{1}{\Omega_{\rm LT}} = \frac{c^2 R^3}{2GJ_h} = \frac{1}{2a}\left(\frac{R}{R_g}\right)^3 \frac{GM}{c^3} \tag{4.3}$$

where $\Omega_{\rm LT}$ is the precession frequency, R is the disc radius, J_h is the black hole angular momentum, a the black hole spin, and $R_g = GM/c^2$ is the gravitational radius of the black hole. Therefore, if we assume the disc to be warped, we can expect the variability

in the precession time scale ($t_{\rm LT}$) to manifest through the disc. In the following section, we can analyse the time variability of NGC 5548 from the data reported in Edelson et al. (2015), as a part of the AGN STORM series (detailed further in section 4.2).

4.1.2 Study of NGC 5548

We consider the data of NGC 5548 reported in Edelson et al. (2015), with its central peak wavelength observed in the UV and optical bands using *Swift* and Hubble Space telescopes (*HST*). Although, the different regions of the disc contributes at all wavelengths, it is important to understand the radial extent of the disc that contributes to the emission in each waveband. For example, each part of the disc may have a certain percentage of emission in the UV or optical band. For simplicity we approximate the radial location of the emission in a given waveband to be the radial location of the temperature given by Wien's displacement law.

From the temperature profile, we aim to learn the radial extent of the UV and optical regions in the disc. Also, we know that the timescale of precession and viscous timescale are both functions of radius. Therefore, from the value of the radius corresponding to each wavelength, the values of the timescale of precession and viscous timescale can be calculated.

From the observed values of central peak wavelength, we can calculate the temperature from the Wien's displacement law given by:

$$\lambda T = 2.9 \times 10^{-3}\text{mK}. \tag{4.4}$$

The quantified equation of temperature as a function of radius (refer equation 3.20 in Peterson (1997)) is

$$T(r) = 6.3 \times 10^{5} \left(\frac{\dot{M}}{\dot{M}_{\rm Edd}}\right)^{1/4} M_8^{-1/4} \left(\frac{r}{R_s}\right)^{-3/4} \text{K} \tag{4.5}$$

where $T(r)$ is the temperature at radius r, $\dot{M}/\dot{M}_{Edd}$ is the Eddington mass accretion rate, assuming a radiative efficiency of $\eta = 0.1$ and M_8 is the blackhole mass in units of 10^8 $M_\odot$. From the observed data of central peak wavelengths given by Edelson et al. (2015), we can calculate the temperatures corresponding to each wavelength using equation (4.4). This value of temperature is further used to calculate the radius in units of the Schwarzschild radius (R_s) using equation 4.5. The radii values are calculated, assuming a black hole of mass $\approx 3.2\times\ 10^7\ M_\odot$ and at a value for $\dot{M}/\dot{M}_{Edd} = 0.03$ (the values used in Edelson et al. (2015)). Thus, we can tabulate (as shown in table 4.1) the central peak wavelengths observed at different bands, along with their calculated values of temperature and radii (in units of R_s).

Band	$\lambda(\mathring{A})$	T(Kelvin)	R(R_s)
HST	1367	2.12×10^4	41.8
UVW2	1928	1.5×10^4	64.9
UVM2	2246	1.29×10^4	79.4
UVW1	2600	1.11×10^4	96.9
U	3465	8.37×10^3	144.4
B	4392	6.6×10^3	193.5
V	5468	5.3×10^3	265.9

Table 4.1: Table representing the various UV and optical bands used for observing NGC 5548, with the corresponding value of their central wavelength (in Angstrom). Also, included are the calculated values of temperature (in Kelvin) along with the radius of each wavelength band (in terms of R_s, where $R_s = 2GM/c^2$). HST (Hubble Space telescope), UVW2, UVM2, UVW1 and U represent the different ultra-violet (UV) wavelengths, whereas B (Blue) and V (Visual) bands represent the optical filters used for observing NGC 5548.

The precessional timescale of an orbit at radius R (in units of R_g) is given as (or refer equation 4.3)

$$t_p = \frac{1}{2a}\left(\frac{R}{R_g}\right)^3 \frac{GM}{c^3} \tag{4.6}$$

where a is the dimensionless spin parameter and R_g is the gravitational radius ($R_g = R_s/2 = GM/c^2$). Also, the viscous timescale at radius R is

$$t_{\rm visc} = \frac{R^2}{\nu} \tag{4.7}$$

where

$$\nu = \alpha c_s H = \frac{\alpha c_s^2}{\Omega} \tag{4.8}$$

with

$$\Omega = \sqrt{\frac{GM}{R^3}}. \tag{4.9}$$

From the value of radius at each band (obtained from equation (4.5)), we now calculate the precessional timescale, the viscous timescale and the light travel time ($t_c = R/c$) at each radius as shown in table 4.2.

Band	R(R_s)	$t_{\rm p}$(years)	$t_{\rm visc}$(years)	$t_{\rm c}$(mins)
HST	41.8	1.4	9.5×10^3	3.6
UVW2	64.9	5.4	1.8×10^4	5.6
UVM2	79.4	10	2.4×10^4	6.8
UVW1	96.9	18.2	3.3×10^4	8.4
U	144.4	60.4	6.1×10^4	12.6
B	193.5	1.4×10^2	9.5×10^4	17
V	265.9	3.7×10^2	1.5×10^5	23.2

Table 4.2: Table representing the radius of each wavelength (in terms of R_g) and the calculated values of the timescale of precession (in years), where we assume the black hole spin to be maximal, i.e. a = 1) and viscous timescale (in years) and the light travel time (in minutes) at different wavelength regimes of the disc of NGC 5548. HST (Hubble Space telescope), UVW2, UVM2, UVW1 and U represent the different ultra-violet (UV) wavelengths, whereas B (Blue) and V (Visual) bands represent the optical filters used for observing NGC 5548.

It can be concluded from this table, that the value of the precessional timescale varied between 1.4 years in the lower UV wavelengths to 100 times more in the optical band of the disc. This proves that it is difficult to see over an observational period of several months, a significant variability in the UV/optical wavelengths. It is also clear that the viscous timescale at these radii is far too long to explain the variability in discs. Numerical models of warped discs can be proven useful, to explain such cases of extreme variability. One idea is by using accretion rate in discs as a proxy to energy dissipation rate and thus luminosity (further detailed in section 4.3). A prominent example by Nixon et al. (2012a) used SPH hydrodynamical simulations to study disc tearing in warped discs around AGNs. As the precession timescale is shorter than the standard viscous timescale

in a warped disc, the effect of precession can increase the accretion rate on to the central object by transferring matter to inner radii faster than that due to the viscous torques. The efficiency of this process is dependent on the misalignment angle between the disc and the black hole. For small angles, the accretion rate may be enhanced by a factor of order unity, whereas at larger angles the gas can fall a considerable distance in radius and increase the accretion rate by several orders of magnitude (Nixon et al., 2012b). In a subsequent work, we aim to extend our work on the numerical analysis to study disc tearing in warped discs (presented in chapter 3) and examine their accretion rate curves to examine the evidence of any aperiodic behaviour, i.e. investigate if they show short or longer timescale variability. In the next section, we review another example of variability in the temperature profiles of NGC 5548. We discuss, Starkey et al. (2017) that finds a steeper slope at $\alpha = 0.99$ in the temperature-radius profile of NGC 5548, contrary to the value for a standard disc predicted by theory, where $\alpha = 0.75$ ($T(r) \propto r^{-\alpha}$).

4.2 Anomalous temperature profiles

Reverberation mapping of accretion discs act as a probe to examine their structure. The discs around AGN vary in their luminosities across the different wavelengths. The observations demonstrate that these variations at different wavelengths show a lag which increases with wavelength (Shappee et al., 2014; Edelson et al., 2015). The light-travel delay originates as the photons from the source, first travel to a reprocessing site on the accretion disc before being re-emitted to the observer (also explained in section 1.2.3).

It has been a continuing challenge to use different models to study variability in accretion discs and measure their sizes, logarithmic slope of the temperature or their inclination with respect to the observer. A simpler model to study the accretion-disc variability is the lamppost model, which assumes that the disc around a compact point source irradiates as a black body accretion disc (Frank et al., 2002). In this model, the

temperature profile of the disc declines as $T(r) \propto r^{-3/4}$ and the wavelength varies with temperature as $\lambda \propto T^{-1}$. Therefore, if we consider the light-travel delay time given by $\langle\tau\rangle = R/c$, it increases with wavelength as $\langle\tau\rangle \propto \lambda^{4/3}$.

A large scale observing campaign named the AGN Space Telescope and Optical Reverberation Mapping Project (STORM) was set up to research on NGC 5548 with it being one of the most thoroughly studied AGNs. The first paper in this project series by De Rosa et al. (2015) demonstrated light curves observed from Hubble Space Telescope (*HST*) and determined the time lags in the CIV and Lyα light curves using a cross corelation analysis. Paper II in the series by Edelson et al. (2015) studied the optical and UV lightcurves from *Swift* and inferred the dependence of time lags on the wavelength, $\langle\tau\rangle \propto \lambda^{4/3}$. Paper III by Fausnaugh et al. (2016) included ground-based observations and analysed the data using cross-correlation (White & Peterson, 1994) and JAVELIN (Zu et al., 2011). Paper IV by Goad et al. (2016) identified and studied the changing behaviour in the broad emission lines also termed as BLR holiday (see also the discussion in Goad et al. (2019)). These emission lines tracked the variations in the continuum in the first 1/3 of the AGN STORM campaign, but went fainter than expected in the latter 2/3 of the campaign. This behaviour deviated from the expected nature of the emission lines to reverberate with time delays relative to the continuum wavelengths. This anomalous behaviour might be either due to the partial obscuring of the Broad Line Region (BLR) or due to a change in the shape of the disc structure (Goad et al., 2019). Paper V (Pei et al., 2017) examined the optical spectroscopic data to measure the velocity delay maps of Hβ and HeII light curves. Paper VII by Mathur et al. (2017) detailed the analysis of X-ray observations. Paper VIII by Kriss et al. (2019) explored the time variability of the emission and absorption lines and paper IX by Horne et al. (2020) examined the velocity-delay maps resulting from the spectral variations. In this section, we discuss paper VI of the AGN STORM series by Starkey et al. (2017) that analysed how to fit

19 overlapping continuum light curves from Hubble Space Telescope (*HST*), *Swift*, and ground-based observations of NGC 5548 to the lamp-post model using a Monte Carlo Markov Chain code, CREAM.

CREAM (**C**ontinuum **RE**processing **A**GN **M**CMC) is a model, firstly introduced in Starkey et al. (2016) to fit the AGN light curves using the lamp-post model and deduce the posterior probability distributions for temperature T, inclination i, slope of the temperature radius profile α and the lamp-post light curve $X(t)$. CREAM analyses the lamp-post light curve as a sum of Fourier sine and cosine terms. The continuum light curve at a wavelength λ is given as:

$$F_\nu(\lambda, t) = \bar{F}_\nu(\lambda) + \Delta F_\nu(\lambda) \int_0^\infty \psi(\tau|\lambda)\ X(t-\tau) d\tau \tag{4.10}$$

where $\bar{F}_\nu(\lambda)$ and $\Delta F_\nu(\lambda)$ are the constant and variable components of the light curve. The contribution of the light curve at earlier time $X(t-\tau)$ is represented by the response function $\psi(\tau|\lambda)$, normalised as:

$$\int_0^\infty \psi(\tau|\lambda)\ d\tau = 1. \tag{4.11}$$

Starkey et al. (2016) explains how CREAM parametrises the response function and shows the dependence of $\psi(\tau|\lambda)$ on T, i and α. This study is further explored in Starkey et al. (2017) which uses the CREAM fitting code to check the convergence of the parameters in 19 AGN STORM continuum light curves of NGC 5548 with the lamp-post model. The posterior probability distributions for i, T of the linearised α disc or lamp post model (labelled as model 1) with $\alpha = 3/4$ is calculated. Starkey et al. (2017) runs the simulation using CREAM to fit the slope of the temperature-radius profile which obtains $\alpha = 0.99 \pm 0.03$, $i = 36 \pm 10^\circ$ and $T = (4.71 \pm 0.46) \times 10^4$ K as shown in figure 4.2.

Therefore, this study finds that the disc of NGC 5548 shows a steeper fall in tem-

perature than the expected standard α disc model. Starkey et al. (2017) also addresses theories which may likely explain this anomalous behaviour in the temperature profile of the disc. Firstly, the two stage reprocessing model proposed by Gardner & Done (2017), where the disc is considered to have a second reprocessing region or a puffed Comptonised region.

Secondly, when the disc is warped (Nixon et al., 2012a; Nealon et al., 2015), i.e. if the inner part of the disc is misaligned to the outer disc. It is a possibility that the observed light curves may be a resultant of reprocessing and emission from the tilted inner disc. Therefore, the presence of a warp in the disc can alter the X-ray reprocessing from the inner to the outer part of the disc as shown using a sketch, in figure 4.3. This sketch shows the reprocessing model in a warped disc, and finds how the presence of a warp in the disc can affect the reprocessing of light from the inner parts, which is further re-emitted at the outer parts of the disc.

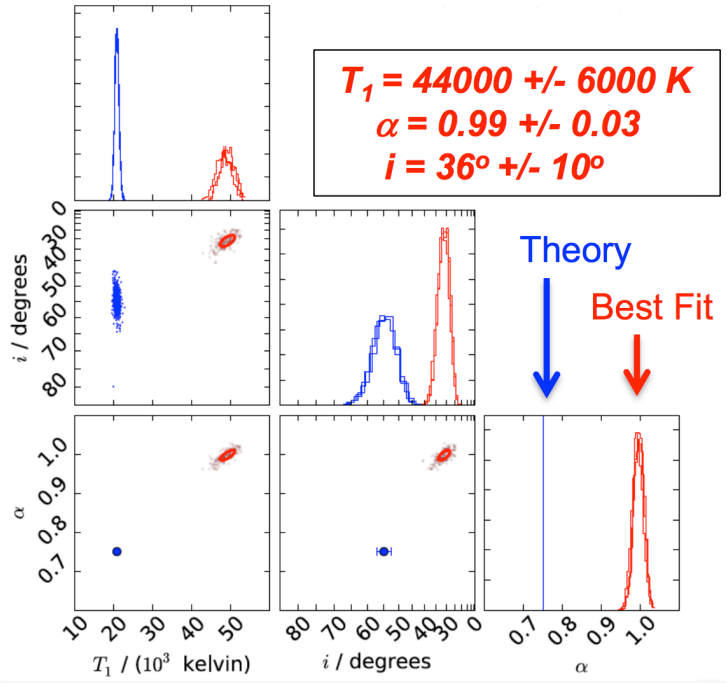

Figure 4.2: This figure from Starkey et al. (2017) demonstrates the posterior distributions of inclination i, temperature − radius slope α and temperature T_1. Model 1 (blue) denotes the theoretical fit for a steady state disc with $\alpha = 0.75$. Model 2 (red) indicates the fitted parameters using CREAM, which discovers a steep temperature profile with $\alpha \sim 1$.

Furthermore in figure 4.3b, we show that the presence of the warp in the inner part

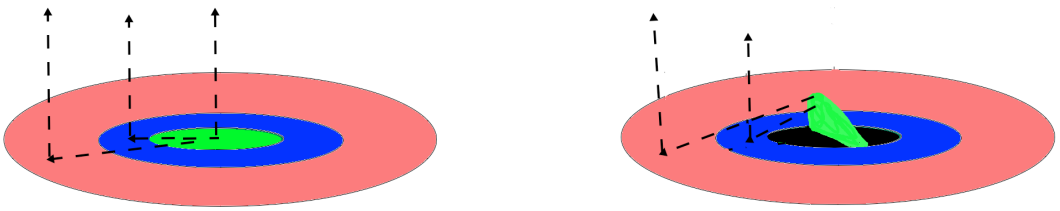

(a) (b)

Figure 4.3: Figure (a) shows the reverberating disc model where the photons from the inner part of the disc are reprocessed at the outer parts of the disc, further re-emitted to the observer. Figure (b) shows the reverberation disc model for a warped disc where the inner disc is misaligned to the outer disc. This figure clearly shows how the presence of a warp can cause a variability in the photons reprocessed and re-emitted at the outer parts of the disc.

of the disc can affect the amount of light reprocessed, re-emitted and observed from the outer parts of the disc. If we consider the scenario of disc tearing in the inner regions of the disc, which forms precessing rings of gas (e.g. due to LT effect in AGN discs), the effect of precession will not only alter the amount of light reaching the outer parts, but can also vary the time lags observed at different wavelengths of the outer disc, with time.

4.3 Variability from disc tearing

It is important that we discuss the implication of disc tearing in warped AGN discs which may explain the variations in the timescale of large amplitude optical/UV fluxes observed in AGN. Numerical simulations of tilted warped discs have revealed that they can break into discrete rings that can subsequently precess independently, and showed how they may provide a source of variability in black hole accretion (Nixon et al., 2012a). The simulation behaviour, which sees rings of matter break off from the rest of the disc in regions where the warp amplitude is high, thus hints at the formation of an underlying instability. Doğan et al. (2018) explored this instability in detail (using the stability analysis of warped disc equations by Ogilvie (2000)) and showed that for $\alpha \leq 0.2$, there is always a critical warp amplitude ($|\psi|_c$ that depends on the value of α) at which the disc becomes unstable. We can connect the instabilities in warped discs with the disc

tearing behaviour, further tested using numerical simulations (refer chapter 3). As the precession timescale (given by equation 4.3) must be shorter than the standard viscous timescale (equation 4.1) in the disc to produce a substantial warp (Nixon et al. (2012a) or refer chapter 3), this process enhances the accretion rate on to the central object by delivering matter to small radii faster than viscous torques could do so. We demonstrate the variability in the accretion rates with time (as shown in figure 4.4), from one of our simulations presented in chapter 3.

The black line in figure 4.4 corresponds to the accretion rate in the simulation with $\alpha = 0.1$, $H/R = 0.01$, and $\beta = 10°$, where β is the initial angle between the disc and black hole spin. The red line corresponds to the accretion rate for the same parameters, except the value of $\beta = 60°$. Our simulations show that, the disc inclined at 10° remains stable with no disc tear, and achieves a mild warp which does not strongly impact the disc structure (refer figures 3.13 and 3.16 in chapter 3) and therefore, its accretion rate remains low. On the other hand, a disc at 60° showed an evidence of disc tear (shown by figures 3.25 and 3.28 in chapter 3), thus forming individual, precessing rings in the unstable disc regions. Furthermore, the accretion rate of the disc tilted at 60° showed substantial variability, as the disc becomes unstable due to disc tearing. As shown in the figure, the inner disc is unstable at early times, resulting in periodic accretion of rings of matter. Therefore, we can conclude that the variations in the accretion rate on to supermassive black holes are induced by the tearing instability in warped discs. We also expect that, this variability reflects highly on the rate of generation of energy from the accretion flow, in the inner regions of the disc. Moreover, this alters the amount of energy reprocessed and remitted from the outer parts of the disc which may be a good explanation to the observed UV/optical variability in AGN discs (Lawrence, 2018).

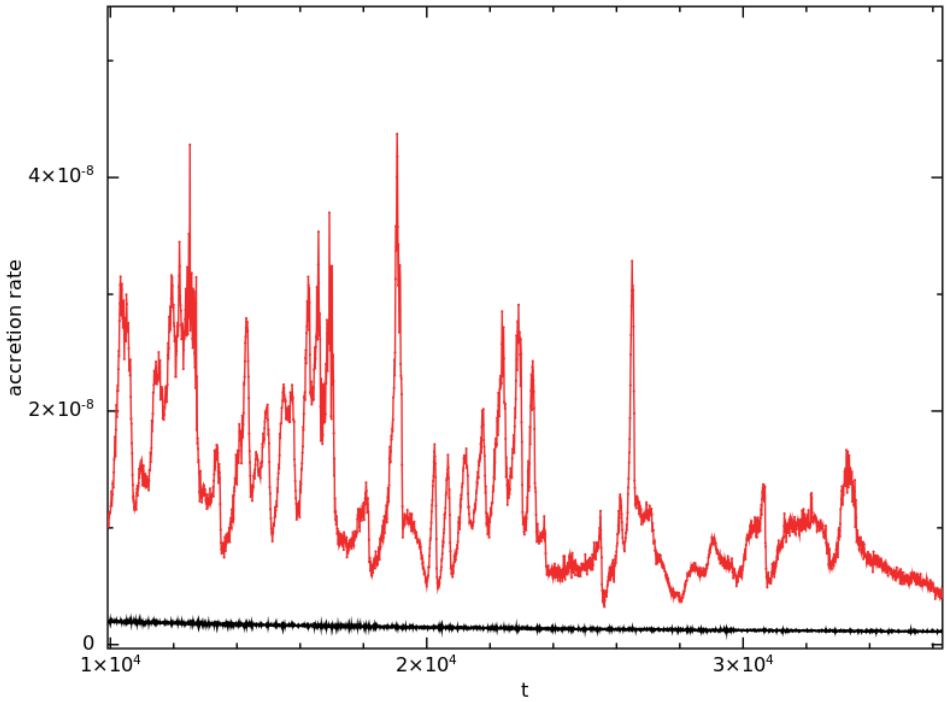

Figure 4.4: The two curves represent the change of accretion rate with time, in discs (refer chapter 3) with $\alpha = 0.1$, $H/R = 0.01$, and at tilts 10° (black line) and 60° (red line) respectively. The change in accretion rate is plotted at times t = $10^4 \approx 10$ orbits at $R_{\rm out}$ to t = 3.61 $\times 10^4 \approx 35$ orbits at $R_{\rm out}$ and the fraction of disc considered for both cases lie at radii between $9R_g$ and $22R_g$ (where G = M = c =1). The disc inclined at 10° does not show much variability in its rate of accretion and remains low, analogous to a planar accretion disc. But the tilted warped disc at 60° shows large variability in the accretion flow rates, which are produced due to its disc tearing instability and form discrete, precessing rings of matter. The peak value of the rate at which mass is accreted when the disc is tilted at 60° is 28 times more than rate of accretion at a tilt of 10°.

The disc dynamics resulting from the instability or disc tearing of warped discs can produce different scenarios. If the innermost regions of the disc are unstable, then we expect the variability to manifest on the precession timescale of the inner disc regions, and the disc matter plunges directly into the hole. If, instead, the disc is unstable further out such that the mass flow from the unstable region does not reach the ISCO, then the matter circularises at a new smaller radius. Therefore, once the material is circularised at the new smaller radius, a strong increase in disc luminosity follows over a timescale of the order of the viscous timescale given by Dexter & Begelman (2019) (refer equation 4.2)[1]. These results may be potentially consistent with the short timescales to explain the large variations in optical/UV fluxes observed in the AGN lightcurves (Lawrence, 2018).

Furthermore, numerical models of disc tearing in warped discs can also be used to

[1]If we assume the matter to circularise at a new smaller radius, say $R \approx 20R_g$, then it follows the viscous timescale given by Dexter & Begelman (2019), i.e. $t_\nu \approx 1.3$ yrs.

examine how the orientation of a disc with respect to the oberver can impact the observable properties. In general, the angle between the black hole spin and the accretion disc angular momentum is expected to decrease over time through dissipation between neighbouring rings; Lense-Thirring precession of each ring maintains the inclination angle with respect to the black hole, and subsequent interaction between neighbouring rings that occupy different planes reduces the inclination to the black hole spin. This means that a line-of-sight that is closer to the black hole spin axis than the original disc misalignment always has a clear view of the disc centre. However, if the line-of-sight to the black hole passes through the disc, then additional variability due to obscuration effects is possible. If the disc warp move into (or out of) the line-of-sight, then the emission properties may vary significantly as the inner regions of the disc are blocked (or revealed). In figure 4.5, we show an example from the 3D hydrodynamic simulations of a disc ($\alpha = 0.03$, $H/R = 0.02$ and $\beta = 60°$) viewed at the same time, but from different orientations. The black hole spin axis is in the z-direction, and the reference views are in the $x - y$ plane, and therefore the black hole spin points out of the page in the left-most panels. The top row of panels, from left to right, are views of the disc starting with the $x - y$ plane, which are subsequently rotated by an angle X around the x-axis. The bottom panels are the same, but now the rotation is performed by an angle Y around the y-axis. In some configurations, the central regions are clearly visible, and in others they are largely blocked from view either by the outer disc or a precessing ring which is crossing the line-of-sight to the disc centre. Therefore, we note that while the geometry may be important for determining which parts of the disc are seen by the observer, it is also important for determining which parts of the disc are available to be seen by the material that makes up the broad line region (which assumed to be clouds orbiting near the outer disc regions as shown in figure 1.5 in chapter 1). As the matter comprising the broad line region is typically expected to orbit close to the disc, it is plausible that precessing rings in the unstable

region of the disc may act to block the central disc emission from fully illuminating the broad line regions. Thus, the flux arriving at the broad line regions may be time variable due to a disconnect between the continuum and emission lines. This may thus offer a potential cause for the recently observed broad line holidays (Goad et al., 2016; Goad et al., 2019).

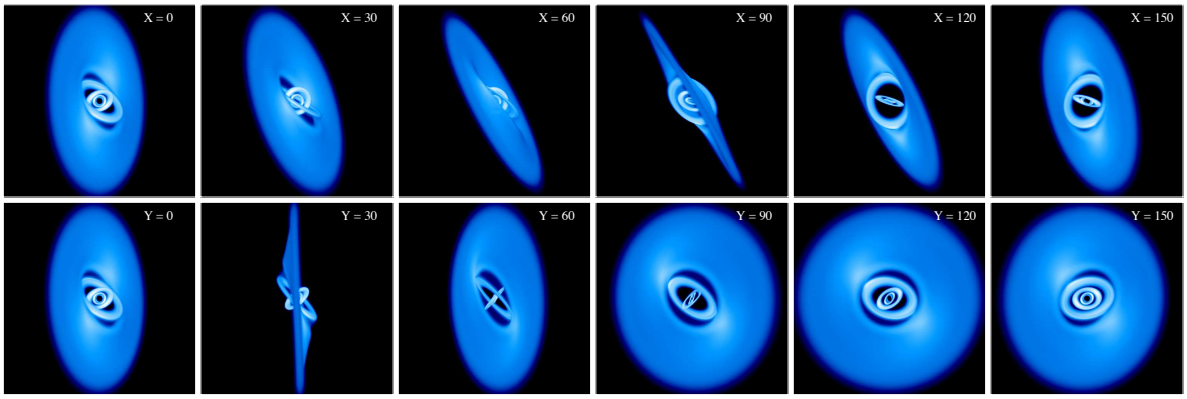

Figure 4.5: 3D simulations which show disc tearing in a warped disc at $\beta = 60°, \alpha = 0.03$ and $H/R = 0.02$. Each panel depicts the same simulation at the same time, viewed from different orientation. The left-hand top and bottom row panels both show the same view (in the x-y plane) where the black hole spin axis which coincides with the z-axis pointing out of the page. Then, from left to right, the top row shows the disc view with the disc rotated by an angle X around the x-axis where the value of X in each case is given in the panel. In contrast, the bottom row is rotated from the x-y plane by an angle Y around the y-axis. In some cases the majority of the disc is visible and pointed predominantly towards the observer. While in other cases, the inner disc regions are highly inclined, or obscured by either the warped outer disc or an interloping ring of matter in the unstable region.

4.4 Discussions and Conclusions

We have reviewed studies that discuss the evidence of extreme variability in AGNs and quasars in the UV and optical wavelengths. The disagreement in the observed values on sizes, luminosities and the disc temperatures of AGN discs and the expected values from a standard α disc model still remains an unresolved issue. This emphasises why numerical analysis of AGN disc models is essential to understand the disparity between theoretical and observational results.

Firstly, we discuss Lawrence (2018) which highlights the issue concerning the timescale of large amplitude luminosity variations in AGN. This study implies that if one calculates the radius in the disc which encompasses enough mass to drive the observed increase

in luminosity (i.e. an increase in accretion rate), then the viscous timescale from this radius is typically orders of magnitude larger than the observed variation timescale. We establish this further, from the data analysis of Edelson et al. (2015) to calculate the temperatures and the corresponding radial extent of the disc at each wavelength observed. The timescale of precession and the viscous timescale are also calculated at each radii. Our results show that these timescales are too long to explain the extreme variability in the UV/optical wavelengths observed over a period of few months. We also summarised Starkey et al. (2017) which details the fitting of light curves observed in NGC 5548 with a linearised α disc model. This analysis yields a steeper temperature fall with a slope of $\alpha = 0.99 \pm 0.03$ which can cause a resultant decline in the surface brightness of the disc. These examples of observational variability exhibited in AGN accretion discs illustrate why its important to use good theoretical and numerical models of evolving accretion discs and obtain a better understanding of these structures.

In this chapter, we explore the possibility of disc tearing in warped accretion discs and investigate whether it plays an important role in producing variable accretion flows around supermassive black holes, and explain their observational variability. Here, we discuss the possibility of how the dynamics of disc tearing may provide a source of variability in black hole accretion, the timescales on which variability might manifest in the observable properties, and how the disc geometry can affect what we see. We also discuss how accretion rate is a reasonable proxy to study the rate at which energy can be extracted from the disc orbits in disc tearing events. The accretion rate/energy dissipation changes for some disc parameters show that the disc tearing instability can occur predominantly at the disc inner edge. In future work, we will develop more sophisticated simulation models to connect in more detail with the observational data and examine if these cases show similarity with the quasi periodic eruptions observed in Seyfert 2 galaxy GSN 069 (Miniutti et al., 2019) and RX J1031.9+2747 (Giustini et al., 2020) or the heartbeat

modes observed in some X-ray binaries (e.g.GRS 1915+105) (Zoghbi et al., 2016).

5

Accretion discs in SPH

Accretion discs occur on many scales in astrophysics, from star and planet formation to supermassive black hole accretion (Pringle & Rees, 1972; Pringle, 1981). We know that accretion discs are formed because gas has angular momentum with respect to the central object it orbits. An initial disc formed from the infalling gas generates an eccentric disc. Angular momentum is conserved within the disc, as it radiates orbital energy and the disc orbits settle into the configuration of least energy for a given angular momentum which is a circle. This circularisation is often assumed to occur faster than the radial evolution of the disc, and thus most discs are considered circular. Sometimes, these orbits may not all be in the same plane and in this case the disc is initially warped (Papaloizou & Pringle, 1983; Ogilvie, 1999). The radial evolution of the disc is enabled by viscosity, caused due to disc turbulence from the magneto-rotational instability (Balbus & Hawley, 1991) which facilitates the spreading of the disc. As a result, angular momentum of the disc is transferred outwards, allowing the mass to flow inwards (Pringle, 1981). This angular momentum transport can be characterised by the turbulent viscosity $\nu = \alpha c_{\rm s} H$ in the disc (Shakura & Sunyaev, 1973).

In many cases the dynamics of discs are complex, and numerical simulations are utilised to make progress. One such method which studies simulating accretion flows in discs is Smoothed Particle Hydrodynamics (SPH; Lucy 1977; Gingold & Monaghan

1977). SPH is a Lagrangian particle based method for solving the equations of motion of a fluid (also detailed in section 1.7). In the next section, we discuss the equations and methods that are employed to create discs of SPH particles for numerical simulations. The initial conditions used in setting up these discs are adequate at the resolution typically employed for SPH discs. However, at higher resolution a lack of dynamical equilibrium in the initial conditions leads to the formation of unwanted pressure waves in the simulations. Although, this lack of equilibrium was previously known, there are past works which argue that no self-consistent analytical disc structure exists when radial pressure gradients are taken into account (Hoshi & Shibazaki, 1977). In this chapter, we summarise a method which is independent of the disc parameters to damp these waves, and importantly a method that does not rely on artificial viscosity - allowing the relaxation time to be independent of resolution.

5.1 Disc density structure

The surface density evolution for the disc is given by:

$$\frac{\partial \Sigma}{\partial t} = \frac{1}{R}\frac{\partial}{\partial R}\left(\frac{\frac{\partial}{\partial R}\left[\nu \Sigma R^3 \left(-\Omega'\right)\right]}{\frac{\partial}{\partial R}\left(R^2\Omega\right)}\right) + \dot{\Sigma}\,, \tag{5.1}$$

where R is the cylindrical radius coordinate, Σ is the disc surface density, ν is the disc viscosity and $\dot{\Sigma}$ defines the rate at which mass is added to the disc given as:

$$\dot{M}_{\rm add} = 2\pi \int_{R_{\rm add}-w_{\rm add}}^{R_{\rm add}+w_{\rm add}} \dot{\Sigma}(R) R \mathrm{d}R\,, \tag{5.2}$$

where mass is added in the interval $[R_{\rm add} - w_{\rm add}, R_{\rm add} + w_{\rm add}]$. The surface density can be written in terms of the volume density, ρ as

$$\Sigma = \int_{z=-\infty}^{z=+\infty} \rho \mathrm{d}z\,. \tag{5.3}$$

In a steady state, a Keplerian disc has a surface density profile given by:

$$\nu\Sigma \approx \text{const} \equiv \frac{\dot{M}}{3\pi} \tag{5.4}$$

where we assume a Shakura & Sunyaev (1973) viscosity with a constant α and $c_\mathrm{s} = c_{\mathrm{s}_0} R^{-q}$, thus $H = H_0 R^{-q+3/2}$ expressed as power-law functions of radius. Therefore, we have

$$\Sigma_\mathrm{pl} = \frac{\dot{M}}{3\pi\nu} = \Sigma_0 R^{2q-3/2}\,. \tag{5.5}$$

However, equation (5.5) does not take account of any radial boundary conditions. The standard approach is to assume a zero-torque inner boundary condition (i.e. $d\Omega/dR = \Omega' = 0$ at R_in) such that the surface density goes to zero there. In this case the standard conservation equations (cf. Appendix A) give

$$\begin{aligned} \Sigma_\mathrm{smoothpl} &= \frac{\dot{M}}{2\pi\nu}\frac{[R_\mathrm{in}^2\Omega_\mathrm{in}/R^2\Omega - 1]}{R\,(\Omega'/\Omega)} \\ &= \frac{\dot{M}}{3\pi\nu}\left[1 - \left(\frac{R_\mathrm{in}}{R}\right)^{1/2}\right]\,. \end{aligned} \tag{5.6}$$

This represents the most often used equation for the initial disc surface density in SPH simulations. It is often assumed that it is not worth smoothing the outer edge of the disc, since there is too little mass there and any propagating pressure waves have too little momentum to drive significant density perturbations in the disc. Furthermore, we can derive the full solution for a disc with mass added at some radius (R_add) and a defined inner (R_in) and outer boundary (R_out). If we apply zero-torque inner and outer boundary conditions, the surface density profile of a steady disc structure is given by

$$\Sigma_\mathrm{steady} = \begin{cases} \dfrac{f\dot{M}_\mathrm{add}}{2\pi\nu(1+f)}\dfrac{[R_\mathrm{in}^2\Omega_\mathrm{in}/R^2\Omega - 1]}{R\,(\Omega'/\Omega)} & \text{for} \quad R \leq R_\mathrm{add} \\ \dfrac{\dot{M}_\mathrm{add}}{2\pi\nu(1+f)}\dfrac{[1 - R_\mathrm{out}^2\Omega_\mathrm{out}/R^2\Omega]}{R\,(\Omega'/\Omega)} & \text{for} \quad R > R_\mathrm{add}\,. \end{cases}$$

where f is given by

$$f = \frac{R_{\rm add}^2\Omega_{\rm add} - R_{\rm out}^2\Omega_{\rm out}}{R_{\rm in}^2\Omega_{\rm in} - R_{\rm add}^2\Omega_{\rm add}} \tag{5.7}$$

The derivation of this steady disc surface density is given in Appendix A. For a disc with e.g. no mass flow off the outer boundary, the solution is given by

$$\Sigma_{\rm steady} = \begin{cases} \dfrac{\dot{M}}{3\pi\nu}\left[1 - \left(\dfrac{R_{\rm in}}{R}\right)^{1/2}\right] & \text{for} \quad R \leq R_{\rm add} \\ \dfrac{\dot{M}}{3\pi\nu}\left[\left(\dfrac{R_{\rm out}}{R}\right)^{1/2} - 1\right] & \text{for} \quad R > R_{\rm add}\,. \end{cases} \tag{5.8}$$

The disc is assumed to be in a vertical hydrostatic equilibrium which allows us to calculate the density structure from the surface density equations. For a disc with a vertically isothermal equation of state (also given by equation 1.39 in section 1.3.2), the density is given by

$$\begin{aligned} \rho(R,z) &= \rho_0 \exp\left(-\frac{z^2}{2H^2}\right) \\ &= \frac{\Sigma(R)}{H\sqrt{2\pi}} \exp\left(-\frac{z^2}{2H^2}\right)\,, \end{aligned} \tag{5.9}$$

where $H = c_{\rm s}/\Omega$. Thus, we have a density profile for the disc which can be created by a set of particles, and this is represented by determining particle positions and velocities in the disc.

5.2 Determining particle positions

In this section we discuss how to position particles to achieve the required density distribution. This is done by a Monte-Carlo method, where particles are drawn from the relevant distribution. Firstly, let's discuss the method and then how it is used in this case.

5.2.1 Monte-Carlo method

For a given function $f(x)$, with total integral $\int_{x_1}^{x_2} F(x)\mathrm{d}x$ where $F(x) = f(x)g(x)$ (with $g(x)$ being the relevant Jacobian), we must define $F_{\max} = \max\{F(x)\}$ for $x \in [x_1, x_2]$. Then the method proceeds as:

```
fx = 0
ftest = 1
do while (ftest > fx)
  set ran1,ran2
  x = x1 + (x2-x1)*ran1
  ftest = Fmax*ran2
  fx = F(x)
enddo
```

where `ran1` & `ran2` are random numbers $\in [0, 1]$ which are newly generated at each step of the loop. Once a value of the function is found to be less than a random fraction of $F_{\max}$, the do loop is exited and the value of x is accepted for this iteration (e.g. for a particular particle). The likelihood of acceptance is then given by $F(x)/F_{\max}$ and thus more particles are placed where $F(x)$ is largest to achieve the desired function $f(x)$. This method can be extended for the surface density distribution of particles at a given radius that corresponds to $\Sigma(R)$, where $M_{\rm d} = 2\pi \int_{R_{\rm in}}^{R_{\rm out}} \Sigma(R) R\mathrm{d}R$ with $F(R) = R\Sigma(R)$. This is given as

```
fx = 0
ftest = 1
do while (ftest > fx)
  set ran1,ran2
  R = rin + (rout-rin)*ran1
```

```
  ftest = Fmax*ran2
  fx = R*sigma_func(R)
enddo
```

where `sigma_func(R)` returns the value of $\Sigma(R)$. The particles at x and y positions are represented by a random angle $\phi \in [0, 2\pi]$, thus assigning $(x, y) = R(\cos\phi, \sin\phi)$. The z position is also produced using the Monte-Carlo method given as:

```
zmin = -3.0*H*sqrt(2)
zmax = -zmin
Fmax = 1
fx = 0
ftest = 1
do while (ftest > fx)
  set ran1,ran2
  z = zmin + (zmax-zmin)*ran1
  ftest = Fmax*ran2
  fx = exp(-(z/(sqrt(2)*H))**2)
enddo
```

where H is calculated at the pre-determined radius R. An initial estimate of the particle smoothing length is also needed and this can be determined from the particle density (5.9), where the smoothing length h is given by (e.g. Price, 2012)

$$h = \eta \left(\frac{m_{\rm p}}{\rho} \right)^{1/3}, \tag{5.10}$$

where $m_{\rm p}$ is the mass of each particle and η is the smoothing length in units of the mean particle spacing (e.g. $\eta = 1.2$ with the cubic spline kernel is the default in PHANTOM).

In the case of the power-law and smoothed power-law setups, the values of Σ_0 and

$F_{\max}$ can be found analytically. However for the steady disc, it is calculated by integrating the diffusion equation 5.1 in time. The value of Σ_0 is evaluated by calculating the surface density without normalisation and then calculating the disc mass and rescaling it to the requested value. To calculate $F_{\max}$, the computed Σ function is used to create an array of values for $R\Sigma$ and find its maximum value.

5.2.2 Setting particle velocities

From the previous section, we now have a set of particles with cartesian positions which map out the disc's density profile. Next, we must set the particle velocities appropriate to the disc properties. For most accretion discs (circular), we have $V_R = V_z = 0$ in the initial conditions. But, we can calculate V_ϕ from radial force balance equation given by:

$$\frac{V_\phi^2}{R} = \frac{1}{\rho}\frac{\partial P}{\partial R} + \frac{\partial \Phi}{\partial R}\,, \tag{5.11}$$

where P is the pressure and Φ is the gravitational potential.

5.3 Code

We can briefly describe the working of the disc setup routine in this section, assuming that appropriate parameters have been set.

1. The first step is to calculate the values of the normalisation constants for the requested sound-speed and surface density power-laws.

2. Next the surface density and mass accretion rate are calculated.

3. We then calculate the derivatives to set up the particle velocities, i.e. dP/dR and $d\Phi/dr$.

4. We then set the particle positions and velocities following the methods as outlined in the previous section.

5.4 Simulation Tests

In this section, we discuss the initial particle distributions and their properties, and how we test the disc evolution with the SPH code PHANTOM. Firstly, we consider a disc composed of one million particles with a central gravitating body of unit mass. We impose an inner boundary at $R_{\rm in} = 1R_g$ and outer boundary $R_{\rm out} = 10R_g$ where $R_g = GM/c^2$, and we assume $G = c = 1$. We also assume that any mass passing these boundaries is removed from the simulation. For the simulations which include mass input, we assume the mass is added at $R_{\rm add} = 7.0$. We assume that the gas is not self-gravitating, and follows a simple locally isothermal equation of state where $c_{\rm s} = c_{\rm s_0} R^{-0.75}$ where the constant $c_{\rm s_0}$ is set by choosing $H/R = 0.03$ at $R_{\rm in}$. We also consider a Shakura-Sunyaev viscosity set at $\alpha = 0.3$.

5.4.1 Discs with no mass added

Here, we plot examples of the surface density of a disc composed of SPH particles against radius where we consider the power law, smoothed power law and steady surface density profiles. Then, evolve these initial conditions to $t = 10^4$ with no injection of mass to examine the stability of the setups. This timescale is ≈ 1600 orbits at $R_{\rm in}$, and 50 orbits at $R_{\rm out}$. The viscous timescale in the inner disc is $\approx 3 \times 10^3$ and the outer disc $\approx 10^6$. The bulk of the disc follows the initial conditions for the duration of these simulations.

We expect to see noticeable evolution of the inner disc regions, and on timescales faster than predicted by the imposed physical viscosity. In the inner disc regions where the surface density goes to zero, there is little mass and therefore has a smaller resolution. This means the numerical viscosity becomes large and disc evolves faster than it

should. We may also see some evolution in the outer parts of the disc in the power-law and smoothed power-law cases. This is because, the boundary conditions applied in the simulations do not match with those assumed in the analytical set up. In figure 5.1, we show the surface density plot (power law setup) for a disc composed of 1 million SPH particles. Although, the bulk of the disc follows the initial conditions for the duration of the simulations, there is noticeable evolution in the inner and outer regions. Since this setup does not take account of boundary conditions, we consider a standard approach to assume a zero torque inner boundary condition given by the smoothed power law. Therefore, we study the surface density profiles with smoothed powerlaw setups comprising of 100,000 (as shown in figure 5.2) and 1 million SPH particles (as shown in figure 5.3). In the inner regions, the surface density evolves faster than it should, which implies an increase in the numerical viscosity. Therefore, the evolution seen here is predominantly due to numerical viscosity near the boundaries where the numerical viscosity is larger than the imposed physical viscosity. At higher resolution, the deviation from the expected surface density shape is lessened. This is shown in figure 5.4 with a disc composed of 10 million particles. However, on close inspection of figure 5.4 (as shown in fig 5.5), there are initially some density waves propagating from the inner boundary which are expected to form due to the divergence between the numerical simulations and the analytical setup.

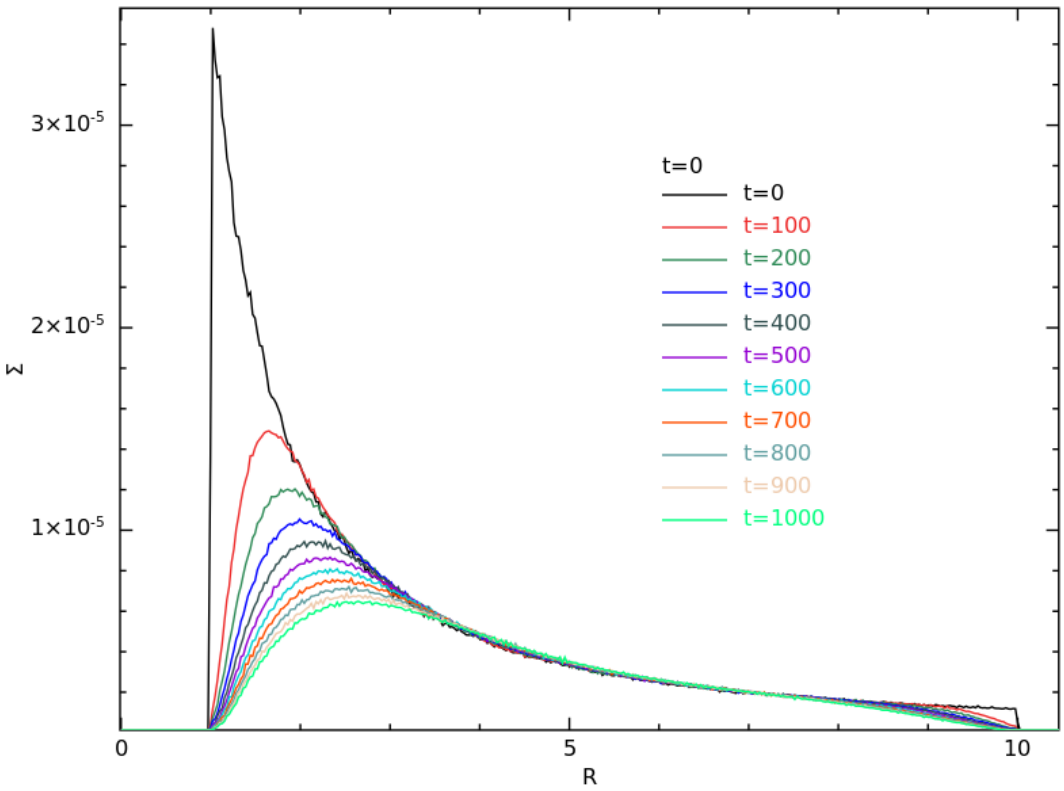

Figure 5.1: The disc surface density profile for a power law case with 1 million particles. There is no mass added and no boundary conditions included in this case. Here, the surface density profile changes in the inner and outer regions, with the inner edge evolving more quickly than the outer edge.

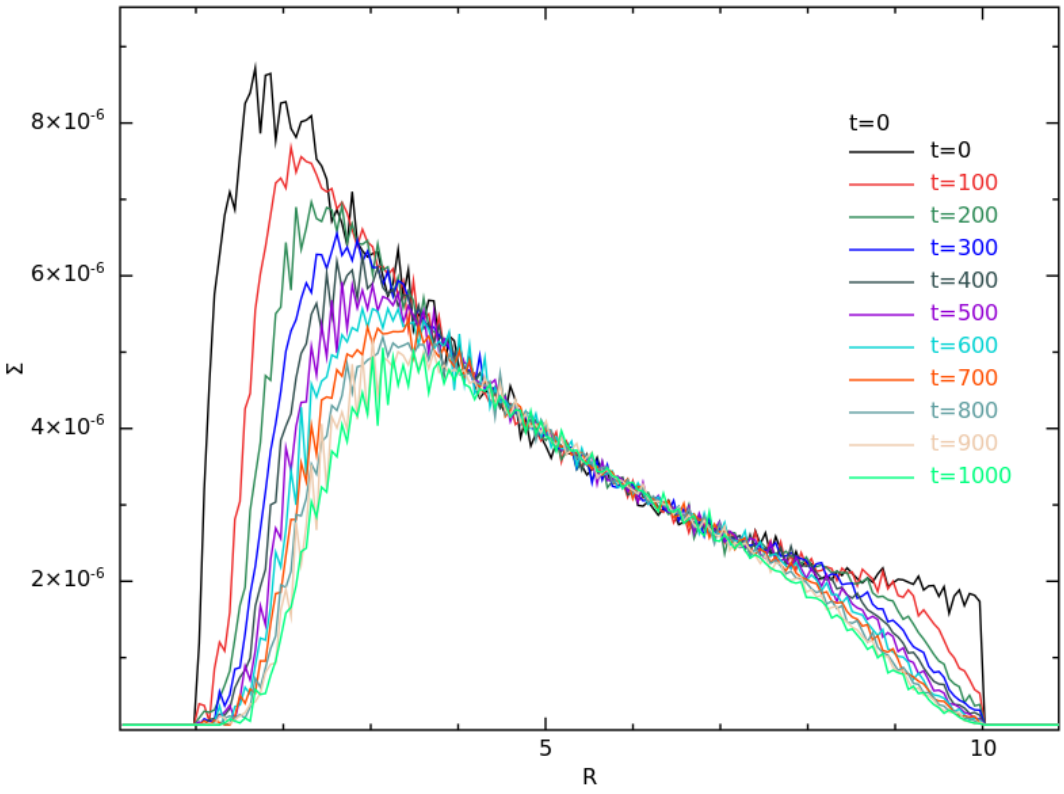

Figure 5.2: The disc surface density profile for a smoothed power law case with 100,000 particles with no mass added. A zero torque inner boundary condition is added. The surface density profile changes in the inner and outer regions, with the inner edge evolving more quickly than the outer edge. The evolution seen here is predominantly due to numerical viscosity near the boundaries where the resolution is the poorest and therefore the numerical viscosity is larger than the imposed physical viscosity.

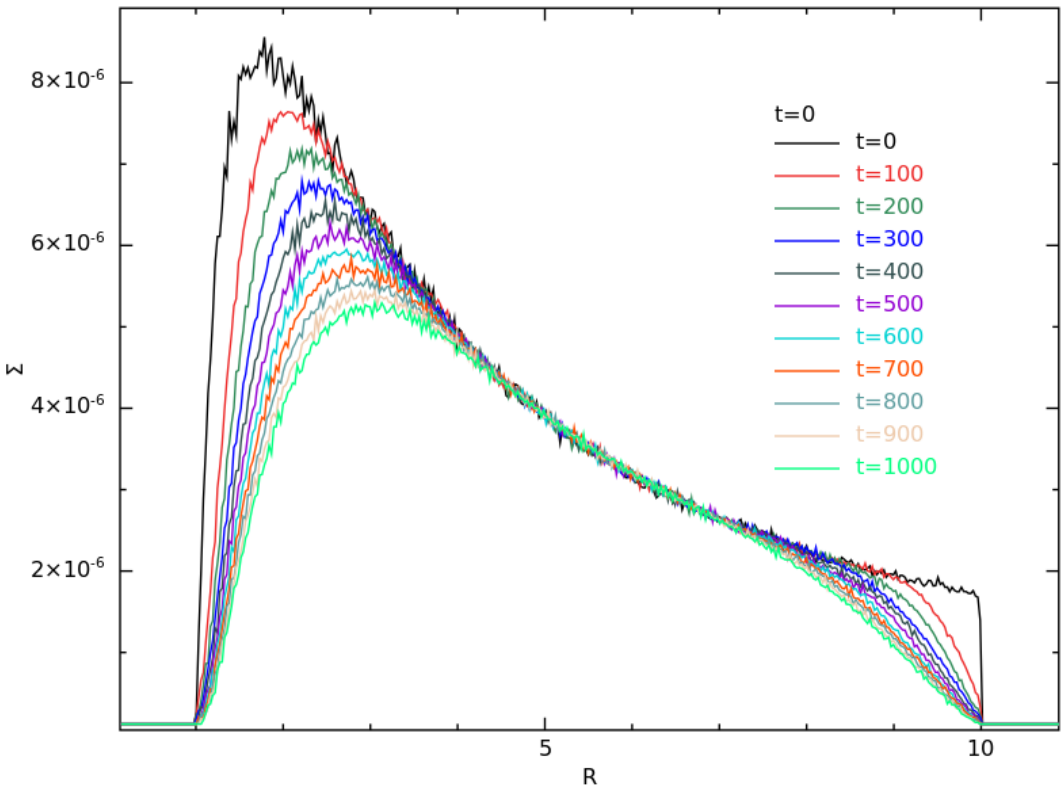

Figure 5.3: The disc surface density profile for a disc obeying smoothed power law and composed of 1 million particles with no mass added. A zero torque inner boundary condition is added. The bulk of the disc follows the initial conditions for the duration these simulations. There is noticeable evolution in the inner disc regions, resultant of the the numerical viscosity being larger than the imposed physical viscosity.

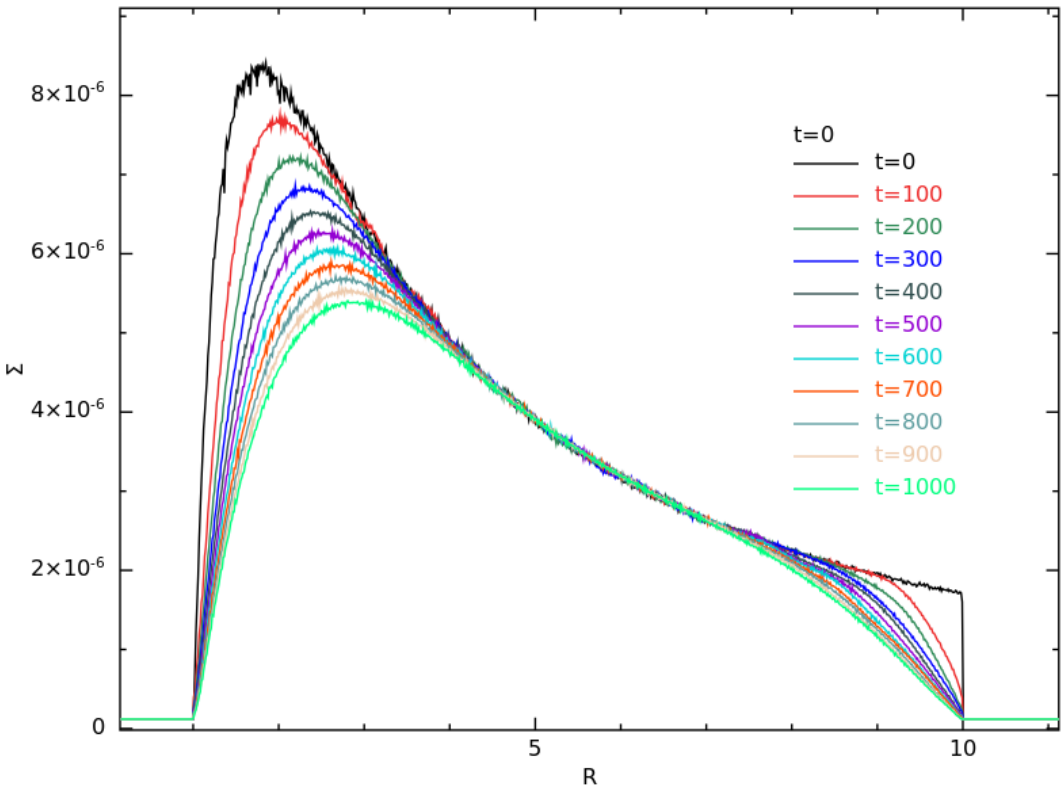

Figure 5.4: The surface density profile for a smoothed power law disc setup composed of 10 million particles with no mass added. In comparison to the simulation with 100,000 or 1 million particles, this simulation is better resolved. There is noticeable evolution in the inner disc regions, with the bulk of the disc following the initial conditions for the duration these simulations.

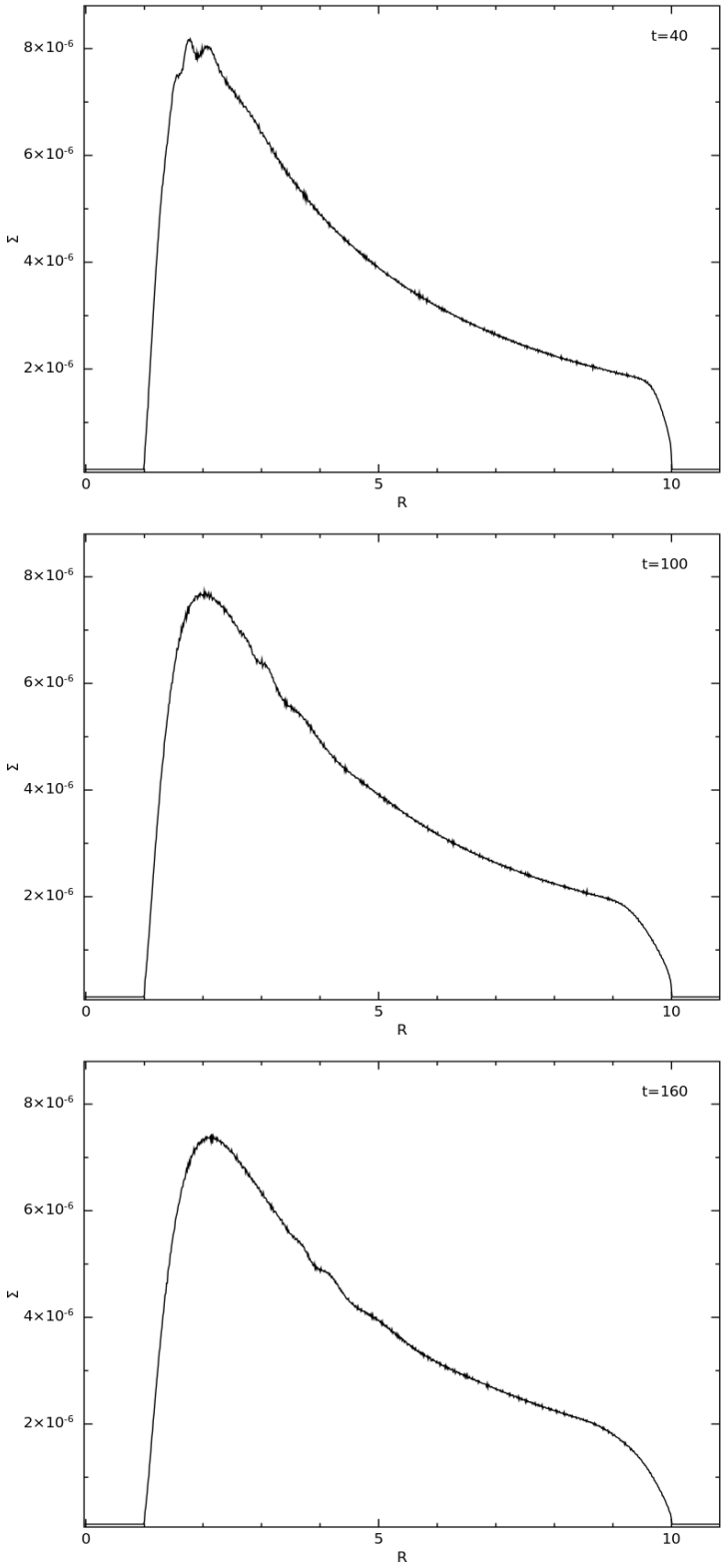

Figure 5.5: This shows how the surface density behaves at the initial time steps in the simulation of a disc with a smoothed power law setup. The disc is composed of 10 million particles and the figure shows density waves propagating from the inner edge towards the outer edge of the disc.

Furthermore, we can check if these waves are present in a steady case. Here we apply,

zero torque conditions at the inner and outer boundaries where the surface density Σ is zero. The simulations are set at different values of disc thickness for 1 million particles. Figure 5.6 shows the surface density evolution for a disc of thickness $H/R = 0.03$ and $\alpha = 0.3$ at consecutive time steps. In addition, the same analysis is considered for a thicker disc at $H/R = 0.1$ (as shown in figure 5.7). One can distinctly see the waves propagating towards the outer edge. Moreover, to examine if the waves are removed at higher resolution we check the same for a disc composed of 10 million particles. Figure 5.8 shows the surface density profile for a disc at $H/R = 0.03$ and $\alpha = 0.3$. We also check the same for discs with 10 million particles at $H/R = 0.1$ and $\alpha = 0.3$ as shown in figure 5.9. These surface density profiles at higher resolution also showed the presence of waves, and it brings us to an important question: how are these waves formed?

The waves are formed because the radial pressure gradient goes to infinity at the boundaries of the disc since the density at the boundary smoothes to zero. Furthermore, when studying the surface density profiles of discs using SPH, the particle velocities diverge at the boundaries where the surface density goes to zero with the pressure correction becoming infinite (as shown in equations 5.9 and 5.11). In SPH calculations where the resolution follows the mass, these boundaries are always under-resolved, leading to an underestimate of the pressure gradients and thus an underestimate of the velocity required for radial balance. However, this small difference between the analytical equations and the numerical solution leads to the production of small amplitude waves at the start of the simulation. For a disc at standard resolution, these waves are damped due to numerical viscosity at a timescale comparable to the time taken for the waves to traverse the disc. But, at higher resolution, a longer relaxing phase is required to damp these waves. This highlights the importance of a method to remove these waves on a timescale independent of resolution and the level of physical viscosity employed, by using a suitable velocity damping scheme that tapers to zero over timescale comparable with the disc's dynamical

timescale.

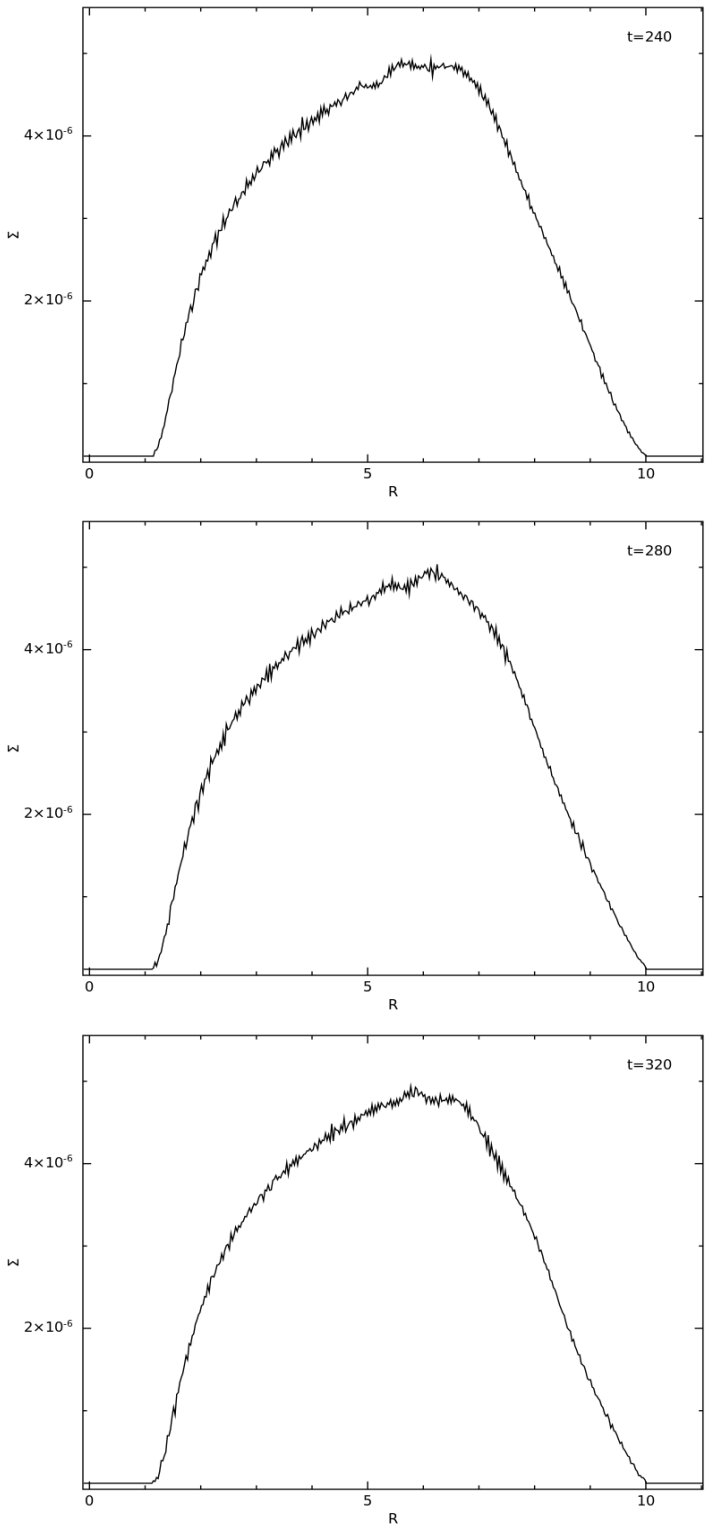

Figure 5.6: This shows the surface density profile of a steady disc setup with zero-torque boundary conditions added, at values of $\alpha = 0.3$, $H/R = 0.03$ and composed of 1 million particles. It shows the formation of small amplitude waves at the start of the simulation, resulting from an infinite pressure gradient (or zero surface density) at the boundaries.

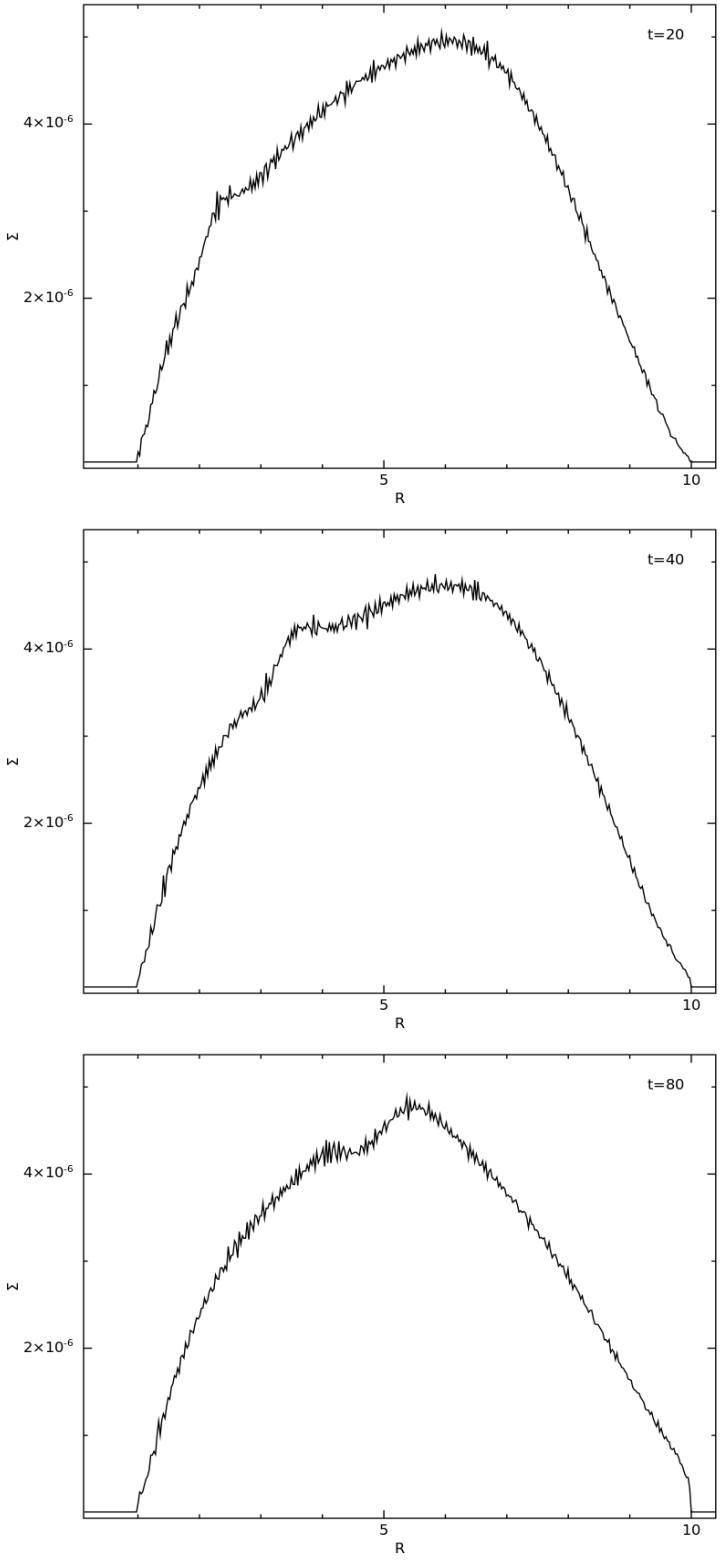

Figure 5.7: This shows the surface density profile for a steady disc setup with zero-torque boundary conditions. The simulation is run for a disc with $\alpha = 0.3$, $H/R = 0.1$ and composed of 1 million particles. It shows the formation of unwanted pressure waves at the start of the simulation. The waves advances quicker in this case, in comparison to a thinner disc at $H/R = 0.03$.

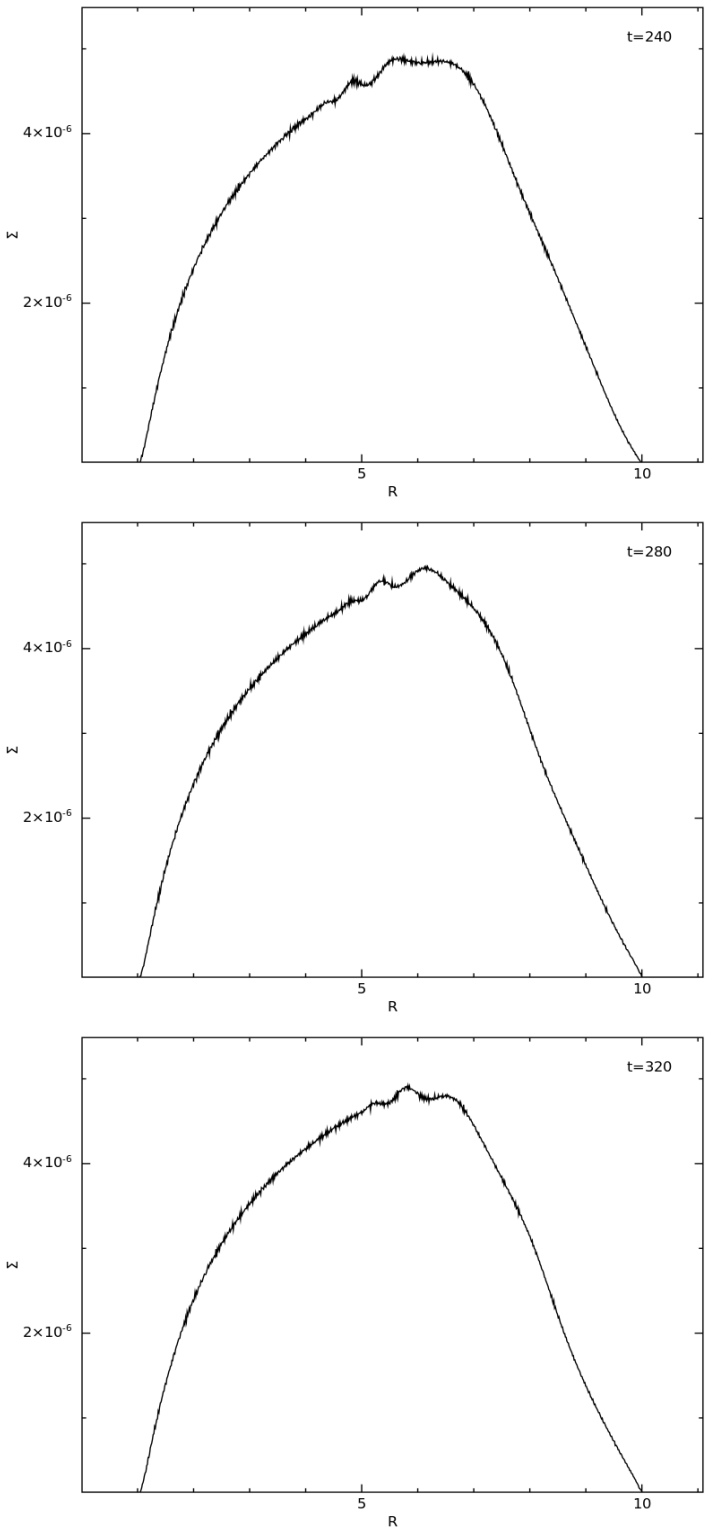

Figure 5.8: Here we show the surface density profile against radius for a steady disc at $\alpha = 0.3$ and $H/R = 0.03$ for 10 million particles. Even at higher resolution, radial pressure waves are seen at the start of the simulation, due to zero-torque boundary conditions with Σ set to 0.

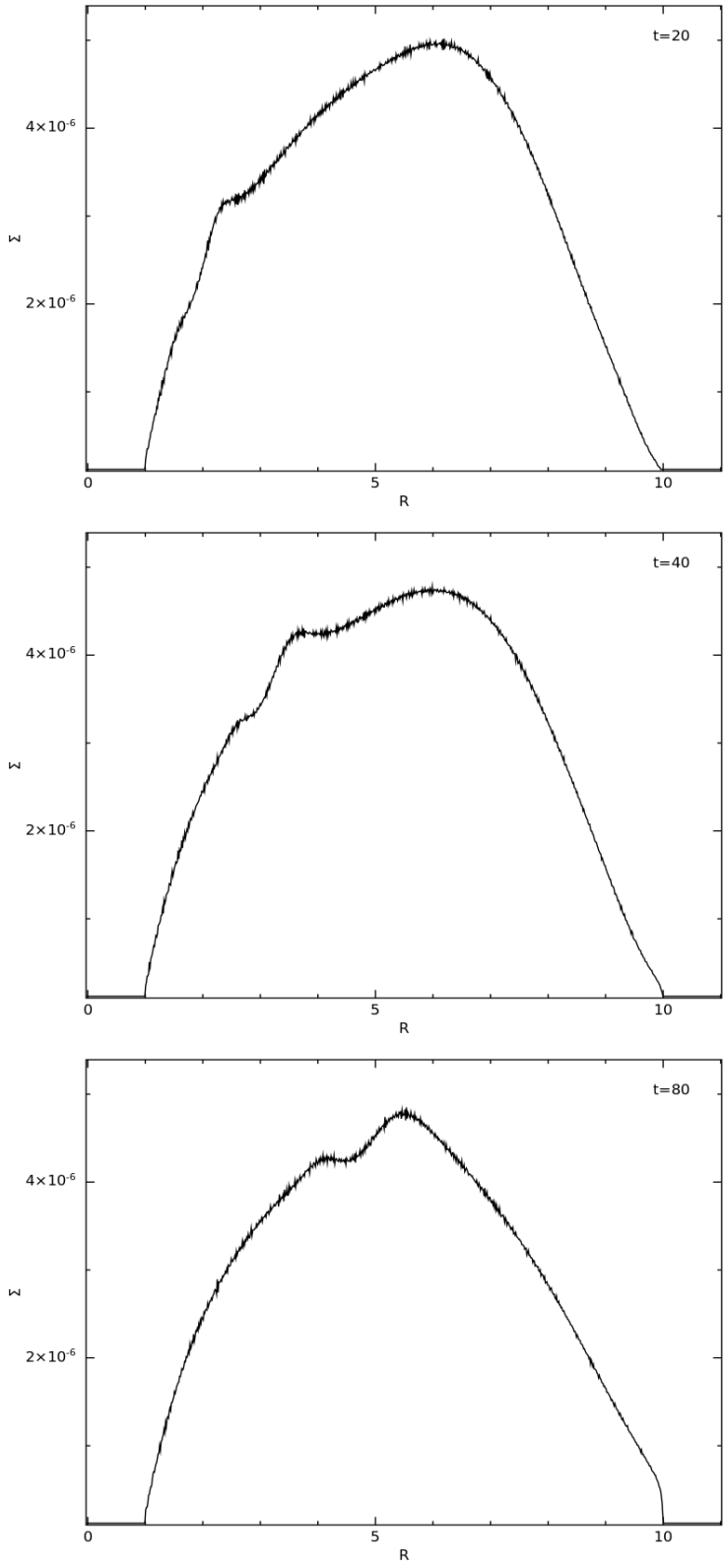

Figure 5.9: Here we show the surface density profile against radius for a steady disc at $\alpha = 0.3$ and $H/R = 0.1$ for 10 million particles. The radial pressure waves are seen at the start of the simulation, resulting from zero-torque boundary conditions with $\Sigma = 0$ at the boundaries.

5.5 Damping of pressure waves

To efficiently damp the pressure waves, without affecting the disc structure, we must damp the correct component of the velocity of the particles. We do not damp v_ϕ as this would alter the disc orbits. There is no need to damp v_z as the disc is in vertical hydrodynamic equilibrium. However, the unbalanced radial pressure gradient at the boundaries creates radially propagating waves, so we must damp v_R. We find that an appropriate method is to apply damping at the start time t_1 to calm the initial pressure waves, then smoothly taper it to zero over a time t_2 and then continue the relax phase with zero damping for a time t_3. We find that a cosine smoothed tapering function will provide a good choice to damp the pressure waves in our numerical simulations.

Our aim is to provide an efficient way of correcting the radial pressure waves generated by inducing a damping acceleration over the shortest damping time scale possible. This damping time represents the relaxed phase of the disc prior to setting up the disc to study its viscous evolution. For a disc with inner and outer radii given by $R_{\rm in}$ and $R_{\rm out}$, the time required for the pressure wave to propagate across the disc is given as:

$$t_{\rm wave} = \int_{R_{\rm in}}^{R_{\rm out}} \frac{dR}{v_{\rm wave}} \approx \frac{R_{\rm out}}{c_s}. \tag{5.12}$$

Since $c_s = H\Omega$, equation (5.12) becomes:

$$t_{\rm wave} = \frac{R}{H}\frac{1}{\Omega}. \tag{5.13}$$

This represents the time taken for the waves to traverse the disc. The aim of our work is to damp the wave-velocities on a time scale (say $t_{\rm damp}$) comparable to the wave propagation time. The idea is to include a damping factor that damps the wave velocities over a time ($t_{\rm damp}$) which produces a damping acceleration. For an $i^{\rm th}$ particle with radial velocity

v_i, the acceleration is given as

$$a_{\rm damp} = -\frac{1}{t_{\rm wave}} v_i. \tag{5.14}$$

In the absence of other effects, this leads to exponential damping as follows:

$$\dot{v_i} = -k v_i, \tag{5.15}$$

$$\frac{dv_i}{dt} = -k v_i. \tag{5.16}$$

This can be integrated to yield,

$$v_i = v_0 \exp(-kt) \tag{5.17}$$

where k is the damping factor that can be added to damp the velocities. The next step is to choose an ideal value (or a function) for k such that it can smoothly taper the wave velocities to zero. In our numerical setup, we use a cosine smoothening term $f(t)$ such that:

$$f(t) = \begin{cases} 1 \quad \text{for} \quad 0 < t < t_{\rm damp} \\ \dfrac{1}{2}\left(1 + \cos\dfrac{\pi(t - t_{\rm damp})}{t_{\rm damp}}\right) \quad \text{for} \quad t_{\rm damp} < t < 2t_{\rm damp} \\ 0 \quad \text{for} \quad t > 2t_{\rm damp} \end{cases} \tag{5.18}$$

By using this function, we initially calm the initial pressure waves upto a time $t_{\rm damp}$, smoothly reduce it to a value of zero until $2t_{\rm damp}$ and continue with zero damping thereafter. In our numerical simulations, we now need to check how the disc behaves with the damping correction added. It is also very important to make sure that this damping correction added must be sufficient enough to get rid of the waves over a timescale long enough to damp the waves upto the outer edge.

5.5.1 Numerical results

In the numerical study, we assume total damping correction added to be given by:

$$\text{damp} = k_{\text{damp}}\ \text{f(t)} \tag{5.19}$$

where k_{damp} is a dimensionless constant that determines the rate at which damping is added and $f(t)$ is the cosine smoothening term added. As previously mentioned, it is important to make sure that sufficient damping is added. This is because, the damping added measures the acceleration (damping acceleration) applied on the radial pressure waves, i.e.

$$a_{\text{damp}} = \text{damp. } \Omega\text{(R). } \text{V}_\text{R}\text{. } \hat{\text{e}_\text{R}} = k_{\text{damp}}\text{f(t). } \Omega\text{(R). } \text{V}_\text{R}\text{. } \hat{\text{e}_\text{R}} \tag{5.20}$$

where $\Omega(R) = \sqrt{GM/R^3}$ at G = M = 1, V_R is the radial velocity of the particles and $\hat{\text{e}_\text{R}}$ is the unit vector in the direction of R. This will make sure that needful amount of damping is added at every radii. We add this damping over a total time of $2t_{\text{damp}}$ which represents the relaxed phase of the disc. We assume that the damping time is of the order (or a factor) of the dynamical time of the disc at its outer radius (R_{out}).

$$t_{\text{damp}} = A_{\text{damp}}\ t_{\text{dyn}}(R_{\text{out}}) \tag{5.21}$$

where A_{damp} is a dimensionless constant. Now we need to test using simulations at different values of k_{damp} and A_{damp}, and investigate if we can effectively damp the waves in the disc, thus achieving the relaxed phase of the disc. Thereafter, we set the disc in the post-relax phase for its viscous evolution.

Figure 5.10 shows the simulation of a disc comprising of 1 million SPH particles at $H/R = 0.03$ and $\alpha = 0.3$. Here, damping is added with values of $k_{\text{damp}} = 0.3$ and $A_{\text{damp}} = 6.28$. We compare the surface density profiles of the disc with and without the damping

correction. The surface density at the post-relaxed (or damped) phase of a disc looks more evolved than for a disc with no damping added. Also, we can carry out the same comparison for a disc at $H/R = 0.1$ (as shown in figure 5.11). In this case, the damped disc setup shows an evident decrease in the surface density since $\nu = \alpha c_s H$ and therefore the disc evolves quicker on the damping timescale for a thicker disc.

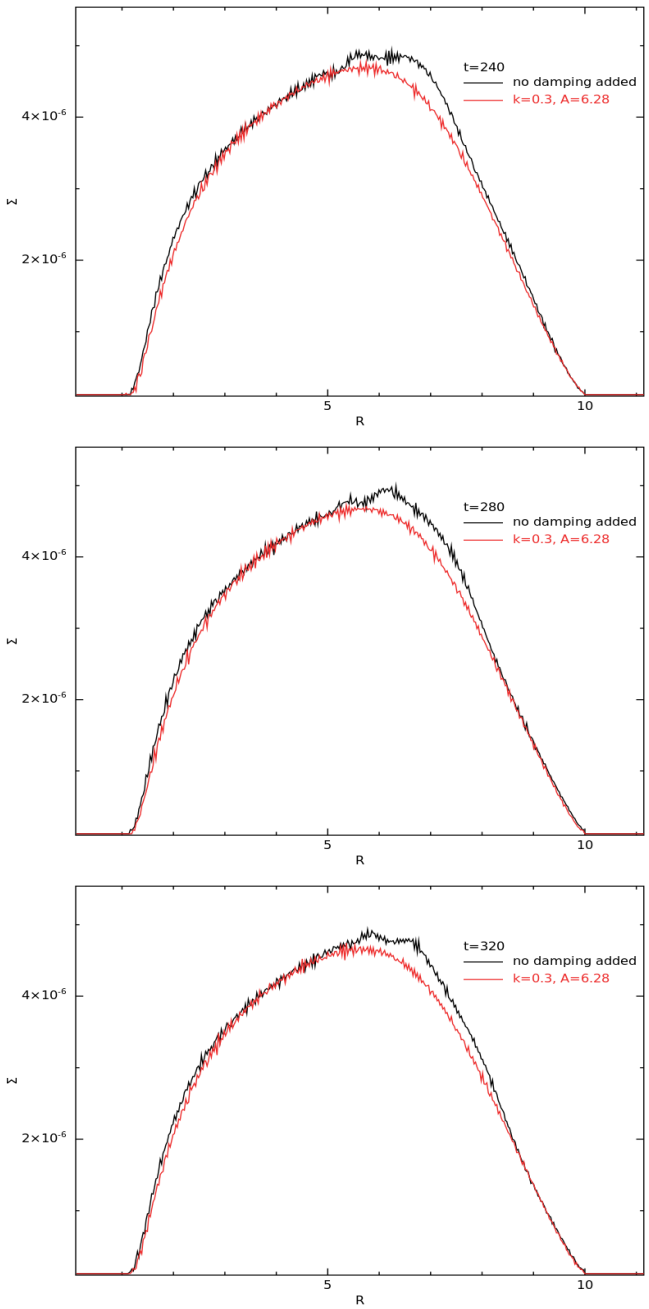

Figure 5.10: Here we show the surface density profile against radius for a steady disc setup with zero-torque boundary conditions at $\alpha = 0.3$ and $H/R = 0.03$ for 1 million particles. The damping correction is added at $k_{\rm damp} = 0.3$ and for a damping time determined by $A_{\rm damp} = 6.28$. The black line shows the profile with no damping added (with the waves present) and the red line is the surface density profile after adding the damping correction.

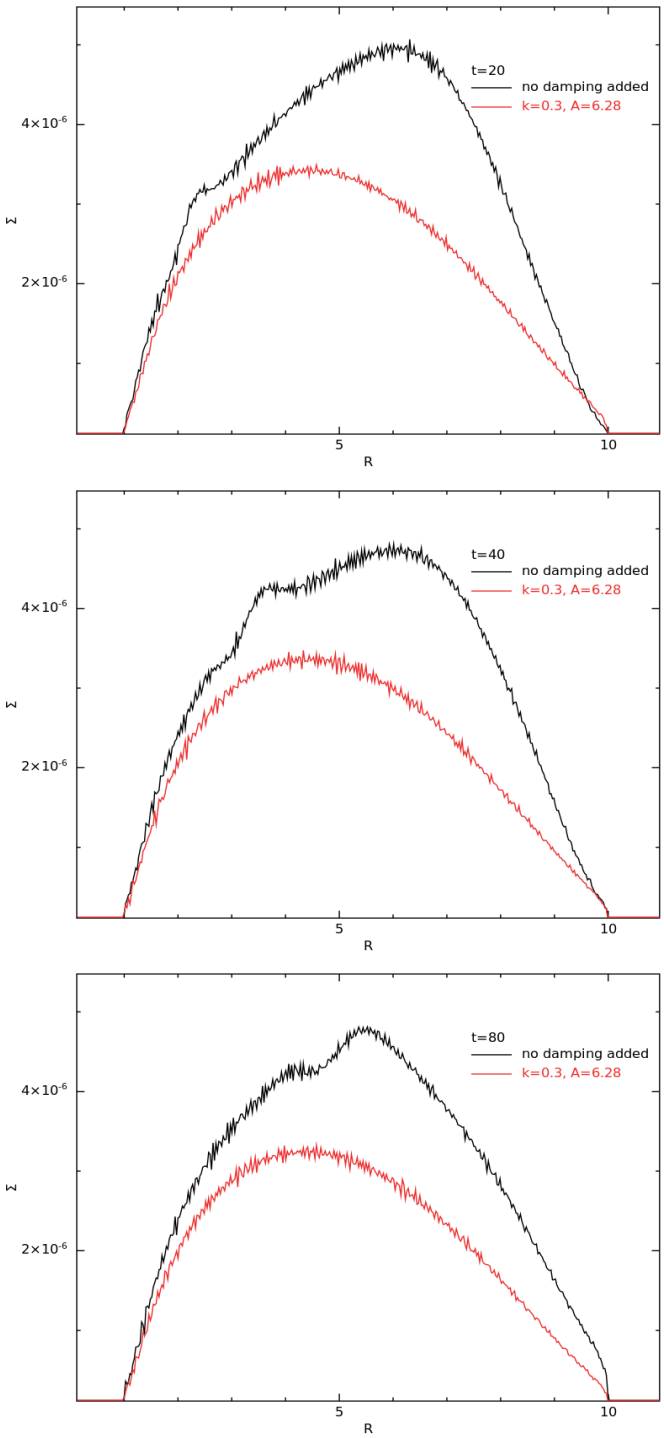

Figure 5.11: Here we show the surface density profile against radius for a steady disc setup with zero-torque boundary conditions at $\alpha = 0.3$ and $H/R = 0.1$ for 1 million particles. The black line is the profile with no damping added and the red line with damping added. After allowing it to relax for a time $t_{\rm damp}$, we clearly see a considerable evolution for the disc with damping added (thick discs evolve quicker).

In addition, we extend and carry out the comparisons for discs composed of 10 million particles with and without damping added. Figures 5.12 and 5.13 show the surface density profiles of discs at a value of $\alpha = 0.3$ and H/R at 0.03 and 0.1 respectively. Much thinner

discs can also be simulated efficiently at higher resolution and therefore we use a 10 million disc setup to study damping in a thin disc at $H/R = 0.01$ (as shown in fig 5.14). These results prove that the waves can be effectively damped (at $k_{\rm damp} = 0.3$ and $A_{\rm damp} = 6.28$) for thinner discs (upto $H/R = 0.01$) by relaxing the disc at a timescale comparable to its dynamical time at the outer edge[1].

Moreover, we can also do disc simulations at different viscosity values. For a given thickness of the disc, we can see how the disc evolves at different α values. Consider, a disc with $H/R = 0.03$ and α values of 0.1 and 0.3 respectively. We expect the disc at a higher α to evolve quicker, and is demonstrated by figure 5.15 for a disc with $H/R = 0.03$. We can repeat the same for a thicker disc at $H/R = 0.1$ as shown in figure 5.16.

In our analysis, we tested simulations at values of $k_{\rm damp}$ between 0.1 and 3, and $A_{\rm damp}$ varying between 3 and 10. From table 5.1, we can conclude that $A_{\rm damp} = 6.28$ is a suitable choice for $t_{\rm damp}$ which is long enough to damp the waves present in the disc-simulations used in our analysis. Furthermore, we also check how effectively this value of $t_{\rm damp}$ can be used in discs at different damping rates ($k_{\rm damp}$) from a smaller value of 0.1 to higher values at 1 and 3. It was found that 0.1 is too small to effectively damp the waves. Moreover, values of $k_{\rm damp}$ at 1 and 3 damp the waves to a large extent that changes the shape of the density profile. But a value of 0.3 for $k_{\rm damp}$ at $t_{\rm damp} = 6.28$ is found to work efficiently as discussed from our results.

[1]For much thinner discs with H/R $\sim 10^{-3}$, the disc needs to be damped over a longer period, i.e. at a higher value of $A_{\rm damp}$

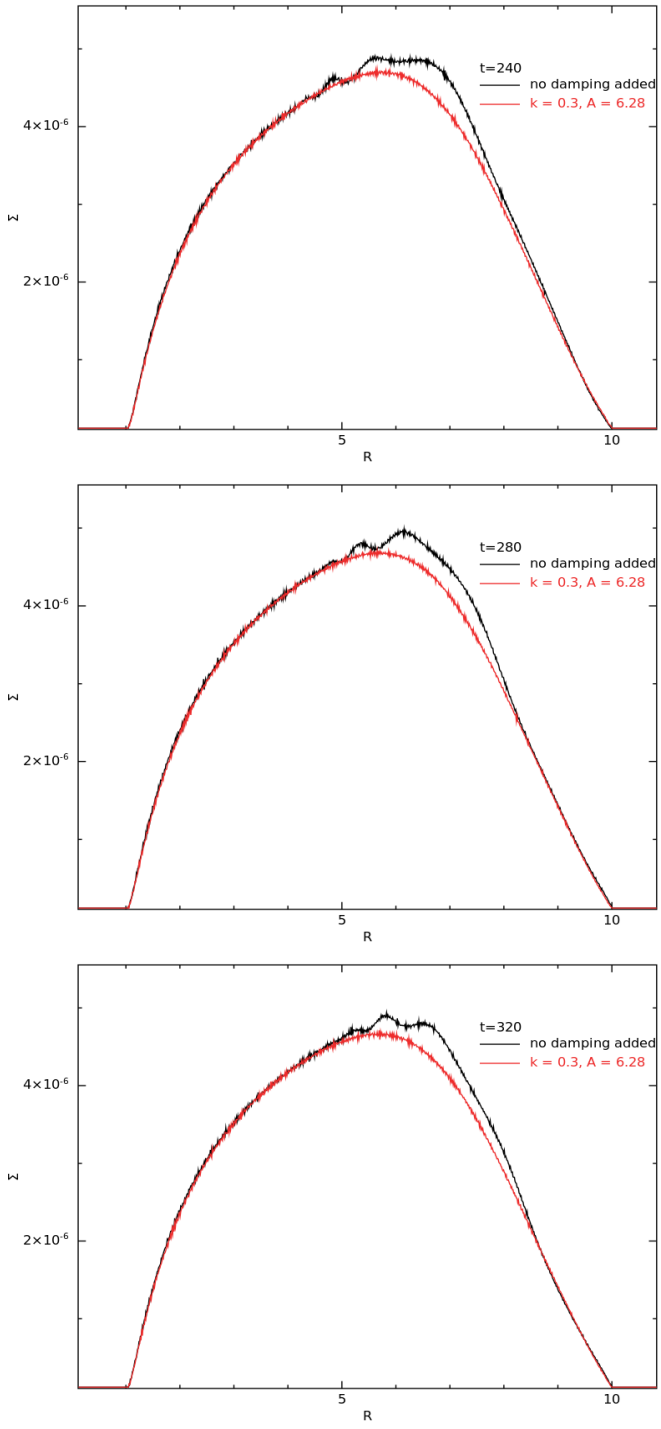

Figure 5.12: This shows the comparison between the surface density profiles against radius for a steady disc setup at $\alpha = 0.3$ and $H/R = 0.03$ for 10 million particles, with (red line) and without (black line) the damping correction.

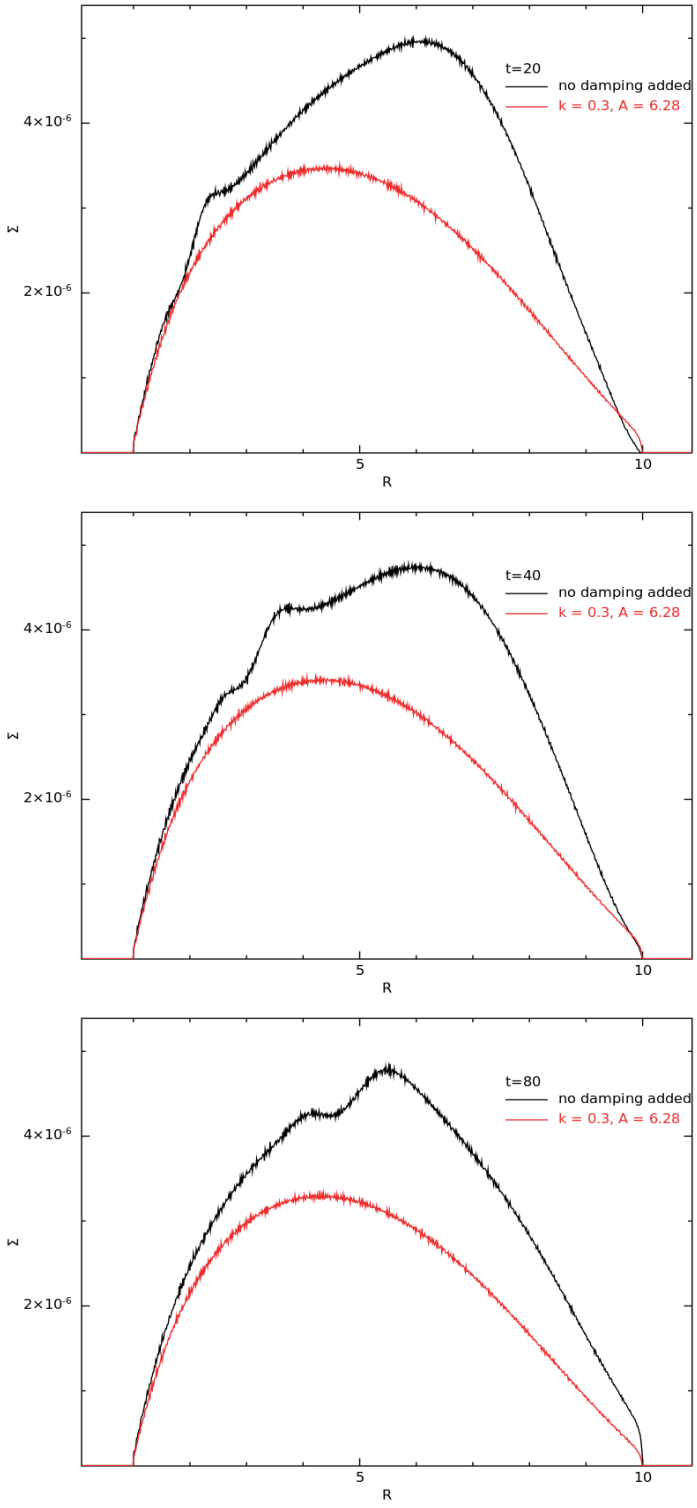

Figure 5.13: This shows the comparison between the surface density profiles against radius for a steady disc setup at $\alpha = 0.3$ and $H/R = 0.1$ for 10 million particles, with and without the damping correction. As mentioned before, the disc with the damping added (red line) over time $t_{\rm damp}$ is found to evolve quicker.

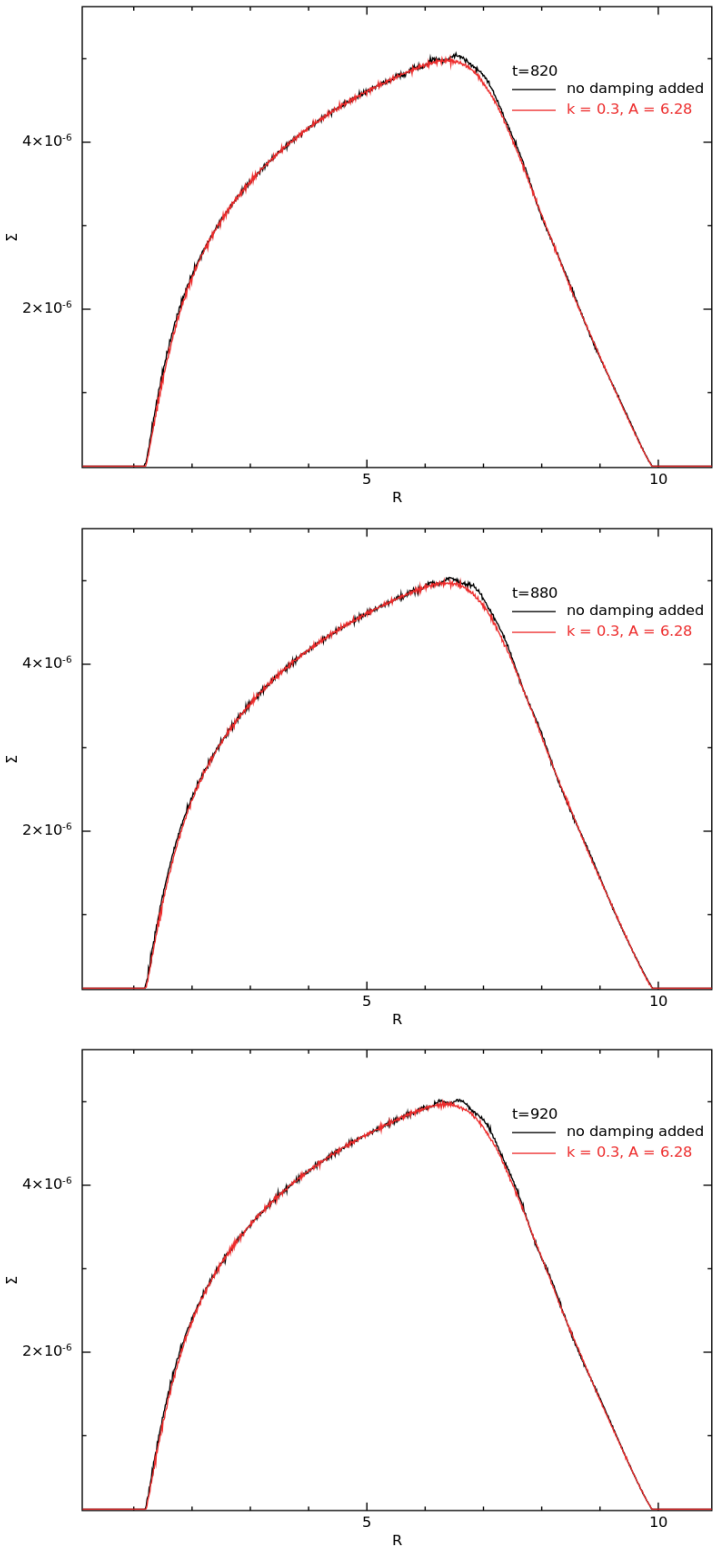

Figure 5.14: Comparison of disc profiles for a steady disc setup at $\alpha = 0.3$ and $H/R = 0.01$ for 10 million particles is shown. The profile in black line shows the presence of waves but the disc profile with damping correction added (red line) shows that the radial pressure waves can be eliminated even for thinner discs at an effective value of $k_{\rm damp}$ and $t_{\rm damp}$, long enough to damp the waves upto the outer edge of the disc.

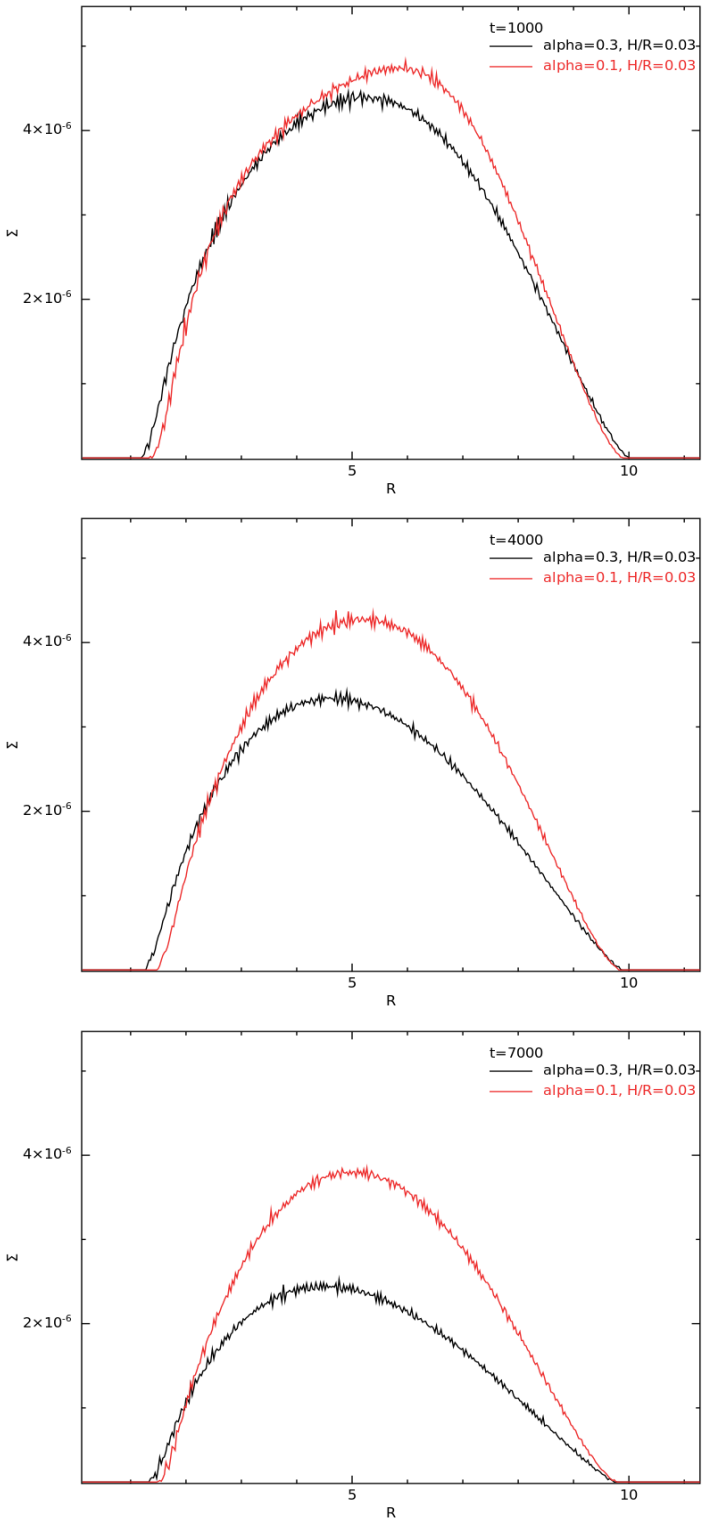

Figure 5.15: Surface density profiles are studied for discs composed of 1 million particles, at different viscosities. This shows the comparison of surface density profiles with damping added for a disc with $H/R = 0.03$ at values of $\alpha = 0.1$ and 0.3 respectively. As expected, the disc with $\alpha = 0.3$ (black line) has a shorter viscous time in comparison to the disc with $\alpha = 0.1$ (red line).

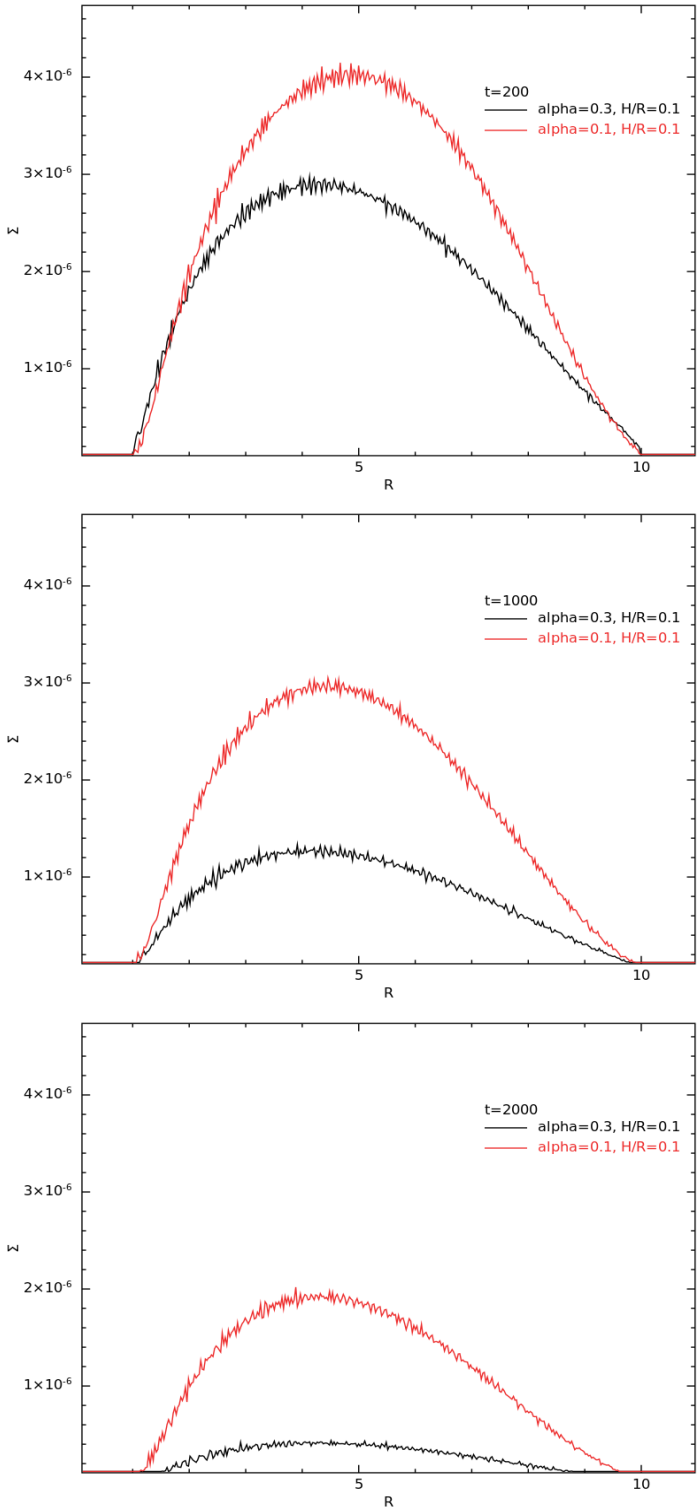

Figure 5.16: Surface density profiles are studied for a disc composed of 1 million particles, with $H/R = 0.1$ at different viscosities. This shows the comparison of surface density profiles with damping added for a disc at values of $\alpha = 0.1$ and 0.3 respectively. As expected, the disc with $\alpha = 0.3$ (black line) has a shorter viscous time in comparison to the disc with $\alpha = 0.1$ (red line).

Simulation tests				
$k_{\rm damp}$	$A_{\rm damp}$	H/R	α	Damping
0.1	3	0.03	0.3	×
0.1	3	0.1	0.3	×
0.1	6.28	0.03	0.3	×
0.1	6.28	0.1	0.3	×
0.3	2	0.03	0.3	×
0.3	2	0.1	0.3	×
0.3	3	0.03	0.3	✓
0.3	3	0.03	0.1	✓
0.3	3	0.1	0.3	✓
0.3	3	0.1	0.1	✓
0.3	5	0.01	0.3	×
0.3	5	0.03	0.3	✓
0.3	5	0.03	0.1	✓
0.3	5	0.1	0.3	✓
0.3	5	0.1	0.1	✓
0.3	6.28	0.01	0.3	✓
0.3	6.28	0.01	0.1	✓
0.3	6.28	0.03	0.3	✓
0.3	6.28	0.03	0.1	✓
0.3	6.28	0.1	0.3	✓
0.3	6.28	0.1	0.1	✓
0.3	7	0.01	0.3	✓
0.3	7	0.03	0.3	✓
0.3	7	0.03	0.1	✓
0.3	7	0.1	0.3	✓
0.3	7	0.1	0.1	✓
0.3	10	0.01	0.3	✓
0.3	10	0.03	0.3	✓
0.3	10	0.03	0.1	✓
0.3	10	0.1	0.3	✓
0.3	10	0.1	0.1	✓
1.0	6.28	0.03	0.3	×
1.0	6.28	0.1	0.3	×
3.0	6.28	0.03	0.3	×
3.0	6.28	0.1	0.3	×

Table 5.1: Table showing the values of $k_{\rm damp}$, $A_{\rm damp}$, α and H/R used, in the simulations to examine the damping of waves in discs. The last column shows if the effective damping of waves can or cannot be established for the values of $k_{\rm damp}$ and $A_{\rm damp}$ used.

5.5.2 Disc with mass added

From figures 5.11 and 5.13 (also fig. 5.16), we notice that when damping correction is added in thicker discs, there is a significant disc evolution in the relaxed phase. The

figures show a considerable decrease in the value of surface density in the post relaxed phase. This set up can be further modelled to study the long term evolution of such discs at higher resolution. One way to resolve this is, by injecting mass in the disc at radius $R_{\rm add}$. Therefore, we check how the disc's surface density looks like in a post relaxed phase with mass input continuously added over time. Figure 5.17 shows the surface density profiles of a disc composed of 1 million particles at values of $\alpha = 0.3$ and $H/R = 0.1$, without any damping as well as with damping correction added (with and without a mass input).

As shown in figure 5.17, the surface density profile with no mass and no damping added (black line) shows waves propagating through the disc and it evolves quickly over time. The surface density denoted by the red line shows the disc in the post-relaxed phase with no mass added, but with damping correction included. Although, it shows no waves, there is a significant evolution observed in the disc. The surface density of the disc (the green line) represents the post relaxed phase with damping correction as well as mass added at $R_{\rm add}$. This setup retains the surface density profile as expected from the initial conditions, since mass is continuously added over time. Thus it can be concluded that, the post relaxed disc simulations with an injection of mass can effectively be used to study the long term viscous evolution of accretion discs.

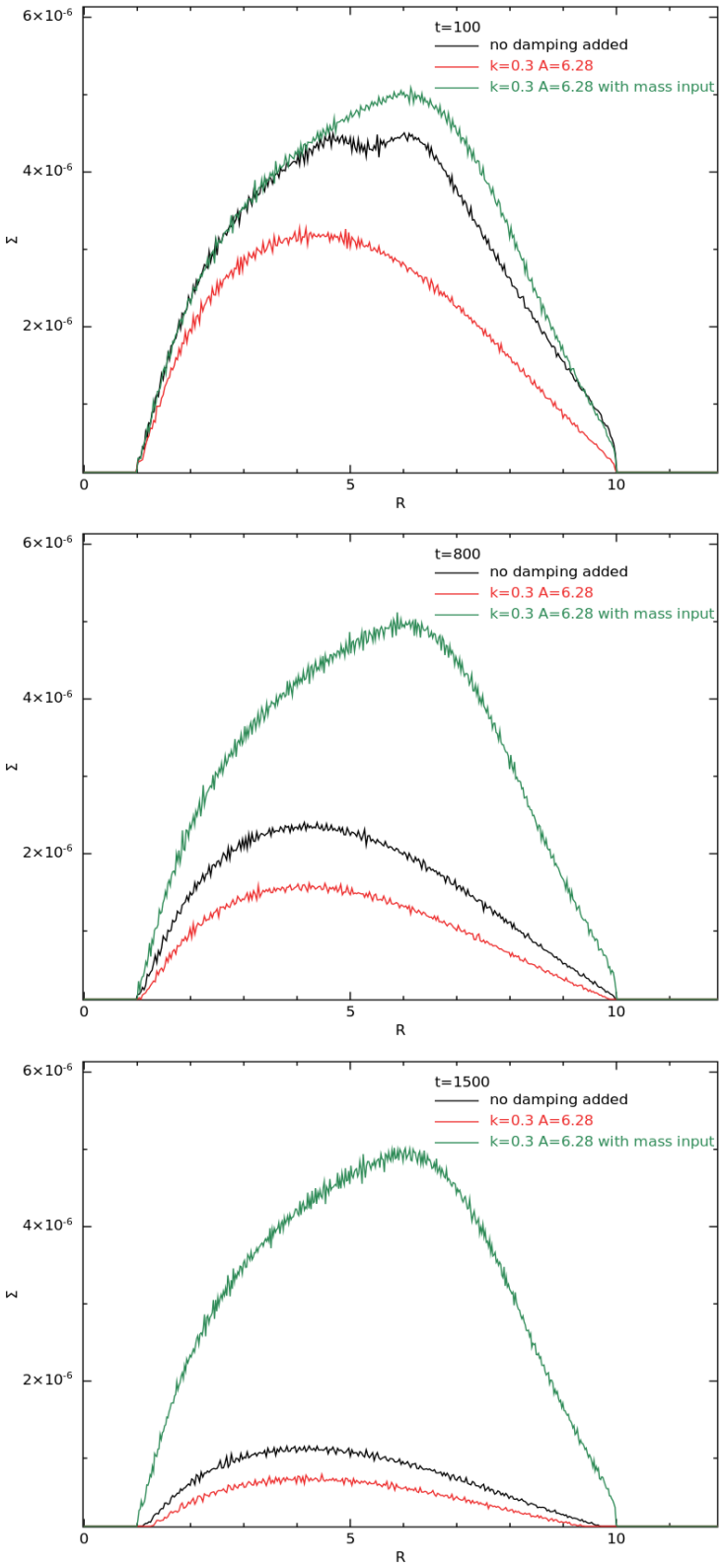

Figure 5.17: The black line shows the surface density profile without any damping added and no mass added for a disc comprising of 1 million SPH particles at $H/R = 0.1$ and $\alpha = 0.3$. The red line shows the evolution of density for a disc with damping added with no mass added. The surface density profile with mass added over time is depicted in green. Over time, we see the profiles depicted in black and red change over time, but for a disc with mass added the disc retains its initial surface density profile throughout the simulation.

5.6 Discussions and Conclusions

As shown in figure 5.17, we examined the three cases on how the surface density profiles change for a disc with $\alpha = 0.3$ and H/R = 0.1: a disc with neither damping nor mass added, a disc with damping added but no mass added and a disc with both damping and mass added. We further check the disc's column density plots in these three cases, at a time step, say t = 100 $\sim$ 16 orbits at R_{in} as shown in figure 5.18. The corresponding surface density profiles for the three cases at t = 100 $\sim$ 16 orbits at R_{in} is shown in figure 5.19.

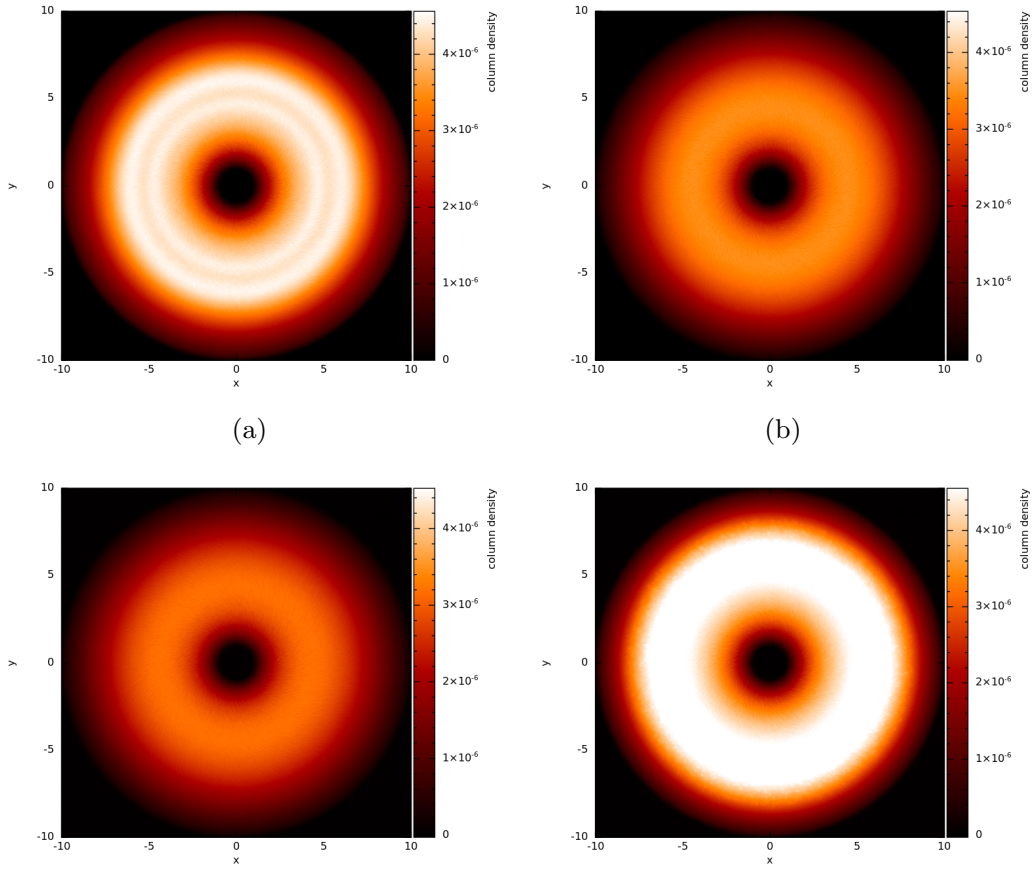

Figure 5.18: Shows how the column density profiles for a disc with $\alpha = 0.3$ and H/R = 0.1, at different scenarios: (a) a disc with neither damping nor mass added, (b) a disc with damping added but no mass added at t = 0 (c) a disc with damping added but no mass added at t = 100 and (d) a disc with both damping and mass input added at t = 100.

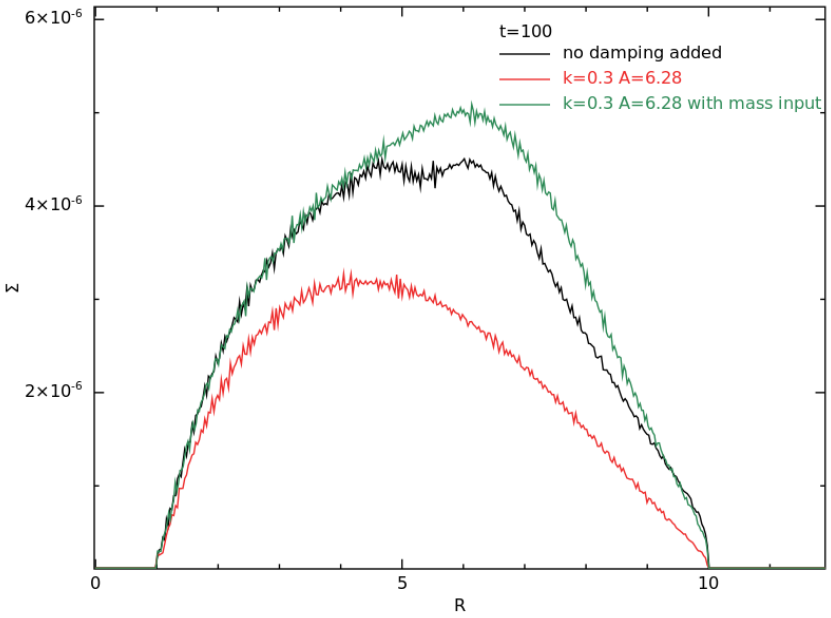

Figure 5.19: Shows how the surface density profiles for a disc with and without mass added at timestep t = 100 ∼ 16 orbits at $R_{\rm in}$.

In figure 5.18:

- (a) shows how the undamped setup of the disc at t = 100 ∼ 16 orbits at $R_{\rm in}$. As expected we can see the presence of a wave or the ring like feature. In figure 5.19 for an undamped profile (the black line), we see the trough of the wave at R ≈ 5. Thus, the density profile clearly traces out the presence of the wave.

- (b) represents the beginning of the post relaxed phase of the disc, i.e. at t = 0 for a disc with damping added. This is how the particle density of the disc looks like after relaxing it over a damping time, $t_{\rm damp}$. There is no mass added in this disc, therefore we expect a viscous evolution of density over this damping timescale. But as shown, this phase of the disc is devoid of any pressure waves.

- (c) represents how the disc, after damping looks like at t = 100 (also shown by the red line in figure 5.19). The disc at this time looks more evolved in comparison to figure (b) for a disc at t = 0. For a disc with H/R = 0.1, it evolves quicker with a considerable decrease in surface density as shown.

- (d) represents the post relaxed phase of the disc at t = 100 with mass added over time at $R_{\rm add} = 7$ (analogous to the green line in figure 5.19). The advantage of this analysis is that, not only we retain the initial shape of the disc as mass is continuously added over time but also damp any unwanted pressure waves with the damping correction added.

In summary, we have outlined the methodology to create discs of SPH particles for numerical simulations. We have provided a method for injecting particles into the disc to mimic a larger disc and run the simulation to achieve a steady state at which more detailed dynamical calculations can be done. We show that when sufficiently high resolution is employed, SPH accurately models the expected disc evolution and when appropriate boundary conditions are taken into account, the surface density behaves as expected. We showed how the divergence in the initial conditions between the numerical and analytical setups of discs can be resolved by including a damping correction. This numerical analysis is a generic case, which can be further extended to a wide range of astrophysical systems from the large scales of accretion discs around supermassive black holes (SMBHs) down to the small scales of planet forming discs.

6

Conclusions & Future work

In this thesis, the main research circles around the complex behaviour of accretion discs around supermassive black holes. Using 3D hydrodynamical simulations, we examine how these discs become unstable and tear into many distinct rings. Here, I give a summary of the main conclusions from each chapter in this thesis.

6.1 Instability of warped discs

In chapter 2, we explored the instability of diffusive and Keplerian warped discs with no precession added. Using the analysis of Doğan et al. (2018), we assume that each disc has a critical warp amplitude value dependent on the viscosity parameter α, to become unstable and break. We conduct a parameter sweep which utilises a warped disc model similar to the model used in Lodato & Pringle (2007), and test the criterion for discs to form instabilities and break.

In our study, we consider warped discs at different values of α $(0.1 - 0.3)$ and $H/R = 0.03$, at different inclinations. The instability criterion is investigated in each case, by calculating the warp amplitude of the disc that is compared to the critical value $|\psi|_c$, dependent on the disc's α parameter. We conclude that the disc becomes unstable and break at small α values and at higher inclinations. The variation in surface density of the disc is consistent with the change in the disc's warp amplitude with values of $|\psi| > |\psi|_c$,

where the disc becomes unstable and breaks. However, in warped discs at higher α values, the disc remains stable and doesn't break as the values of $|\psi| << |\psi|_c$, thus proving that it is difficult for instabilities to form in these discs.

6.2 A parameter study of disc tearing

In chapter 3, we test the disc tearing criterion in precessing discs around supermassive black holes warped due to LT effect using numerical simulations. We conduct the numerical analysis of diffusive discs ($\alpha > H/R$) at different values of α ($0.05 - 0.1$), H/R ($0.01 - 0.03$) and initially inclined at different tilts. The criterion of disc tearing derived from Doğan et al. (2018) is tested in each disc by examining if the warp amplitude of the disc exceeds its critical value or not. From the 3D simulations and the corresponding surface density, tilt and twist plots of the disc, we observe the possibility of tearing in these discs at higher inclinations. The warp amplitude of the disc is calculated and it shows an agreement with the expected results, i.e. $|\psi| > |\psi_c|$ at the exact points on the disc where it tears to form distinct rings. We also prove from our numerical analysis that the critical warp amplitude at which a disc becomes unstable is dependent on the value of α, i.e. the value of $|\psi|_c|$ is smaller for smaller values of α and our analysis also presents a higher growth rate of instabilities at low α values. Hence, our results are found in agreement with the theoretical prediction by Doğan et al. (2018).

Furthermore, the maximum value of warp amplitude ($|\psi|_{\rm max}$) for the instabilities to grow in a disc at tilt β is also studied. Our results show that discs which are thin and highly tilted become unstable, as their maximum warp amplitude is higher than the critical warp amplitude required for instability. However, discs which are thick and close to alignment has a maximum warp amplitude value less than the critical warp amplitude for instabilities to occur.

6.3 Implications of tearing in AGN discs

In chapter 4, we discuss two observational studies which examine the extreme variability in the luminosities of the disc in the UV/optical wavelengths and the slope of temperature-radii profiles in the disc of a changing look AGN, namely NGC 5548. We also review how numerical models of accretion discs can be used to explain the deviation of the observational results from the theoretical predictions of a standard α disc model.

The study by Edelson et al. (2015) explains the variability in the UV/optical wavelengths observed over a period of few months for NGC 5548. In addition, the analysis of Starkey et al. (2017) calculates a steeper slope at $\alpha = 0.99$ in the temperature-radius profile of NGC 5548, contrary to the value for a steady disc predicted by theory where $\alpha = 0.75$. These studies also highlight how theoretical and numerical models of evolving accretion discs can explain their anomalous behaviour and yield a better understanding of their complex dynamics. We have suggested that the large amplitude, short timescale variability exhibited by AGN may be explained by the possibility of the disc tearing instability in warped accretion discs (Nixon et al. (2012a); Doğan et al. (2018), or refer chapter 3), which plays an important role in producing variable accretion flows around black holes. As mentioned earlier in chapters 2 and 3, we presented the numerical simulations of disc tearing instability in warped discs and their resulting dynamics. In this chapter, we discussed the implications of this dynamics for accretion on to black holes, with particular focus on the variability of Active Galactic Nuclei (AGN). We examined the timescales on which variability might manifest in the observable features of these systems, and the impact of the observer orientation with respect to the black hole spin. In addition, we investigated the variations in the accretion rate on to supermassive black holes which are induced by the tearing instability in warped discs. These variations affect the rate of generation of energy from the accretion flow, especially in the inner regions of

the disc. As future work, we aim to examine if our numerical models show similarity with the recent quasi periodic eruptions observed in GSN 069 and in the galactic nucleus of RX J1301.9+2747 or the eruptions (or heartbeat modes) observed in some X-ray binaries.

6.4 Accretion discs in SPH

In chapter 5, we discuss the numerical methodology of creating discs composed of SPH particles. The zero torque boundary conditions applied in the setting up of discs of SPH particles cause the particle velocities to diverge at the boundaries. This lack of equilibrium in the initial conditions of the disc forms radial pressure waves in the surface density profiles of these discs. We find that in cases of discs at higher resolution with 10 million particles, the numerical viscosity is not capable of damping these waves at a timescale comparable to the time for these waves to propagate through the disc. Thus, we propose a method which employs an initial relaxing phase to damp these waves using damping correction that tapers to zero over timescale comparable with the disc's dynamical timescale.

Our results show, how a sufficient damping correction can be used to get rid of the unwanted radial pressure waves over a timescale, long enough to damp these waves and achieve the relaxed phase of the disc. This damping correction sets the disc to continue with zero damping in the post relaxed phase where we can effectively model the long term viscous evolution of the disc.

6.5 Future work

- The analytical work on disc tearing has made use of the assumption that the viscosity is a form of the Navier-Stokes fluid viscosity. Pringle (1992) remarks that this may not be a case for viscosity driven by magnetic effects. In particular, Pringle

(1992) notes that while ν_1 that corresponds to (R, ϕ) shear is secular, the (R, z) shear that corresponds to ν_2 is oscillatory. Therefore, it is important to compare numerical simulations that employ a Navier-Stokes viscosity with the simulations that model MRI driven turbulence explicitly. Such a comparison was performed by Nealon et al. (2016) who found good agreement between the two methods in modelling warped discs. Recently, Liska et al. (2020) have argued that magnetic fields alter the properties of disc tearing when strong magnetic fields are included. In the future, it would be useful to directly compare using the sane numerical method and the same numerical parameters, the differences created between a Navier-Stokes and a magnetic viscosity.

- The numerical analysis to test disc tearing in accretion discs around SMBHs, warped due to Lense-Thirring precession can be extended to larger discs at higher values of the outer radius $R_{\rm out}$ (Raj et al. (2020) *in prep*). We can examine the stability of these discs (assuming the discs are Keplerian with the rate of orbital shear $q = 1.5$) by studying how the warp amplitude changes in the SPH simulations, similar to the study explained in chapter 3. The criterion of each disc is tested by assuming that the disc remains stable until $|\psi| > |\psi|_c$ (Doğan et al., 2018).

- Recently, the instabilitiy criterion for discs (at $1.5 < q < 2$) to become unstable is derived in Doğan & Nixon (2020). The criterion for instabilities to occur in non-Keplerian discs at different values of the orbital shear parameter q, is investigated in the diffusive case where $\alpha > H/R$. The critical warp amplitudes for instabilities to occur are demonstrated at $\alpha = 0.01, 0.03$ and 0.1 for discs at various q values. I would like to test this instability criterion in non-Keplerian discs using SPH simulations.

Bibliography

Abbott, B. P., Abbott, R., Abbott, T. D., et al. 2016, , 116, 061102

Akiyama, K., Alberdi, A., Alef, W., et al. 2019, APJL, 875, L1

Alloin, D., Pelat, D., Phillips, M., & Whittle, M. 1985, APJ, 288, 205

Aly, H., & Lodato, G. 2020, MNRAS, 492, 3306

Andrews, S. M. 2020, arXiv e-prints, arXiv:2001.05007

Antonucci, R. 2018, Nature Astronomy, 2, 504

Balbus, S. A. 2009, arXiv e-prints, arXiv:0906.0854

Balbus, S. A., & Hawley, J. F. 1991, APJ, 376, 214

Balsara, D. S. 1995, Journal of Computational Physics, 121, 357

Bambi, C. 2019, arXiv e-prints, arXiv:1906.03871

Bardeen, J. M. 1970, Nature, 226, 64

Bardeen, J. M., & Petterson, J. A. 1975, APJL, 195, L65

Bath, G. T., & Pringle, J. E. 1982, MNRAS, 199, 267

Belczynski, K., Bulik, T., Fryer, C. L., et al. 2010, APJ, 714, 1217

Blackburne, J. A., Pooley, D., Rappaport, S., & Schechter, P. L. 2011, The Astrophysical Journal, 729, 34

Blandford, R. D., & McKee, C. F. 1982, APJ, 255, 419

Bragg, A. E., Greenhill, L. J., Moran, J. M., & Henkel, C. 2000, The Astrophysical Journal, 535, 73

Brenneman, L. W., & Reynolds, C. S. 2006, APJ, 652, 1028

Cannizzaro, G., Fraser, M., Jonker, P. G., et al. 2020, MNRAS, 493, 477

Casares, J., & Jonker, P. G. 2014, , 183, 223

Clavel, J., Reichert, G. A., Alloin, D., et al. 1991, APJ, 366, 64

Colbert, E. J. M., & Mushotzky, R. F. 1999, APJ, 519, 89

Cossins, P. J. 2010, PhD thesis, -

Cullen, L., & Dehnen, W. 2010, MNRAS, 408, 669

De Rosa, A., Uttley, P., Gou, L., et al. 2019, Science China Physics, Mechanics, and Astronomy, 62, 29504

De Rosa, G., Peterson, B. M., Ely, J., et al. 2015, APJ, 806, 128

Dexter, J., & Begelman, M. C. 2019, MNRAS, 483, L17

Doğan, S., Nixon, C., King, A., & Price, D. J. 2015, MNRAS, 449, 1251

Doğan, S., & Nixon, C. J. 2020, MNRAS, 495, 1148

Doğan, S., Nixon, C. J., King, A. R., & Pringle, J. E. 2018, MNRAS, 476, 1519

Edelson, R., Gelbord, J. M., Horne, K., et al. 2015, APJ, 806, 129

Edelson, R. A., Alexander, T., Crenshaw, D. M., et al. 1996, APJ, 470, 364

Farrell, S. A., Webb, N. A., Barret, D., Godet, O., & Rodrigues, J. M. 2009, Nature, 460, 73

Faulkner, J., Lin, D. N. C., & Papaloizou, J. 1983, MNRAS, 205, 359

Fausnaugh, M. M., Denney, K. D., Barth, A. J., et al. 2016, APJ, 821, 56

Francis, P. J., Hewett, P. C., Foltz, C. B., et al. 1991, APJ, 373, 465

Frank, J., King, A., & Raine, D. J. 2002, Accretion Power in Astrophysics: Third Edition, 398

Fromang, S., & Papaloizou, J. 2006, AAP, 452, 751

Gardner, E., & Done, C. 2017, MNRAS, 470, 3591

Gebhardt, K., Rich, R. M., & Ho, L. C. 2002, The Astrophysical Journal, 578, L41L45

Gebhardt, K., Rich, R. M., & Ho, L. C. 2005, APJ, 634, 1093

Gingold, R. A., & Monaghan, J. J. 1977, MNRAS, 181, 375

—. 1982, Journal of Computational Physics, 46, 429

Giustini, M., Miniutti, G., & Saxton, R. D. 2020, AAP, 636, L2

Goad, M. R., Korista, K. T., Rosa, G. D., et al. 2016, The Astrophysical Journal, 824, 11

Goad, M. R., Knigge, C., Korista, K. T., et al. 2019, MNRAS, 486, 5362

Greenhill, L. J., Jiang, D. R., Moran, J. M., et al. 1995, APJ, 440, 619

Greenhill, L. J., Booth, R. S., Ellingsen, S. P., et al. 2003, APJ, 590, 162

Hartmann, L., & Kenyon, S. J. 1996, Annual Review of Astronomy and Astrophysics, 34, 207

Hatchett, S. P., Begelman, M. C., & Sarazin, C. L. 1981, APJ, 247, 677

Hobson, M. P., Efstathiou, G. P., & Lasenby, A. N. 2005, General Relativity

Horne, K., De Rosa, G., Peterson, B. M., et al. 2020, arXiv e-prints, arXiv:2003.01448

Hoshi, R., & Shibazaki, N. 1977, Progress of Theoretical Physics - PROG THEOR PHYS KYOTO, 58, 1759

Kalogera, V., & Baym, G. 1996, APJL, 470, L61

Khachikian, E. Y., & Weedman, D. W. 1974, APJ, 192, 581

King, A. R., & Pringle, J. E. 2006, MNRAS, 373, L90

—. 2007, MNRAS, 377, L25

King, A. R., Pringle, J. E., & Hofmann, J. A. 2008, MNRAS, 385, 1621

King, A. R., Pringle, J. E., & Livio, M. 2007, MNRAS, 376, 1740

King, A. R., Pringle, J. E., West, R. G., & Livio, M. 2004, MNRAS, 348, 111

Koratkar, A., & Blaes, O. 1999, , 111, 1

Kormendy, J., & Richstone, D. 1995, ARA&A, 33, 581

Kraus, S., Kreplin, A., Young, A. K., et al. 2020, arXiv e-prints, arXiv:2004.01204

Kriss, G. A., De Rosa, G., Ely, J., et al. 2019, APJ, 881, 153

Lasota, J.-P. 2001, **??**jnlNew Ast., 45, 449

Lattimer, J. M. 2012, Annual Review of Nuclear and Particle Science, 62, 485

Lawrence, A. 2018, Nature Astronomy, 2, 102

Lense, J. 1918, Astronomische Nachrichten, 207, 161

Lense, J., & Thirring, H. 1918, Physikalische Zeitschrift, 19, 156

Liska, M., Hesp, C., Tchekhovskoy, A., et al. 2020, MNRAS, arXiv:1904.08428

Lodato, G., & Price, D. J. 2010, MNRAS, 405, 1212

Lodato, G., & Pringle, J. E. 2007, MNRAS, 381, 1287

Lodato, G., & Rice, W. K. M. 2004, MNRAS, 351, 630

Lubow, S. H., & Ogilvie, G. I. 2000, APJ, 538, 326

Lubow, S. H., & Ogilvie, G. I. 2000, The Astrophysical Journal, 538, 326

Lucy, L. B. 1977, AJ, 82, 1013

Lynden-Bell, D. 1969, Nature, 223, 690

Lynden-Bell, D., & Pringle, J. E. 1974, MNRAS, 168, 603

MacLeod, C. L., Ross, N. P., Lawrence, A., et al. 2016, MNRAS, 457, 389

Martin, R. G., Nixon, C. J., Pringle, J. E., & Livio, M. 2019, arXiv e-prints, arXiv:1901.01580

Mathur, S., Gupta, A., Page, K., et al. 2017, The Astrophysical Journal, 846, 55

Matthews, T. A., Morgan, W. W., & Schmidt, M. 1964, APJ, 140, 35

McClintock, J. E., Narayan, R., & Steiner, J. F. 2014, , 183, 295

McHardy, I. M., Connolly, S. D., Peterson, B. M., et al. 2016, Astronomische Nachrichten, 337, 500

McLure, R. J., & Jarvis, M. J. 2002, MNRAS, 337, 109

Meru, F., & Bate, M. R. 2012, MNRAS, 427, 2022

Meyer, F., & Meyer-Hofmeister, E. 1981, AAP, 104, L10

Miniutti, G., Saxton, R. D., Giustini, M., et al. 2019, Nature, 573, 381

Miyoshi, M., Moran, J., Herrnstein, J., et al. 1995, Nature, 373, 127

Monaghan, J. J. 1992, ARA&A, 30, 543

Monaghan, J. J., & Lattanzio, J. C. 1985, AAP, 149, 135

Morgan, C. W., Kochanek, C. S., Morgan, N. D., & Falco, E. E. 2010, APJ, 712, 1129

Morris, J. P., & Monaghan, J. J. 1997, Journal of Computational Physics, 136, 41

Natarajan, P., & Pringle, J. E. 1998, APJL, 506, L97

Nealon, R., Nixon, C., Price, D. J., & King, A. 2016, MNRAS, 455, L62

Nealon, R., Price, D., & Nixon, C. 2015, Monthly Notices of the Royal Astronomical Society, 448, doi:10.1093/mnras/stv014

Nelson, R. P., & Papaloizou, J. C. B. 2000, MNRAS, 315, 570

Nixon, C., & King, A. 2016, Warp Propagation in Astrophysical Discs, ed. F. Haardt, V. Gorini, U. Moschella, A. Treves, & M. Colpi, Vol. 905, 45

Nixon, C., King, A., & Price, D. 2013, Monthly Notices of the Royal Astronomical Society, 434, 19461954

Nixon, C., King, A., Price, D., & Frank, J. 2012a, APJL, 757, L24

Nixon, C. J., & King, A. R. 2012, MNRAS, 421, 1201

Nixon, C. J., King, A. R., & Price, D. J. 2012b, MNRAS, 422, 2547

Novikov, I. D., & Thorne, K. S. 1973, in Black Holes (Les Astres Occlus), 343–450

Ogilvie, G. I. 1999, MNRAS, 304, 557

—. 2000, MNRAS, 317, 607

Ogilvie, G. I., & Latter, H. N. 2013, MNRAS, 433, 2420

Paardekooper, S.-J., & Mellema, G. 2006, AAP, 459, L17

Paczyńsky, B., & Wiita, P. J. 1980, AAP, 500, 203

Papaloizou, J. C. B., & Lin, D. N. C. 1995, APJ, 438, 841

Papaloizou, J. C. B., & Pringle, J. E. 1983, MNRAS, 202, 1181

Pei, L., Fausnaugh, M. M., Barth, A. J., et al. 2017, APJ, 837, 131

Peterson, B. M. 1993, , 105, 247

—. 1997, An Introduction to Active Galactic Nuclei

—. 2014, , 183, 253

Peterson, B. M., & Horne, K. 2004, Astronomische Nachrichten, 325, 248

Peterson, B. M., & Wandel, A. 1999, APJL, 521, L95

Peterson, B. M., & Wandel, A. 2000, The Astrophysical Journal, 540, L13

Price, D. J. 2012, Journal of Computational Physics, 231, 759

Pringle, J. E. 1981, ARA&A, 19, 137

—. 1992, MNRAS, 258, 811

—. 1996, MNRAS, 281, 357

—. 1997, MNRAS, 292, 136

Pringle, J. E., & Rees, M. J. 1972, AAP, 21, 1

Remillard, R. A., & McClintock, J. E. 2006, ARA&A, 44, 49

Reynolds, C. S. 2014, , 183, 277

Rhoades, C. E., & Ruffini, R. 1974, Phys. Rev. Lett., 32, 324

Salpeter, E. E. 1964, APJ, 140, 796

Schandl, S., & Meyer, F. 1994, AAP, 289, 149

Schechter, P. L., Pooley, D., Blackburne, J. A., & Wambsganss, J. 2014, The Astrophysical Journal, 793, 96

Scheuer, P. A. G., & Feiler, R. 1996, MNRAS, 282, 291

Schödel, R., Ott, T., Genzel, R., et al. 2002, Nature, 419, 694

Shakura, N. I., & Sunyaev, R. A. 1973, AAP, 24, 337

Shapiro, S. L., & Teukolsky, S. A. 1983, Black holes, white dwarfs, and neutron stars : the physics of compact objects

Shappee, B. J., Prieto, J. L., Grupe, D., et al. 2014, APJ, 788, 48

Sniegowska, M., Czerny, B., Bon, E., & Bon, N. 2020, arXiv e-prints, arXiv:2007.06441

Soltan, A. 1982, MNRAS, 200, 115

Springel, V. 2010, ARA&A, 48, 391

Springel, V., & Hernquist, L. 2002, MNRAS, 333, 649

Starkey, D., Horne, K., Fausnaugh, M. M., et al. 2017, APJ, 835, 65

Starkey, D. A., Horne, K., & Villforth, C. 2016, MNRAS, 456, 1960

Toomre, A. 1964, APJ, 139, 1217

Urry, C. M., & Padovani, P. 1995, , 107, 803

Volonteri, M. 2010, AAPR, 18, 279

Von Neumann, J., & Richtmyer, R. D. 1950, Journal of Applied Physics, 21, 232

Warner, B. 2003, Cataclysmic Variable Stars, doi:10.1017/CBO9780511586491

White, R. J., & Peterson, B. M. 1994, , 106, 879

Willott, C. J., McLure, R. J., & Jarvis, M. J. 2003, APJL, 587, L15

Wu, X.-B., Wang, F., Fan, X., Yi, W., & et al. 2015, Nature, 518, 512

Zel'dovich, Y. B. 1964, Soviet Physics Doklady, 9, 195

Zhang, S. N., Cui, W., & Chen, W. 1997, APJL, 482, L155

Zoghbi, A., Miller, J. M., King, A. L., et al. 2016, APJ, 833, 165

Zu, Y., Kochanek, C. S., & Peterson, B. M. 2011, APJ, 735, 80

Appendices

APPENDIX A

Steady disc surface density

Following Frank et al. (2002), we use mass conservation and angular momentum conservation for a steady state disc. The mass conservation equation is given as:

$$R\frac{\partial \Sigma}{\partial t} + \frac{\partial}{\partial R}\left(R\Sigma V_R\right) = 0\,. \tag{A.1}$$

where the radial velocity,

$$V_R = -\frac{3}{\Sigma R^{1/2}}\frac{\partial}{\partial R}(\nu \Sigma R^{1/2}). \tag{A.2}$$

Using the steady-state assumption ($\partial/\partial t = 0$) in equation A.1 gives

$$\frac{\partial}{\partial R}\left(R\Sigma V_R\right) = 0 \implies R\Sigma V_R = \text{const.} \tag{A.3}$$

Dimensionally this constant is a mass flow rate, and we can define the mass accretion rate through the disc as

$$2\pi R\Sigma\left(-V_R\right) = \dot{M}\,, \tag{A.4}$$

As the disc is time steady, $\dot{M}$ must be a constant with radius and time. The angular momentum conservation equation is

$$R\frac{\partial}{\partial t}\left(\Sigma R^2\Omega\right) + \frac{\partial}{\partial R}\left(R\Sigma V_R R^2\Omega\right) = \frac{1}{2\pi}\frac{\partial G}{\partial R} \tag{A.5}$$

where

$$G = 2\pi R\nu\Sigma R^2\Omega' \,. \tag{A.6}$$

Using a steady state assumption gives

$$R\Sigma V_R R^2\Omega = \frac{G}{2\pi} + \frac{C}{2\pi} \,, \tag{A.7}$$

where C is a constant. Rearranging gives

$$-\nu\Sigma\Omega' = \Sigma\left(-V_R\right)\Omega + \frac{C}{2\pi R^3} \,. \tag{A.8}$$

To evaluate the constant C, we must apply a boundary condition at $R_{\rm in}$. For black hole accretion, matter typically accretes at $R_{\rm in}$ and plunges dynamically into the hole (see Appendix B), and thus the torque is zero (i.e. $\Omega' = 0$). This gives

$$2\pi R\Sigma\left(-V_R\right)R^2\Omega + C = 0 \implies C = -\dot{M}R_{\rm in}^2\Omega_{\rm in}. \tag{A.9}$$

where we have used (A.4) to replace V_R. Putting this into (A.8) and rearranging gives

$$\nu\Sigma = \frac{\dot{M}}{2\pi}\frac{\left[R_{\rm in}^2\Omega_{\rm in}/R^2\Omega - 1\right]}{R\left(\Omega'/\Omega\right)} \,, \tag{A.10}$$

and

$$\nu\Sigma = \frac{\dot{M}_{\rm in}}{2\pi}\frac{\left[R_{\rm in}^2\Omega_{\rm in}/R^2\Omega - 1\right]}{R\left(\Omega'/\Omega\right)} \quad \text{for} \quad R < R_{\rm add} \,. \tag{A.11}$$

This provides the solution for Σ inside the radius at which mass is added in the disc, at a radius $R_{\rm add}$. For $R > R_{\rm add}$, we must use a different boundary condition. We can apply the zero-torque outer boundary condition at $R_{\rm out}$ and we define $\dot{M}_{\rm out} = 2\pi R\Sigma V_R$ (in this part of the disc, mass is flowing outwards). Zero-torque at $R_{\rm out}$ gives

$$-\Sigma V_R\Omega + \frac{C}{2\pi R^3} = 0 \implies C = \dot{M}_{\rm out}R_{\rm out}^2\Omega_{\rm out} \,. \tag{A.12}$$

Therefore,

$$\nu\Sigma = \frac{\dot{M}_{\rm out}}{2\pi}\frac{[1-R_{\rm out}^2\Omega_{\rm out}/R^2\Omega]}{R\,(\Omega'/\Omega)} \quad \text{for} \quad R > R_{\rm add}\,. \tag{A.13}$$

We require $\Sigma(R)$ to be continuous at $R_{\rm add}$, and we use the fact that the total mass added must equal the mass leaving the two boundaries, i.e.

$$\dot{M}_{\rm add} = \dot{M}_{\rm in} + \dot{M}_{\rm out}\,. \tag{A.14}$$

Continuity at $R_{\rm add}$ implies

$$\frac{\dot{M}_{\rm in}}{2\pi}\left[R_{\rm in}^2\Omega_{\rm in}/R_{\rm add}^2\Omega_{\rm add}-1\right] = \frac{\dot{M}_{\rm out}}{2\pi}\left[1-R_{\rm out}^2\Omega_{\rm out}/R_{\rm add}^2\Omega_{\rm add}\right]\,. \tag{A.15}$$

This implies

$$f = \frac{\dot{M}_{\rm in}}{\dot{M}_{\rm out}} = \frac{R_{\rm add}^2\Omega_{\rm add}-R_{\rm out}^2\Omega_{\rm out}}{R_{\rm in}^2\Omega_{\rm in}-R_{\rm add}^2\Omega_{\rm add}}\,, \tag{A.16}$$

and this can be combined with (A.14) to give

$$\dot{M}_{\rm out} = \frac{\dot{M}_{\rm add}}{1+f} \quad \& \quad \dot{M}_{\rm in} = \frac{f\dot{M}_{\rm add}}{1+f}\,. \tag{A.17}$$

Therefore, the final disc structure is given by

$$\nu\Sigma = \begin{cases} \dfrac{f\dot{M}_{\rm add}}{2\pi(1+f)}\dfrac{[R_{\rm in}^2\Omega_{\rm in}/R^2\Omega-1]}{R\,(\Omega'/\Omega)} & \text{for} \quad R \le R_{\rm add} \\ \dfrac{\dot{M}_{\rm add}}{2\pi(1+f)}\dfrac{[1-R_{\rm out}^2\Omega_{\rm out}/R^2\Omega]}{R\,(\Omega'/\Omega)} & \text{for} \quad R > R_{\rm add} \end{cases}$$

APPENDIX B

Innermost Stable Circular Orbit

The innermost stable circular orbit or ISCO is a key concept considered when studying circular orbits around black holes. Consider a blob of gas or matter at a large radii in an accretion disk spiralling in through a sequence of circular orbits as it viscously loses its angular momentum. When the gas reaches the ISCO, no more stable circular orbits are available and the gas free falls into the black hole. Therefore, the ISCO serves effectively as the inner edge of the accretion disc.

1 Paczynski-Wiita Potential

Paczynski realized that a properly chosen gravitational potential is needed to accurately model the general relativistic effects that determine motion of matter near black holes. Therefore, the Paczynski-Wiita potential was proven to be a practical choice (Paczyński & Wiita, 1980), used by numerous researchers in the black hole accretion theory. The energy equation for a test particle orbiting a point mass is given as

$$E = \frac{v^2}{2} + \Phi \tag{B.1}$$

where E is the total energy, $\frac{v^2}{2}$ and Φ represent the kinetic and potential energies. Using cylindrical polars (R, θ) we have

$$v^2 = \dot{r^2} + r^2\dot{\theta^2} \tag{B.2}$$

with specific angular momentum h given as

$$h = r^2\dot{\theta}. \tag{B.3}$$

We have

$$\frac{h^2}{r^2} = \frac{r^4\dot{\theta^2}}{r^2} = r^2\dot{\theta^2}. \tag{B.4}$$

Hence,

$$\frac{v^2}{2} = \frac{\dot{r^2}}{2} + \frac{h^2}{2r^2}. \tag{B.5}$$

where $\dot{r} = 0$ for a circular orbit. Therefore,

$$\frac{v^2}{2} = \frac{h^2}{2r^2}. \tag{B.6}$$

Thus, equation (B.1) for a circular orbit becomes,

$$E = \frac{h^2}{2r^2} + \Phi. \tag{B.7}$$

Furthermore, the equation for the Paczynski-Wiita potential is given as:

$$\Phi_{PW} = -\frac{GM}{r - R_s} \tag{B.8}$$

where R_s is the Schwarzschild radius,

$$R_s = \frac{2GM}{c^2}. \tag{B.9}$$

Energy equation for the Paczynski-Wiita potential is given by

$$E = \frac{h^2}{2r^2} + \Phi_{PW}. \tag{B.10}$$

Substituting equation (B.8) in equation (B.10) gives

$$E = \frac{h^2}{2r^2} - \frac{GM}{r - R_s}. \tag{B.11}$$

For a circular orbit, the total energy is a constant and $\dot{r} = 0$. We have $E = V_{\text{eff}}$ and therefore $\frac{dV_{\text{eff}}}{dr} = 0$. Thus,

$$V_{\text{eff}} = \frac{h^2}{2r^2} - \frac{GM}{r - R_s} \tag{B.12}$$

and

$$\frac{dV_{\text{eff}}}{dr} = -\frac{h^2}{r^3} + \frac{GM}{(r - R_s)^2} = 0, \tag{B.13}$$

$$\frac{h^2}{r^3} = \frac{GM}{(r - R_s)^2}. \tag{B.14}$$

Therefore,

$$h^2 = \frac{GMr^3}{(r - R_s)^2} \tag{B.15}$$

where h is the specific angular momentum of a point mass particle at Paczynski-Wiita potential. To check if the Paczynski-Wiita potential has a point of local minima and calculate its location of the innermost stable orbit, we perform the second derivative test.

If the first derivative of the effective potential is zero at a certain point, then we have a circular orbit there. Its second derivative at the same point determines if the orbit is stable or unstable via

- < 0 : This gives the local maximum value where the orbit is unstable.
- > 0 : This is local minimum value where the orbit is stable.

Therefore, the second derivative of equation (B.12) is given by

$$\frac{d^2V_{\text{eff}}}{dr^2} = \frac{3h^2}{r^4} - \frac{2GM}{(r-R_s)^3}. \tag{B.16}$$

Substituting equation (B.15) in equation (B.16) gives

$$\frac{d^2V_{\text{eff}}}{dr^2} = \frac{3GM}{r(r-R_s)^2} - \frac{2GM}{(r-R_s)^3}, \tag{B.17}$$

$$\frac{d^2V_{\text{eff}}}{dr^2} = \frac{3GMr - 3GMR_s - 2GMr}{(r-R_s)^3} = \frac{GMr - 3GMR_s}{(r-R_s)^3}. \tag{B.18}$$

We do the second derivative test (where $\frac{d^2V_{\text{eff}}}{dr^2} \geq 0$), which gives

$$\frac{GM(r-3R_s)}{(r-R_s)^3} \geq 0 \tag{B.19}$$

and

$$r \geq 3R_s. \tag{B.20}$$

The radius of the innermost stable orbit for Paczynski-Wiita is therefore, $R_{\text{ISCO}} = 3R_s = 6GM/c^2$ same as that of a Schwarzschild black hole. This conveys that stable orbits exist at values $\geq 3R_s$ and orbits are unstable at values of $r < 3\ R_s$.

2 Einstein Potential

Einstein potential Φ_E is given as:

$$\Phi_E = \frac{-GM}{r}\left(1 + \frac{3R_g}{r}\right) \tag{B.21}$$

where R_g is the gravitational radius. Energy equation in this case is given by:

$$E = \frac{h^2}{2r^2} + \Phi_E, \tag{B.22}$$

Since $E = V_{\text{eff}}$ and $\frac{dV_{\text{eff}}}{dr} = 0$, we have

$$V_{\text{eff}} = \frac{h^2}{2r^2} - \frac{GM}{r} - \frac{3GMR_g}{r^2} \tag{B.23}$$

and the first derivative gives

$$\frac{dV_{\text{eff}}}{dr} = -\frac{h^2}{r^3} + \frac{GM}{r^2} + \frac{6GMR_g}{r^3} = 0, \tag{B.24}$$

$$\frac{1}{r^3}\left(6GMR_g - h^2\right) = -\frac{GM}{r^2}, \tag{B.25}$$

$$6GMR_g - h^2 = -GMr. \tag{B.26}$$

Hence,

$$r = \frac{h^2}{GM} - 6R_g. \tag{B.27}$$

This proves that for Einstein potential, circular orbits are possible at any radius. In order to determine if the orbits are stable or not, we consider the second derivative test. Our aim is now to check, if the second derivative of the effective potential with respect to the radius is less than or greater than zero at a value with

$$h^2 = 6GMR_g + GMr. \tag{B.28}$$

The second derivative of equation B.23 gives,

$$\frac{d^2V_{\text{eff}}}{dr^2} = \frac{3h^2}{r^4} - \frac{2GM}{r^3} - \frac{18GMR_g}{r^4}. \tag{B.29}$$

Substituting equation B.28 in B.29 gives

$$\frac{d^2V_{\text{eff}}}{dr^2} = \frac{3(6GMR_g + GMr)}{r^4} - \frac{2GM}{r^3} - \frac{18GMR_g}{r^4}. \tag{B.30}$$

This becomes,

$$\frac{d^2V_{\text{eff}}}{dr^2} = \frac{18GMR_g}{r^4} + \frac{3GMr}{r^4} - \frac{2GM}{r^3} - \frac{18GMR_g}{r^4}. \tag{B.31}$$

Therefore,

$$\frac{d^2V_{\text{eff}}}{dr^2} = \frac{GM}{r^3} > 0 \tag{B.32}$$

which is therefore the local minimum value. This concludes that, stable circular orbits are possible in the Einstein potential for any value of radius. As discussed in chapter 3, the Einstein potential is useful as it provides a good description of the apsidal precession rate for a disc around a black hole (Nelson & Papaloizou, 2000). However, a drawback of the Einstein potential is that it cannot produce ISCO.